Cover Page

Universiteit Leiden

Author: Vos, J.G.
Title: Selectivity and competition between the anodic evolution of oxygen and chlorine
Issue Date: 2019-12-04

SELECTIVITY and COMPETITION

between the

ANODIC EVOLUTION of OXYGEN and CHLORINE

JOHANNES GODFRIED VOS

Selectivity and competition between the anodic evolution of oxygen and chlorine

Proefschrift

ter verkrijging van
de graad van Doctor aan de Universiteit Leiden,
op gezag van Rector Magnificus prof.mr. C.J.J.M. Stolker,
volgens besluit van het College voor Promoties
te verdedigen op woensdag 4 december 2019
klokke 12:30 uur

door

Johannes Godfried Vos

geboren te 's Gravenhage in 1987

Samenstelling promotiecommissie

Promotor: Prof. dr. Marc T.M. Koper (Universiteit Leiden)

Copromotor: Prof. dr. G. Mul (Universiteit Twente)

Overige leden: Prof. dr. H.S. Overkleeft (Universiteit Leiden)

                     Prof. dr. H.J.M. de Groot (Universiteit Leiden)

                     Dr. P. Krtil (The Czech Academy of Sciences, Czech Republic)

                     Prof. dr. A. Cornell (KTH Royal Institute of Technology, Sweden)

"Whatever is rightly done, however humble, is noble"

Henry Royce

Contents

1

1.1. Electrochemistry at the center of future energy

Humanity faces important environmental challenges in the coming century. The most pressing of these issues is by far the global rise in CO_2 emissions, which has significantly disbalanced the earth's natural carbon cycle since the start of the industrial revolution.[1] To prevent climate change, which may have highly detrimental consequences for humanity's prosperity, the world economy will have to make significant changes in its energy infrastructure.

The issue of carbon-induced climate change is intimately coupled to a more general one, which is the source of energy used for driving human enterprise. Since the industrial revolution, humanity has been almost exclusively dependent on the burning of fossil fuels for its energy needs and economic development.[2] Besides their environmental impact, fossil fuels are inherently constrained by political instability, as well as ultimately by their limited supply.[3]

The most compelling alternative to fossil fuels is solar energy, where radiation emitted by the sun may be captured using photovoltaics.[4] This leads to the direct generation of electricity, which is the most useful form of energy. This generated electricity can facilitate virtually every function that fossil fuels serve present day, and it is essentially an endless source of energy since the sun is eternal within a human lifetime.[5–7]
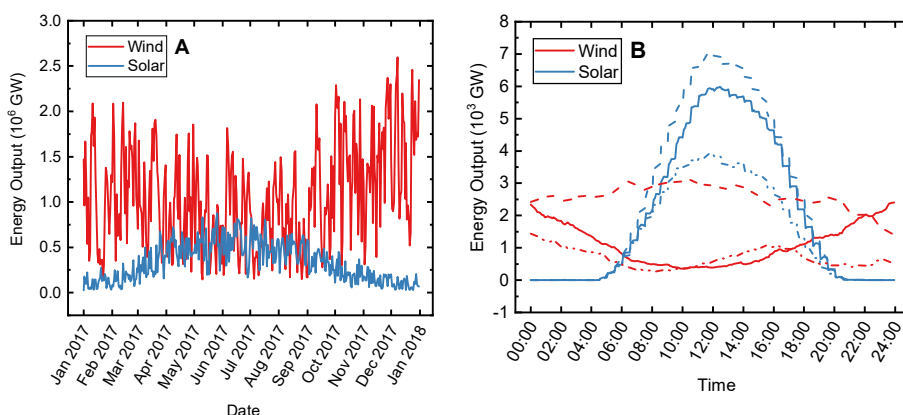
Figure 1.1: Power output data of the UK power grid, showing wind and solar, during the year 2017 (A), as well as three consecutive days around the end of May, 2017 (B). Data downloaded from https://gridwatch.co.uk/, October 2018.

Electrical energy can be involved in inducing chemical transformations; this is the domain of electrochemistry.[8] Electrochemical reactions can play a key role in rebalancing the world's carbon footprint, which requires that the net emission of carbon into the atmosphere must be reduced. Instead of burning fossil fuels and harnessing the resulting heat and gas expansion work, energy from the sun is converted to electrical energy which can then be coupled to the making and breaking of chemical bonds. An electrochemistry-facilitated method for harnessing solar energy that especially appeals to the imagination is water electrolysis coupled to fuel cells, where hydrogen (H_2) is used as energy carrier.[9–11] Only water, H_2 gas and oxygen

gas (O_2) are involved as chemicals, making the overall process extremely environmentally friendly. In effect, one can use it to power a car or any other electrical device with nothing but solar energy and water. The process can serve as a means to capture and store energy from solar power and other renewables. This is direly needed, since photovoltaic devices and wind turbines, which are the primary sources of renewable electricity, have a highly intermittent output (see Figure 1.1).[12–14]
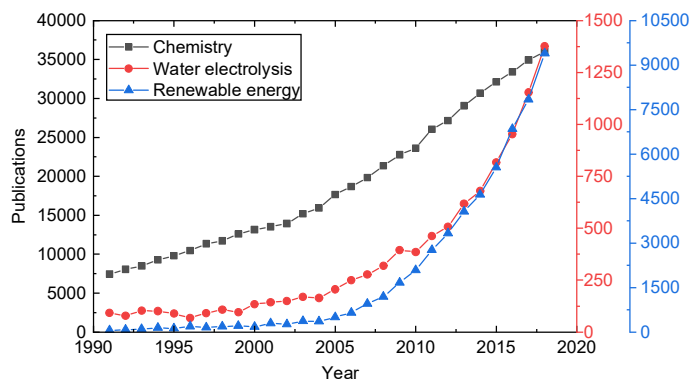
Figure 1.2: Publications since 1990 related to topics "Water electrolysis" and "Renewable energy", compared to publication output related to the more general term "Chemistry". Data downloaded from Web of Science (webofknowledge.com), September 2019.

Electrochemical processes related to energy storage have always been associated with high capital costs due to the price of electricity and the necessary electrolyzer designs.[15,16] Additionally, the most attractive of these processes are plagued by energy efficiency problems that have yet to be resolved. In case of the aforementioned combination of water electrolysis and fuel cells, these issues are caused in large part by the slow reactivity of O_2-related reactions.[17–20] They will be discussed in more detail throughout this thesis.
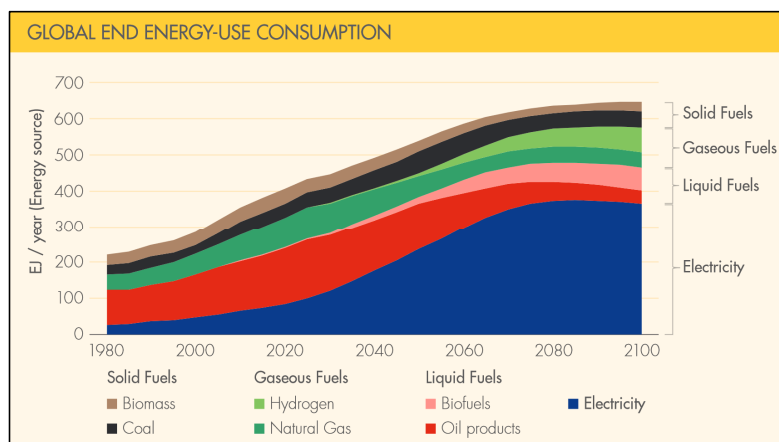
Figure 1.3: Predicted distribution of world-wide energy consumption up until 2100. Image and data by Shell, from Shell Sky Scenario (October 2018).

Fortunately, the research interest in electrochemistry and sustainable energy research has increased significantly in recent years (Figure 1.2); this trend has been driven in part by increasing public awareness of climate change and the recent Paris climate agreement.[21] Electrochemistry will play an increasingly important role in the decades to come as the world energy infrastructure becomes more and more electrified (Figure 1.3).

1.2. Water electrolysis and the oxidation of chloride

As mentioned in section 1.1, electrical energy can be used in an electrolyzer that generates H_2 on the cathode and O_2 on the anode, splitting water according to:

$$2\,H_2O \rightarrow 2\,H_2 + O_2 \qquad \text{Eq. 1.1}$$

The H_2 produced according to Eq. 1.1 can be said to contain the energy input that was used to drive the reaction. It can be stored, transported and used as feedstock in a fuel cell where it is recombined with atmospheric O_2 to form water. This route of energy capture, storage and utilization avoids the burning of fossil fuels if electricity generated by renewables is used. Moreover, it then has zero net-emission of CO_2 and does not involve environmental pollutants in any of its stages. The overall splitting reaction proceeds as two half-reactions within the electrolyzer, where H_2 is produced by the reduction of protons in the aqueous solution:

$$2\,H^+ + 2\,e^- \rightarrow H_2 \qquad \text{Eq. 1.2}$$
$$E^0_{H^+/H_2} = 0 \text{ V vs. RHE}$$

Another promising electrochemical approach for achieving zero net-carbon emissions is to capture CO_2 at emission hotspots and convert it to useful starting materials. Instead of directly targeting protons, the cathodic reaction is then the reduction of CO_2, which can lead to a wide range of useful products, such as methanol, ethylene, or CO (shown below):[22–24]

$$CO_2 + 2\,H^+ + 2\,e^- \rightarrow CO + H_2O \qquad \text{Eq. 1.3}$$
$$E^0_{CO_2/CO} = -0.11 \text{ V vs. RHE}$$
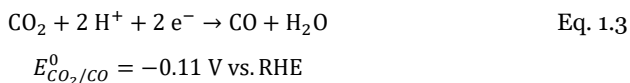
Regardless of the reduction reaction, it must always be coupled to an oxidation reaction to complete the electrochemical device. This reaction can be the oxidation of water to form oxygen (O_2), which is essentially a by-product:

$$2\,H_2O \rightarrow O_2 + 4\,H^+ + 4\,e^- \qquad \text{Eq. 1.4}$$
$$E^0_{O_2/H_2O} = 1.229 \text{ V vs. RHE}$$

Eq. 1.4 is known as the Oxygen Evolution Reaction (OER). It is a highly desirable counter reaction because water as a reactant is readily available on earth, and O_2 is environmentally harmless, meaning that it can be safely released into the atmosphere.

It must be noted that industrial-scale electrolysis would require large amounts of water as feedstock. However, freshwater on earth is a precious and scarce commodity. Furthermore, areas where the influx of renewable energy from wind and solar are the highest, are often at or near the sea.[25–27] Seawater, which is also vastly more earth-abundant than freshwater, would thus be a much better substrate for use in large-scale electrolysis.[25,27,28] The original idea of a 'hydrogen economy', as first proposed by Bockris in the 1970s, was in fact based on the direct electrochemical splitting of seawater using nuclear or solar power near arid sea coasts, where the influx of solar energy is high and reliable.[9,26] Saline water, which contains high concentrations of chloride ions (~0.6 M), unfortunately raises a major challenge when used as substrate in an electrolyzer; in chloride solutions, Cl^- may oxidize to form labile and powerful oxidizing agents, such as chlorine gas (Cl_2).[29–32] Contrary to O_2, such species cannot be easily disposed of in an environmentally friendly way, and the rate of their formation usually dwarfs the rate of the OER, as will be discussed in more detail below.

The reaction where Cl_2 is formed directly from Cl^- is termed the Chlorine Evolution Reaction (CER). The CER is highly unwanted in electrolyzers where only the cathodic reaction is of interest, such as for renewable energy storage. There are however several areas of industry where chloride oxidation is a reaction of great importance, such as the chlor-alkali process.[33–35] The CER is the desired anodic reaction in this process, where brine (concentrated NaCl) is electrolyzed according to:

$$2\,H_2O + 2\,Na^+ + 2\,Cl^- \rightarrow H_2 + Cl_2 + 2\,Na^+ + 2\,OH^- \qquad\qquad \text{Eq. 1.5}$$
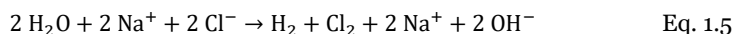
The jointly generated Cl_2 and NaOH are bulk chemicals that underpin approximately 50% of the global chemical industry.[36–39] The chlor-alkali process is very energy intensive; the required power input to drive chlorine formation is the most significant economic (and environmental) cost.[33,40–42] In 2006 the process consumed approximately 334 PJ of electrical energy in the U.S. alone.[43] A substantial body of research has thus gone in studying optimum process conditions for the CER, since the large scale of the process means that even small efficiency gains can have a large impact.[34,44,45] In this regard, the OER is highly unwanted in the chlor-alkali process; the formation of O_2 not only compromises the overall process efficiency and catalyst stability, but also represents a safety risk.[34,35,46–48] Competition between the OER and CER is also relevant to electrochemical water treatment, where strongly oxidizing 'active chlorine' may be electrochemically generated to eliminate pollutants.[49–51] However, its formation has to be tightly controlled or is sometimes unwanted.[52,53] Finally, the OER is usually the sole desired counter reaction in electrowinning, where the electrolysis bath often contains traces of chloride.[54] The OER and CER thus both lie at the heart of large-scale electricity-to-chemical conversion steps, which makes them highly important to a renewable-based energy infrastructure.

Both the OER and CER have been the subject of intense study over the past five decades, with significant improvements in catalyst performance for both of them.[33] They are most readily catalyzed on metal oxides.[55–57] The CER is usually carried out in acidic media because of thermodynamic restrictions (see section 1.3), on anodes made of mixtures of RuO_2 and TiO_2,

so-called Dimensionally Stable Anodes (DSA®).[33] Pt is also known to catalyze the CER at high intrinsic rates, but suffers from inhibition due to transient formation of platinum oxides (see Chapter 4).[58] The OER can be carried out in a wide pH range, but performance wise, the current state of the art is represented by polymer electrolyte membrane (PEM) electrolyzers which employ acidic pH and are equipped with Ir-based mixed metal oxides.[59] Unfortunately, Ir is a highly scarce, expensive material, and the strong reliance of acidic PEM electrolyzers on Ir forms a severe bottleneck against wide-spread implementation. Major research effort is currently being devoted to finding alternatives that are stable and OER-active in an acidic environment without relying on rare precious metals.[60–62]

1.3. Kinetics and competition of the OER and CER

The oxidation of Cl^- in aqueous media can lead to a variety of products. In acidic media, the CER is the thermodynamically preferred reaction, which can be written as:

$$2\,Cl^- \rightarrow Cl_2 + 2\,e^- \qquad\qquad \text{Eq. 1.6}$$

$$E^0_{Cl_2/Cl^-} = (1.358 + 0.059\text{pH})\,\text{V vs. RHE}$$
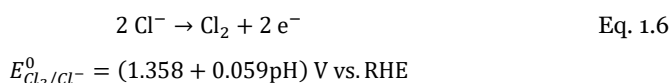
In acidic aqueous solution, the CER has an equilibrium potential that is close to the OER (Eq. 1.4), and will therefore be a competing reaction. The OER is a notoriously slow reaction for which no perfect catalyst has been found yet, despite enormous research efforts. Its difficult kinetics lead to a significant overpotential (typically between 0.25 - 0.35 V) and corresponding energy losses. This is one of the reasons that large-scale energy storage by means of water electrolysis has not yet been realized.[20,63–66] The difficulty of catalyzing the OER lies in its four-electron nature, which implicates a complex reaction pathway involving a minimum of three or even four intermediates.[64,67,68] The CER on the other hand involves the transfer of only two electrons and presumably only a single catalytic intermediate, therefore it is intrinsically a much faster reaction.[68] It was previously estimated that the CER exchange current density is 4-7 orders of magnitude higher than that of the OER.[25] For a pH of around 1-2, this leads to the situation that Cl_2 can be evolved exclusively, despite the thermodynamic preference for the OER. In fact, the facile CER kinetics relative to the OER is what makes it possible to vigorously evolve chlorine in acidic aqueous media during the chlor-alkali process, with minimal anodic decomposition of the aqueous solvent.

Note that the equilibrium potential for the OER is pH-dependent, and therefore pH-independent on the reversible hydrogen electrode (RHE) scale, whereas the reverse is true for the CER. The selectivity between the OER and oxidation of chloride is thus expected to shift with differences in bulk acidity. As the solution pH increases, there is an increasing thermodynamic preference towards the formation of hypochlorous acid or hypochlorite:[29]

$$Cl^- + H_2O \rightarrow HClO + H^+ + 2\,e^- \qquad\qquad \text{Eq. 1.7}$$

$$E^0_{HClO/Cl^-} = (1.482 + 0.030\text{pH})\,\text{V vs. RHE}$$

$$Cl^- + H_2O \rightarrow ClO^- + 2\,H^+ + 2\,e^- \qquad\qquad \text{Eq. 1.8}$$
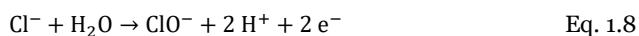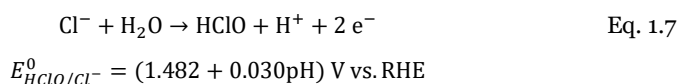
$$E^0_{ClO^-/Cl^-} = 1.636 \text{ V vs. RHE}$$

These reactions come into play because higher pH favors the disproportionation of Cl_2 into HClO and ClO^-, according to:

$$Cl_2(aq) + H_2O \rightleftharpoons HClO(aq) + H^+ + Cl^- \qquad \text{Eq. 1.9}$$

$$pK_a = 2.98$$

$$HClO(aq) \rightleftharpoons H^+ + ClO^- \qquad \text{Eq. 1.10}$$
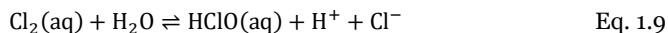
$$pK_a = 7.53$$

From Eq. 1.9 and Eq. 1.10, the reactions in Eq. 1.7 and Eq. 1.8 have equilibrium potentials equivalent to the CER at pH $\approx$ 4 and pH $\approx$ 4.7, respectively. The extent to which these reactions compete with the CER has never been investigated, since the rapid disproportionation of Cl_2 in alkaline media makes it difficult to quantify them. We will offer an indirect indication of their occurrence based on arguments and data from sections 2.3.1 and 8.3.2. The CER is by far the most studied reaction, as it is the most relevant industrially (see section 1.2). At pH values higher than 7, the competition between this reaction and the OER becomes dictated by thermodynamics. While this is a useful practical approach for enhancing OER selectivity over the oxidation of chloride, it prohibits an in-depth investigation in how the reactions interact mechanistically.

Although the OER and CER look like fundamentally different reactions at first glance, it has often been observed that their activities are coupled; catalyst materials proficient at the OER are often also highly active for the CER.[55,69–71] This implies that the two reactions have a similar active site, or partially shared reaction pathways. It also suggests that the key intermediates related to oxygen and chlorine have similar binding modes on OER catalysts. This leads to a so-called scaling relationship between them, as has been suggested by recent work using Density Functional Theory (DFT) to study possible kinetic mechanisms of the OER and CER.[72–77] Existence of such a scaling implies that control over selectivity between the two reactions can be a serious challenge. It may be difficult, if not impossible, to efficiently separate the two reactions on the basis of kinetic considerations alone, such as by finding an appropriate catalyst.[71,78,79]

The OER is usually accompanied by catalyst degradation, which is a major problem for the durability of practical electrolyzers.[80–82] For pure metal oxides, the OER activity and extent of catalyst degradation have been directly correlated,[81,83] implying an additional 'scaling relation' between the evolution of O_2 and some catalyst dissolution pathway.[84] However, it has also been reported that OER activity and catalyst degradation can be decoupled, such as by mixing with appropriate heterometal oxides.[85,86] The CER also seems to correlate with catalyst degradation, but not in the same way that the OER does.[87–90]

1.4. Review of microkinetic models

The OER is a highly complex reaction that proceeds through at least three reaction intermediates, which can be written schematically as S-OH, S=O and S-O-OH, where S denotes a surface site on the catalyst.[91–93] There is involvement of multiple intermediates simultaneously adsorbed on the surface, and the reaction pathway may also diverge; O-O bond formation may take place through the conversion of the 'oxo' intermediate S=O into the 'peroxo' intermediate S-O-OH, or through a (non-electrochemical) recombination of two oxo-intermediates.[94–97] Mars-van Krevelen type behavior, where lattice oxygen in the catalyst surface itself actively participates and reconstructs during the reaction, has been repeatedly observed,[65,98–100] as well as a dependency of the apparent OER kinetics on gas transport and the porosity of the used catalyst.[101–104] The OER is thus best studied on simplified, non-porous model surfaces (such as single crystals),[105–107] which falls outside the scope of this thesis. We will therefore mostly refrain from modelling kinetic parameters measured during the evolution of oxygen.

In contrast to the OER, a microkinetic model of the CER is more straightforward, because the reaction involves the transfer of only two electrons. In the following, we will discuss kinetic models for the CER, summarizing from existing literature.[35,108–113] This discussion is also relevant to other two-step mechanisms involving two electrons, such as the evolution of bromine or hydrogen. In the literature, the first step towards the formation of Cl_2 is typically assumed to be the fast adsorption and discharge of a chloride atom on the catalyst surface, termed the Volmer step (Eq. 1.11):

$$Cl^- + * \rightleftarrows Cl^* + e^- \qquad \text{Eq. 1.11}$$

Here, $*$ represents a free catalytic site, and Cl^* is a reactive chlorine intermediate adsorbed on the surface. On metal oxide catalysts such as RuO_2 and IrO_2, the exact nature of $*$ and Cl^* in Eq. 1.11 has not been completely resolved. It is probably intricately coupled to the surface chemistry of the oxide, as the CER rate has been shown to be slowed down by H^+ in very high concentrations.[35,56] Eq. 1.11 is thus likely a simplification, but the reaction it represents is not rate-limiting as long as extremely low pH (< 0) is avoided. The Cl^* surface coverage θ_{Cl} is then in quasi-equilibrium with the subsequent rate-limiting step, and can be written as a fraction (between 0 and 1) of the 'maximum coverage'. As a further approximation, one can assume that the adsorption of chloride obeys the Langmuir isotherm, based on the mean-field approximation.[114] The adsorption of Cl^* can then be described by:

$$\theta_{Cl} = \frac{K_{Cl}[Cl^-]e^{f\eta}}{K_{Cl}[Cl^-]e^{f\eta} + 1} \qquad \text{Eq. 1.12}$$

In Eq. 1.12, η is an overpotential defined as $\eta = E - E^0$, where E^0 can be the standard equilibrium potential of the overall reaction, or any other suitable reference potential. K_{Cl} is then the chloride adsorption constant at $\eta = 0$, $[Cl^-]$ is the chloride concentration, and $f = F/(RT)$.

The Volmer discharge is thought to be followed by several different types of step, depending on the catalyst material and system conditions. In the Heyrovský step, the evolution of a Cl_2 molecule follows from an electron transfer reaction between Cl^* and a second Cl^- ion from solution, reminiscent of the Eley–Rideal mechanism in heterogeneous gas-phase reactions:

$$Cl^* + Cl^- \rightleftarrows Cl_2 + e^- + * \qquad \text{Eq. 1.13}$$

At overpotentials high enough that the backward reaction of Eq. 1.13 is negligible, the j vs. E relationship predicted by the Volmer-Heyrovský (V-H) mechanism can be written as:

$$j_{VH} = 2Fk_H\theta_{Cl}e^{\alpha_H f\eta}[Cl^-] = 2Fk_H \frac{K_{Cl}[Cl^-]^2 e^{(\alpha_H+1)f\eta}}{K_{Cl}[Cl^-]e^{f\eta} + 1} \qquad \text{Eq. 1.14}$$

In the above, k_H is the rate constant of the Heyrovský reaction when $\eta = 0$, and α_H is the corresponding transfer coefficient. Alternatively, the Krishtalik mechanism assumes that desorption is a two-step process, involving a second type of chlorine intermediate:

$$Cl^* \rightleftarrows Cl^{*+} + e^- \qquad \text{Eq. 1.15}$$

$$Cl^{*+} + Cl^- \rightleftarrows Cl_2 + * \qquad \text{Eq. 1.16}$$

This mechanism is only expected to occur on metal oxides.[35] The electron transfer in Eq. 1.15 is assumed to be rate-limiting relative to the (non-electrochemical) desorption step in Eq. 1.16, where the rather exotic chloronium (Cl^{*+}) intermediate would be stabilized by the metal oxide surface, as its structure is usually proposed to be $(O - Cl^*)^+$. When again assuming that η is positive enough that the forward reaction dominates, Eq. 1.15 predicts that:

$$j_{VK} = 2Fk_K\theta_{Cl}e^{\alpha_K f\eta} = 2Fk_K \frac{K_{Cl}[Cl^-]e^{(\alpha_K+1)f\eta}}{K_{Cl}[Cl^-]e^{f\eta} + 1} \qquad \text{Eq. 1.17}$$

where the symbols have similar meanings as in Eq. 1.14. The Volmer-Krishtalik (V-K) mechanism predicts the same functional j vs. E relationship as V-T, but it differs in its $[Cl^-]$ dependence.

Finally, a third type of rate-limiting step has also been described, similar to the Langmuir-Hinshelwood mechanism in gas-phase catalysis. It is termed the Tafel step:

$$2\,Cl^* \rightarrow Cl_2 + 2\,* \qquad \text{Eq. 1.18}$$

This mechanism assumes that the reaction is fully dependent on surface-bound species, and that the rate-limiting step is non-electrochemical. The Volmer-Tafel (V-T) mechanism implies that the forward current density follows:

$$j_{VT} = 2Fk_T(\theta_{Cl})^2 = 2Fk_T \left(\frac{K_{Cl}[Cl^-]e^{f\eta}}{K_{Cl}[Cl^-]e^{f\eta} + 1} \right)^2 \qquad \text{Eq. 1.19}$$

where k_T is the non-electrochemical rate constant for Cl* recombination. The Volmer-Tafel mechanism is dominant during the CER on Pt and is usually not considered on metal oxides.

The V-H, V-K and V-T mechanisms all make specific predictions about the observed kinetics of the CER. We will primarily consider Tafel slopes (b) and reaction orders ($\mathcal{R}$). These quantities, defined as $b = \partial\eta / \partial\log(j)$ and $\mathcal{R} = \partial\ln(j) / \partial\ln([Cl^-])$, are easily accessible through experiment and in this way provide convenient diagnostic tools for the underlying mechanism. Their derivations are shown in Table 1.1, and some general limiting cases are summarized in Table 1.2. These values will be discussed frequently throughout Chapters 3, 4 and 5.

We note that Tafel analysis can prove very useful for kinetic investigations, but the 'meaning' of the slope can be obfuscated by a wide variety of phenomena.[109,115,116] There is also significant width and overlap of the predicted Tafel slopes between the various mechanisms. One must thus exert caution when using Tafel values as a comprehensive diagnosis of the 'real mechanism'. One of the key points of Table 1.1 is that reaction orders and Tafel slopes of reactions involving a chemisorbed intermediate are never expected to remain constant as function of potential or concentration in the bulk, because of varying surface coverage of the intermediate. This has been comprehensively described by Conway and co-workers,[112] and more recently by Rosestolato and co-workers.[117]

Table 1.1: Theoretical Tafel slopes and reaction orders for two-step reaction mechanisms for the CER, under the assumption that $\alpha_H = \alpha_K$.

	Volmer-Heyrovský	**Volmer-Krishtalik**
Tafel slope $b = \left(\dfrac{\partial \log j}{\partial \eta}\right)^{-1}$	$\dfrac{\ln(10)}{f}\left(\dfrac{K_{Cl}[Cl^-]e^{f\eta} + 1}{\alpha_H(K_{Cl}[Cl^-]e^{f\eta} + 1) + 1}\right)$	Same as Volmer-Heyrovský
Cl$^-$ reaction order $\mathcal{R}_{Cl^-} = \dfrac{\partial \ln j}{\partial \ln[Cl^-]}$	$2 - \theta_{Cl}$ $= \dfrac{K_{Cl}[Cl^-]e^{f\eta} + 2}{K_{Cl}[Cl^-]e^{f\eta} + 1}$	$1 - \theta_{Cl}$ $= \dfrac{1}{K_{Cl}[Cl^-]e^{f\eta} + 1}$
	Volmer-Tafel	
Tafel slope $b = \left(\dfrac{\partial \log j}{\partial \eta}\right)^{-1}$	$\dfrac{\ln(10)}{2f}\dfrac{1}{(1 - \theta_{Cl})}$ $= \dfrac{1}{2f\log(e)}(K_{Cl}[Cl^-]e^{f\eta} + 1)$	
Cl$^-$ reaction order $\mathcal{R}_{Cl^-} = \dfrac{\partial \ln j}{\partial \ln[Cl^-]}$	$2(1 - \theta_{Cl})$ $= 2\left(\dfrac{1}{K_{Cl}[Cl^-]e^{f\eta} + 1}\right)$	

Table 1.2: Cases of limiting behavior for two-step reaction mechanisms for the CER. Data is shown as function of the overpotential η and 'chloride adsorption strength' $K_{Cl}[Cl^-]$. It was assumed that $\alpha_H = \alpha_K = 0.5$.

Limiting case		Volmer-Heyrovský	Volmer-Krishtalik
Tafel slope b	$\eta \to 0$	$b \approx 40 \text{ mV dec}^{-1}$ if $K_{Cl}[Cl^-] \approx 0$ $b \to 120 \text{ mV dec}^{-1}$ if $K_{Cl}[Cl^-] \to \infty$	Same as Volmer-Heyrovský
	$\eta \to \infty$	$b \to 120 \text{ mV dec}^{-1}$	
Cl^- reaction order $\mathcal{R}_{Cl^-}$	$\eta \to 0$	$\mathcal{R}_{Cl^-} \approx 2$ if $K_{Cl}[Cl^-] \approx 0$ $\mathcal{R}_{Cl^-} \to 1$ if $K_{Cl}[Cl^-] \to \infty$	$\mathcal{R}_{Cl^-} \approx 1$ if $K_{Cl}[Cl^-] \approx 0$ $\mathcal{R}_{Cl^-} \to 0$ if $K_{Cl}[Cl^-] \to \infty$
	$\eta \to \infty$	$\mathcal{R}_{Cl^-} \to 1$	$\mathcal{R}_{Cl^-} \to 0$

Limiting case		Volmer-Tafel
Tafel slope b	$\eta \to 0$	$b \approx 30 \text{ mV dec}^{-1}$ if $K_{Cl}[Cl^-] \approx 0$ $b \to \infty$ if $K_{Cl}[Cl^-] \to \infty$
	$\eta \to \infty$	$b \to \infty$
Cl^- reaction order $\mathcal{R}_{Cl^-}$	$\eta \to 0$	$\mathcal{R}_{Cl^-} \approx 2$ if $K_{Cl}[Cl^-] \approx 0$ $\mathcal{R}_{Cl^-} \to 0$ if $K_{Cl}[Cl^-] \to \infty$
	$\eta \to \infty$	$\mathcal{R}_{Cl^-} \to 0$

The above models all make use of a Langmuir model isotherm for chloride adsorption. In reality, repulsive interactions between adsorbed chloride (and halides in general) will exist.[114] If this is taken into account by using a Frumkin isotherm, this will lead to a broadening of the isotherm, i.e. a broader range of chloride concentrations or potential is needed to reach maximum coverage. For the models described above, this implies that the basic predictions remain the same, but the range of chloride concentrations and potential where changes are observed will widen.

1.5. Previous literature and the outline of this thesis

The encompassing goal of the work in this thesis is to deepen the understanding of the OER and CER, in the context of the two gas-evolving reactions taking place simultaneously on a catalyst surface. The central question is selectivity and the interplay between the reactions, and how these relate to mutual kinetic competition. There is almost no situation imaginable where the formation of a mixture of O_2 and Cl_2 is an attractive outcome; the 'perfect selectivities' would be 100% or 0% of either species evolved.

Of special interest are anodes that evolve oxygen exclusively during seawater splitting, as these would be highly valued, but due to the OER's kinetic disadvantage, also by far the most challenging to develop. A large body of research concerning the OER has been published, but

the majority concerns electrolytes that are free of chloride. Interest in saline water splitting is relatively sparse, although there has been an increase recently.

On the other hand, the perspective of CER research is dominated by the chlor-alkali industry. Most CER papers are restricted to concentrated chloride solutions (1 M or higher) and high current densities comparable to industrial operation, as well as DSA®-based industrial model catalysts, which have relatively poorly defined surfaces. The OER is usually only considered for its effect on catalyst stability; its selectivity during the CER is ignored. Outside of some work in electrochemical water treatment, behavior of the CER from relatively dilute chloride solutions (< 100 mM) has seen little attention, even though this limiting region may contain especially relevant details concerning its mechanism and the effect on the OER.

This thesis is thus specifically focused on the selectivity between the CER and OER in such dilute acidic chloride solutions, where the OER and CER have comparable onset potentials and current densities, and are in direct kinetic competition. By studying multiple reactions simultaneously, 'cross-linked' insights may be obtained, deepening the understanding of the OER as well as the CER. This may aid the development of better catalytic materials for both. Chapter 2 describes a new method for measuring CER selectivities in relevant dilute chloride solutions, which enables rapid and accurate screening of OER vs. CER behavior over a wide potential range. Chapter 3 looks deeper into the coupling between OER and CER activity on a series of closely related Ir-based double perovskite electrocatalysts, and how the oxidation of water and chloride affect their stability. Chapters 4 and 5 investigate the parallel oxidation of chloride, bromide and water. As seawater contains a small fraction of bromide in addition to chloride, these systems would better resemble the situation in an actual electrolyzer. Close attention is paid to how bromide and its oxidation affects both the CER and OER. Chapters 6 and 7 focus on OER-selective anodes. Chapter 6 investigates the origin of manganese oxide-based anodes, and their unusual preference for evolving oxygen. We find that the manganese oxide overlayer actually induces the selectivity by forming an electrochemically inert barrier, that prevents Cl^- from reacting. This represents a highly promising method for decreasing CER selectivity, which is explored further in Chapter 7. Finally, Chapter 8 documents pitfalls for quantifying gas-evolving reactions on a rotating ring-disk electrode, which were often encountered during experiments throughout this thesis. Possible solutions are offered to increase the gas collection reliability. Chapter 9 contains all supporting information, ordered in subsections according to the corresponding chapter numbers.

MEASUREMENT OF COMPETITION BETWEEN THE EVOLUTION OF OXYGEN AND CHLORINE USING RRDE VOLTAMETRY

2

Selectivity determination between chlorine evolution and oxygen evolution is not always straightforward, as most methods for measuring chlorine evolved are cumbersome and have slow response times. We therefore developed a new method to quickly measure that a Pt ring fixed at 0.95 V vs. RHE in a solution of pH 0.88 can selectively reduce the Cl_2 formed on the disk, which allows precise and flexible data acquisition. Using this method, we demonstrate that oxygen evolution and chlorine evolution on a glassy carbon supported IrO_x catalyst proceed independently, and that the selectivity towards chlorine evolution rapidly approaches 100% as $[Cl^-]$ increases from 0 to 100 mM. Our results suggest that on IrOx, oxygen evolution is not suppressed or influenced by the presence of Cl^- or by the chlorine evolution reaction taking place simultaneously on the surface.

THIS CHAPTER IS BASED ON THE FOLLOWING

PUBLICATION:

2.1. Introduction

The OER and CER are strongly coupled reactions, and will proceed simultaneously on most catalysts. If we want to develop anodes selective for the OER in (acidic) brine solutions or further minimize efficiency losses in the electrolysis step of the chlor-alkali process, the selectivity must be optimized towards only a single reaction. For that, one will need to understand the competition between the OER and CER in more detail. A reliable and easy method for the determination of the selectivity between the OER and CER would be of great interest.

Previous research on the CER in aqueous media has generally been done in acidic solutions with very high Cl^- concentrations, often in the range of 3-5 M.[56,113,118–122] CER activity and Tafel slopes in such studies were derived from raw electrode current densities, with the assumption that all observed current could be ascribed to the CER and that the OER plays a negligible role. Although this assumption is reasonable for high Cl^- concentrations, a complete picture of the competition between the OER and CER in chloride-containing media cannot be drawn in this way.

An analytical method to measure Cl_2 and O_2 evolution separately, irrespective of chloride concentration, is Differential Electrochemical Mass Spectrometry (DEMS),[71,123–126] which directly probes Cl_2 vs. O_2 formation near the electrode surface and can provide highly accurate and quantitative results online.[29,70,127] However, DEMS suffers from inflexibility due to specific cell and electrode requirements, and relatively slow response times. Alternatively, a common method of selectivity determination is long-term bulk electrolysis, followed by titration of the working solution using diethyl-phenylenediamine salts (DPD) or iodometry, to determine the amount of Cl_2 formed.[29,73,128,129] This type of method, although accurate, is not suitable for generation of extended data sets and does not offer the online selectivity determination that DEMS does.

In this chapter, we explore a new method for measuring selectivity between the OER and CER in acidic chloride-containing media, based on conventional electrochemical methods. We develop and study the suitability of a rotating ring-disk electrode (RRDE) setup, which has been well established for faradaic efficiency (FE) measurements in benchmarking OER catalysts,[66,130,131] and for the detection of the formation of H_2O_2 during the oxygen reduction reaction (ORR) on model PEM fuel cell cathodes.[132–134] To the best of our knowledge, an RRDE approach for OER vs. CER selectivity measurements has not been previously reported. We used a Pt ring for Cl_2 detection during catalyst operation, as Pt was previously established as an effective catalyst for the chlorine reduction reaction (CRR), which is the opposite of the CER.[135] Other materials (such as Ru or Ir) may also be possible for Cl_2 detection,[136] but we have not pursued this in detail. As proof of concept, we explore the CER vs. OER behavior of IrO_x nanoparticles, as this material constitutes a stable and active acidic OER and CER catalyst.

2.2. Experimental

$KHSO_4$ (EMSURE), KCl (EMSURE), and $HClO_4$ (60%, EMSURE) were purchased from Merck. $Na_2IrCl_6 \cdot 6H_2O$ (99.9%, trace metals basis) and NaOH (30% solution, TraceSelect) were purchased from Sigma-Aldrich. All chemicals were used as received. The water used for cleaning glassware and preparing solutions was filtered and deionized using a Merck Millipore Milli-Q system (resistivity 18.2 MΩcm, TOC < 5 p.p.b.). Experiments were done in a home-made two-compartment borosilicate glass cell of 100 mL volume. IrO_x deposition experiments were done in a borosilicate glass vial of approximately 5 mL. Before the first-time use, all glassware was thoroughly cleared from organic contaminants by boiling in a 3:1 mixture of concentrated H_2SO_4 and HNO_3. When not in use, all glassware was stored in a 1 g/L solution of $KMnO_4$ in 0.5 M H_2SO_4. Before each experiment, glassware was thoroughly rinsed with water, and then submerged in a dilute solution of H_2SO_4 and H_2O_2 to remove all traces of $KMnO_4$ and MnO_2. The glassware was then rinsed three times with water, followed by triple boiling in Millipore water.

All experiments were carried out at room temperature (~20 °C). Hydrodynamic measurements were performed using an MSR rotator coupled to E6 ChangeDisk RRDE tips in a PEEK shroud (Pine Research Instrumentation). As counter electrode, a Pt mesh separated from the main solution by a glass frit was used. The reference electrode was a HydroFlex® reversible hydrogen electrode (Gaskatel). All potentials in this chapter are reported using the RHE scale. Using a Luggin capillary, the RHE reference was aligned to the center of the RRDE tip to minimize electrical cross-talk.[137,138] The liquid phase collection factor of the ring-disk system, N_l, was determined to be 0.245 in at least four separate experiments, where the GC disk was exchanged in between. The value was found using a conventional collection factor experiment on a freshly prepared blank GC electrode with a Pt ring, studying the reduction/re-oxidation of 10 mM $K_3Fe[CN]_6$ in 0.1 M KNO_3. 0.5 M $KHSO_4$ solutions were used for all CER activity experiments. pH values were 0.88 ± 0.05, as measured with a Lab 855 meter equipped with a glass electrode (SI Analytics). pH values were verified by measuring the potential of a calibrated Ag/AgCl reference electrode in the solutions. All working solutions were saturated with either O_2 or Ar (Linde, purity 6.0) before experiments. Mild gas bubbling through the solution was allowed during forced convection experiments, in all other cases gas was used to blanket the solution.

The electrochemical experiments were controlled with an IviumStat potentiostat (Ivium Technologies). For all experiments, the solution resistance was measured with electrochemical impedance spectroscopy, by observing the absolute impedance in the high frequency domain (100 KHz). Potentials were 85% corrected for these values during measurements. Before a CER activity experiment, the Pt ring was electropolished by cyclic voltammetry (CV) from -0.1 V to 1.7 V at 500 mV s^{-1} for 30 scans at a 1500 RPM rotation rate, after which the individual scans did not change. This step is vital to the removal of traces of alumina, as well as traces of IrO_x that tend to remain on the ring after being swept outward during IrO_x electroflocculation under rotation.[139] OER and CER experiments were done under hydrodynamic conditions at 1500 RPM by scanning the disk electrode in the range of 1.3 − 1.55 V at 10 mV s^{-1}. For quantitative analysis, the forward and backward sweeps were averaged to reduce

contributions from double layer charging and IrO_x pseudocapacitance. In between experiments, the IrO_x film was kept at 1.3 V. Ring currents were corrected for background currents and collection delay, which was approximately 200 ms at 1500 RPM. Before proceeding with OER and CER activity measurements, the IrO_x film was treated by performing 20 scans between 1.3 – 1.55 V, in absence of Cl^-. This was done to ensure stable and reproducible catalyst behavior during experiments.

IrO_x nanoparticles electroflocculated on glassy carbon were used as active OER/CER catalyst. The IrO_x/GC electrodes were prepared as described in sections 9.1.1 and 9.1.2. Al_2O_3 was used for GC polishing, followed by rinsing and 5 minutes sonication in acetone and water. A time duration of 600 s was used for the electroflocculation amperometry step.

For iodometry experiments, amperometry was performed for 60s at 1500 RPM in 16 mL of 0.5 M $KHSO_4$, in the presence of Cl^-, followed by titration of the bulk solution. Under identical conditions, amperometry was performed for 20s and the Pt ring was used to measure selectivity towards the CER. This selectivity was then applied to disk currents of the iodometry experiment to calculate the amount of Cl_2 that must have formed according to the RRDE method. In this way, both methods could be applied to a single experiment. The experiments were done in a glass vial without headspace, of approximately 16 mL volume. The vial was vertically elongated to minimize the contact area of the solution with air, and thus to prevent gaseous Cl_2 from escaping the acidic solution. All solutions were pretreated by briefly evolving chlorine and then purging the solution with Ar. Immediately after finishing an experiment, a large (~100x) excess of NaI was rapidly added to the solution to trap all Cl_2 as I_3^- and to minimize the equilibrium concentration of volatile I_2. The vial was then closed air-tight and the solution was allowed to equilibrate for approximately 1 minute. Iodometry was performed directly after. Reported values were the average of four titrations. For the sake of verification, RRDE experiments in the iodometry vial were compared to those in a standard glass RRDE cell of 100 mL volume. Although the absolute measured currents of the iodometry vial were slightly lower than the RRDE cell, the ratio ${i_R}/{i_D}$ (the 'apparent chlorine collection factor', N_{Cl_2}) was found to be exactly the same, indicating proper transport of Cl_2 from the disk to the ring in the iodometry vial. This justifies the comparison of our RRDE method and iodometry. We attribute the lower CER currents in the small volume iodometric cell to distortion of the hydrodynamic flow field, leading to lowered Cl^- mass transport.

2.3. Results and discussion

2.3.1. *Aspects of selectivity between the OER and CER*

As discussed in section 1.3, the formation of hypochlorous acid or hypochlorite becomes thermodynamically favorable as the solution pH increases. These species might form directly from an electrochemical reaction (Eq. 1.7 and Eq. 1.8), or through solution hydrolysis of Cl_2 formed during the CER (Eq. 1.9 and Eq. 1.10). Contrary to chlorine, the reduction of ClO^- and HClO are sluggish reactions on Pt, which reach diffusion limited conditions only at overpotentials near $\eta = 1$ V.[140,141] As such, we do not expect it possible to quantify these species

by means of the RRDE, since the criterion of reaching diffusion limitations before the ORR (which has an onset of approximately 0.95 V on Pt) cannot be reached. The formation of ClO^-/HClO thus has to be kept minimal, and $Cl_2(g)$ is the desired chlorine species for reduction. We expect that the RRDE approach is limited to acidic environments (pH < 2), where the focus is on direct (kinetic) competition of the OER vs. CER, and where both products are gases dissolved in the working solution.

2.3.2. *Application of the RRDE to OER vs. CER selectivity measurements*

To demonstrate the application of our RRDE method to measure the CER, Figure 2.1 shows the forward and backward scan average of an IrO_x catalyst in the potential region of 1.3 − 1.55 V, in an acidic electrolyte in presence of 20 mM Cl^-. Figure A 9.2.1 in the Supporting information shows a typical characterization CV in the region 0 V - 1.4 V. In Figure 2.1, the disk current (black line) was measured until 1.55 V, leading to a competition between the OER and CER above ca. 1.48 V. The Pt ring (grey line) was fixed at E_R = 0.95 V and performs reduction of Cl_2 (CRR, see next section). The ring potential 0.95 V was chosen well in the diffusion-limited regime of the CRR near the edge of the ORR onset on Pt in a chloride-free solution. In this way, the ring allows very precise observation of the onset and the rate of the CER.
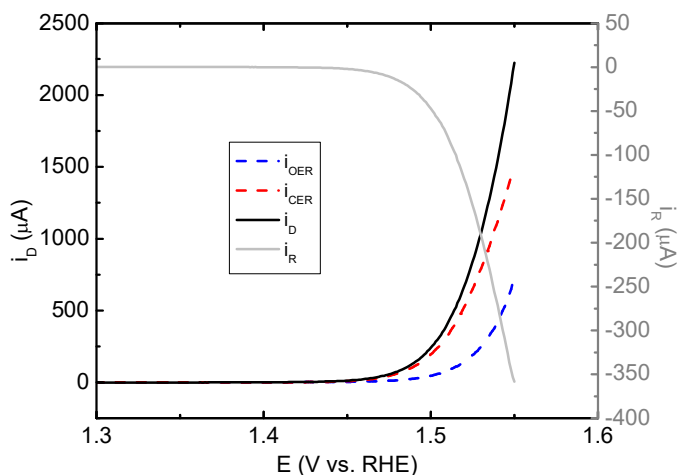

Figure 2.1: CV of IrO_x/GC in the OER + CER region in 0.5 M $KHSO_4$ + 20 mM KCl, scan rate 10 mV s⁻¹, rotation rate 1500 RPM. pH = 0.88, solution saturated with Ar. Ring potential was fixed at E_R = 0.95 V. The forward and backward scans of the disk were averaged, i_R was corrected for collection delay. i_{OER} and i_{CER} curves were calculated as described in the text.

To minimize capacitive charging contributions on the disk, a relatively slow scan rate of 10 mV/s was used, and values of forward and average scans were averaged. The magnitude of capacitive charging in the potential region of 1.3 V to approximately 1.4 V, where IrO_x experiences the onset of the Ir^{IV} to Ir^V transition, was approximately 10 μA. Such currents were usually less than 1% of the OER charge measured. Using the average of forward and backward scans eliminated most of this possible source of error, noting that our IrO_x showed no significant hysteresis in the 1.3 − 1.55 V potential range (see Figure A 9.2.1).

Since IrO_x is established as a stable acidic OER catalyst within the time frame of our experiments,[83] we assume that the measured disk current can be ascribed exclusively to either the OER or CER, after minimizing capacitive contributions. From the ring current, we can then separate the current contributions of the OER and CER on the disk. Since the chlorine reduction reaction taking place on the ring is simply the reverse of the CER, the current contribution originating from the CER, i_{CER}, will be:

$$i_{CER} = \left| \frac{i_R}{N_l} \right| \qquad \text{Eq. 2.1}$$

where i_R is the current measured on the ring, and N_l is the liquid phase collection factor (N_l = 0.245). The OER current contribution is simply the current remaining after subtracting CER activity:

$$i_{OER} = i_D - i_{CER} = i_D - \left| \frac{i_R}{N_l} \right| \qquad \text{Eq. 2.2}$$

where i_D is the total current measured on the disk. In Figure 2.1, i_{OER} and i_{CER} (blue and red dotted lines) were constructed by the above method. The OER onset is near 1.480 V, equivalent to an overpotential $\eta_{OER} \approx 0.25$ V, in agreement with previous studies.[142,143] The CER shows a much earlier onset of ~ 1.420 V, equivalent to a negligible overpotential at pH = 0.88.

At this point we must describe a significant caveat, namely, that there is always the risk of forming gas bubbles at high current densities. The problem is mainly related to high OER currents, which may rapidly lead to local supersaturation of poorly soluble O_2.[144−146] Gas bubbles may strongly persist on the electrode surface and hinder the transport of products to the ring,[147] compromising the quantitative nature of the experiment. This is a universal problem in the use of RRDE for gas forming reactions and makes OER FE experiments at high overpotentials extremely challenging. The solubility of Cl_2 around pH 1 is approximately 10³ times higher than that of O_2,[148] making high CER currents less troublesome, although extreme CER current densities may additionally lead to formation of Cl_2 bubbles. Chapter 8 looks into this problem in much more detail.

2.3.3. *Effect of chloride adsorption and PtO$_x$ formation on chlorine detection with the Pt ring*

To explore the behavior of the CRR (and the ORR) on the Pt ring in presence of Cl^-, we used the disk to generate a stepwise increasing Cl_2 flux, by fixing the disk potential in the range $1.420\,V < E_D < 1.480\,V$, where only the CER is expected to occur at pH = 0.88. We simultaneously recorded forward linear sweep voltammograms at 1500 RPM on the ring, using a slow scan rate of 5 mV s⁻¹ to minimize transient charging current. The steady state disk currents and corresponding ring LSV profiles are shown in Figure 2.2. The working solution was saturated with O_2 to accurately monitor the ORR onset as function of $[Cl^-]$ and (locally) $[Cl_2]$. We assume that the increased concentration of O_2 does not majorly affect the CRR kinetics.
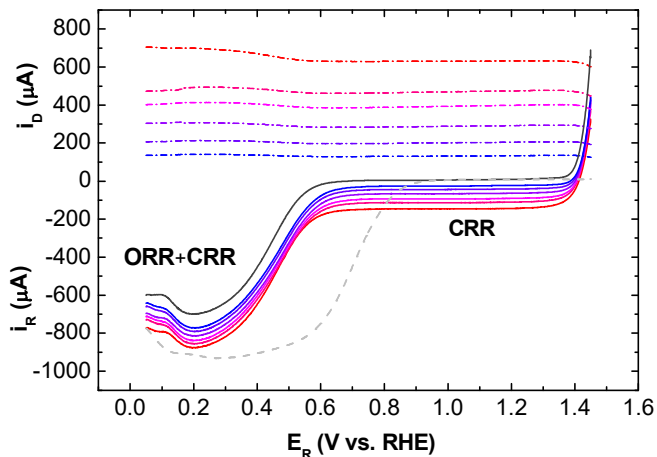
Figure 2.2: LSV of the Pt ring electrode, while keeping the IrO_x/GC disk electrode at constant potential in 0.5 M $KHSO_4$ + 100 mM KCl, scan rate 5 mV s⁻¹, rotation rate 1500 RPM. pH = 0.88, solution saturated with O_2. Dotted curves with positive values correspond to disk currents, remaining curves correspond to ring currents. The ring LSV sweeps were taken in the positive-going direction. Disk potentials were chosen in the region of exclusive chlorine evolution, with values increasing from the blue curve to the red curve, $E_D = 1.449\,V$, $1.456\,V$, $1.462\,V$, $1.467\,V$, $1.470\,V$, and $1.475\,V$. Black curve shows ring response while disk is not connected. Grey dashed curve shows ring response while disk is not connected, in Cl^--free conditions.

In Figure 2.2, the ring first traverses a region of the superimposed ORR and CRR between $0.2\,V < E_R < 0.7\,V$. When comparing the ORR in chloride-free conditions (grey dashed curve), its onset potential in presence of 100 mM Cl^- is shifted 200 mV negatively, which prohibits the ORR from reaching diffusion limited current before the onset of hydrogen adsorption. Such a suppressing effect was previously observed by Schmidt *et al.*[149] even at $[Cl^-]$ as low as 100 µM.

Following the ORR + CRR region, a region of constant negative current follows in the range of $0.7\,V < E_R < 1.3\,V$, which we ascribe to the CRR under diffusion limited conditions. At potentials higher than 1.3 V, the ring approaches $E^0_{Cl_2/Cl^-}$, and the onset of the CER on the ring can be observed. The experiments shown in Figure 2.2 were also performed for $[Cl^-]$ = 150 mM and 200 mM.

It is reasonable to assume that the constant current in Figure 2.2 in the region of $0.7\,V < E_R < 1.3\,V$ arises from the diffusion limited CRR. However, previous studies by Conway *et al.*[58,118] showed that chloride adsorption causes CER self-retardation on Pt for $[Cl^-]$ ranges near 1 M by affecting the rate-limiting Tafel recombination step. To verify that the ring current response is completely diffusion controlled at $E_R = 0.95\,V$, we propose a simple method: as long as only the CER occurs on the disk, a of plot i_R vs. i_D would yield a straight line, with the 'apparent chlorine collection factor' N_{Cl_2} as slope. If N_{Cl_2} approaches the liquid phase collection factor N_l, the ring reaction is indeed diffusion limited, and the measured CRR current is quantitative. Kinetic limitations of the CRR on the ring would manifest as $N_{Cl_2} < N_l$.
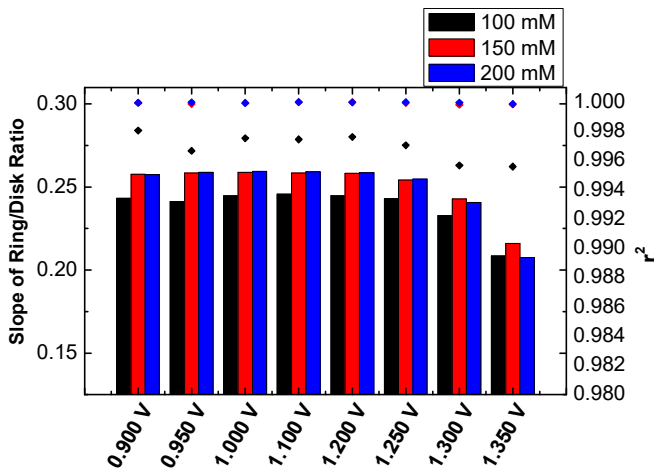
Figure 2.3: Apparent chlorine collection factors N_{Cl_2} (equivalent to slopes of ring/disk ratios) plotted as function of potential on the ring electrode, for $[Cl^-]$ = 100 mM (black), 150 mM (red) and 200 mM (blue). Diamonds (correspondingly coloured) indicate the determination coefficient r^2 of the found slopes. Data derived from Figure 2.2.

Using data from Figure 2.2, we plotted the i_R vs. i_D response at various ring potentials (see Figure A 9.2.2). We generally observed strong linearity between i_R and i_D, with determination coefficients r^2 approaching 1. Furthermore, as shown in Figure 2.3, N_{Cl_2} converges to a constant value of ~ 0.244 for $[Cl^-]$ = 100 mM, and ~ 0.258 for 150 mM and 200 mM, as E_R is lowered. Only for $E_R \geq 1.300$ V do we observe ring-disk ratios that significantly differ from these values. At these potentials, $E^0_{Cl_2/Cl^-}$ is approached ($\eta_{CER} < 100$ mV), and the CRR kinetics become kinetically limited. For $[Cl^-]$ = 150 mM and 200 mM, the value to which N_{Cl_2} converges is approximately 5% higher than N_l. We ascribe this discrepancy to electrochemical crosstalk,[137,138] which we could not eliminate experimentally despite intensive efforts (see also the slight downward slope in disk currents within 1.4-1.45 V, in Figure 2.2). Nonetheless, the most important point is that N_{Cl_2} reaches limiting values close or identical to N_l well before the ORR onset potential.

To explore the effect of pH on Cl_2 detection, and to corroborate the discussion in section 2.3.1 concerning pH-dependent Cl_2 disproportionation into hypochlorous acid, we have probed the apparent chlorine collection factor N_{Cl_2} in pH = 0.90 and pH = 2.91, using a forward linear sweep in a Pt-Pt RRDE setup. Figure A 9.2.3 in the Supporting information shows that N_{Cl_2} decreases from 0.242 at pH = 0.90 to 0.214 at pH = 2.91. We ascribe this 12% decrease in collection efficiency to the partial disproportionation of Cl_2 into HClO, a species which is undetectable by Pt at E = 0.95 V. Cl_2 detection is thus no longer quantitative at pH ~ 3, although it could still be used qualitatively, such as for mechanistic studies.
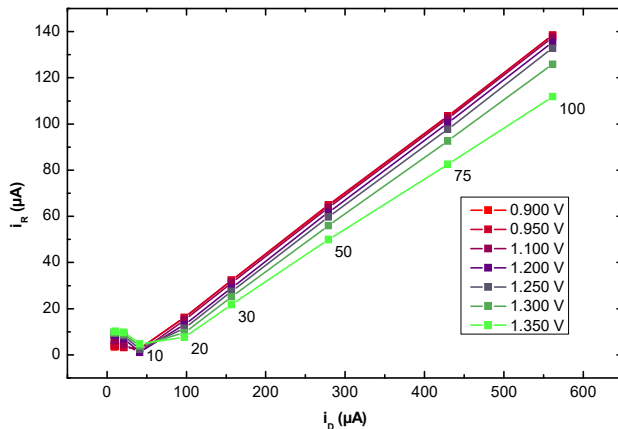
Figure 2.4: Behavior of i_R vs. i_D at various ring potentials. IrO_x/GC disk electrode fixed at 1.475 V, in 0.5 M $KHSO_4$ + $[Cl^-]$ increasing from 1 to 100 mM. Numeric labels next to data points show the concentration of chloride, in mM. Labels for $[Cl^-] < 10$ mM are not displayed.

Another factor that needs to be considered for the CRR on Pt is the presence of platinum oxide, which is known to be a sluggish CER/CRR catalyst in comparison with Pt.[58,108,135,136] In Figure 2.3, where $[Cl^-]$ is always 100 mM or higher, the formation of PtO_x can be assumed absent due to inhibition by Cl^- adsorption,[58] but lower $[Cl^-]$ would allow significant growth of oxides. To investigate the presence and effect of PtO_x on the CRR, we performed experiments as in Figure 2.2 and Figure 2.3, but instead, we fixed E_D = 1.475 V and studied the CRR on the Pt ring as function of $[Cl^-]$ increasing from 1 to 100 mM.

Like Figure A 9.2.2, Figure 2.4 displays slopes of i_R vs. i_D, together with the corresponding $[Cl^-]$ values. We note that an increase in $[Cl^-]$ will now have a twofold effect: a) it will increase CER current on the disk electrode, leading to higher Cl_2 flux to the ring and thus larger CRR currents, and b) it is expected to progressively inhibit PtO_x growth on the ring, affecting measured ring current profiles. Linearity between i_R vs. i_D is generally observed, except for data for which $[Cl^-] < 10$ mM. The corresponding LSV curves (see Figure A 9.2.4 in the Supporting information, inset) suggest significant PtO_x formation is taking place for measurements in the 1-10 mM range when comparing against the black curve taken in Cl^--free conditions. There is clear nonlinear behavior of increases in CRR current versus $[Cl^-]$. Only for $[Cl^-] > 10$ mM we observe the desired linearity. We explain these results as follows: for very low $[Cl^-]$, detrimental PtO_x formation occurs on the ring in the forward scan within the timescale of our experiments. For $[Cl^-] > 10$ mM, PtO_x growth becomes inhibited and the CRR may proceed on an oxide-free surface. For higher chloride concentrations, the i_R vs. i_D slopes show behavior identical to Figure 2.3, converging to $N_{Cl_2} \approx 0.247$ as E_R becomes lower.

To summarize our findings regarding the use of a Pt ring for chlorine detection: contrary to the ORR, the specific adsorption of chloride at Pt does not seem to have a detrimental effect on the CRR, at least not up to $[Cl^-]$ = 200 mM. Somewhat ironically, Cl adsorption actually seems favorable for carrying out the CRR as it inhibits the formation of PtO_x, which *is* detrimental. Furthermore, in case of $[Cl^-] > 10$ mM, ring potentials of 1.250 V already seem

adequate to ensure that, at pH 0.88, the CRR proceeds diffusion limited. It is however recommended to keep the potential at the lowest possible limit, 0.95 V, to minimize growth and interference of PtO_x at lower chloride concentrations.

2.3.4. OER vs. CER selectivity as a function of E_D and [Cl⁻]

Based on the method described in section 2.3.2, we define the selectivity towards the CER (ε_{CER}) as the molar ratio of Cl_2 formed versus the total amount of Cl_2 and O_2 formed. This is equivalent to the ratio of CER current and combined OER and CER currents after normalizing them to the number of electrons in each reaction:

$$\varepsilon_{CER} = 1 - \varepsilon_{OER} = \frac{i_{CER}/2}{i_{CER}/2 + i_{OER}/4} \qquad \text{Eq. 2.3}$$

Typical results are displayed in Figure 2.5. We have plotted the data of three different disk potentials, namely a) 1.48 V, b) 1.52 V and c) 1.55 V. These potentials correspond to regimes where a) the CER is present and the OER is virtually absent, b) chlorine evolution is the major reaction but the OER takes place with a modest rate, c) both the CER and the OER take place.

From Figure 2.5 we can make several interesting conclusions. The CER activity is approximately linear with [Cl⁻] at all potentials, indicating a reaction order of one within the whole potential range. Only at very low [Cl⁻] we observe a slope smaller than one, likely due to PtO_x formation on the ring, as discussed in section 2.3.3. Furthermore, the OER rates show a constant value for a given E_D as function of [Cl⁻], and this trend persists in the entire measured potential range. Thus, the OER does not seem strongly affected by either the presence of Cl⁻ or the competing CER. Figure 2.5 suggests that the OER and CER proceed independently within the measured potential range. This implies that the OER and CER do not share the same active site on this catalyst, even though a scaling relationship between their activities has been suggested in previous literature.[55,72,76]

Extensive DFT calculations on model RuO_2(110) surfaces have suggested that the OER and CER proceed on the same active site, namely, oxygen atoms (O_{ot}) bound to Ru atoms which are coordinatively unsaturated on the pristine model surface.[74,75] Although our results appear to exclude a model of two reactants competing for the same active site, it can be assumed that the amorphous, hydrous IrO_x catalyst in our study is far removed from the Ru single crystalline model surfaces used in the DFT studies, making a direct comparison difficult. Additionally, an independence of OER activity versus [Cl⁻] was previously found in DEMS studies on heterometal doped RuO_2 mixtures, indicating that such behavior is not unusual.[73,79]

As the chloride concentration increases, ε_{CER} appears to rise sharply. Near [Cl⁻] = 20 mM, ε_{CER} generally exceeds 80%, and at 40 mM it exceeds 90%. When the chloride concentration increases to 100 mM, ε_{CER} converges to values above 95%. For comparison, Figure A 9.2.5 shows a similar ε_{CER} vs. [Cl⁻] plot for commercial RuO_2 (available from Sigma-Aldrich).

Interestingly, RuO_2 generally shows a higher selectivity towards the CER compared to the IrO_x catalyst, since ε_{CER} converges towards 100% CER more rapidly as $[Cl^-]$ increases.
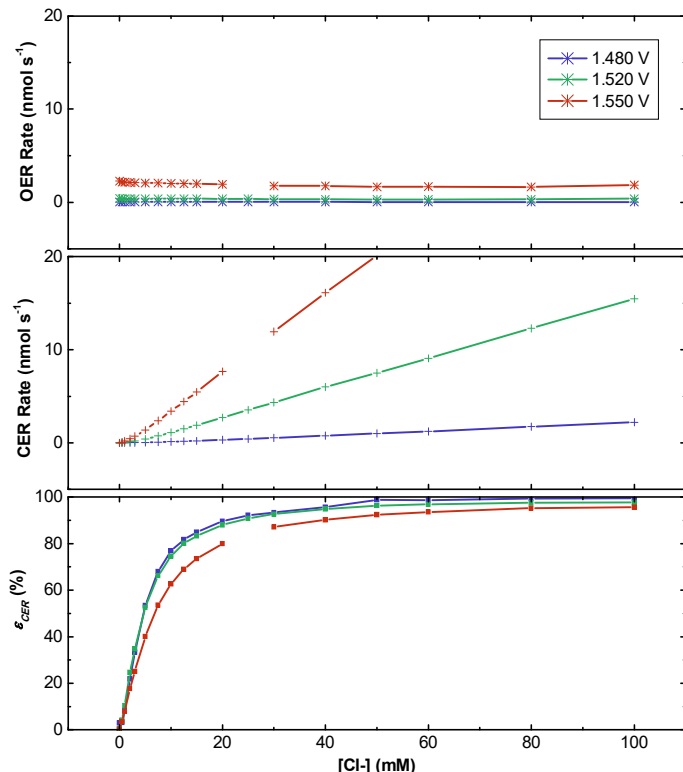

Figure 2.5: Plots of OER and CER reaction rates as function of $[Cl^-]$, for three disk potentials: $E_D = 1.480\,V$ (blue lines), $1.520\,V$ (green lines), and $1.550\,V$ (red lines). Values were obtained from CVs identical to Figure 2.1, while varying $[Cl^-]$. Rates were obtained by dividing currents by nF, the number of electrons transferred and Faraday's constant.

When the potential increases to 1.55 V, the CER starts becoming diffusion controlled, as indicated by increasingly higher Tafel slopes (not shown). Also, the CER selectivity starts to

decrease due to diffusion limitations and increasing contributions of the competing OER. There is thus a range of low $[Cl^-]$ where significant (more than 10%) oxygen evolution is present regardless of potential, up to about $[Cl^-] = 40\,mM$. Most importantly, higher potentials of catalyst operation will increasingly favor the OER. This trend is very similar to a previous DEMS study on OER vs. CER selectivity on pristine and doped IrO_x nanoparticulate catalysts.[150]

It needs to be stressed that that all measurements in this chapter were done in presence of 0.5 M HSO_4^-, which is known to adsorb on Pt.[151] To investigate the effect of anion adsorption on PtO_x formation and CER detection, ε_{CER} vs $[Cl^-]$ was measured in electrolytes of pH ~0.8 composed of 0.5 M $NaHSO_4$ and 0.5 M $NaClO_4$ (Figure A 9.2.6). A small but clear difference is apparent: although the two electrolytes show similar selectivities, ε_{CER} appears to lag behind in low $[Cl^-]$ regimes in presence of non-adsorbing ClO_4^-. We ascribe this to a greater degree of

PtO_x formation, which hinders Cl_2 detection and distorts the apparent selectivity. As discussed in section 2.3.3, the problem resolves itself as $[Cl^-]$ increases.
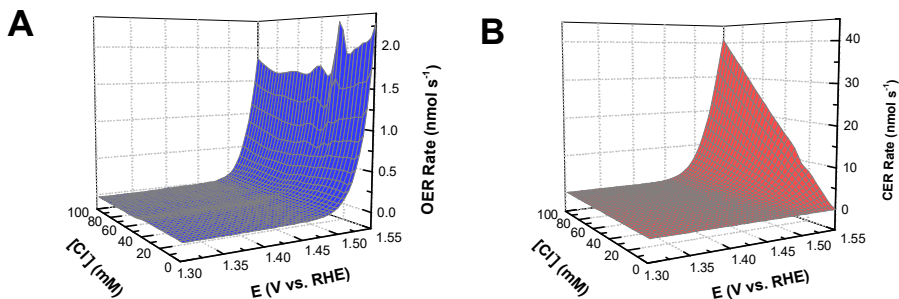

Figure 2.6: Plots of A) OER rates and B) CER rates as function of E_D and $[Cl^-]$, constructed from CVs identical to Figure 2.5, while varying $[Cl^-]$. Rates were obtained by dividing currents by nF, the number of electrons transferred and Faraday's constant.

Owing to the scanning nature of the experiments, we have sampled the complete potential range within $1.3 - 1.55$ V. This allows the construction of 3-dimensional plots showing OER rates and CER rates as a function of E_D and $[Cl^-]$, as shown in Figure 2.6. We remark that 'dynamic' potential methods such as cyclic voltammetry may lead to different catalyst behavior than steady state measurements, especially concerning gas forming reactions.[82,152] In this chapter, we have only included cyclic voltammetry to serve as a proof of principle for the RRDE method, although steady-state amperometry experiments are also possible. Lastly, we stress that plots like Figure 2.5 and Figure 2.6 are only valid for stable catalysts. Side reactions and transient dissolution of the catalyst will distort the results. Caution is advised with the assumption that all remaining current is related to the OER.
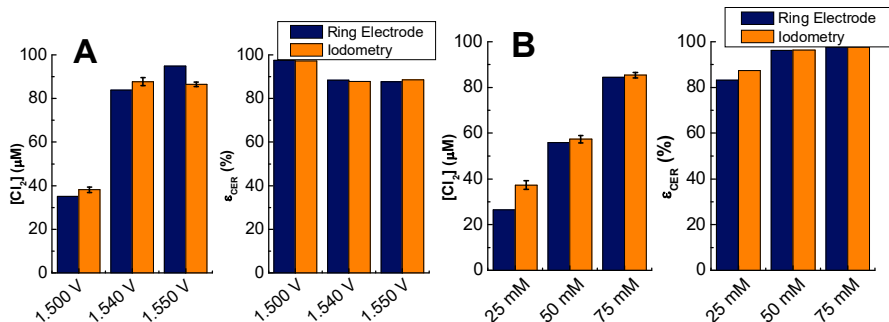

Figure 2.7: Cl_2 concentrations and corresponding ε_{CER} as determined by iodometry and the RRDE method, in 0.5 M KHSO$_4$. A: 50 mM KCl, as function of E_D. B: $E_D = 1.53$ V, as function of $[Cl^-]$. Error bars show 95% confidence intervals of the titration.

Finally, to confirm that the RRDE method yields trustworthy results, we employed iodometry to compare values of CER faradaic efficiency as determined by iodometric titration versus those determined by the RRDE method. Values of $[Cl_2]$ obtained versus E_D and $[Cl^-]$ are shown in Figure 2.7, and agree well with each other between the two techniques. Values of ε_{CER} versus E_D and $[Cl^-]$ correspond to those in Figure 2.5, but are approximately 3% lower.

As described in the experimental section, we ascribe this difference to a slight hindrance of Cl^- mass transport in the iodometry setup.

2.4. Conclusions

In this work, we described the application of an RRDE setup to measure rates of the chlorine evolution reaction in the context of selectivity between chlorine evolution and the evolution of oxygen in acidic aqueous media. We used a Pt ring to selectively reduce the Cl_2 formed on the disk by fixing the ring potential at 0.95 V vs. RHE in pH 0.88, which gives reliable diffusion limited chlorine reduction rates and allows precise and flexible data acquisition. Using this method, we demonstrated that the evolution of O_2 and Cl_2 on a glassy carbon supported IrO_x catalyst proceed independently, and that the selectivity towards chlorine evolution rapidly approaches 100% as the chloride concentration increases from 0 to 100 mM. Moreover, our results suggest that on IrO_x, oxygen evolution is not suppressed or influenced by the presence of Cl^- or by chloride oxidation taking place simultaneously on the surface.

SELECTIVITY TRENDS BETWEEN OXYGEN EVOLUTION AND CHLORINE EVOLUTION ON IRIDIUM-BASED DOUBLE PEROVSKITE

3

Optimization of the selectivity between oxygen evolution and chlorine evolution is highly desired for several energy-intensive electrochemical processes, but the strong correlation between occurrence of the two reactions prevents a straight-forward approach of doing so. In this chapter, we look deeper into this correlation by studying the selectivity and interdependence of the OER and CER on a series of iridium-based double perovskites, which are materials that have shown high OER activity and may be usable in acidic electrolyzers. For all studied catalysts, we found a comparable selectivity, strengthening the long-proposed and OER activity, as well as comparable selectivity, strengthening the long-proposed notion that a scaling relationship exists between the two reactions. We also employed online inductively coupled plasma mass spectrometry (ICP-MS) measurements to probe the material stability and how this is affected by chloride. We found that chloride selectively enhances the dissolution of the noble metal component. A reaction order analysis was performed to gain insight in the CER mechanism, the effect of surface area changes due to adventitious leaching, and the observed suppressing effect of chloride on the OER.

3.1. Introduction

Proton Exchange Membrane (PEM) electrolyzers, which currently offer the best performance for water splitting on the industrial scale, generally employ acidic pH. Ir is the only material known to retain long-term stability under acidic OER operation, either as a pure oxide or as a dopant. Virtually no acidic OER anode is known that does not rely on Ir.[152] Unfortunately, the scarcity of Ir is a crippling limitation to large-scale implementation of PEM electrolyzers, and a large body of research has been devoted to reducing the needed Ir loading, such as by increasing the catalyst active surface area, or developing Ir-based materials with higher intrinsic activity. A recent example of Ir-based materials with lower intrinsic Ir mass loading are Ir-based double perovskites, which offer a way to reduce the amount of Ir needed while retaining the high catalytic OER performance.[153] Previous work by some of us showed that the high OER performance of these materials is related to their surface instability in acid, leading to amorphization of the surface and formation of a highly active surface layer.[154] An interesting question is how these Ir-based double perovskites perform as CER electrocatalysts, and how parallel CER impacts their stability. They represent an attractive system of study also because of the possibility of studying a series of closely related structures. The Ir double perovskite structure is represented by A_2BIrO_6 and allows a degree of freedom in the type of A and B cations, meaning that many different perovskites can be prepared.

In this chapter, we explore parallel evolution of oxygen and chlorine on a series of double perovskites and investigate their selectivity and stability, as well as the interdependence between the two reactions in acidic media of pH ~ 1. We applied the RRDE method and scanning protocol described in Chapter 2 to measure the OER and CER on GC-supported, dropcasted double perovskite microparticles. Similar to Chapter 2, relatively low chloride concentrations ($0 < [Cl^-] < 120$ mM) were chosen to study the CER, since the competition between the OER and CER is the most prevalent under these conditions. The double perovskites used can be written as Ba_2BIrO_6, where B = Pr, Nd, La, Sn, Y, Tb, and Ce. The material Sr_2YIrO_6 was also included with the aim to vary the A cation. Commercial IrO_2 was included as reference material.

3.2. Experimental

3.2.1. *Chemicals*

$HClO_4$ (60%) and NaCl (EMSURE/Analysis grade) were purchased from Merck. Ir-based double perovskites were synthesized as reported previously.[153] IrO_2 nanoparticles (Premion, 99.99%) were purchased from Alfa-Aesar. All purchased chemicals were used as received. The water used for all experiments was prepared by a Merck Millipore Milli-Q system (resistivity 18.2 MΩcm, TOC < 5 p.p.b.).

3.2.2. Synthesis of the double perovskites and X-ray powder diffraction

Samples of A_2BIrO_6 (A = Ba and Sr; B = Lanthanides, Y and Sn) were prepared from $BaCO_3$, $SrCO_3$, La_2O_3, CeO_2, Pr_6O_{11}, Nd_2O_3, Tb_4O_7, Y_2O_3, SnO_2 and Ir metal using methods based on standard solid-state reactions.[155,156] The La_2O_3 and Nd_2O_3 powders were preheated at 950 °C overnight before use. The well-ground mixtures were placed in alumina crucibles and allowed to react at 800 °C overnight. The resultant powders were then sintered at 1250 °C for two days with intermittent regrinding, and, finally, the samples were furnace cooled to room temperature. Every synthesis was carried out in air.

X-ray powder diffraction patterns were collected on a Philips X'Pert diffractometer in Bragg-Brentano geometry, equipped with a X'Celerator detector and a Cu-Kα source. Diffraction patterns were collected in steps of 2θ = 0.020°, with a 10 s counting time per step in the range 15° < 2θ < 90°.

3.2.3. Online electrochemical ICP-MS analysis

Investigations of the chloride impact on the stability of iridium based double perovskites were performed using an electrochemical scanning flow cell (SFC) with online inductively coupled plasma mass spectrometry (ICP-MS) analysis to detect dissolution products in direct correlation to potential and current density. The SFC is a small polycarbonate cell with an electrolyte flow of 192 µL min⁻¹ able to perform classical three electrode electrochemical experiments. The cell's inlet is connected to a counter electrode compartment, housing a graphite rod (Sigma Aldrich, 99.995%), while a Ag/AgCl reference electrode (Metrohm) is connected by a separate channel directly to the working electrode. The reference electrode was calibrated vs. the RHE, against which all potentials are reported. The working electrode can be moved with an xyz-stage (Physik Instrumente, M-403), which allows fast screening of multiple catalyst spots on a 5x5 cm glassy carbon plate (HTW, SIGRADUR® G, 5×5 cm). The outlet of the SFC is connected to the ICP-MS (Perkin Elmer, NexION 350x) to detect dissolution products. The ICP-MS was calibrated for the elements A, B and Ir with a four-point calibration slope by adding specific amounts of standard solutions (Merck, Certipur®, Ir, Pr, Y, Ba, Sr) to the electrolyte. More details about the online SFC ICP-MS system can be found in previous publications.[157–159] The SFC was operated using 0.1 M $HClO_4$ (Merck, Suprapur®) as an electrolyte in control experiments, and addition of 50 mM NaCl (Sigma Aldrich, 99.5%) provided information of chloride impact on the stability. Catalysts were dropcasted from water based suspensions containing 0.27 mg(Ir)/mL and 20 µL of Nafion (Sigma Aldrich, 5wt.% in aliphatic alcohols). Using 0.3 µL of those suspensions for dropcasting resulted in dried catalyst spots whose sizes (see Table A 9.3.1) were measured using a Keyence Laser Profilometer (VK-X200 series). Surface area normalization was based on these spot sizes. Each measurement was carried out in duplo to ensure reproducibility. Data from single measurements are reported.

3.2.4. General electrochemical procedures

All experiments were carried out at room temperature (~20 °C).

The electrochemical experiments were done using home-made two-compartment borosilicate glass cells with solution volumes of 100 mL. Before first-time use, all glassware was thoroughly cleaned by boiling in a 3:1 mixture of concentrated H_2SO_4 and HNO_3. When not in use, all glassware was stored in a 0.5 M H_2SO_4 solution containing 1 g/L $KMnO_4$. Before each experiment, glassware was thoroughly rinsed with water, and then submerged in a dilute (~0.01 M) solution of H_2SO_4 and H_2O_2 to remove all traces of $KMnO_4$ and MnO_2. The glassware was then rinsed three times with water and boiled in water. The rinsing-boiling procedure was repeated two more times.

An IviumStat potentiostat (Ivium Technologies) was used during electrochemistry experiments. All experiments except voltammetric characterizations were 85% iR-compensated in-situ. The solution resistance was measured with electrochemical impedance spectroscopy at 0.75 V vs. RHE, by observing the absolute impedance in the high frequency domain (100-50 KHz) corresponding to a zero-degree phase angle.

3.2.5. *Rotating ring-disk electrode (RRDE) procedures*

RRDE experiments were performed in 0.1 M $HClO_4$ solutions with a pH value of 1.20 ± 0.05, as measured with a Lab 855 meter equipped with a glass electrode (SI Analytics). The solutions were saturated with Ar (Linde, purity 6.0) before experiments. Solutions were bubbled with Ar gas during forced convection experiments, Ar was used to blanket the solution in stationary conditions. The reference electrode was a HydroFlex® reversible hydrogen electrode (Gaskatel), separated from the main solution using a Luggin capillary, to fix the reference sensing point and to prevent mixed potentials at the reference due to dissolved Cl_2 gas. The Luggin tip was distanced ~2 cm from the working electrode, to minimize distortion of the current distribution across the electrode surface,[116] and it was aligned to the center of the working electrode, to minimize electrical cross-talk.[137,138] All potentials in this chapter are reported on the RHE scale. A Pt mesh was used as counter electrode, separated from the main solution with a coarse sintered glass frit.

RRDE measurements were done with an MSR rotator and E6 ChangeDisk RRDE tips in a PEEK shroud (Pine Research). GC disks (Pine Research Instrumentation, surface area 0.196 cm^2) were prepared to a mirror finish by hand polishing on Microcloth pads with diamond paste suspensions down to 0.05 µm particle size (Buehler), followed by rinsing and sonication of the electrode in water for 3 minutes. The fine-ground catalyst powders were prepared as suspensions of 3 mg/mL (total catalyst mass) in EtOH (AR/Analysis grade, Acros organics). After drying the prepared GC surface with compressed air, the RRDE tip was placed upside down in the MSR rotator. Thin films of catalyst were prepared by dropcasting 2.5 µL well-stirred EtOH suspension (formal loading ~38 µg * cm^{-2}, total catalyst mass) onto the GC surface, followed by drying under rotation at 175 RPM. After the solvent had visibly evaporated, the surface was further dried with hot air for several minutes.

Before any RRDE experiment, the Pt ring was electrochemically reactivated by scanning from -0.1 V to 1.7 V at 500 mV s^{-1} for 20 scans at 1500 RPM. Hydrodynamic experiments were done at 1500 RPM by scanning the disk electrode in the range of 1.3 – 1.55 V at 10 mV s^{-1}. In between

experiments, the disk electrode was kept at 1.3 V. Ring currents were corrected for constant background currents and product collection delay. The latter arises from the time needed for products formed on the disk to reach the ring, and was approximately 200 ms at 1500 RPM.

The liquid phase collection factor of the ring-disk system, N_l, was determined by studying the $Fe[CN]_6^{3-}/Fe[CN]_6^{4-}$ redox couple in a solution of 10 mM $K_3Fe[CN]_6$ and 0.1 M KNO_3, using the Pt ring with a freshly prepared blank GC electrode. The value was 0.241 within 5% accuracy. The collection factor for dissolved Cl_2 was also measured in the same setup, by evolving chlorine selectively on Ba_2PrIrO_6 in 0.1 M $HClO_4$ + 0.1 M NaCl at a potential of 1.48 V vs. RHE, right before the kinetic onset of OER. The collection factor for dissolved chlorine, N_{Cl_2}, was found to be 0.215 within 3% accuracy, slightly lower than N_l. The difference can be attributed to the higher solution pH compared to the work in Chapter 2, which causes an increase in the degree of Cl_2 dissociation into Cl^- and HClO, the latter of which is not detectable using present methods (see section 2.3.1). The value for N_{Cl_2} was used in all calculations concerning OER and CER current separation.

3.2.6. *Parallel OER and CER – Activity measurements*

Before initiating quantitative measurements, the GC-supported thin films were scanned 20 times in chloride-free 0.1 M $HClO_4$ between 1.3 − 1.55 V, into the OER region, at 1500 RPM. This was done to ensure unchanging catalyst behavior during experiments. The Pt ring was initially deactivated. The final scan of this procedure was taken as the data for 'pure' OER activity. In the next step, the double layer capacitance was determined to allow a degree of normalization of the currents vs. electrochemical surface area (see below). Finally, 20 mM NaCl was added to the solution, and the GC supported thin film was scanned once again between 1.3 − 1.55 V at 1500 RPM, with the Pt ring fixed at 0.95 V vs. RHE for Cl_2 detection. These three steps were performed strictly sequentially using the same film and setup. The procedure of steps was repeated for each catalyst material at least three times, in independently prepared solutions and glassware, and using freshly prepared electrode films.

Measurement of the double layer capacitance $(C_{dl})_E$ was done by scanning the electrode in the potential window of 0.05 − 0.15 V at scan rates of 25, 50, 75 and 100 mV/s (see Figure A 9.3.7). The value of the double layer capacitance $(C_{dl})_E$ was calculated from the slope of the charging current around 0.1 V vs. scan rate, $i_{(C_{dl})_{0.1V}} = (C_{dl})_{0.1V} * v$ (see Figure A 9.3.8). From $(C_{dl})_{0.1V}$, the electrochemical surface area could be approximated for each individual experiment by normalizing the activity to the specific capacitance of the double layer, assuming 0.059 mF cm^{-2} for the latter.[66] Reported values for each type of catalyst are averaged from individually normalized activities.

3.2.7. *Parallel OER and CER – CER selectivity vs. [Cl⁻] measurements*

Just like the activity measurements, the GC-supported thin films were scanned at least 20 times in chloride-free 0.1 M $HClO_4$ between 1.3 − 1.55 V at 1500 RPM, to ensure unchanging catalyst behavior during experiments. Following this, the ring was activated and kept at 0.95 V vs. RHE during all measurements. The electrode was then again scanned between 1.3 − 1.55

V at 1500 RPM, while increasing the concentration of NaCl in steps from 0 mM to 120 mM. No attempt at normalization versus surface area was undertaken for these experiments, since we were interested in OER vs. CER selectivity and their reaction orders only, which are not affected by current normalization. Details about the preparation of the amorphous, hydrated IrO_x/GC catalyst can be found in section 9.1.2.

3.3. Results and discussion

3.3.1. *ICP-MS measurements and effect of chloride on stability*

A series of Ba_2BIrO_6 compounds (B = Pr, Nd, La, Sn, Y, Tb, Ce) and Sr_2YIrO_6 were synthesized and investigated for OER and CER activity and selectivity. We first investigated the stability of these materials under representative electrochemical conditions, since it has recently been shown that Ir-based perovskites are unstable in acidic media. Ba_2PrIrO_6[153,154] and the single perovskite $SrIrO_3$[160] tend to leach out both Ir and non-noble metals from their lattice during sustained oxygen evolution, leading to an amorphous IrO_x outer surface layer that is highly active towards the OER, expectedly more so than the bulk material. The main driver for this instability appears to be the favorable thermodynamics of non-noble metal dissolution in acidic media, followed by co-dissolution and/or collapse of the interspaced IrO_6 octahedra. Since our experiments involve CER in addition to the OER, it was necessary to study the effect of chloride on the leaching behavior of the studied materials.

We performed online electrochemical ICP-MS measurements to follow the dissolution of Ir and the A + B cations under electrochemical conditions in 0.1 M $HClO_4$, in presence and absence of 50 mM NaCl. Each experiment was comprised of the same electrochemical protocol seen in Figure 3.1A (top). Contact was made at 0.05 V, while subsequent potential cycling at 200 mV s^{-1} to 1.6 V was used to reach reproducible CVs. After a "resting" period at 1.2 V in which the dissolution subsided to its background signal, a linear sweep voltammogram (LSV) at 10 mV s^{-1} to 1.65 V, along with the integral of Ir dissolution, was used to calculate the stability number (*S-number*).[154] In the presence of chlorides, the formula for calculating the S-number was adapted according to Eq. A 9.3.3 to include the formation of chlorine gas. Ba_2PrIrO_6, Ba_2YIrO_6, Sr_2YIrO_6 and Ba_2CeIrO_6 were chosen as representative double perovskites.
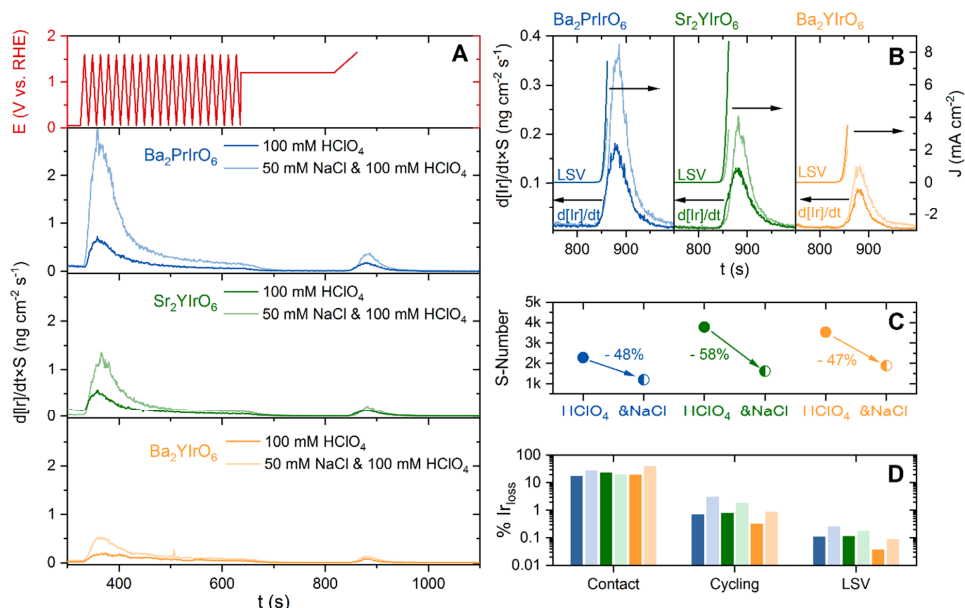
Figure 3.1: Online electrochemical iridium dissolution from ICP-MS measurements. Panel A: Ir dissolution over time correlated with the applied E vs. t protocol (red) for Ba_2PrIrO_6 (blue), Sr_2YIrO_6 (green), and Ba_2YIrO_6 (yellow), in 0.1 M $HClO_4$ (solid) and 0.1 M $HClO_4$ with 50 mM NaCl (pale). For clarity reasons, the initial contact peak is not shown (see Figure A 9.3.1 for the full version). Panel B: Ir dissolution along with the current density of the LSV of the E vs. t protocol. Panel C: S-number (amount of gases evolved per amount of Ir dissolved) comparison in presence and absence of 50 mM NaCl. Panel D: Total dissolved amount of Ir during initial contact with the electrolyte, cycling and the LSV, as determined from the initial spot loading (see also Table A 9.3.1).

Figure 3.1 summarizes online ICP-MS Ir dissolution from Ba_2PrIrO_6, Ba_2YIrO_6 and Sr_2YIrO_6 during the electrochemical protocol. Additional dissolution data for Ba_2CeIrO_6 is shown in the SI. Similar to a previous report,[154] all materials experience major Ir leaching immediately upon contact with the acidic electrolyte (Figure 3.1D), during which the electrode is conditioned at 0.05 V vs. RHE. Cycling of the electrode promotes the rate of iridium leaching, suggesting that the effect is strongly dependent on transient changes in the catalyst matrix.[82] Non-noble components (Ba, Pr, Sr, Y and Ce) however show little to no potential dependent dissolution and merely dissolve upon electrolyte contact. Table A 9.3.2 offers an overview of all integrated dissolution rates. In this table, Ba_2PrIrO_6 in chloride-free electrolyte shows enhanced contact dissolution rates of Ba compared to Pr and Ir. This conforms to previously reported XPS data on Ba_2PrIrO_6 which was exposed to a similar environment.[153] Interestingly, Sr in Sr_2YIrO_6 shows a small but more pronounced potential dependent dissolution during cycling than Ba in Ba_2PrIrO_6 and Ba_2YIrO_6. A lack of a clear trend for the total dissolution of any element in the presence of chloride is due to the big percentage of the contact dissolution on the overall dissolved amount (90-100%). The contact peak is rarely reproducible for the same catalyst as it depends on many factors. We therefore limit the following discussion to the dissolution observed during potentiodynamic control. Most importantly, the dissolution of Ir is increased significantly during both the cycling and the linear potential ramp (Figure 1D). To look into this aspect in more detail, the extent of Ir leaching was correlated with the catalytic current in

the voltammogram during the final LSV (Figure 1B). This allowed the calculation of the S-numbers for both the pure OER in $HClO_4$, as well as a competitive oxygen and chlorine evolution in the presence of chloride (Figure 3.1C). A faradaic efficiency of 100% towards the OER, and 90% chlorine evolution to 10% oxygen was assumed according to RRDE experiments, respectively (see section 3.2.7). The stability number S (plotted in Figure 3.1C) had a very similar value for Ba_2PrIrO_6, Ba_2YIrO_6 and Sr_2YIrO_6. For Ba_2CeIrO_6, OER activity and Ir dissolution during the linear sweep were too low to accurately measure, and S could not be determined. In presence of chloride, all materials experience more Ir dissolution, as illustrated by a roughly 50% decrease in S, which is in line with previous results on the stability of noble metals such as Pt and Rh in presence of chloride.[90] These results suggest that the dissolution of noble metal centers is impacted very differently during CER than during the OER. We speculate that whereas during the OER, the dissolution is driven by formation of higher oxide species, Cl^- may enhance Ir dissolution specifically by forming chloro-iridate complexes such as $IrCl_3$ and $Ir[Cl]_6^{3-}$. We note that the total amount of Ir that dissolved from the double perovskites during these experiments is several orders of magnitude larger than what has been reported for IrO_2.[161] This means that IrO_2 represents an interesting, transiently stable material for comparison in this study.

3.3.2. *Catalyst characterization*

To verify the bulk properties of the materials tested in this study, powder XRD patterns were measured (Figure A 9.3.2). The patterns generally agree with those reported in the literature;[155,156,162] in particular, the presence of the super lattice lines at about 18° and 35°, which in the double cubic cell are indexed as (111) and (311) respectively, suggest an ordered arrangement of the BO_6 and IrO_6 octahedra. The IrO_2 shows poor crystallinity, displaying a single broad peak of overlapping rutile (110) and (101) reflections around 28° and 35°, as well as a wide (200) reflection around 40°. A trace of metallic Ir is also present. This trace disappeared quickly upon cycling (see Figure A 9.3.5).
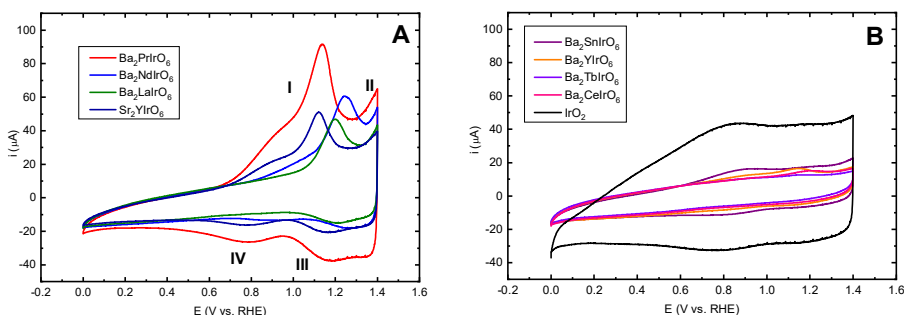

Figure 3.2: Voltammetric characterization of the Ir-based double perovskites used in this study, in a 0.1 M $HClO_4$ solution, supported on GC. All materials were scanned at least 20 times in the range of 1.30 – 1.55 V at 1500 RPM prior to characterization. Catalysts are shown in groups with pronounced Ir redox transitions (A) and those with less obvious features, plus the IrO_2 reference (B). Scan rate: 50 mV s⁻¹.

For the RRDE measurements, ethanol suspensions of the fine powders were dropcasted directly onto polished GC substrates and dried, followed by submersion and electrochemical

measurements. We avoided the use of binders such as Nafion,[153,163,164] since it was found that Nafion had a major depressing effect on CER selectivity, likely due to its permselective behavior for cations (see Figure A 9.3.3).[165] ICP-MS control experiments showed that Nafion slightly enhanced Ir dissolution in Ba_2PrIrO_6 during the electrocatalytic LSV (Table A 9.3.2). The S-number however decreased very similarly (-47% vs. -48%) under the effect of chloride. These results suggest that dissolution is much less strongly affected by chloride mass transport than the CER.

Figure 3.2 displays the voltammetric characterization of ~38 μg cm^{-2} formal catalyst mass loadings of the investigated double perovskites and IrO_2 in the potential window of 0 – 1.4 V. On the basis of the stability results (section 3.3.1), we expect transient dissolution in all double perovskites during the RRDE measurements. All characterizations in Figure 3.2 were therefore taken from electrodes that were scanned at least 20 times in the potential region 1.30 – 1.55 V in 0.1 M $HClO_4$ at a rotation rate of 1500 RPM, to ensure that the voltammograms correspond to the actual catalyst surfaces that were used for subsequent OER and CER catalysis. The plots cannot be ascribed to idealized double perovskite surface structures but should be considered as double perovskite-derived thin IrO_x films in varying states of amorphization.

On the basis of their voltammetric characterization, we divided the materials into two groups. First, we consider Ba_2PrIrO_6, Ba_2NdIrO_6, Ba_2LaIrO_6 and Sr_2YIrO_6, which show strong redox transitions in the range of 0.6 – 1.4 V (Figure 3.2A). These transitions are tentatively ascribed to Ir redox transitions, as was done previously for Ba_2PrIrO_6.[154] Ba_2PrIrO_6 and Sr_2YIrO_6 show two sets of peaks in the forward scan (marked I and II) and in the backward scan (marked III and IV). Considering the position and irreversibility of the peaks, we ascribe these peaks to the formation of an amorphous IrO_x surface layer as a result of the leaching of A and B cations. Peaks I and IV likely correspond to a transition between Ir^{3+} and Ir^{4+}, whereas peaks II and III represent further Ir oxidation that may be beneficial for OER catalysis (either formation of Ir^{5+} centers,[166–168] or the more recently proposed formation of Ir^{4+}-O^--moieties).[169,170] Second, the group of Ba_2SnIrO_6, Ba_2YIrO_6, Ba_2TbIrO_6 and Ba_2CeIrO_6 shows more subtle features (Figure 3.2B). It is somewhat surprising that Ba_2YIrO_6 and Ba_2CeIrO_6 do not have pronounced Ir redox peaks, since they also displayed significant dissolution upon contact in ICP-MS measurements (Table A 9.3.2). Possibly, an amorphous IrO_x layer is formed not during contact dissolution, but during potential scanning in the OER region. The rate of Ir dissolution during this scanning, which differs between catalysts, perhaps controls the extent to which the layer forms. The IrO_2 reference shows a broad profile with small reversible peaks around 0.8 V and 1.2 V, in accordance with previous studies on IrO_2.[150] We observed a trace of hydrogen evolution near 0 V for 'pristine' IrO_2 before scanning repeatedly into the OER, which we ascribe to a small amount of metallic Ir present in the bulk (see also Figure A 9.3.5). This behavior is no longer visible in Figure 3.2B because of the irreversible conversion of interfacial metallic Ir into its oxide, which is a much worse HER electrocatalyst.[171] See Figure A 9.3.5 for comparisons of the curves in Figure 3.2 with the catalysts in their 'pristine' state.

We must note that, in the context of this thesis, the focus is on selectivity and OER/CER interdependence, meaning we are not interested in absolute activities per se. It is however still

desirable to apply normalization of current vs. the catalytically active surface area to allow comparison between different catalysts, even though the 'active site' could become ambiguous in the case of two distinct reactions. The most common and straightforward approach is normalization vs. the electrochemically active surface area (ECSA) by measuring the double layer capacitance $(C_{dl})_E$ around potential E, which is expected to scale with the ECSA according to:

$$\text{ECSA} = \frac{(C_{dl})_E}{C_{dl}^*} \qquad \text{Eq. 3.1}$$

where C_{dl}^* is the specific capacitance per surface area of the material. $(C_{dl})_E$ can be determined from the slope of the double layer charging current vs. the scan rate (Figure A 9.3.7). Unfortunately, accurate ECSA determination is a persistent problem throughout electrocatalysis,[172] for four main reasons: i) accurate values of C_{dl}^* generally do not exist, ii) $(C_{dl})_E$ has to be measured in a region completely free of faradaic processes, iii) $(C_{dl})_E$ may be affected by the (potential-dependent) conductivity of the material, iv) determination of $(C_{dl})_E$ is not a selective chemical surface titration method, so that its value may actually not be the best measure of the ECSA.

Ideally, $(C_{dl})_E$ should be measured at the same potential for all materials. Considering Figure 3.2, there is large variation in behaviors for the studied materials within the potential window of $0 - 1.4$ V. The Ir-related redox transitions in Figure 3.2A are visible in a wide potential range up until the OER/CER onset, which means that any $(C_{dl})_E$ measurement in this potential range is distorted by pseudo-capacitive contributions. McCrory *et al.* recommend measuring C_{dl} around the open circuit potential, but almost all measured materials assumed an open-circuit potential value that fell in the pseudo-capacitance area. In fact, the E_{OCP} value is likely not suitable in this regard, since it almost invariably depends on mixed potentials, i.e. the occurrence of multiple surface reactions resulting in zero net current. Other authors recommend electrochemical impedance modelling to measure the adsorption capacitance of reaction intermediates as an estimate of the ESCA.[173] In the end, we resorted to measuring $(C_{dl})_E$ in a 0.1 V interval centred around 0.1 V, hereby termed $(C_{dl})_{0.1\,V}$. This area appeared free of pseudo-capacitive processes for all materials (Figure 3.2). Assuming a specific capacitance $C_{dl}^* = 0.059$ mF cm^{-2}, an 'average' of reported literature values for oxides in acidic conditions,[66,153] we obtained ECSAs with similar magnitudes as the geometrical surface area. The caveat of this method is the large separation of OER-relevant potentials and the ECSA determination. Under the assumption that the Ir centers dictate the observed pseudo-capacitive behavior, we also cannot exclude interference from conductivity (category iii), since amorphous Ir oxides show a notable decrease of conductivity below 0.5 V.[174] In effect, this means that part of $(C_{dl})_{0.1\,V}$ may originate from the GC substrate.[175,176] Despite the shortcomings of this normalization method, it has to be noted again that the activity normalization affects neither the slope of Tafel curves, the reaction order analysis, or OER vs. CER selectivity.

3.3.3. *OER and CER activity trends*

In consideration of section 3.3.1 and 3.3.2, we will not theorize about catalyst structure vs. catalytic activity relationships, since the true structure of the double perovskite surfaces is not known. The materials show rather diverse catalytic behavior as will be shown below.

In the following sections, the RRDE method described in Chapter 2 will be implemented to measure individual OER and CER current densities. As discussed in that chapter, the total current on the disk electrode (i_D) is assumed to be the sum of CER current (i_{CER}), OER current (i_{OER}), and a residual current originating from scanning (pseudo)capacitance. The capacitive contribution was effectively minimized by using a relatively slow scan rate of 10 mV s^{-1} and averaging forward and backward scans, yielding approximately only catalytic current from the catalytic OER and CER, which are solution-controlled processes. Values of i_{CER} were again obtained by correcting the ring currents (i_R) for the collection factor of chlorine, which had a value of $N_{Cl_2} \approx 0.215$ in 0.1 M HClO$_4$. The remaining current on the disk was then assumed to originate from the OER. See Figure A 9.3.6 for an example curve measured during a typical experiment.

Due to the perceived instability of the catalysts under study, we must note that the ring measurements may be affected by dissolved species coming from the disk. These species could cause additional stray reduction reactions, or interfere with Cl$_2$ detection by re-depositing as species which are not active towards Cl$_2$ reduction. As evidenced by their Pourbaix diagrams,[177] most A and B cations used in this study are expected to be electrochemically inert at 0.95 V in acidic solution, meaning they will not react or deposit on the Pt ring. Only Sn and solution-phase Ir species may possibly deposit as oxides under the studied conditions. From the Ir dissolution rates in ICP-MS measurements, we estimate that the error due to reduction reactions involving Ir is at least two orders of magnitude lower than the smallest ring currents related to CER (Figure A 9.3.4). Furthermore, a rough estimate shows that it would take at least 10 minutes of continuous operation at high potential to form a perfect IrO$_2$ monolayer on
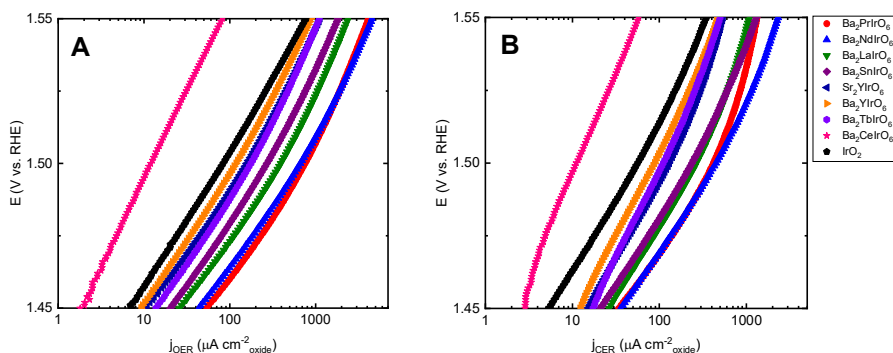

Figure 3.3: OER (A) and CER (B) Tafel curves obtained by scanning the electrode between 1.30 and 1.55 V at 10 mV s^{-1}. A: 'pure' OER current densities in a 0.1 M HClO$_4$ solution. B: CER current densities in a 0.1 M HClO$_4$ + 20 mM NaCl solution, derived from ring currents on a Pt ring fixed at 0.95 V vs. RHE. Values shown are the average of at least three independent measurements (see Figure A 9.3.9 for a version containing error bars). Solutions saturated with Ar, rotation rate 1500 RPM.

the ring. Serious interference at the Pt ring can thus be safely excluded (see section 9.3.1 for full details).

The value of the Tafel slope has been used as a 'benchmark' for catalytic OER performance, with a lower Tafel slope correlating with a 'better catalyst'.[178–180] It must be noted that strictly speaking, the catalytic performance of a material is not governed by the Tafel slope only. A low Tafel slope is only favorable if it leads to a low(er) overpotential at the desired current density. The experimental findings related to the Tafel slope are discussed in this spirit; namely, that catalytic performance and the Tafel slope are not by definition correlated.

Initially, 'pure OER' currents (in absence of Cl^-), as well as CER currents were measured during the parallel evolution of oxygen and chlorine. Figure 3.3A shows OER Tafel plots constructed from capacitance-corrected disk current densities, in absence of Cl^-. Figure 3.3B shows CER Tafel plots constructed from ring currents in presence of 20 mM Cl^-. The activities for the OER roughly follow the order $Pr \approx Nd > La > Sn > Sr_2Y \approx Tb > Ba_2Y > IrO_2 > Ce$. The most catalytically active DPs Ba_2PrIrO_6, Ba_2NdIrO_6, Ba_2LaIrO_6 and Sr_2YIrO_6, also show a redox transition in their blank CVs (see Figure 3.2A). We speculate that activities correlate to the extent of surface leaching, although a definite correlation between activity and total dissolved
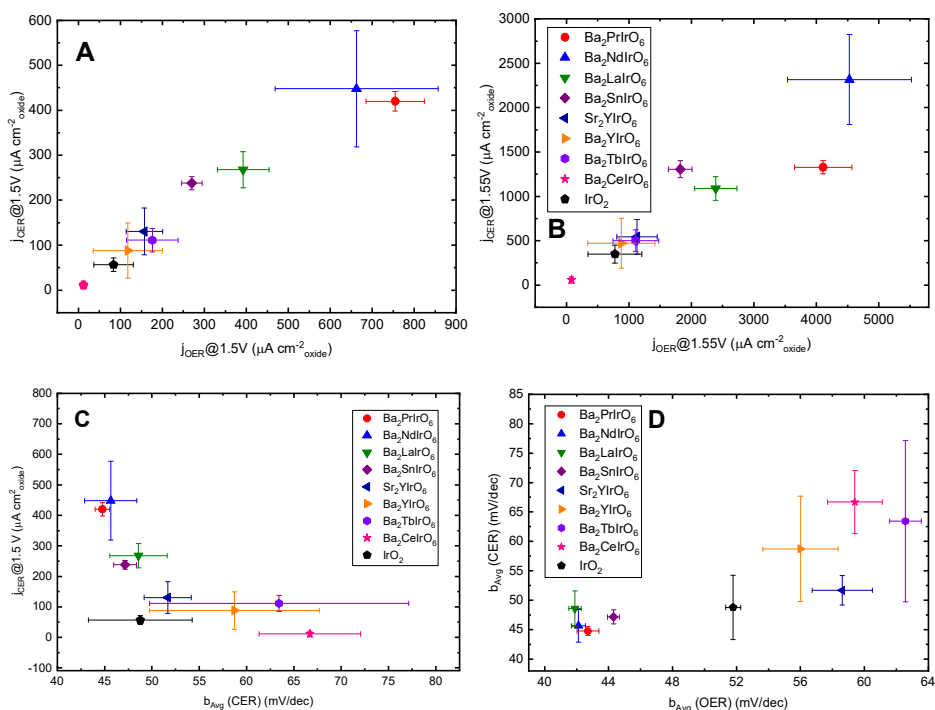
Figure 3.4: Correlations between OER and CER activities, data derived from Figure 3.3 (CER measured in 20 mM NaCl). A and B: OER vs. CER current densities compared at 1.50 V and 1.55 V, respectively. C: Comparison of CER Tafel slope vs. current densities measured at 1.50 V, the upper potential limit of the linear portion. D: Comparison of Tafel slopes from linear portions (1.45-1.50 V) of the OER and CER. All data are averages of at least three independent measurements. Error bars represent corresponding standard deviations.

amounts could not be established (see sections 3.3.1 and 3.3.2). Interestingly, the same order in activity is observed for the CER, indicating scaling between OER and CER activities. To minimize mass transport control in case of CER, the experiments were performed at 1500 RPM. The highest measured CER current densities per geometric area, as measured at 1.55 V on Ba_2PrIrO_6, were approximately 10% of the theoretical diffusion limited current as predicted by the Levich equation. Therefore, it can be assumed that mass transport effects on CER are negligible in the potential ranges studied. The OER is considered effectively immune to mass transport effects.

Figure 3.4A and B show a comparison of CER and OER current densities for all materials, plotted at 1.50 V and 1.55 V. As already faintly visible from Figure 3.3, there is a linear scaling relationship between OER and CER activity. Although such a relationship has been observed in previous literature, it must be noted that this is one of the few reports directly showing a correlation between CER and OER activity among a group of catalysts.[55] Furthermore, all materials, including the least active ones, showed regions of linear Tafel phenomena for both the OER and CER ($R^2 > 0.98$). The slopes of these linear CER Tafel sections are shown in Figure 3.4C, in comparison to CER current densities at 1.50 V. A lower Tafel slope generally correlates with higher CER current densities, which is a reasonable finding due to the exponential nature of the j/E curves. Furthermore, the catalytically most active materials display linear Tafel slopes in the range 45-50 mV/dec for the CER, and slopes of 40-45 mV/dec for the OER (D). For the less active materials, higher Tafel slopes with a higher variance are observed (see Table A 9.3.3 for all numerical Tafel slope values).

Considering the instability of the materials, we must comment on the possible origin of the linear relation between OER and CER activity. As previously mentioned, the selective leaching of non-noble A and B cations from the lattice will to a varying extent form an amorphous IrO_x surface layer on all materials. Since the double perovskites share identical structural motifs,

one can expect them to follow comparable amorphization behavior. This could result in thin catalytically active IrO_x layers with perhaps varying surface area but similar kinetics, and thus a linear OER vs. CER relation would always be observed. However, the variance in Tafel slopes for the CER strongly speaks against this effect being the only descriptor for the OER and CER activity;[56,181] if identical IrO_x is formed, then all semi-logarithmic i-E curves should display nearly identical (±5 mV/dec) Tafel slopes, which is not the case. The IrO_2 reference furthermore fits in the scaling trend very well, despite possessing a rather different structure compared to the double perovskites. All in all, although the true nature and structure of the active catalyst phases cannot be discerned, we can still conclude that they vary among catalysts, and that despite this, a linear scaling relationship between the CER and OER is observed. The origin of this scaling has been commented on by Trasatti.[55] It is possibly a similarity between the way that chloride binds to surfaces, as compared to the several key oxygen intermediates believed to be involved in the OER.[72] Most importantly, scaling suggests that a catalyst with a kinetic preference towards only one of the reactions may be very hard to find.

CER selectivity as a function of chloride concentration

Similar to Chapter 2, we further probed the OER vs. CER selectivity of the materials by varying the chloride concentration stepwise between 0 and 120 mM. Molar selectivities towards CER (ε_{CER}) were defined according to Eq. 2.3. Measured values of ε_{CER} for all materials are shown in Figure 3.5, at 1.50 V and 1.55 V. At 1.50 V, ε_{CER} is very similar among materials and shows a strong dependence on chloride concentration. At 1.55 V (Figure 3.5B), selectivity towards the OER increases and there is more variance among materials. A group consisting of Ba_2PrIrO_6, Ba_2NdIrO_6, Ba_2LaIrO_6 and Sr_2YIrO_6 shows particularly high OER selectivity. At both potentials shown, the least active materials generally show higher selectivity towards CER. An important exception is Ba_2SnIrO_6. This material shows relatively high CER selectivity at both 1.50 V and 1.55 V while also possessing relatively high activity.
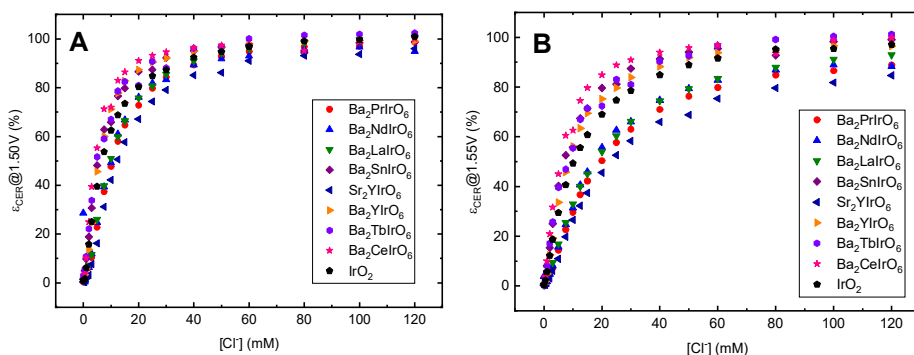
Figure 3.5: CER selectivity (ε_{CER}, definition in main text) as a function of $[Cl^-]$, for different Ir double perovskites and the IrO_2 reference. Values shown at 1.50 V (A) and 1.55 V (B). Values were obtained with the RRDE method as described in section 3.3.3.

Despite these differences, it can be said that ε_{CER} is globally governed by a single relationship none of the materials show extremely diverging values (>20%) in their selectivity between the OER and CER. This conclusion is in-line with Figure 3.4A and Figure 3.4B, where a scaling trend was seen at the single concentration $[Cl^-] = 20$ mM. This tendency seems to be applicable to higher chloride concentrations as well. The effect of mass transport on the measured CER currents should not be high. A 10% decrease in CER current, the prediction for maximum mass transport control in the experiments (see also the discussion of Figure 3.3), should lead to a decrease in ε_{CER} of less than 2% for virtually all chloride concentrations. At potentials above 1.55 V, selectivity towards the OER will presumably increase, since CER will become increasingly mass transport limited whereas the OER is much less affected. Unfortunately it was not possible to probe this potential region due to formation of persistent O_2 bubbles at high current densities on the electrode tip, which interfered with the collection efficiency. See Chapter 8 for a deeper discussion of this problem.

3.3.4. OER vs. CER interdependence and effect of chloride concentration

In this section, we look more deeply into the parallel evolution of oxygen and chlorine as a function of chloride concentration. Figure 3.6 shows the effect of chloride regarding the OER Tafel curves, as well as relative OER and CER activity. The chloride concentration exhibits a
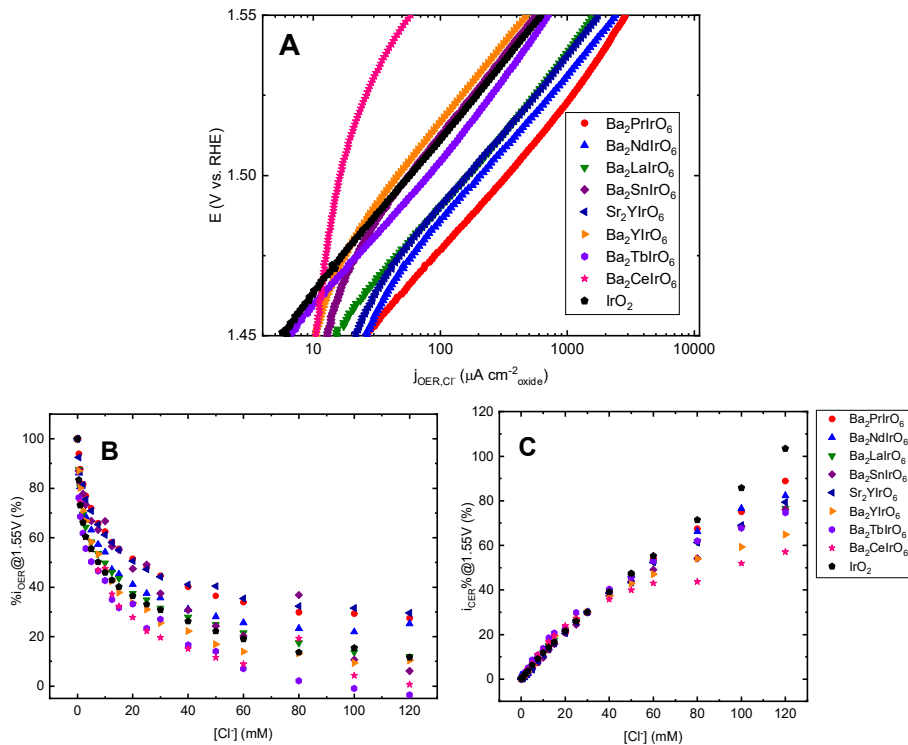

Figure 3.6: Effect of chloride concentration on the OER and CER. A: OER currents measured in the presence of 20 mM NaCl, in parallel with CER. B and C: Relative OER current (B) and CER current (C) as function of increasing chloride concentration. %OER currents shown relative to chloride free conditions (0 mM NaCl), %CER currents shown relative to 30 mM NaCl. See Figure A 9.3.12 for versions of A and B containing absolute currents.

pronounced influence on all catalysts under study regarding both the CER and OER. When comparing Figure 3.6A to Figure 3.3A, the presence of 20 mM Cl^- induces a shift of the OER Tafel curves towards higher potentials, a reduction in the apparent OER exchange current density and thus a decrease in the OER activity (a factor of 2 for most materials). A scaling relationship was again apparent when OER data from Figure 3.6A was compared to CER data from Figure 3.3B (see Figure A 9.3.10). Figure 3.6B and Figure 3.6C show relative OER and CER currents as a function of increasing $[Cl^-]$. For the OER, all values are shown as percentages relative to the value at chloride free conditions ($[Cl^-] = 0$ mM). Likewise, all values for the CER are shown relative to $[Cl^-] = 30$ mM, where the value of the current at this concentration was taken as '30%'. This normalization was done due to the different current densities, and allows a clearer comparison between trends among materials as chloride concentrations increase (see Figure A 9.3.12 for the absolute currents). Figure 3.6B shows a

nonlinear decrease in OER current as a function of $[Cl^-]$ on all materials, in some cases (Ba_2TbIrO_6 and Ba_2CeIrO_6) approaching virtually complete OER suppression at 120 mM. At the same time, all materials show a continuous CER increase with increasing $[Cl^-]$ (Figure 3.6C), but there is significant downward curvature in all plots except for the IrO_2 reference.

For further analysis of the interdependence between the OER and CER, we consider a model for the apparent suppressing effect of Cl^- on the OER activity. The simplest approach to explain this phenomenon would be to assume a simple site blocking, similar to previous work by Fernández and co-workers:[182]

$$i_{OER} = i^0_{OER}(1 - \theta_{Cl}) = i^0_{OER}\left(1 - \frac{K_{Cl}[Cl^-]e^{f\eta}}{1 + K_{Cl}[Cl^-]e^{f\eta}}\right) \qquad \text{Eq. 3.2}$$

In this equation, i_{OER} describes the measured OER current; i^0_{OER} describes the OER current that would have been measured in absence of chloride. The other symbols again relate to a Volmer-type adsorption of chloride in pseudo-equilibrium. The corresponding OER chloride reaction order dependence then becomes:

$$\mathcal{R}^{OER}_{Cl^-} = \left(\frac{\partial \ln i_{OER}}{\partial \ln[Cl^-]}\right)_E = -\frac{K_{Cl}[Cl^-]e^{f\eta}}{1 + K_{Cl}[Cl^-]e^{f\eta}} \qquad \text{Eq. 3.3}$$

From this expression, we expect $\mathcal{R}^{OER}_{Cl^-}$ to change from 0 to -1 as $[Cl^-]$ increases, the rate of change depending on the overpotential and K_{Cl}. We will also consider the chloride reaction orders of the CER ($\mathcal{R}^{CER}_{Cl^-}$), and compare them with predictions from microkinetic models described in section 1.4.

The experimental OER and CER reaction orders can be approximated from the derivative of log-log plots (see Figure A 9.3.15) of the i vs. $[Cl^-]$ curves. The results are shown in Figure 3.7. Reaction orders for the OER and CER that were measured on IrO_x/GC in Chapter 2 (section 2.3.4) have been included for comparison. As described in 2.3.3, the results for values of $[Cl^-]$ < 10 mM in Figure 3.7 may not be fully reliable due to possible interference of oxide formation on the Pt ring used for detection.
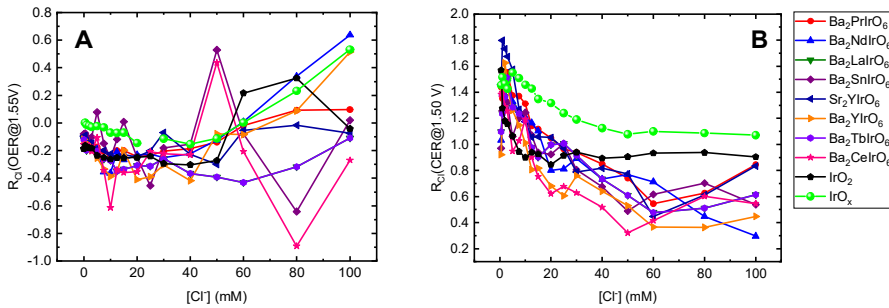

Figure 3.7: Reaction orders vs. chloride concentration ($\mathcal{R}_{Cl^-}$) for the OER (A) and CER (B). Values were derived using the $[Cl^-]$-dependent slopes of Figure A 9.3.15.

The initial focus of the discussion will lie on the OER chloride reaction order, for $[Cl^-]$ concentrations of up to 50 mM (see Figure A 9.3.16 for a close-up of this region). In this range, $\mathcal{R}_{Cl^-}^{OER}$ has a negative fractional value between -0.2 and -0.4 for all materials tested in this study, as was already apparent from the continuous decrease in OER activity in Figure 3.6B. Interestingly, the previously characterized IrO_x has a value of $\mathcal{R}_{Cl^-}^{OER}$ closest to 0, varying between 0 and -0.1. This is illustrative of this material's OER kinetics being almost impervious to the presence of chloride or parallel chlorine evolution, in contrast with the double perovskites. For these materials, $\mathcal{R}_{Cl^-}^{OER}$ is generally less negative the higher the intrinsic activity of the material, except for the lrO_2 reference, which shows relatively low activity but globally also one of the least negative values of $\mathcal{R}_{Cl^-}^{OER}$. Furthermore, most OER Tafel curves exhibit negligible changes in slope after the addition of Cl^-, except for Ba_2CeIrO_6 (see Figure A 9.3.11 for a comparison and Table A 9.3.3 for the full data). This suggests that Cl^- does not change the OER mechanism, which (along with the decreasing fractional reaction order in Figure 3.7A) is in agreement with the simple site blocking model. However, the extent of blocking appears to depend sensitively on the type of material. We hypothesize that site blocking for a more amorphous catalyst is different from that in a less amorphous system. The OER data at $[Cl^-]$ exceeding 50 mM are subject to increasing levels of uncertainty, due to inherent limitations of the experiment. With rising chloride concentration, the CER contribution starts to dominate the OER current, as a result of which the experimental noise is greatly amplified in subtle slope changes of the log-log plots. Extensive averaging or smoothing may alleviate the noise, but we chose to present the data as-is to illustrate limitations of the method. Despite the noise, the overall trend nonetheless suggests that the reaction order never reaches -1, but rather seems to increase again, occasionally reaching positive values. This may reflect the influence of chloride on the actual structure of the catalytic interface.

Regarding the CER in Figure 3.7B, $\mathcal{R}_{Cl^-}^{CER}$ also decreases continuously for all double perovskites, down to values of roughly 0.5. For lrO_2 however, it stays at a constant value close to unity, $\mathcal{R}_{Cl^-}^{CER} \approx 0.92$. The IrO_x reference material shows even different values, with $\mathcal{R}_{Cl^-}^{CER} \approx 1.45$ around $[Cl^-] = 10$ mM, which then progressively decreases to a steady value of 1.07. A $\mathcal{R}_{Cl^-}^{CER}$ value close to one has often been reported on metal oxides.[35,55,112,183,184] Furthermore, a decrease in $\mathcal{R}_{Cl^-}^{CER}$ as a result of an increase in $[Cl^-]$ has been reported previously on RuO_2.[185] Judging from reaction orders alone, it thus seems likely that both IrO_x and lrO_2 follow a Volmer-Heyrovský mechanism, as their reaction orders converge near 1 at higher $[Cl^-]$. This is in agreement with previous reports.[35] On the other hand, reaction orders on all double perovskites continuously decrease to values much lower than 1. Such behavior is more expected of either a Volmer-Tafel or Volmer-Krishtalik mechanism dominating the kinetics. We further investigated the CER mechanism using test plots devised by Conway *et al.*[118] and Ferro *et al.*[113] By re-ordering the measured CER i-E curves, one can test whether a Volmer-Tafel or Volmer-Heyrovský mechanism applies (see Figure A 9.3.13 and its description for details about the method). For lrO_2, we obtained a straight line in a Ferro-de Battisti test plot only, indicating Volmer-Heyrovský kinetics. We note that a straight line in such a plot can also indicate Volmer-Krishtalik kinetics. However, the y-intercept is then expected to be independent of $[Cl^-]$. Instead, the intercept shows an inverse $[Cl^-]$ dependence, which

matches well with the V-H pathway (see Figure A 9.3.14 for more details). On the other hand, Ba_2PrIrO_6 only showed a straight line in a Conway-Novák test plot, suggesting that CER proceeds via a Volmer-Tafel mechanism on this material (and perhaps also on the other perovskites), in agreement with the reaction order findings.

As a final note, it can be expected that the apparent OER and CER chloride reaction orders on the double perovskites are affected by adventitious surface leaching as described in section 3.3.1. This leaching should lead to transient changes of the active surface area, and its effect on either $\mathcal{R}_{Cl^-}^{OER}$ or $\mathcal{R}_{Cl^-}^{CER}$ can be modelled via:

$$i = A([Cl^-])j \qquad \text{Eq. 3.4}$$

where i is the measured current for either the OER or CER, j is the current density as modelled by either the V-T or V-H model, and A is the real electrochemical surface area, which is dependent on chloride concentration due to leaching. It then follows that:

$$\mathcal{R}_{Cl^-} = \left(\frac{\partial \ln i}{\partial \ln[Cl^-]}\right)_E = \frac{\partial \ln j}{\partial \ln[Cl^-]} + \frac{\partial \ln A([Cl^-])}{\partial \ln[Cl^-]} \qquad \text{Eq. 3.5}$$

On the right-hand side, the first term corresponds to the 'kinetic' reaction order, as discussed earlier in this section. The second term represents the influence of chloride on the real surface area. As seen in Figure 3.1 and Table A 9.3.2, the leaching rates of both noble and non-noble components are chloride-dependent, but not in the same manner; a complex interplay can be expected from surface area changes due to increasing chloride concentration. Not much is currently known on the growth of amorphous surface phases on these materials in acidic media, meaning that the value and range of the A term is not easy to quantify. A reasonable assumption is that the term $\partial \ln A([Cl^-]) / \partial \ln[Cl^-]$ is positive immediately upon contacting the pristine perovskite with acidic electrolyte, during which the majority of surface leaching takes place and the change in surface area should be the largest. Considering that the rate of leaching steadily decreases over time in Figure 3.1, we may expect A to approach a constant value for all values of $[Cl^-]$, and its contribution to the reaction order should then tend to 0. On the other hand, if the rate of leaching increases strongly with increasing $[Cl^-]$, increasing changes of A could explain the apparent rise in reaction orders for both the OER and CER at higher Cl^- concentrations.

3.4. Conclusions

In this chapter, we report that iridium-based double perovskites with structures Ba_2BIrO_6 (B = Pr, Nd, La, Sn, Y, Tb, Ce) and Sr_2YIrO_6, previously reported having high oxygen evolution activity in acidic media, also show high catalytic activity towards chlorine evolution in relatively low chloride concentrations (0 – 120 mM). A strong linear correlation between the CER and OER activity was found on all catalysts employed, and also comparable selectivity. This strengthens the suggestion that the OER and CER follow a scaling relationship, as suggested in previous studies. On the basis of these results, it can be expected that promoting one reaction over the other on the basis of kinetic considerations alone may be exceedingly

difficult, if not impossible. Alternative pathways, such as affecting the CER thermodynamics through pH changes, or the mass transport of chloride to the active catalyst, are likely more successful in enhancing selectivity. Electrochemical ICP-MS measurements showed that chloride has mixed effects on the stability of the perovskites. Whereas non-noble dissolution effects were inconclusive, it significantly enhanced iridium dissolution during potentiodynamic control and active OER/CER, as evidenced by a lower value of the *S*-number. Dissolution pathways related to the OER and CER are therefore likely different, which must be taken into account when considering an active catalyst for either of the reactions. Reaction order analysis indicates that CER proceeds via Volmer-Tafel mechanism on the double perovskites, whereas it follows a Volmer-Heyrovský mechanism on IrO_2 and amorphous IrO_x. Contrary to amorphous IrO_x, the OER activity on the double perovskites and IrO_2 is strongly impacted by chloride concentration, displaying fractional, negative reaction orders.

COMPETITION AND INTERHALOGEN FORMATION DURING PARALLEL ELECTROCATALYTIC OXIDATION OF BROMIDE AND CHLORIDE ON PT

4

Hydrogen production from seawater electrolysis is highly promising for the capture and storage of intermittent renewable energy. However, it is hindered by possible oxidation reactions of chloride and (to a lesser extent) bromide, which can occur in parallel to the evolution of oxygen and form harmful by-products. In this and the following chapter, we look deeper into these two unwanted side-reactions. First, we present general considerations of solution chemistry and oxidation products that may be expected in an acidic Br^-/Cl^- electrolyte. We then perform model studies of the parallel oxidation of Br^- and Cl^- and their mutual interaction on a Pt electrocatalyst, to increase the understanding of the anodic competition problem. Our results suggest that the oxidation of bromide is hindered by competing chloride adsorption on Pt, in a way that can be modelled quite well by a simple Langmuir isotherm describing the adsorption and reactivity of all species. The oxidation of chloride was however not properly captured by this same model. Furthermore, the formation of the interhalogen compound BrCl seems to occur in-between the oxidation of bromide and chloride.

4.1. Introduction

As mentioned in section 1.2, seawater would be an extremely attractive substrate for solar energy conversion. Unfortunately, attempting to directly electrolyze a chloride-containing electrolyte may lead to the formation of large amounts of toxic chlorine on the anode. In addition to Cl^-, seawater contains a small but significant amount of Br^-, roughly 0.3mol% relative to chloride.[186] Analogous to the CER, bromide can rapidly be oxidized on the anode via the bromine evolution reaction (BER):

$$2\ Br^- \rightarrow Br_2 + 2\ e^- \qquad\qquad \text{Eq. 4.1}$$

$$E^0_{Br_2/Br^-} = 1.087\ V\ vs.\ NHE$$

Like chlorine, Br_2 is corrosive and toxic, and not easily disposed of in an environmentally friendly way. Its formation is unwanted but kinetically highly favorable during seawater electrolysis, due to the relatively low equilibrium potential relative to the OER. Bromide oxidation is also an especially important consideration during the electrochemical treatment and disinfection of wastewater, because it is strongly linked to bromination of organic waste compounds present in the water. This is highly detrimental to the detoxification performance.[187–189] The BER also is relevant to the energy intensive chlor-alkali process, where Br^- is a common contaminant in the brine feedstock.[190]

Previous literature has devoted far more attention to the CER than to the BER, in light of the former's industrial importance (see section 1.2). There has recently been a moderate increase in interest in the BER as it may be a useful reaction in redox flow batteries.[191,192] Much less research has gone into systems where both Cl^- and Br^- are present, such as when using seawater or a seawater-derived electrolyte, in which the BER and CER can occur simultaneously. To the best of our knowledge, the literature on this rather complex situation is scarce, and is mostly carried out from the perspective of wastewater treatment.[193–195] Our interest goes out specifically to the fundamental understanding of the parallel halogen oxidation reactions, which can be beneficial to seawater electrolysis and water treatment alike. The BER and CER seem to follow similar electrocatalytic pathways,[118,196–198] which implies that the active sites involved in the reactions would be the same, and that some form of interaction between them can be expected. One could then imagine that the two reactions simply mutually inhibit each other, or form an intimate coupling that can lead to changes in the reaction pathway and the formation of interhalogen compounds. Either case can have important practical implications, since in the first case, one reaction may block the occurrence of the other one if the ratio between reactants is unbalanced enough. In the latter, interaction between the two reactants can lead to unexpected outcomes.

In this chapter, we explore the parallel oxidation of bromide and chloride on a Pt electrocatalyst, which exhibits significant electrocatalytic activity for both the CER and BER. As a simplified model system, we use solutions containing HCl and HBr in varying ratios with additional $HClO_4$ as background electrolyte. This prevents the presence of cations in solution, which may have an influence on the kinetics.[96,199,200] The low pH was intended to prevent

complications from the formation of oxygenated chlorine or bromine species (such as ClO^- or BrO_3^-), which is favored by high pH,[201,202] and also allowed to study both the BER and CER on Pt with minimal interference from the OER. We utilize forced convection studies using an RRDE to gain insight into the kinetic competition and interdependence of the two reactions, coupled to a Pt ring that allows quantitative detection of soluble halogen products, similar to the discussion in Chapter 2. Special focus was on Tafel behavior and reaction orders as a function of potential and reactant concentration. Of special interest were mutual inhibiting effects, and the possible electrochemical formation of interhalogen compounds, such as BrCl. Kinetic studies were complemented with in-situ electrochemical UV-Vis experiments on stationary electrodes, to probe the formation of products as a function of potential and time near the electrode surface. The combination of these techniques sheds light on how chloride and bromide interact on a model electrocatalyst, and the implications this may have in a practical setting.

4.2. Experimental

All experiments were carried out at room temperature (~20 °C). Cleanliness protocols for the RRDE experiments were considerably more rigorous than those for the UV-Vis experiments, because forced-convection techniques are inherently more sensitive to contamination.

4.2.1. *Chemicals*

For the RRDE experiments, $HClO_4$ (70%, Suprapur®/Trace analysis grade) and HCl (30%, Ultrapur®/Trace analysis grade) were purchased from Merck. HBr (47%, Normapur®/Analysis grade) was purchased from VWR Chemicals. For the UV-Vis experiments, $HClO_4$ (60%, EMSURE/Analysis grade), HCl (32%, EMSURE/Analysis grade) and HBr (47%, EMSURE/Analysis grade) were purchased from Merck. All purchased chemicals were used as received. The water used for all experiments was prepared by a Merck Millipore Milli-Q system (resistivity 18.2 MΩcm, TOC < 5 p.p.b.).

4.2.2. *Cleaning procedures*

For the RRDE experiments, all glassware was thoroughly cleaned before first-time use by boiling in a 3:1 mixture of concentrated H_2SO_4 and HNO_3. When not in use, all glassware was stored in a 0.5 M H_2SO_4 solution containing 1 g/L $KMnO_4$. Before each RRDE experiment, glassware was thoroughly rinsed with water, and then submerged in a dilute (~0.01 M) solution of H_2SO_4 and H_2O_2 to remove all traces of $KMnO_4$ and MnO_2. The glassware was then rinsed three times with water and boiled in water. The rinsing-boiling procedure was repeated two more times.

The glassware and custom-built cell for UV-Vis experiments were cleaned by soaking in warm reagent grade 98% H_2SO_4 for an hour, followed by copious rinsing with Milli-Q water and boiling three times in Milli-Q water. When not in use, they were stored submerged in Milli-Q water.

4.2.3. *Electrode preparation*

4.2.3.1. RRDE experiments

Pt disks of 5 mm diameter (0.196 cm^2 geometrical surface area) were used as primary working electrode, along with a Pt ring as secondary electrode. At the beginning of an experimental session, the assembled Pt-Pt tip was rinsed with copious amounts of Milli-Q water, treated for 3 minutes with a solution of 0.5 M H_2SO_4 containing 0.5 g/L $KMnO_4$, rinsed with Milli-Q water, treated with a dilute (~0.01 M) solution of H_2SO_4 and H_2O_2 to remove any traces of $KMnO_4$ and MnO_2, and then extensively rinsed with warm (~50 °C) Milli-Q water. During RRDE experiments, the Pt disk and ring electrodes were electropolished by scanning from -0.1 V to 1.7 V at 500 mV s^{-1} for 20 scans at 1500 RPM. In-between experiments, the disk electrode was kept at 0.7 V vs. RHE. Ring currents were corrected for constant background currents and product collection delay. The latter arises from the time needed for products formed on the disk to reach the ring. The delay for each used rotation rate was empirically determined by stepping the potential to evolve Br_2 on the disk, and investigating the ring response as a function of time.

Before each experiment, the Pt electrode was subjected to a pre-treatment step to ensure an oxide-free, reproducible surface. The electrode was first kept at 0.4 V vs. RHE for 10 s, to reduce any residual trace of platinum oxide of preceding experiments, followed by a 3 s hold at 0.7 V vs RHE, to equilibrate the electrode and allow capacitive double layer charging to minimize. Scanning commenced immediately afterwards (see Figure A 9.3.1).

4.2.3.2. UV-Vis experiments

A 5 nm platinum layer was sputtered onto a conductive fluorine doped tin oxide (FTO) substrate (TEC-15, Hartford glass co.) for the in-situ UV-Vis transmission measurements. The deposition was performed at 3 µbar deposition pressure, with a deposition rate of ~0.593 Å/s, using an AJA sputtering system (ATC 2400). The FTO substrate was cleaned, prior to the deposition, using a sequence of laboratory soap, Milli-Q water, acetone and isopropanol and eventually drying the substrates with nitrogen gas. Subsequently, the FTO substrate surface was treated using argon plasma for 2 minutes, prior to the platinum layer deposition.

4.2.4. *Cell preparation*

4.2.4.1. RRDE experiments

RRDE experiments were done with home-made two-compartment borosilicate glass cells with solution volumes of 100 mL. An IviumStat potentiostat (Ivium Technologies) run by the IviumSoft software package was used for potential control. All experiments were done with an MSR rotator and E6 ChangeDisk RRDE tips in a PEEK shroud (Pine Research). All experiments were 95% iR-compensated during the experiment, by measuring the solution resistance with electrochemical impedance spectroscopy at 0.70 V vs. RHE, and observing the absolute impedance in the high frequency domain (100-50 KHz) corresponding to a zero-

degree phase angle. All solutions used were saturated with Ar (Linde, purity 6.0) before experiments. During forced convection experiments, solutions were continuously bubbled with Ar gas. The reference electrode was a HydroFlex® reversible hydrogen electrode (Gaskatel), separated from the main solution using a Luggin capillary. An additional LowProfile Ag/AgCl reference electrode (Pine Research) served to measure the solution pH and was used for conversion to the NHE scale. The Ag/AgCl reference was externally calibrated on a regular basis and had a value of 198 ± 0.5 mV vs. NHE. All potentials in this chapter are reported on the NHE scale unless explicitly mentioned otherwise. A flame-annealed Pt mesh was used as counter electrode, separated from the main solution by a coarse sintered glass frit.

4.2.4.2. UV-Vis experiments

A Vertex potentiostat (Ivium Technologies) run by the IviumSoft software package was used for potential control. The transmission measurements were performed in a custom-built setup, consisting of a PTFE electrochemical cell housing equipped with quartz windows. A coiled platinum wire acted as the counter electrode, and a LowProfile Ag/AgCl reference electrode (Pine Research) was placed in fixed position relative to the Pt/FTO working electrode. The Ag/AgCl electrode was calibrated at 199 ± 0.5 mV vs. NHE. All applied potentials were 90% iR-compensated according to the solution resistance. The latter was measured using a similar procedure as in the RRDE experiments (section 4.2.4.1). A combination of light sources, a deuterium lamp (Mikropack D-2000) and a halogen lamp (Ocean Optics HL 2000 – FHSA), were used in the setup. These sources were combined using an optical fiber arrangement and this fiber acted as the illumination source for the transmission measurements. The setup also included a spectrometer (Ocean Optics, Maya 2000 Pro), which was used to capture the transmitted light. The setup was aligned in such a way that the platinum/FTO sample was illuminated from the back side and the transmitted light was captured on the opposite side of the electrochemical cell. The transmission data was continuously recorded in-situ, while performing the electrochemical measurements.

4.3. Results and discussion

4.3.1. *Brief review of the BER and CER kinetics on Pt*

The experimental CER kinetics on Pt appear the most compatible with the Volmer-Tafel (V-T) mechanism, as suggested by Conway and co-workers. Evidence comes from impedance studies,[108] potential-relaxation experiments[203] and recombination test plots,[204] showing that Eq. 1.19 gives a good fit of the experimental data. However, the interpretation of experimental reaction orders has been much less straightforward. This may be in large part due to the complicating effect of transient formation of platinum oxide (PtO_x), which readily occurs at potentials where the CER takes place (section 4.3.5). The oxide layer competes with Cl^- adsorption during CER electrocatalysis, and may itself have an effect on intrinsic catalytic rates.[56,205] Conway and Novák obtained chloride reaction order values close to 1 when $[Cl^-]$ = 100 mM, decreasing to zero when $[Cl^-]$ increased to 1 M and higher.[118] These values were

measured at constant overpotential, for which the V-T mechanism predicts that $\mathcal{R}_{Cl^-} = 0$ (see section 9.4.3). The authors explained the non-zero values by the effect of specifically adsorbed chloride anion (Cl^{-*}) on the PtO_x layer, but no further analysis was undertaken to explore this. The BER mechanism on Pt has been much less studied,[206–208] but previous work by Conway *et al.* with similar methodology as used for the CER indicates that it follows V-T characteristics when $[Br^-] > 1$ M.[196] The bromide reaction order was however not investigated in their work. The effect of oxides during the BER should be much lower, because the BER takes place at lower potentials than the CER. Additionally, bromide has a much stronger oxide suppressing effect compared to chloride. In a mixed $Br^- + Cl^-$ electrolyte, the situation becomes more complex, since multiple electroactive species are involved with differing adsorption strengths.[209] We will focus our study on mutual competitive blocking effects, since these should be relevant to the catalytic activity in an actual electrolyzer. Additionally, co-adsorption of the two halogens could lead to the evolution of interhalogen compounds, such as BrCl. We will show below that this compound may indeed be electrochemically formed. We assume that the direct electrochemical formation of triatomic interhalogen ions through a trimolecular reaction, such as $BrCl_2^-$, is highly improbable.

4.3.2. *Considerations of interhalogen formation reactions*

When carrying out electrolysis in a mixture of halogen anions, one needs to consider various electrode reactions and solution reactions, as summarized in Scheme 1. The corresponding equilibrium constants of these reactions are given in Table A 9.4.1.[202,210]
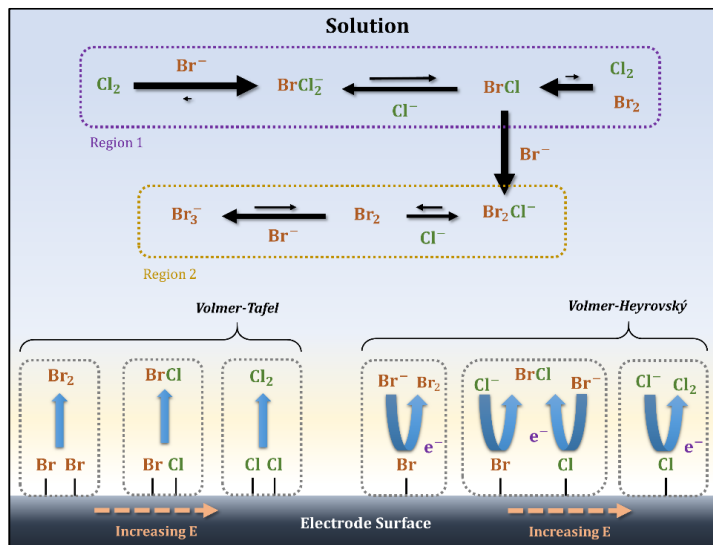
Scheme 4.1: *Halogen reaction pathways on Pt during the parallel oxidation of aqueous Br^- and Cl^- in an acidic solution, according to data from literature[210] and Table A 9.4.1. Black arrows represent solution phase reactions, relative sizes and thicknesses between pairs are illustrative of the direction of the corresponding equilibrium. Blue arrows represent elementary steps in electrochemical reactions on the electrode surface. Bottom area left shows rate-limiting reaction steps according to the Volmer-Tafel mechanism, which most likely dominates on Pt. The right shows rate-limiting reaction steps according to a Volmer-Heyrovský or Volmer-Krishtalik-type mechanism. We exclude trimolecular reactions in this scheme.*

In Scheme 4.1, solution phase reactions are drawn starting from Cl_2 and ending in Br_3^- as the most stable species. Two 'regions' can be discerned in the overall pathway: one that comprises the interconversion between stronger oxidizing species Cl_2, $BrCl_2^-$ and BrCl, and region 2 consisting of Br_2, Br_2Cl^-, and Br_3^-, species with higher stability. Besides effects of kinetic competition, we are interested if electrocatalytic interhalogen formation can occur in a mixture of Br^- and Cl^-. As discussed in section 4.3.1, the main reaction of interest is the formation of BrCl according to:

$$Br^- + Cl^- \rightleftharpoons BrCl + 2\ e^- \qquad\qquad \text{Eq. 4.2}$$

This previously unreported reaction falls thermodynamically in-between the BER and the CER (see Table A 9.4.1). It is illustrated in the lower part of Scheme 4.1, along with the BER and CER, displaying the Tafel reaction (bottom left) or electrochemical desorption (bottom right) as the rate-limiting step.

Unfortunately, accurate determination of products formed electrochemically on the electrode is not straightforward in this system, because the aqueous interhalogen reactions shown in Scheme 4.1 and Table A 9.4.1 are extremely rapid (values of rate constants are typically in the order of 10^9). Any 'oxidizing equivalents' (thermodynamically labile species) generated on the electrode will therefore tend to dissipate by reacting with bulk surplus of Br^- and Cl^- in solution, which obfuscates the identity of the electrochemical product originally formed.[211] Given sufficient mixing, the system will always evolve towards a mixture of primarily Br_2, Br_3^- and Br_2Cl^-, regardless of the electrode potential applied. Although we thus cannot pinpoint exactly the origin of any halogen species near the electrode, we can still rationalize the occurrence of reactions happening in-between the BER and the CER from thermodynamic constraints. Equilibrium constants in Table A 9.4.1 show large differences in the stability of several species. In case that only Br_2 is being generated at the electrode, this implies that no interhalogen other than Br_2Cl^- should be formed spontaneously in solution, as the driving force for the other interhalogen species is too small. The occurrence of either BrCl or $BrCl_2^-$ at electrode potentials lower than the thermodynamic onset of Cl_2 evolution can then only be rationalized by the occurrence of an electrochemical reaction. When the potential is high enough to allow Cl_2 evolution, all species Scheme 4.1 can in principle be formed. The most interesting potential region is thus in-between the BER and CER.

4.3.3. *RRDE studies of parallel oxidation of bromide and chloride*

We used RRDE voltammetry to study the kinetics of parallel oxidation of Br^- and Cl^- under hydrodynamic conditions, as this greatly simplifies the analysis by keeping the diffusion layer thickness constant. It also removes products from the surface that may possibly react further and in this way influence the apparent electrochemical kinetics;[208] this could be either follow-up electrochemical reactions on the surface, such as the oxidation of Br_2 into BrO_3^-, or through interhalogen reactions in the solution (see section 4.3.2). The RRDE also allows following the formation of soluble reaction products by utilizing a Pt ring as detector. The ring potential was fixed at 0.7 V vs. RHE, to reduce halogen species formed on the disk without also reducing O_2.

Although the onset for oxygen reduction is around 0.95 V vs. RHE on Pt in $HClO_4$, the adsorption of Br^- significantly increases the overpotential, reducing oxygen reduction to negligible rates for potential values down to 0.7 V vs. RHE.[212] It was found that Br_2 reduction becomes diffusion limited at an overpotential of approximately $\eta \approx 150$ mV (see Figure A 9.4.1 for details). Additionally, in Chapter 2 we showed that Cl_2 reduction on Pt becomes diffusion limited at $\eta \approx 250$ mV. Ring currents at 0.7 V vs. RHE can thus be taken as quantitative.
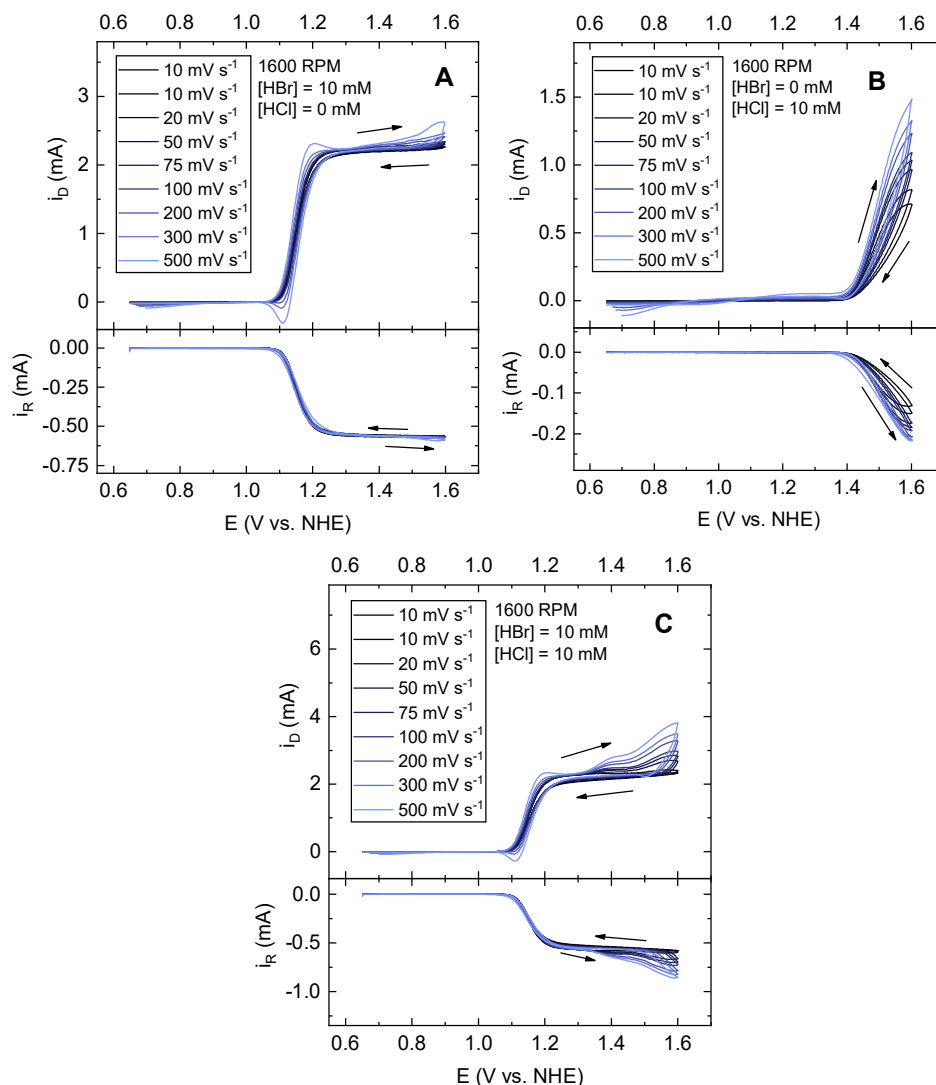
Figure 4.1: Cyclic voltammograms of a Pt-Pt RRDE in a solution of 0.1 M $HClO_4$, showing the BER in presence of 10 mM HBr (Panel A), the CER in presence of 10 mM HCl (Panel B), and parallel oxidation of Br^- and Cl^- in presence of 10 mM HBr + 10 mM HCl (Panel C). Varying scan rates are shown in shades of blue at a fixed rotation rate of 1600 RPM. Top panels show disk currents, bottom panels show ring currents while keeping the ring potential at 0.7 V. Arrows indicate scan direction.

Throughout this chapter we generally use the NHE as potential scale. We note that the pH-dependent formation of platinum oxide (PtO_x) can have a large effect on the apparent reaction kinetics.[58,203,205] A change in acid concentration can thus cause a shift in the potential of oxidation of the Pt surface on the NHE scale, and correspondingly the catalytic activity. The significant background acid concentration of 0.1 M $HClO_4$ served to dampen pH changes as the total acid concentration was changed. The highest observed pH change was around 0.3 pH unit, when going from 100 mM $HClO_4$ to 100 mM $HClO_4$ + 10 mM HBr + 100 mM HCl, which is equivalent to a potential difference of about 20 mV.

Figure 4.1 shows the BER and CER (panels A and B) as well as parallel Br^- and Cl^- oxidation (panel C) on a Pt-Pt RRDE, for varying scan rates. In Figure 4.1A, the BER starts at a potential of 1.05 V, corresponding to a negligible overpotential, and reaches a plateau current at approximately 1.25 V. In control experiments using 5 mM HBr (not shown), the measured values of the BER limiting current correspond within a few % to a previous report by Xu *et al*.[208] The value is approximately 90% of the theoretical value predicted by the Levich equation, suggesting that the limitation stems from mass transport and that it is not due to kinetic limitations which may occur at much higher bromide concentrations.[196] The effect of scan rate on the BER is minimal for slow to modest scan rates up to 75 mV s^{-1}. At higher rates, the inability of Br_2 to be transported away from the surface fast enough leads to additional reactions. The oxidation of Br_2 to BrO_3^- is visible around 1.50 V in the forward scan,[213] and the reduction of Br_2 to Br^- in the backward scan near 1.10 V. The CER in Figure 4.1B starts at 1.37 V, which like the BER is very close to its thermodynamic value. Contrary to the BER, it has a rather strong scan rate dependence. This effect can be explained by transient oxidation of the
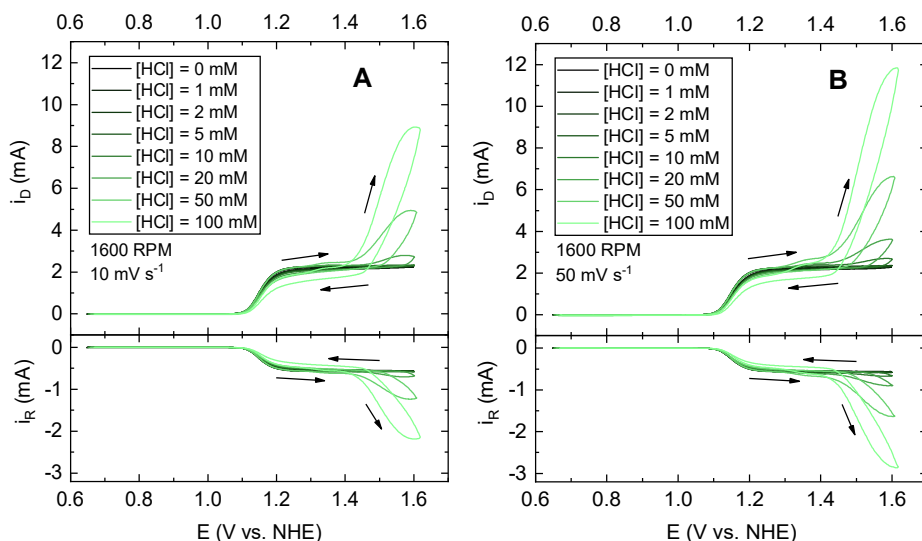
Figure 4.2: Cyclic voltammograms of a Pt-Pt RRDE in a solution of 0.1 M $HClO_4$ + 10 mM HBr, showing the effect of varying HCl concentrations in shades of green, recorded at 10 mV s^{-1} (A) and 50 mV s^{-1} (B) at a fixed rotation rate of 1600 RPM. Top and bottom panels like those described in Figure 4.1. Arrows indicate scan direction.

Pt surface. PtO_x has very poor catalytic activity for the CER, and its formation is a relatively slow process on the timescale of this experiment.[108,196] A faster scan rate then leads to a Pt surface that is less oxidized when CER becomes thermodynamically favorable, and thereby results in higher reaction rates. This will be discussed in more detail below. In Figure 4.1C, the presence of both 10 mM HBr and 10 mM HCl leads to the same current plateau as seen in the BER wave in Figure 4.1A, followed by two superimposed current waves, a first with an onset around 1.30 V, and a second one with an onset potential of 1.42 V. The latter one should correspond to CER. The wave starting at 1.30 V must correspond to the interaction between bromide and chloride. We will analyze the competition between BER and CER and their interaction in more detail in the subsequent sections.

Figure 4.2 shows parallel Br^- and Cl^- oxidation with varying HCl concentration, for two different scan rates. The superimposed oxidation wave between $1.30 - 1.65$ V is chloride concentration dependent, including the 'pre-peak' that starts around 1.30 V. They experience an increase in current and lowering of the onset potential with increasing Cl^- concentration. The pre-peak is also clearly captured in the ring currents (Figure 4.2 bottom panels), so that it must correspond to a halogen evolution reaction. Diffusion-limited bromide oxidation (potential region of $1.20 - 1.30$ V) seems rather unaffected by the increasing presence of chloride, except when $[Cl^-] = 100$ mM, where a kind of inhibition occurs.

The Pt ring electrode was used to quantify the extent to which the currents observed on the disk corresponded to the evolution of soluble product species (Figure 4.1 and Figure 4.2, bottom panels). The ring currents clearly mark the onset of the halogen oxidation reactions. Particularly in Figure 4.1C, the ring effectively mirrors the disk during halogen oxidation. Once halogen oxidation reactions start occurring, the ratio $|i_R/i_D|$ generally converges to a constant value that is within 2% of the RRDE collection factor (Figure A 9.4.3 and Figure A 9.4.4). Scan rates faster than 100 mV s^{-1} lead to some deviation from steady-state values, due to pseudocapacitive contributions on the disk (such as from PtO_x-related reactions), as well as a decrease in the time resolution of the ring response.[214] At high CER overpotentials in high Cl^- concentrations we also saw systematic deviations (Figure A 9.4.6), likely because the ring response became distorted by bubble formation during intense gas evolution on the disk (see also Chapter 8). In low Cl^- concentrations all scan rates show a slight decrease in ring/disk ratios above 1.55 V, likely due to the onset of slow parallel evolution of O_2 on the disk. The OER contribution on the disk is nonetheless rather small (less than 1%). In summary, all disk current can be ascribed to only halogen oxidation for any combination of [HCl], scan rate or rotation rate, as long as the scan rate does not exceed extreme values (see also Figure A 9.4.5).

4.3.4. *Bromide oxidation and the effect of chloride*

In this section, a closer look into the effect of chloride on the oxidation of bromide will be taken, primarily by investigating Tafel slopes, reaction orders and the effect of mass transport. Koutecký-Levich plots of the bromide oxidation wave at various chloride concentrations were constructed using the forward sweeps of CVs (See Figure A 9.4.10). The y-intercepts were then calculated as function of potential (Figure A 9.4.11). These results show that a higher $[Cl^-]$

causes an increasing degree of kinetic control over the reaction, although the effect is very subtle when $[Cl^-] < 100$ mM.
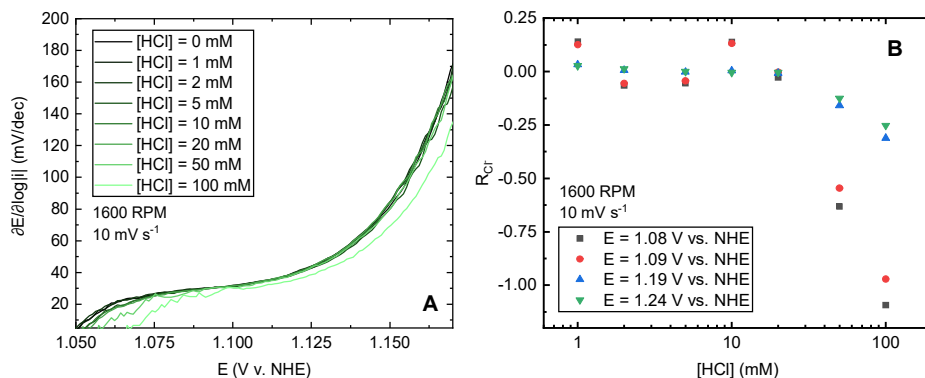

Figure 4.3: Tafel slope values in the bromide oxidation region of Figure 4.2A (A) for various measured chloride concentrations. Only forward scans are shown. B: Chloride reaction order $\mathcal{R}_{Cl^-}$ as function of chloride concentration, based on data shown in Figure A 9.4.9B.

Figure 4.3A shows Tafel slopes (derived from Figure A 9.4.8B) as a function of potential. From Figure A 9.4.11, we can discern the potential region of roughly $1.075 - 1.125$ V as kinetically limited. In this region the Tafel slopes show a fairly constant value between 25-35 mV/dec, agreeing well with previously reported values.[196] Addition of chloride up to concentrations of 50 mM does not change the Tafel slope values, and chloride reaction order analysis (Figure 4.3B) shows that $\mathcal{R}_{Cl^-}$ stays close to 0. The effect of changes in PtO_x coverage due to varying pH should be very minor. Control experiments with 10 mM HBr and no chloride showed that the BER rates show no hysteresis up to 1.40 V, suggesting that inhibiting PtO_x, though it may be formed,[207] plays no significant role in the apparent catalytic activity (Figure A 9.4.12). The reaction becomes notably affected when the chloride concentration increases to 100 mM, where the Tafel slope values rise less quickly as function of potential, and $\mathcal{R}_{Cl^-}$ decreases to around -1.

We also measured the BER dependence on bromide, in absence and presence of an excess of chloride as to further probe the latter's competition behavior. Figure A 9.4.13 and Figure A 9.4.14 show bromide oxidation curves and derived Tafel slopes as function of $[Br^-]$. Tafel slope values of the BER in 1 M HCl (Figure A 9.4.14B) are overall higher (30-50 mV/dec) and significantly less linear, as would be expected on the basis of Langmuirian competitive adsorption (Section 1.2 of the SI). Figure A 9.4.15 displays $\mathcal{R}_{Br^-}$ for 10 mM $\leq [Br^-] \leq 100$ mM. The values around each given $[Br^-]$ are shown versus potential, because the BER is too fast to measure activation controlled currents over a wider range of $[Br^-]$ at a fixed potential, without running into diffusion limitations. The quasi-linear regions in Figure A 9.4.14 were used to approximate the activation-controlled region for each $[Br^-]$. Experimental error from very small currents and the possible influence of the backward reaction led to unexpectedly high values of $\mathcal{R}_{Br^-}$ at very low overpotentials. Nonetheless, for each $[Br^-]$ in their respective activation controlled potential region, $\mathcal{R}_{Br^-}$ values are arguably close to 2, as predicted by the V-T mechanism. The apparent reaction orders rapidly approach 1 as the potential increases,

due to mass transport control. Interestingly, Ferro *et al.* obtained $\mathcal{R}_{Br^-} \approx 1$ on a stationary Pt electrode;[213] these values were obtained at constant overpotential, but the value of E_{eq} was kept fixed by adding equimolar amounts of Br^- + Br_2, such that expected values of $\mathcal{R}_{Br^-}$ are within 2 and 0. Considering the rather narrow (roughly 50 mV) potential ranges in Figure A 9.4.15 where the BER appears activation controlled, it is possible that their values were unintentionally obtained under diffusion controlled conditions.

When regarding the effect of competitive Cl^- adsorption, one can extend the bromide adsorption isotherm to include both Br^- and Cl^- according to:

$$\theta_{Br} = \frac{K_{Br}[\text{Br}^-]e^{f\eta}}{K_{Br}[\text{Br}^-]e^{f\eta} + K_{Cl}[\text{Cl}^-]e^{f\eta} + 1} \qquad \text{Eq. 4.3}$$

A detailed discussion of the mechanistic implications of Eq. 4.3 can be found in section 9.4.2. Importantly, it leads to the same predictions for $\mathcal{R}_{Br^-}$ as in absence of competition, namely that $\mathcal{R}_{Br^-}$ should consistently decrease from 2 to 0 as a function of $[\text{Br}^-]$ in the V-T mechanism. In presence of an excess of 1 M Cl^- in Figure A 9.4.15A, $\mathcal{R}_{Br^-}$ has overall slightly lower values. The reaction is no longer fully diffusion-controlled such that $\mathcal{R}_{Br^-}$ is no longer strictly 1 at higher potentials. The data seem to approach a non-zero value with higher potential, and again approach 2 at low overpotentials. Both observations are predicted by the V-T pathway under the assumption of Langmuirian, competitive adsorption. From this, we conclude that chloride acts as an inhibitor on bromide oxidation and is otherwise uninvolved. Because chloride typically binds weaker to surfaces than bromide,[215] we expect that only at high ratios of chloride versus bromide (such as in seawater), where $K_{Br}[\text{Br}^-] \ll K_{Cl}[\text{Cl}^-]$, the BER may become significantly slowed down.[216]

4.3.5. *Chloride oxidation and the effect of bromide*

In this section, we look more closely how the oxidation of chloride is affected in a mixed Br^- + Cl^- electrolyte. The pre-peak starting at 1.30 V (Figure 4.1 and Figure 4.2) suggests a more complex Br and Cl interdependence than only competitive adsorption, which is most likely due to the formation of BrCl. The nature of this process will be discussed separately in section 4.3.6. For a meaningful analysis, it is necessary to isolate the chloride oxidation current from the superimposed BER current plateau. A strict separation is complicated, because the oxidation pathways of Br^- and Cl^- are clearly mutually dependent and the underlying contribution of each pathway is not exactly known. As a first approximation, we assumed that the BER follows an ideal sigmoidal curve, which appears justified by results from section 4.3.4 and Figure A 9.4.12. The BER wave could then be fitted using a 5-parameter generalized logistic function, whose relative complexity allowed modelling the asymmetry that is inherent to reaction mechanisms more complex than a single electron transfer step.[217] The procedure is illustrated in Figure A 9.4.23.
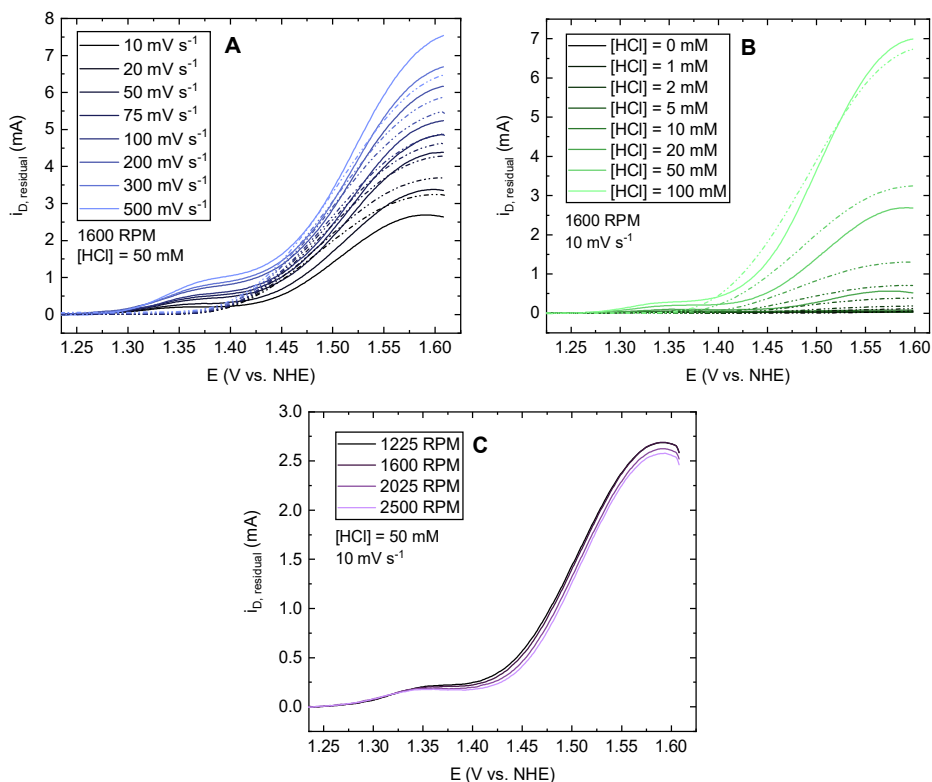
Figure 4.4: Residual chloride oxidation currents after subtraction of BER-related current using a generalized logistic baseline. Shown are the effect of scan rate (A), HCl concentration (B), and rotation rate (C). Dashed lines in A and B correspond to CER data measured in absence of Br⁻ under otherwise identical conditions.

Figure 4.4 shows the effect of various experimental parameters on the current related to chloride oxidation, after applying a logistic baseline correction for the superimposed BER current. In comparison with the dashed traces of 'pure CER current' under bromide-free conditions, there are significant differences. The 'main' oxidation wave, with an onset of 1.45 V in Figure 4.4A, can be ascribed to the CER. The overpotential for the CER in Figure 4.4A and B is generally increased relative to bromide-free conditions, except for the experiments with the highest scan rates and chloride concentrations. Figure 4.4C furthermore shows that the CER current slightly decreases with rotation rate. This behavior may be caused by an increase of the steady-state bromide coverage θ_{Br} as a result of increased mass transport, leading to suppression of the CER. When [Cl⁻] was increased to 100 mM such that the BER became more inhibited (section 4.3.4), the CER displayed an increase in current with rotation rate, but a more clear rotation rate dependence could not be established (Figure A 9.4.16).

The CER is much more likely to be affected by PtO_x formation, for which the driving force is significant near the CER equilibrium potential. Oxide growth causes the CER current in Figure 4.4 to level off or sometimes even decrease with higher potential. The highest recorded currents in Figure 4.4B are less than 10% of the diffusion limitation predicted by the Levich equation, showing that the reactivity limitation is a kinetic effect.
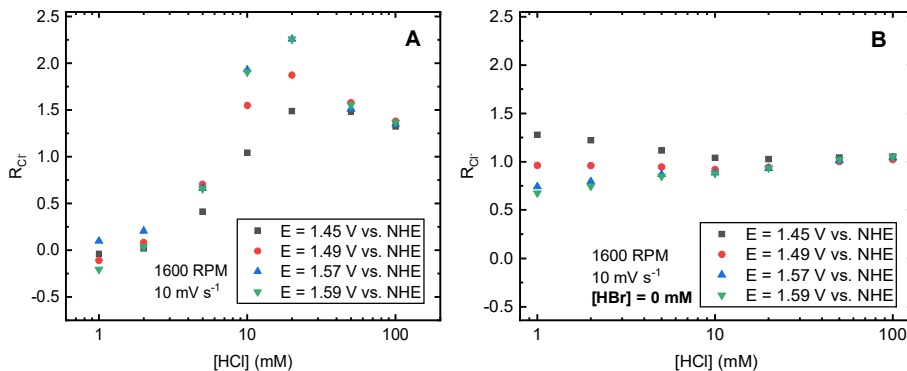
Figure 4.5: Chloride reaction order $\mathcal{R}_{Cl^-}$ as function of chloride concentration, based on data from Figure 4.4B. Shown are values in presence of 10 mM HBr (A), as well as those in bromide-free conditions (B).

Figure 4.5 shows chloride reaction orders based on data from Figure 4.4B. In presence of Br^- (Figure 4.5A) the reaction order is close to 0 at low chloride concentration, but then increases to values close to 2, and then assumes a value of ~1.4 at $[Cl^-] = 100$ mM. This is in remarkable contrast to the results obtained in absence of Br^- (Figure 4.5B), for which reaction orders are close to 1, regardless of potential or chloride concentration.

All results in Figure 4.5 should contain a contribution from transient formation of the PtO_x layer. For the CER, this 'oxide reaction order' has been studied previously by Conway and Novák, who obtained steady $\mathcal{R}_{Cl^-}$ values between 0.8 - 0.9 which quite suddenly decreased to 0 as $[Cl^-]$ increased to 1 M, at constant overpotential (see also section 4.3.1). As mentioned previously, the V-T mechanism predicts that $\mathcal{R}_{Cl^-}$ is always zero when considered at constant overpotential. The contradicting non-zero values were ascribed to specific adsorption by Cl^- at the expense of the oxide layer, forming co-adsorbed 'Cl^{-*}' which saturates to a constant value at higher concentrations. This explanation is however not completely sufficient, since the surface reaction order $\partial \ln \theta_{Cl} / \partial \ln[Cl^-]$ is then still expected to vary between 1 and 0, and thus the overall reaction order should again be $0 \leq \mathcal{R}_{Cl^-} \leq 2$. Most importantly, $\mathcal{R}_{Cl^-}$ should not be consistently near unity, but should vary as a function of $[Cl^-]$ and potential. The V-T mechanism predicts the same when measurements are made at constant potential, such as in our results in Figure 4.5B. Similar to Conway and Novák's results, they do not agree satisfactorily with the usual kinetic models.

Br^- is also known to inhibit the oxidation of platinum, and does so more strongly than Cl^-.[206,218] Br^- may thus affect the CER indirectly by replacing PtO_x as the competitive adsorbate, which could change the apparent reaction order values between Figure 4.5A and B. In order to look into this more closely, one could describe the effect of adsorption from either Br^- or PtO_x using a site-blocking model. Previous studies have shown that the oxide layer on Pt initially forms up to a monolayer of OH^*, and O^*, coupled to a slow place-exchange between O and Pt as oxidation progresses.[219,220] For a fixed potential E, this oxide growth depends on time according to:[205]

$$Q_{PtO_x}(t) = A(E) \log(t + t_0) \approx A(E) \log(t) \qquad \text{Eq. 4.4}$$

In this equation, Q_{PtO_x} is the charge transferred in the formation of the layer, which can be measured from the corresponding reduction peak, t_0 is a offset time present at the start of the linear $\log(t)$ region (usually, $t_0 \ll t$), and A is an empirical constant that depends on the potential. The oxide growth has been reported to depend on time as $\log(t)$ over a wide range of time and potential values, including when chloride is present in the electrolyte.[205] In our potentiodynamic experiments, the overall polarization time and thus the expected oxide thickness should then approximately depend on the scan rate v for a given potential window and electrolyte composition according to:

$$Q_{PtO_x} \propto \log\left(\frac{1}{v}\right)$$
Eq. 4.5

Values of Q_{PtO_x} were obtained from the PtO_x reduction peak (Figure A 9.4.17). As predicted by Eq. 4.5, a plot of Q_{PtO_x} vs. $\log(v)$ resulted in a straight line with negative slope in 0.1 M $HClO_4$. This relationship was preserved in presence of 10 mM Br^- (Figure A 9.4.18). It was also preserved in the combined presence of $Br^- + Cl^-$, suggesting that PtO_x shows the same growth characteristics under influence of the two halogen anions. When CER current values are then compared versus Q_{PtO_x}, a quite linear relationship emerges (Figure A 9.4.19 and Figure A 9.4.20). It can be reasonably assumed that sub-monolayers of oxide were present during most experiments, since in our case the charge of a 'monolayer' oxide on a perfectly flat surface corresponds to roughly 80 μC.[205] These results thus suggest that the effect of PtO_x on the CER activity is primarily through site-blocking. A similar observation underlies the work of Patil *et al.*[221] Further evidence comes from Figure A 9.4.23: Currents recorded at 1.57 V (Figure A 9.4.22) were extrapolated to $Q_{PtO_x} = 0$ (a 'PtO_x-free' surface), and were normalized to the chloride concentration. Comparison with diffusion-limited currents predicted by the Levich equation (blue) suggests that the CER would reach diffusion-limited currents in absence of oxides at 1.57 V. There may also be an intrinsic catalytic effect of the oxide layer, but this is likely most significant at specific oxide coverages that are close to (formally) a monolayer.[118,205]

Contrary to PtO_x, the adsorption of Br^- is in pseudo-equilibrium and should be regarded in the same way as the CER, such as by using the competitive Langmuir isotherm in Eq. 4.3. However, the results from Figure 4.5A strongly disagree with the prediction that $\mathcal{R}_{Cl^-}$ should consistently decrease from 2 to 0 as a function of $[Cl^-]$. Instead, $\mathcal{R}_{Cl^-}$ stays close to 0 for an appreciable concentration range and then increases. A simple Langmuirian site-blocking description therefore seems inadequate. The chloride reaction orders in Figure 4.5A also seem incompatible with a change in reaction pathway towards BrCl formation, since it is expected that $\mathcal{R}_{Cl^-} \leq 1$ for this reaction.

Figure 4.6 shows measured Tafel slope values for the CER in presence (A) and absence (B) of Br^-. 'Pure CER' in Figure 4.6B for various chloride concentrations has linear Tafel regions with a slope between 35-45 mV/dec, in agreement with previous results,[58] followed by a continuous increase in slope with higher potential. The latter is explained by (transient) inhibition of the CER due to PtO_x formation, as was previously noted. The effect lessens as the chloride concentration increases. Like in Figure 4.5, the presence of Br^- imparts significant
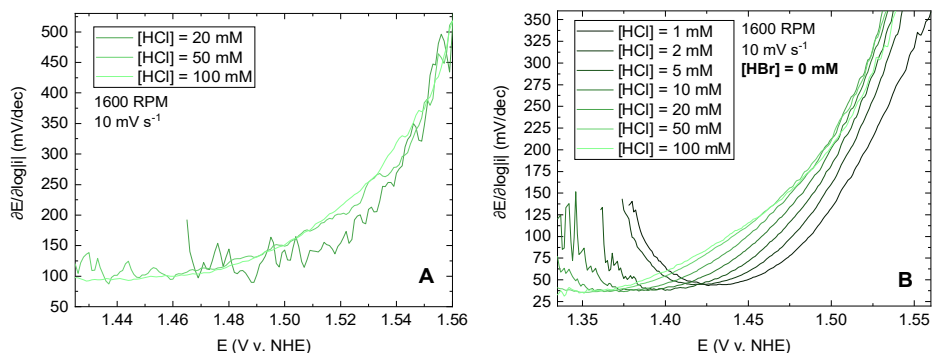
Figure 4.6: Tafel slope values in the CER region of Figure 4.4B following the pre-peak, for the various measured chloride concentrations. Only forward scans are shown. Shown are values in presence of Br^- (A), and values for 'pure CER' in absence of Br^- (B). Several traces in A and B involving 0-10 mM chloride have low signal/noise ratios and are not shown or have been cut off at lower potentials.

changes. Intriguingly, the linear Tafel regions now have a value of around 100 mV/dec. In the Langmuir isotherm, competition leads to higher Tafel slope values (see Table A 9.4.2), but only in combination with increasing curvature. It cannot explain Tafel regions that have a higher value, but also stay linear. The linear value of 100 mV/dec could imply that a change in the rate-determining step of the CER mechanism has taken place, the most straightforward possibility being rate-limiting Volmer discharge. This, however, is in contradiction with $\mathcal{R}_{Cl^-}$ being greater than 1 in Figure 4.5A. In summary, chlorine evolution seems to be the major reaction in the chloride oxidation region, but presence of Br^- induces a large change in the apparent kinetics. This change does not stem from a change in how the oxide layer forms during the experiments, but seems to be the result of a complex interaction of Br^- or Br^* with the CER reaction pathway on the surface. The CER on Pt, regardless of the presence of Br^-, is not captured by the usual microkinetic models in a fully satisfactory way, as was previously hinted at by Tilak and Conway.[112]

4.3.6. *Nature of the chloride oxidation pre-peak*

As mentioned above, the pre-peak that starts at 1.30 V only appears when both Br^- and Cl^- are both present, at a potential where the BER is diffusion limited, and where the CER is thermodynamically not yet allowed, meaning it cannot be ascribed to the evolution of either Br_2 or Cl_2. At the same time, the pre-peak current is always registered on the ring, so that it is associated with the evolution of a soluble reaction product. Therefore, it likely involves formation of an interhalogen compound, where BrCl is the most probable candidate, as its standard potential (1.19 V vs. NHE) lies in-between CER and BER.

To investigate the pre-peak in more detail, it was necessary to extend the fitting procedure discussed in section 4.3.5 to 'isolate' the relevant current. It must be noted that the pre-peak is always convoluted by parallel evolution of bromine and chlorine. The BER contribution was previously modelled using a generalized logistic function, such that the residual current contains the CER wave with the pre-peak superimposed. To isolate the pre-peak current, the CER wave was modelled using a simple exponential function according to the Butler-Volmer

relation. CER curves were fitted using narrow potential regions where the Tafel slope was roughly constant as in Figure 4.6. The resulting exponentials were then extrapolated under the pre-peak, forming a nonlinear baseline together with the generalized logistic function for the BER. The multistep nature of the reaction could justify a more complex fitting function, but as discussed in section 4.3.5, this relation need not hold at potentials higher than the linear Tafel regions, where the real kinetics are obscured by PtO_x formation. The entire procedure thus assumes that the BER and CER are the main reactions occurring in a mixed Br^- and Cl^- electrolyte, behaving respectively as an asymmetric sigmoid and (at low overpotentials) a superimposed exponential, and that the pre-peak is a third process overlapping with the previous two. In case that the CER currents were too small to observe a linear Tafel region, a simple linear baseline was used instead.
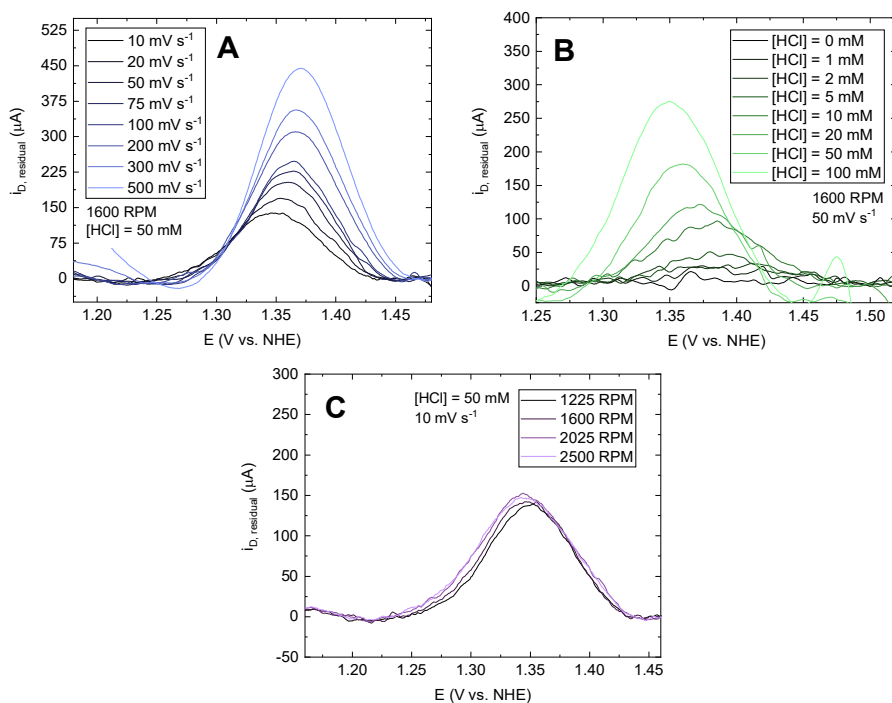
Figure 4.7: Examples of chloride oxidation pre-peak current determined from RRDE experiments, after separating BER and CER contributions using a generalized logistic and exponential function, respectively. Shown are the effect of scan rate (A), HCl concentration (B), and rotation rate (C).

Figure 4.7 shows the pre-peak current determined after applying the two-step baseline to correct for the superimposed BER and CER currents, and its response to various experimental parameters. No effect from rotation rate is apparent, suggesting that the rate-limiting step is surface-confined. The peak also shows complex dependencies on scan rate and chloride concentration, as shown in Figure 4.8.
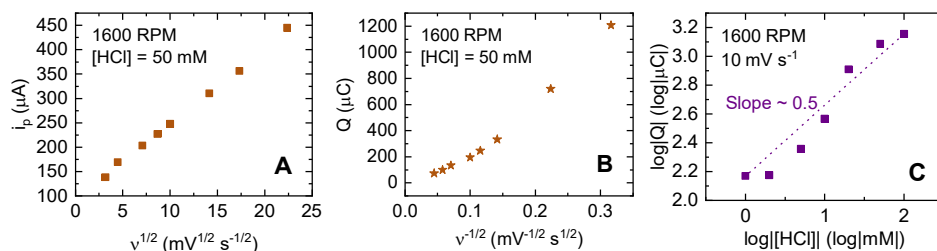
Figure 4.8: Scan rate and [Cl⁻] relationships as determined for the CER pre-peak, using data from Figure 4.7. Shown are the dependency of the peak current vs. the square root of the scan rate (A), dependency of the peak charge on the inverse square root of the scan rate (B), and a log-log plot of the peak charge versus chloride concentration (C).

In case of a surface-confined reaction, one would expect a linear dependence between peak current and scan rate, but this is not observed in Figure 4.8. The pre-peak has a linear dependence of the peak current on the *square root* of the scan rate, an approximately linear dependence of peak charge with the inverse square root of the scan rate, and a 'surface charge order' of about 0.5 (i.e. a square root relationship between peak charge and chloride concentration). Especially the linear dependency of peak current vs. square root scan rate is striking. This outcome is usually expected for a solution species reacting at a stationary electrode, where the square root relationship arises from the dependence of the diffusion layer thickness on time. It should not apply under hydrodynamic conditions, where the thickness is constant in time. A possible explanation for this, as well as the general behavior of the pre-peak, is that surface diffusion is involved. Formation of BrCl is expected to proceed via an electrochemical Langmuir-Hinshelwood mechanism, such as during CO stripping from Pt,[222] which requires concerted steps of two different reaction surface species instead of one. We found that the pre-peak is effectively irreversible and does not re-appear in the backward scan, even when using a lower potential of scan reversal (Figure A 9.4.24). This implies that it requires a precursor that is only formed during the forward scan (Figure A 9.4.25).

4.3.7. *UV-Vis studies of parallel oxidation of bromide and chloride*

In the RRDE experiments, we ascribed the three main oxidation events to the formation of Br_2, BrCl and Cl_2 based on a kinetic analysis. It is highly desirable to corroborate these results with a method capable of ascertaining the identity of the products formed. UV-Vis spectroscopy allows this, since all species in Table A 9.4.1 (except Br^- and Cl^-) have a secondary adsorption band (or shoulder, in case of Br_3^-) that falls in the range 325 – 390 nm, which is accessible when measuring a transparent electrode on a glass substrate. We applied a stepwise potential vs. time program constituting 25 mV steps with a 30 s duration, between 1.060 – 1.485 V vs. NHE (Figure A 9.4.26A), in order to study both the effect of increasing potential, as well as shifts in solution composition during progressing oxidation reactions for each constant potential. Changes in the total transmission were measured after passing the beam through the back of the Pt/FTO electrodes and through the electrolyte, to probe the Pt interface as well as halogen species in the surface layer.

The spectra in Figure 4.9 show the effect of increasing bromide concentration and were taken at potentials related to regions of interest, as seen in the corresponding currents in D. The BER
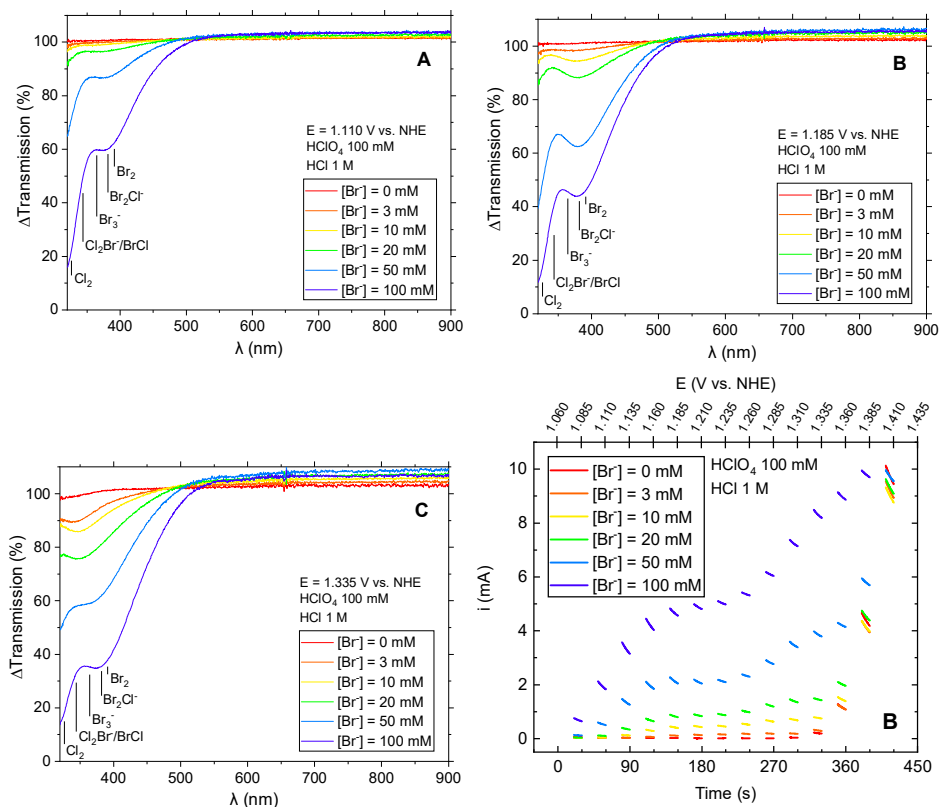
Figure 4.9: UV-Vis measurements of a stationary Pt/FTO electrode in a solution of 0.1 M HClO₄ + 1 M HCl, in presence of various [HBr]. A, B and C: UV-Vis spectra measured as function of bromide concentration, after stepping the potential up to 1.110 V (A), 1.185 V (B) and 1.335 V (C), in 25 mV steps of 30 s each. Spectra are shown 10 seconds after applying the relevant potential. Previously published[210] wavelengths of peak adsorption are indicated for each relevant species. D: Corresponding currents measured during the experiments. Only the final 10 seconds of each potential step are shown for clarity (see Figure A 9.4.26B for full data). Upper axis shows the potentials applied at each moment in time.

has significant activity at 1.110 V (A) and reaches a plateau around 1.185 V (B). The CER becomes just possible at 1.335 V (C), based on the comparison with bromide-free experiments (red trace in D). Features seen in the spectra are always the sum of a mixture of species (section 4.3.2). In Figure 4.9A, Br_3^- contributes the most strongly to the signal due to its high extinction coefficient.[210] Once the potential increases to 1.185 V (Figure 4.9B), the dominant species is Br_2Cl^-. This can be explained by depletion of Br^- near the surface, which shifts the local equilibrium from Br_3^- to Br_2 and subsequent reaction with Cl^-. This is supported by a strong correlation between the peak height relative to its shoulder at 383 nm and the extent to which the BER approaches the current plateau (Figure A 9.4.27). Increasing the potential further to 1.335 V, where the CER can occur, leads to a substantial decrease in transmission in the region 320 – 360 nm. This is clearly related to the formation of Cl_2, $BrCl_2^-$ and BrCl in solution, which all adsorb in this wavelength window.
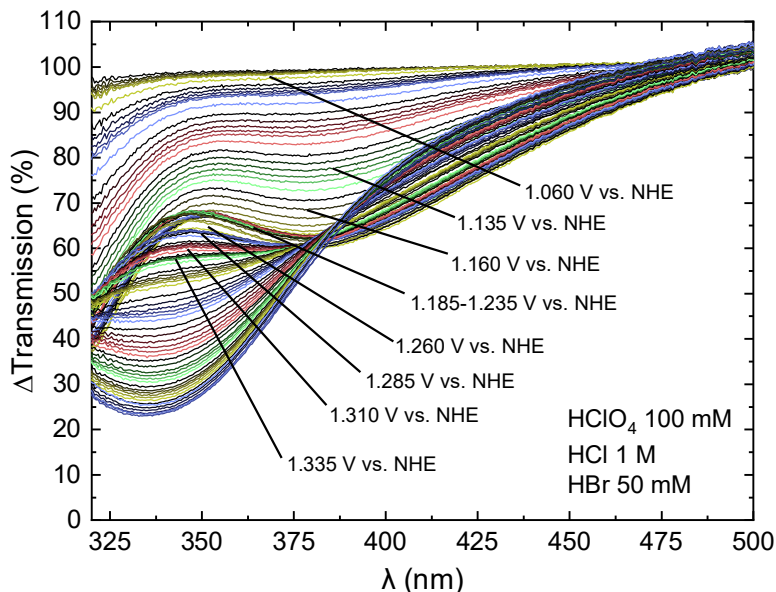
Figure 4.10: Complete set of UV-Vis experiments for parallel bromide and chloride oxidation in 1 M HCl and 50 mM HBr, zoomed on the region where the halogen species adsorb. Colors denote different potential steps, some values of which are indicated. Color gradients from dark to light indicate time evolution of the spectra during each potential step.

When examining the currents recorded in parallel with UV-Vis in Figure 4.9D, we once more observe a pre-wave that precedes the CER onset (onset 1.260 V), and becomes more prevalent as the bromide concentration increases. This pre-wave corresponds quite well to results from the RRDE experiments, and suggests that BrCl is formed electrochemically. Further evidence for its formation comes from Figure 4.10, where we regard the complete time evolution of a typical UV-Vis experiment during parallel bromide and chloride oxidation. Between 1.110 V and 1.260 V, the spectra show the previously described peak of Br_2Cl^- near 380 nm. As the potential is stepped beyond 1.260 V, the transmission in the region 340 – 360 nm disproportionally lowers, which can only be caused by the formation of Cl_2, BrCl or $BrCl_2^-$. We note that in bromide-free conditions, Cl_2 becomes only just detectable around 1.350 V, and dominates at 1.400 V (Figure A 9.4.28). The change at 1.260 V therefore implies the formation of BrCl or $BrCl_2^-$ without the presence of Cl_2 in solution, such that they must have been formed directly by BrCl formation on the electrode. Similar results were obtained under conditions of higher bromide concentrations (Figure A 9.4.29), as well as lower overall halide concentrations (Figure A 9.4.30 and Figure A 9.4.31). The UV-Vis spectra thus confirm the observation in the RRDE experiments of an intermediate oxidation reaction occurring between the BER and CER.

In Figure 4.9, we note an increase in transmission in the wide region of 550 – 900 nm for experiments involving high bromide concentrations combined with high potentials. This increase was likely caused by transient Pt dissolution during vigorous halogen oxidation. The used Pt samples had a low thickness of roughly 5 nm, to limit scattering of the beam. Therefore any dissolution had a relatively large effect on the transmission.

4.4. Discussion and conclusions

The study of parallel Br^- and Cl^- oxidation on Pt revealed significant differences in their interaction. Bromine evolution exhibited linear Tafel slopes of 25-35 mV/dec and a Br^- reaction order $\mathcal{R}_{Br^-}$ that is probably close to 2 at low overpotentials. In the presence of chloride, the reaction becomes increasingly kinetically controlled, and Tafel curves have steeper slopes and becomes less linear. The BER chloride reaction order $\mathcal{R}_{Cl^-}$ progressed from roughly 0 to -1 as the chloride concentration $[Cl^-]$ increases. All these phenomena could be quite well modelled by the Tafel recombination-controlled mechanism, describing the competitive adsorption of Br^- and Cl^- with a simple Langmuir isotherm in the Volmer pre-equilibrium. The results suggest that the effect of Cl^- on the BER is 'simple' competitive adsorption through site blocking. The competing effect of Cl adsorption will likely become more prevalent at higher $[Cl^-]/[Br^-]$ ratios, such as in seawater.

Contrary to the BER, the Langmuirian Volmer-Tafel approach fails for accurately modelling the CER kinetics and the competing effect of bromide, as neither the CER itself (in absence of Br^-) nor the CER during parallel Br^- and Cl^- oxidation are properly described by this model. In absence of Br^-, the CER displays linear Tafel regions between 35-45 mV/dec, and $\mathcal{R}_{Cl^-}$ values that are consistently close to 1, irrespective of $[Cl^-]$ or overpotential η. The addition of Br^- again leads to linear Tafel regions but with significantly higher values of ~100 mV/dec, and $\mathcal{R}_{Cl^-}$ varies between 0 and 2 as function of Cl^-. The parallel formation of a platinum oxide layer at CER-relevant potentials and its effect on the apparent oxidation kinetics remains an incompletely understood issue, but it should not be the origin of the Br^--induced drastic change in the CER kinetics. The suppressing effect of 10 mM Br^- leads to a decrease of the PtO_x charges during CER experiments of 10-30% (Figure A 9.4.19 and Figure A 9.4.20), but the oxide growth behavior was very similar to Br^--free conditions. It thus seems reasonable that the interaction of the PtO_x layer with the occurring CER, although not exactly understood due to its complexity, is not changed significantly by bromide. The change in CER kinetics should originate from a direct effect of Br^- on the adsorption and recombination of chloride.

In addition to the BER and CER, the formation of the interhalogen BrCl likely takes place during parallel Br^- and Cl^- oxidation on Pt. Evidence for this comes from an oxidation 'pre-peak' that thermodynamically precedes the CER, and UV-VIS experiments that indicate that an 'intermediate' oxidizing species is formed at potentials lower than the CER onset. RRDE experiments suggested that BrCl evolution takes place via an irreversible surface reaction with a dependence on scan rate that suggests that surface diffusion plays a role. The process was strongly dependent on the preceding electrode treatment and probably depends on a specific intermediate.

This study has shown that 2-electron halogen oxidation reactions may still be more complicated than previously thought. While the BER conformed surprisingly well to a simple Langmuir pre-equilibrium model, previous studies on poly- and monocrystalline Pt surfaces show that the surface should be virtually saturated with Br^* near the onset of the BER.[223–225] A similar argument holds for Cl^* and the CER.[226–228] The value of θ should thus be essentially constant versus potential when the respective halogen evolution conditions proceed, and the reaction rate should be virtually independent of E or $[X^-]$ in case of the V-T mechanism. The

reactions nonetheless behave as if θ is still low near the onset, which suggests that the pre-adsorbed species are not the actual reactants. This situation is very similar to the evolution of H_2 on Pt, which takes place while Pt is demonstrably saturated by H^*, yet shows Tafel slopes of ~ 30 mV/dec at low overpotentials. To explain this disparity, the concept of 'overpotential-deposited hydrogen'[229] has been invoked. A similar approach might be advisable for the BER and the CER. The apparent differences between the reactions is then perhaps due to differing interactions of overpotential-deposited Br^* and Cl^* with the emerging PtO_x layer. To better describe the CER, an approach that also includes a description of local interactions between adsorbed species may be needed, as has been done previously for competitive adsorption of Br^- and H^+ on Pt(100).[230] The use of a more complex isotherm (such as Frumkin) will probably not be more accurate as long as it still relies on the mean-field approximation, which cannot account for structured adlayers. In this regard, additional studies of halogen evolution on single crystal Pt surfaces would be very insightful.

5

COMPETITION AND SELECTIVITY DURING PARALLEL EVOLUTION OF BROMINE, CHLORINE AND OXYGEN ON IrO$_x$ ELECTRODES

Oxidation reactions related to bromide have a very low thermodynamic threshold relative to the OER and CER, and present a substantial problem in electrolyzers where seawater is the desired feedstock. In this chapter we continue the work and analysis methods used in Chapter 4 in order to understand parallel evolution of bromine and chlorine on Pt, and extend it to IrO$_x$, focusing on the OER and how it is affected in the presence of chloride and bromide. Chloride and bromide absorb competitively on IrO$_x$, but contrary to Pt, we found no evidence of interhalogen BrCl formation. We also found that even a relatively small amount of bromide strongly slows down both the CER and OER, where especially the OER and its selectivity is highly affected. This knowledge can lead to a deeper understanding of the challenges to be faced when developing an OER-selective anode for seawater electrolysis.

5.1. Introduction

In Chapter 4, we explored the parallel oxidation of chloride and bromide on Pt within the context of seawater electrolysis, which would involve electrolytes that contain both Cl^- and Br^- salts. On Pt, we observed competitive effects and the likely formation of the interhalogen BrCl during halogen evolution. In this chapter, we extend this work to the previously studied amorphous IrO_x catalyst, which is OER-capable and representative for typical metal oxides used in neutral and acid PEM electrolyzers. The OER is the sole desired anodic reaction in such an electrolyzer; the oxidation of either Cl^- or Br^- leads to toxic side-products that undermine the environmentally friendly potential of the electrolysis process, and should therefore ultimately be avoided. Having studied the effect of parallel CER on the OER in Chapters 2 and 3, we hope to aid progress towards an OER-selective anode in seawater by now including the effect of the parallel CER and BER (Eq. 4.1) on the evolution of oxygen.

The BER is generally ignored in the context of seawater electrolysis, because the bromide concentration in seawater is relatively low (0.3%mol relative to the chloride concentration).[186] However, its standard potential is notably lower than that of the CER and OER. Bromide oxidation can thus easily occur in an electrolyzer, especially since like the CER, the overpotential of the BER can be vanishingly small. Additionally, scaling behavior between the OER and CER has been reported in previous literature and Chapter 3 of this thesis (see also section 1.3). As the BER and CER appear to have very similar reaction mechanisms on a variety of surfaces,[118,196–198] it is expected that a similar scaling exists between the BER and the OER. Both the CER and BER are thus serious competitors to the sluggish OER, which is associated with a significant overpotential.

Despite its particular relevance to seawater electrolysis, the simultaneous evolution of Br_2, Cl_2 and O_2 has been little explored.[193–195] Furthermore, very little is known of the BER mechanism on a metal oxide catalyst, and how it may influence the concurrent CER and OER. Br^- likely competes for adsorption on the same active sites on the catalyst, which would slow down the other two reactions. As was observed during the parallel CER and BER on Pt in Chapter 4, adsorbed reactive Br and Cl species could also lead to formation of interhalogen compounds, such as BrCl, making the system more unpredictable. By simultaneously studying the BER, CER and OER, and looking deeper into their competitive behavior, it is intended to expand knowledge on these issues and also broaden the general understanding of the individual reaction mechanisms.

In this chapter, the parallel evolution of Br_2 and Cl_2 during O_2 evolution is studied in acidic media (pH $\approx$ 0.35), where they can be studied with minimum interference from reactions that lead to oxygenated halogen species, such as BrO_3^- or ClO^-.[201,202,210] The previously studied GC-supported IrO_x was taken as anodic electrocatalyst. Heavy use will be made of the RRDE technique described in Chapter 2, where the Pt ring served as a detector for Cl_2 evolved. This technique will be extended and appended with modelling to separate the individual BER, CER and OER related activities. The IrO_x electrocatalyst could also be conveniently electrodeposited as optically transparent thin layers, once more allowing the analysis of the

identities of halogen oxidation products near stationary electrode surfaces, using online transmission UV-Vis experiments.

5.2. Experimental

All experiments were carried out at room temperature (~20 °C). RRDE experiments are inherently more susceptible to contamination than stationary UV-Vis experiments. Cleaning preparations for forced convection experiments were therefore significantly more elaborate.

5.2.1. *Chemicals*

For the RRDE experiments, $HClO_4$ (70%, Suprapur®/Trace analysis grade) $KHSO_4$ (EMSURE/Analysis grade), KCl (EMSURE/Analysis grade) and HCl (30%, Ultrapur®/Trace analysis grade) were purchased from Merck. HBr (47%, Normapur®/Analysis grade) was purchased from VWR Chemicals. For the UV-Vis experiments, $HClO_4$ (60%, EMSURE/Analysis grade), HCl (32%, EMSURE/Analysis grade) and HBr (47%, EMSURE/Analysis grade) were purchased from Merck. $Na_2IrCl_6 \cdot 6H_2O$ (99.9%, trace metals basis) and NaOH (30% solution, TraceSelect) were purchased from Sigma-Aldrich. All purchased chemicals were used as received. The water used for all experiments was prepared by a Merck Millipore Milli-Q system (resistivity 18.2 MΩcm, TOC < 5 p.p.b.).

5.2.2. *Cleaning procedures*

All glassware in the RRDE experiments was boiled in a 3:1 mixture of concentrated H_2SO_4 and HNO_3 before first-time use. When not in use, all glassware was stored in a 0.5 M H_2SO_4 solution containing 1 g/L $KMnO_4$. Before each RRDE experiment, all glassware was first rinsed with water, and then submerged in a dilute (~0.01 M) solution of H_2SO_4 and H_2O_2 to remove all traces of $KMnO_4$ and MnO_2. It was then rinsed three times with water and boiled in water. The final rinsing-boiling procedure was repeated two more times.

The glassware and custom-built PTFE cell for UV-Vis experiments were cleaned by soaking in warm reagent grade 98% H_2SO_4 for an hour, followed by thorough rinsing with Milli-Q water and boiling three times in Milli-Q water. When not in use, they were stored submerged in Milli-Q water.

5.2.3. *Electrode preparation*

5.2.3.1. *RRDE experiments*

IrO_x/GC electrodes were prepared via electroflocculation of IrO_x nanoparticles, as described in sections 9.1.1 and 9.1.2. Diamond paste was used for GC polishing, and the electrode was then rinsed and sonicated in water for 3 minutes. A time duration of 300 s was used for the electroflocculation amperometry step.

Before each experiment, the IrO_x surface was subjected to a pre-treatment step to ensure reproducible activity (see Figure A 9.5.2). The electrode was first kept at 0 V vs. RHE for 10 s,

followed by a 3 s hold at 0.9 V, in order to equilibrate the electrode and allow pseudocapacitive charging to decay to a minimum. Scanning commenced immediately afterwards. The Pt ring electrode was electropolished before experiments by scanning from -0.1 V to 1.7 V at 500 mV s^{-1} for 20 scans at 1500 RPM, followed by removal of gas bubbles adhered to the tip (see also Chapter 8). Ring currents were corrected for constant background currents and product collection delay. The latter arises from the time needed for products formed on the disk to reach the ring and was empirically determined for each investigated rotation rate.

5.2.3.2. UV-Vis experiments

Conductive fluorine doped tin oxide (FTO) substrates (TEC-15) were purchased from Hartford glass co. The FTO substrates were cleaned by sonication, using a sequence of laboratory soap, Milli-Q water, acetone, isopropanol and water, followed by drying the substrates with compressed air. IrO_x deposition was then performed using the same prepared colloid solutions and voltammetry-amperometry protocol described in section 5.2.3.1. The FTO substrates were placed upright in the solution, with a LowProfile Ag/AgCl reference electrode aligned to the center of the electroactive surface and a circular Pt counter electrode placed symmetrically around the bottom. Instead of a rotating tip, a stirrer bar at the bottom of the cell rotating at ~400 RPM was used to induce mass flow of the IrO_x particles during deposition.

5.2.4. Cell preparation

5.2.4.1. RRDE experiments

An IviumStat potentiostat (Ivium Technologies) with IviumSoft software was used in all experiments for potential control. The electrode assemblies were E6 ChangeDisk RRDE tips with a PEEK shroud, attached to an MSR rotator (Pine Research). All experiments were 95% iR-compensated in-situ, by measuring the solution resistance with electrochemical impedance spectroscopy at 0.90 V vs. RHE on the disk, and observing the absolute impedance in the high frequency domain (100-50 KHz) corresponding to a zero-degree phase angle. All used solutions were saturated and continuously bubbled with Ar gas (Linde, purity 6.0) during experiments. The reference electrode was a HydroFlex® reversible hydrogen electrode (Gaskatel), separated from the main solution using a Luggin capillary, with the capillary tip purposely aligned to the center of the working electrode.[231] An additional LowProfile Ag/AgCl reference electrode served to measure the solution pH and was used for interconversion between the NHE and RHE scale. The Ag/AgCl reference was externally calibrated on a regular basis and had a value of 199 ± 0.5 mV vs. NHE. A Pt mesh was used as counter electrode, separated from the main solution by a coarse sintered glass frit.

5.2.4.2. UV-Vis experiments

A Vertex potentiostat (Ivium Technologies) run by the IviumSoft software package was used for potential control. Transmission measurements were performed in a custom-built setup, consisting of a PTFE electrochemical cell housing equipped with quartz windows. A coiled platinum wire was used as the counter electrode, and a LowProfile Ag/AgCl reference

electrode (Pine Research) was placed in fixed position relative to the IrO_x/FTO working electrode. The Ag/AgCl electrode was calibrated at 199 ± 1 mV vs. NHE. All applied potentials were 90% iR-compensated according to the solution resistance, which was measured using a similar procedure as in section 5.2.4.1. To achieve a wide spectrum in the incoming beam, a deuterium lamp (Mikropack D-2000) and a halogen lamp (Ocean Optics HL 2000 – FHSA), were used in the setup. These light sources were combined using an optical fiber arrangement and this fiber acted as the illumination source for the transmission measurements. A Maya 2000 Pro spectrometer (Ocean Optics) was used to capture the transmitted light. The setup was aligned in such a way that the IrO_x/FTO samples were illuminated from the back side and the transmitted light was captured on the opposite side of the electrochemical cell. The transmission data was recorded simultaneously with the electrochemical measurements.

5.3. Results and discussion

5.3.1. *Brief review of the BER and CER kinetics on metal oxides*

Similar to Chapter 4, we will again look closely at experimentally determined Tafel slopes (*b*) and reaction orders ($\mathcal{R}$) to better understand the underlying halogen oxidation mechanisms (see section 1.4). The Langmuir isotherm assumed in the models is likely an oversimplification, but the use of a more complex isotherm, such as devised by Frumkin, does not change the previously described limits for *b* and $\mathcal{R}$ when either $\theta \to 0$ or $\theta \to 1$. Their shape and width as function of *E* and $[Cl^-]$ will however depend sensitively on the isotherm. The discussion of experimental findings will be restricted to some general trends and possible limiting values.

In previous literature, the mechanism of the CER on metal oxides has been studied extensively, but despite this it still has some uncertainty. The main issue is that combined $\mathcal{R}_{Cl^-}$ values and Tafel slopes often do not satisfactorily agree with predictions of either the Volmer-Heyrovský (V-H) or Volmer-Krishtalik (V-K) mechanisms. As can be seen from Eq. 1.12, the driving force for Cl^- adsorption depends on both the potential *E* and the bulk chloride concentration. As θ_{Cl} changes from 0 to 1 under the effect of increasing η and/or $[Cl^-]$, the V-H mechanism predicts that the chloride reaction order $\mathcal{R}_{Cl^-}$ decreases from 2 to 1, and that the Tafel slope increases from ~40 mV/dec to ~120 mV/dec (under the assumption that $\alpha_H \approx 0.5$). Tafel slopes of ~40 mV/dec at low overpotentials have indeed often been observed in experiments, pointing to the theoretical limit of $\theta_{Cl} \approx 0$. However, the corresponding experimental values for $\mathcal{R}_{Cl^-}$ were almost universally close to 1, suggesting the limit of $\theta_{Cl} \approx 1$.[35,55,110,112,183,184,232] Often, they were also practically invariant versus *E* and $[Cl^-]$. The V-K mechanism was in fact specifically invoked to account for this problem, as it predicts that $0 \leq \mathcal{R}_{Cl^-} \leq 1$, which is slightly more in-line with these results. Conway and Tilak have postulated that the CER mechanism on metal oxides follows rather the Volmer-Tafel mechanism,[112] but this view is not widely shared. We will discuss our results in adherence with previous literature, although the established discrepancies between the models and experimental results must be kept in mind.

5.3.2. *Parallel RRDE oxidation currents as function of chloride concentration*

We will first describe our methods and a few general results regarding the parallel BER, CER and OER on the IrO_x/GC catalyst. RRDE cyclic voltammetry was used for all kinetic studies, since both the BER and CER are rapid reactions which quickly become diffusion controlled as the overpotential increases. Hydrodynamic conditions keeps the diffusion layer thickness constant in time, simplifying the analysis and allowing a deeper investigation of the role of mass transport. Sufficiently high rotation rates also prevented Br^--related follow-up reactions by removing Br_2 formed near the surface. In the spirit of Chapter 2, it was possible to use the RRDE with a Pt ring to selectively reduce halogen species formed in parallel with OER, so that the reactions can be separated and analyzed independently. As in Chapter 4, the ring potential
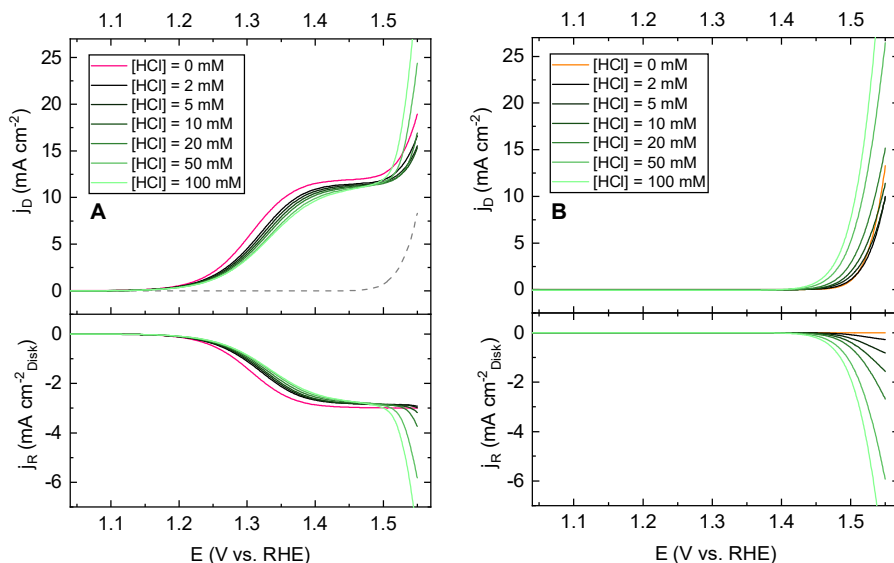
Figure 5.1: Measured current densities of OER and halogen evolution on an IrO_x/GC electrode in 0.5 M $HClO_4$. Top panels show forward, pseudo-capacitance corrected scans of the disk, lower panels show corresponding ring signals measured at 0.7 V vs RHE, corrected for background and collection delay. The effect of increasing HCl concentration is shown from black to green. A: OER in parallel with Br^- and Cl^- oxidation, in presence of 10 mM HBr and 0 – 100 mM HCl. Results in chloride-free conditions (only the BER and OER) are shown in pink. Also shown is the OER activity in absence of both Br^- and Cl^- (grey dotted trace). B: Experiments similar to A, but in Br^--free conditions, with the ring at 0.95 V vs. RHE. Orange trace shows OER activity in absence of Cl^-. Solution purged with Ar, rotation rate 1600 RPM, CV's recorded at 50 mV s^{-1}.

was fixed at 0.7 V vs. RHE, where the reduction of oxygen has negligible activity in presence of Br^-, and where halogen reduction reactions should thus be fully diffusion limited.

All experimental data were gathered with cyclic voltammograms recorded at 10 mV s^{-1}. Forward scans were used for catalytic analysis, while forward and backward scans were used to estimate capacitive currents. These non-catalytic contributions were usually a minor factor (less than 0.1%) in the total current, and were minimized by subtracting a constant value from the forward scan currents. Results were recorded versus the RHE, which is the 'natural' potential scale of the pH-dependent OER. Generally, this scale will be used to report OER-

related results. The studied halogen evolution reactions are however pH-independent. A relatively acidic supporting electrolyte of 0.5 M HClO$_4$ (pH ≈ 0.35) was used to reduce pH changes from the addition of HBr or HCl. Data involving Br$^-$ or Cl$^-$ oxidation are reported versus the NHE scale to account for potential shifts from pH effects, which were very minor (<5 mV).

Figure 5.1A shows some typical results measured on GC-supported IrO$_x$ in a mixed Br$^-$ and Cl$^-$ electrolyte. The onset of bromide oxidation from 10 mM HBr is clearly visible around 1.12 V vs. RHE, and the reaction reaches a plateau near 1.40 V vs. RHE. This plateau stems from diffusion limitations, because its current density is about 95% of the limiting value predicted by the Levich equation. The OER starts around 1.45 V vs. RHE in absence of HBr and HCl (dotted trace in upper panel). In presence of only 10 mM HBr (pink trace in upper panel), the OER appears superimposed on the limiting current of bromide oxidation. A closer inspection shows that its onset is at a slightly higher potential, and the activity is lower than in absence of Br$^-$. As intended, the OER is not captured in the corresponding ring data (lower panel), which only detects the limiting current of bromine evolution. When HCl is added, the ring data show an additional halogen oxidation reaction around 1.45 V vs. RHE, which suggests chloride oxidation starts taking place in parallel with OER. Compared to Figure 5.1B, which shows the parallel evolution of O$_2$ and Cl$_2$ in absence of bromide under otherwise identical conditions, the CER activity is significantly reduced, and has a much higher onset potential. Reciprocally, HCl also imparts some notable changes on the bromide oxidation wave. The bromide oxidation activity is lowered in the whole measured potential range, which becomes more obvious with increasing [Cl$^-$]. Diffusion limitations for bromide oxidation are again apparent around 1.40 V vs. RHE. While bromide and chloride are being oxidized simultaneously, there is no immediate sign of a new onset somewhere in-between the BER and CER, in contrast to results from Figure 4.1C concerning Pt. This suggests that no interhalogen reactions are taking place.

5.3.3. *Kinetic analysis and reaction orders of bromide oxidation*

The bromide oxidation waves in Figure 5.1 between 1.10 − 1.45 V vs. RHE will be investigated in more detail. For this, Koutecký-Levich plots were constructed by varying the rotation rate (see Figure A 9.5.5 and Figure A 9.5.6) for each combination of [HCl] + 10 mM HBr. The y-intercept of these plots and their closeness to zero can be unambiguously interpreted as a degree of mass transport control over the reaction, especially if the plots are highly linear.

Data in Figure 5.2 was derived from measured disk current densities j_D, where up to 1.45 V, no evolution of Cl$_2$ or O$_2$ occurs. In presence of Cl$^-$, formation of the interhalogen BrCl is thermodynamically allowed around potentials >1.19 V vs. NHE (see Table A 9.4.1). We will discuss this issue further below, and for the moment refer to positive currents within 1.10 − 1.40 V vs. NHE in presence of Cl$^-$ as 'bromide oxidation'.

Figure 5.2A shows that the BER (pink trace) is essentially fully diffusion controlled near 1.35 V vs. NHE (~1.38 V vs. RHE). When HCl is present, the intercept values become slightly larger as [Cl$^-$] increases, indicating that the reaction becomes slightly more kinetically controlled
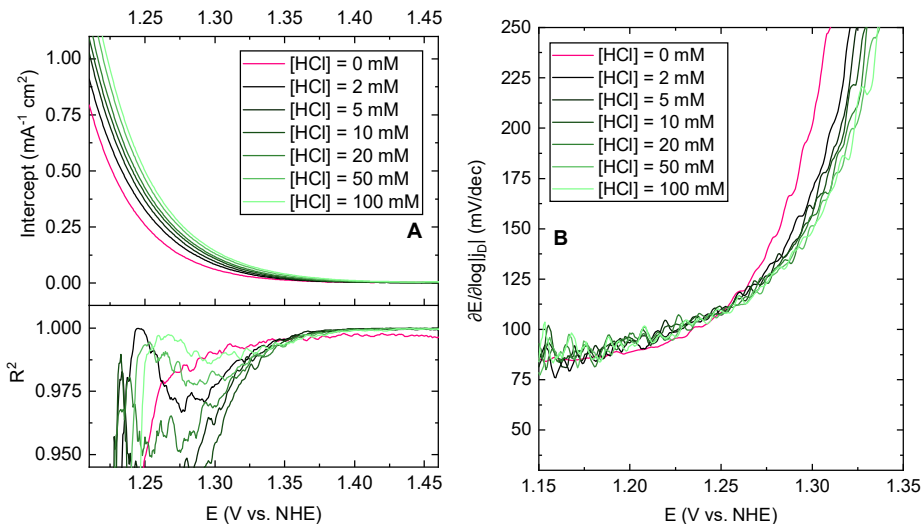
Figure 5.2: Kinetic data measured in the potential region of bromide oxidation, in 0.5 M HClO₄ + 10 mM HBr, for varying concentrations of HCl. Data is shown on the NHE potential scale to account for minor (±4 mV) pH shifts. A: Values of the intercept as function of potential, derived from Koutecký-Levich plots as in Figure A 9.5.6. Pink trace shows data when [HCl] = 0 mM. Top panel shows values of the intercept; lower panel shows corresponding values of the linear correlation coefficient R². B: Tafel slopes obtained from semi-logarithmic data of Figure 5.1 (see Figure A 9.5.11).

and diffusion limitations are approached more slowly as a function of potential. The reaction nonetheless always becomes diffusion controlled above 1.40 V vs. NHE. In Figure 5.2B, the BER (pink trace) shows a quasi-linear Tafel region between 1.15 – 1.25 V vs. NHE, where values are initially 90 mV/dec and gradually increase with potential. In this region, the effect of HCl is a slight increase of the Tafel slope values. All slopes increase sharply at potentials higher than 1.25 V vs. NHE, which can clearly be ascribed to the onset of mass transport control. The effect of Cl^- is a somewhat more extended potential window of kinetic control.
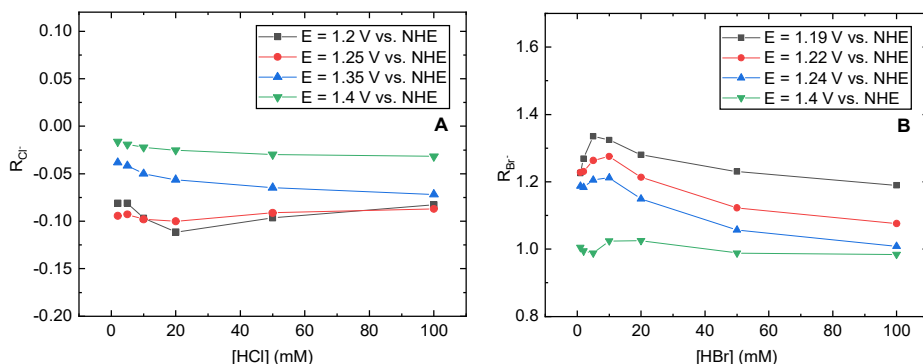
Figure 5.3: Chloride and bromide reaction orders measured in the potential region of bromide oxidation, in 0.5 M HClO₄. Data is shown on the NHE potential scale to account for minor (±4 mV) pH shifts. A: Chloride reaction orders $\mathcal{R}_{Cl^-}$ at several potentials, obtained by varying the HCl concentration at a fixed value [HBr] = 10 mM. B: Bromide reaction orders $\mathcal{R}_{Br^-}$ at several potentials, obtained by varying the HBr concentration in Cl^--free conditions.

Figure 5.3A shows chloride reaction orders ($\mathcal{R}_{Cl^-}$) for bromide oxidation at a constant [HBr] = 10 mM, derived from log-log plots of current density at constant potential (Figure A 9.5.12). Values for $\mathcal{R}_{Cl^-}$ are slightly negative at all times, as can be visualized by a reduction in bromide oxidation currents by Cl^- in the curves in Figure 5.1A. Observing the quasi-linear Tafel slopes in Figure 5.2B, the reaction is irreversible and kinetically controlled within 1.18-1.25 V vs. NHE; here, $\mathcal{R}_{Cl^-} \approx -0.1$, regardless of potential or chloride concentration. At higher potentials where diffusion limitations dominate, $\mathcal{R}_{Cl^-}$ approaches 0. Furthermore, Figure 5.3B shows bromide reaction orders ($\mathcal{R}_{Br^-}$) for the BER, in absence of Cl^- (see also Figure A 9.5.9). The BER, due to its rather high intrinsic rate, approaches diffusion limitations very quickly. This leads to only a rather narrow potential window of around 1.19 - 1.22 V in which the reaction was kinetically controlled at all measured bromide concentrations. Values of $\mathcal{R}_{Br^-}$ within this window were found to be significantly higher than 1 at low concentrations, and leveled off to lower values as [Br^-] increased. For diffusion-controlled potentials, $\mathcal{R}_{Br^-} \approx 1$, as can be expected when transport of Br^- to the surface is rate-limiting.

The $\mathcal{R}_{Br^-}$ values in Figure 5.3B are best captured by the V-H mechanism, as they are appreciably higher than 1, and (at kinetically controlled potentials) appear to level off to 1 as both E and [Br^-] increase. However, within the Langmuir V-H or V-K formalism, the 'onset value' of ~90 mV/dec for Tafel slopes in Figure 5.2B is quite different from the expected value of ~40 mV/dec at low overpotentials, provided that $\alpha \approx 0.5$. For the BER in a Cl^--free electrolyte, a similar effect was observed (Figure A 9.5.8). Tafel curves in the range of 1 mM $\leq$ [Br^-] $\leq$ 100 mM had quasi-linear regions, but the slope at the onset of these quasi-linear regions itself depended on the concentration. The most straight-forward interpretation of these results is a coverage effect of Br^*. At the onset of the reaction, θ_{Br} is perhaps significantly high, and the Tafel slope is already changing from 40 to 120 mV/dec. It is also possible that repulsive adsorbate interactions (which are ignored by the Langmuir approximation) play a role. Alternatively, the change in slope may be caused by the formation of higher oxidation states in the IrO_x, which starts occurring in the same region where the BER is kinetically controlled. The catalytic capability of IrO_x towards the OER has been shown to sensibly depend on this transition, such that it may also affect intrinsic rates of the BER. In any case, the theoretical upper limit of 120 mV/dec is never observed, possibly because diffusion limitations set in before the required overpotential is reached. To further investigate the bromide oxidation mechanism, we used Conway-Novák and Ferro-de Battisti test plots (Figure A 9.5.10), which offer a method to distinguish between the V-T or V-H mechanisms, respectively. The basis of this method is to rearrange the j vs. E relationship predicted by those mechanisms (i.e. Eq. 1.14 and Eq. 1.19), to give a straight line. Redrawing the experimental data in the same way and comparing the linearity provides a qualitative indication as to which mechanism the data adhere the best. We found that both Conway-Novák and Ferro-de Battisti plots of the BER data resulted in linearity, but significantly diverged in the high overpotential limit. Current densities in this region increased faster than expected by either mechanism, but Ferro-de Battisti plots gave better linearity overall. Similar results emerged from test plots involving bromide oxidation in presence of Cl^-. Like the unusual Tafel slopes, it is possible that transient redox changes in the IrO_x play a role.

When HCl is added, competitive adsorption of Cl^- will take place. The Langmuir V-H and V-K mechanisms predict that, approximately, all Tafel slopes shift horizontally to lower potentials when this happens (see the SI for full details). The change in Tafel slopes in Figure 5.2B versus [HCl] qualitatively agrees with this, but the effect is rather subtle. Additionally it is noted that $\mathcal{R}_{Cl^-}$ for bromide oxidation is always negative. Its value is predicted to be $\mathcal{R}_{Cl^-} = -\theta_{Cl}$ by both the V-H and V-K pathways, where $0 \le \theta_{Cl} \le 1$, such that the experimental value of -0.1 can be accommodated. The BER on IrO_x and the effect of Cl^- on this reaction can thus be modelled quite well by the V-H pathway, although describing the competitively adsorbing Br^* and Cl^* adsorbates with the Langmuir isotherm is likely an oversimplification.

We note that parallel adsorbing Cl^- may lead to the formation of interhalogen products. This can be excluded primarily because Cl^- has only a suppressive effect on the activity. If chloride was involved in any reaction, one would intuitively expect an increase in the mass-transport limited current densities of bromide oxidation. Instead, $\mathcal{R}_{Cl^-}$ is close to zero in this region, so that the formation of BrCl, as previously observed on Pt, seems unlikely. Up until roughly 1.40 V vs. NHE, the BER is the only reaction occurring in a mixed $Br^- + Cl^-$ electrolyte.

5.3.4. *UV-Vis studies of halogen evolution*

At potentials near the onset of the CER and OER, the measured currents become increasingly convoluted. Although the formation of interhalogen compounds, like BrCl, could be excluded up to 1.40 V vs. NHE by kinetic analysis, it becomes difficult to unambiguously assign the disk activity to specific reactions at higher potentials. To reduce this complexity, we investigated the product distribution of halogen species near the surface using electrochemical UV-Vis spectroscopy. We observed the formation of BrCl on Pt in a mixture of Br^- and Cl^- in Chapter 4; of particular interest would be whether a similar phenomenon takes places on IrO_x. Interhalogen reactions happening in solution again need to be taken into account, as described in section 4.3.2; we will approach this issue similarly as described in that section and in the discussion of UV-Vis results on Pt. By increasing the potential in 25 mV steps, with a step duration of 30 s, we studied the effect of increasing potential and shifts in solution composition during progressive oxidation reactions for a given constant potential. For the current experiments, a potential range between 1.100 – 1.500 V vs. RHE was chosen (Figure A 9.5.17A). Changes in the total transmission were measured after passing the beam through the back of the IrO_x/FTO electrodes and through the electrolyte. These experiments were carried out in 0.1 M $HClO_4$ + 0.1 M HCl, so that pH changes from HBr addition were negligible (on the order of 0.05 unit).

Figure 5.4 shows currents and the complete time-evolution of a typical UV-Vis experiment on an IrO_x/FTO electrode during the parallel oxidation of Br^- and Cl^-. The currents in Figure 5.4A show the BER onset around 1.20 V vs. RHE, reaching a (diffusion-limited) peak at 1.325 V followed by the onset of a second reaction around 1.425 V vs. RHE. The latter is clearly due to the CER, and appears to be shifted to a ~50 mV higher potential compared to the CER in absence of Br^-, similar to results from RRDE experiments. The suppressive effect of Br^- on the chloride oxidation activity is also apparent. As shown in the corresponding UV-Vis spectra
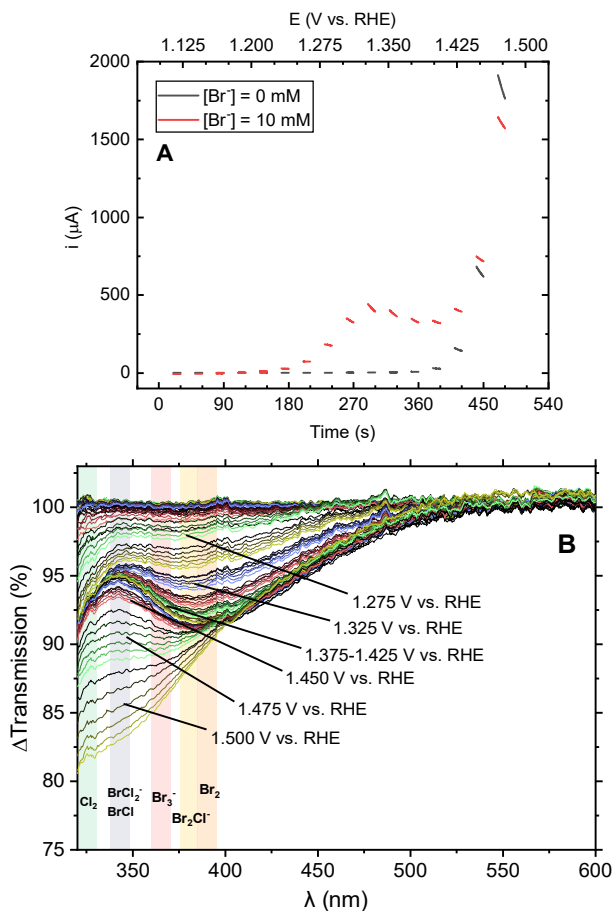
Figure 5.4: UV-Vis measurements of a stationary IrO_x/FTO electrode in a solution of 0.1 M $HClO_4$ + 0.1 M HCl + 10 mM HBr. A: Currents measured during the experiment, where only the final 10 seconds of each potential step are shown for clarity (see Figure A 9.5.17B for full data). Currents in Br^--free conditions are shown for comparison, upper axis shows the potentials applied at each moment in time. B: Corresponding transmission data of the region where the halogen species adsorb. Varying colors among traces correspond to different potential steps, of which some are indicated. Color gradients from dark to light indicate time evolution of the spectra during each potential step.

in Figure 5.4B, all relevant (inter)halogen species have a secondary adsorption band (or shoulder, in case of Br_3^-) that falls in the range $325 - 400$ nm. Up until 1.275 V vs. RHE, we observe mild adsorption with a broad shoulder spanning $340 - 450$ nm, which suggests that the main species formed is Br_3^-.[210] Higher potentials then lead to the sustained growth of a peak around 385 nm, which can be attributed to the formation of Br_2 and Br_2Cl^-. The currents in Figure 5.4A suggest that bromide oxidation starts to become transport limited around 1.30 V vs. RHE, depleting Br^- near the surface and reversing Br_3^- to Br_2 and Br_2Cl^- under the effect of Cl^-. This trend then persists over a rather wide potential range, where up until 1.425 V vs. RHE, the only significant change is the growing of the Br_2 and Br_2Cl^- signals. Cl_2 starts to evolve around 1.450 V vs. RHE, coupled to a sharp decrease in transmission in the wavelengths corresponding to Cl_2, BrCl and $BrCl_2^-$. As Cl_2 is the most powerful oxidizer in the system under

study, any interhalogen species previously described can now be formed in solution from follow-up reactions with Br^-. Crucially, we note that up until 1.425 V vs. RHE, the transmission within $335 - 345$ nm is virtually constant, and no shift of the peak around 385 nm to shorter wavelengths is observed. Both observations suggest that BrCl is not formed before the onset of the CER, which was a general finding during experiments with varying concentrations and ratios of $[Br^-]$ and $[Cl^-]$ (see also Figure A 9.5.18 and Figure A 9.5.19). Although the formation of BrCl in parallel with the CER cannot be excluded, it seems reasonable that evolution of Cl_2 is the fastest and most prevalent reaction at the high potential limit. In the remainder of this chapter, we will thus assume that the only major electrode reactions are the BER, CER and OER.

5.3.5. *Kinetic analysis of chlorine and oxygen evolution*

To investigate the CER and OER in the high potential region of Figure 5.1A, the two reactions have to be separated from each other and the underlying BER. We will first describe a method for isolating and modelling these individual currents. As mentioned previously, the ring potential was optimized to selectively reduce halogen evolution products while leaving O_2 untouched. The ring response is then proportional to j_{XER}, the total halogen evolution current density on the disk, according to (see also Eq. 2.1):

$$j_{XER} = \left| \frac{i_R}{N} \right|$$

Eq. 5.1

where j_R is the ring current normalized to the disk geometrical surface area (therefore with the same units as j_D, mA cm_{Disk}^{-2}) and N is the ring-disk collection factor. From the ring currents, it is thus possible to derive j_{XER}, which is the sum of the BER and CER current densities, $j_{BER} + j_{CER}$ (Figure A 9.5.3A). Under the reasonable assumption that the IrO_x catalyst is stable, we may then assume that the remainder of j_D after subtraction of j_{XER} is due to OER (see also Eq. 2.2):

$$j_{OER} = j_D - j_{XER}$$

Eq. 5.2

After calculating j_{XER} from j_R, the CER must then be separated from the BER. As in Chapter 4, a strict separation is complex, because the CER and BER are always superimposed, and the underlying contributions of each are not exactly known. However, the bromide oxidation wave generally is fully diffusion controlled at potentials higher than 1.40 V vs. NHE (see section 5.3.2), implying that it follows a sigmoidal trend in the region that is obscured by the onset of chloride oxidation. Like the work concerning Pt (see section 4.3.5), the foot and the top of the bromide oxidation wave were modelled as sigmoidal curves using a 5-parameter generalized logistic function, similar as described in section 4.3.5. Due to competitive adsorption by Cl^- (section 5.3.2), the wave can show notable asymmetry between the foot and the top. This asymmetry was nonetheless captured well by the relatively complex fitting functions (Figure A 9.5.3B). The generalized logistic function at the top of the wave was then used to extrapolate limiting current densities from bromide oxidation near the upper potential limit in j_{XER}. The

remaining current density after subtraction can be assigned to the CER. Figure A 9.5.3 shows an example of this procedure.
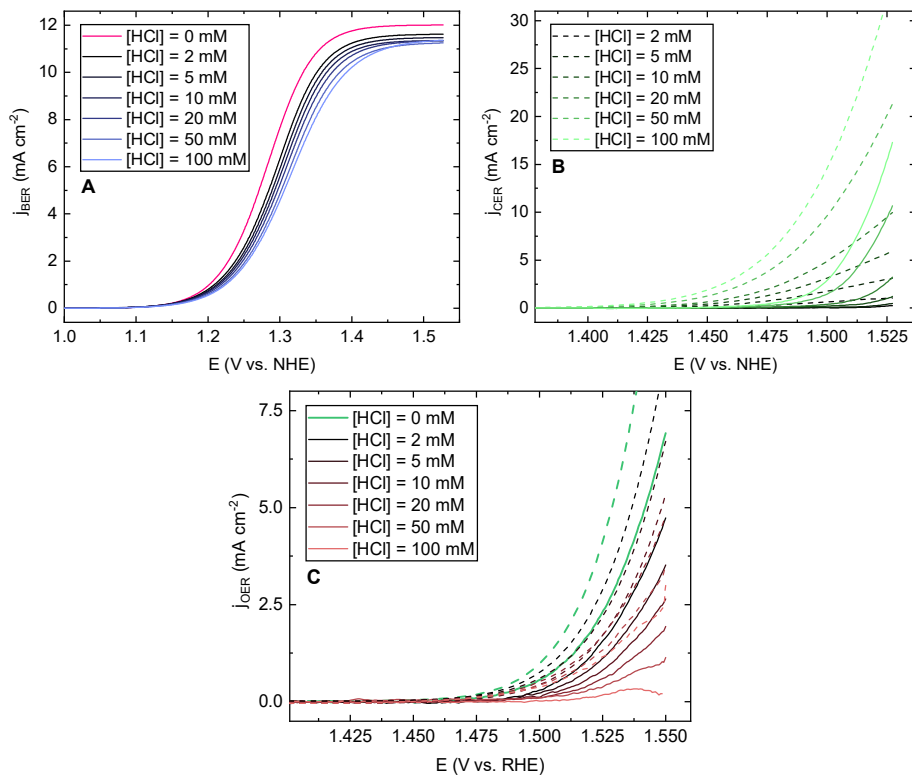
Figure 5.5: Individual BER, CER and OER current densities during parallel Br^-, Cl^- and H_2O oxidation as function of [HCl], on an IrO_x/GC electrode in 0.5 M $HClO_4$ and 10 mM HBr. A: BER current densities derived from generalized logistic fits of the foot and top of BER waves in Figure 5.1A. Pink trace shows chloride-free conditions. B and C: CER and OER current densities derived from BER logistic fits and the ring response. Solid traces show CER (B) and OER (C) in presence of 10 mM HBr. Dashed traces are similar experiments in solutions free of Br^-. Green, solid trace in C shows OER measured in 0.5 M $HClO_4$ and 10 mM HBr only (no Cl^-). Green, dashed trace in C shows 'pure OER', measured in 0.5 M $HClO_4$ (no Cl^- and Br^-).

Figure 5.5 shows the fitted and calculated individual current densities for the BER, CER and OER according to the above procedure. As previously established, the BER is suppressed by Cl^-, illustrated by negative values for $\mathcal{R}_{Cl^-}$. The CER is mutually strongly inhibited by Br^-, which shifts the onset potential for the CER around 50 mV more positive (Figure 5.5B). The OER is also negatively affected by Br^- (thick, green traces in Figure 5.5C), and Cl^- further decreases the activity, showing that Br^- and Cl^- suppress the OER in an additive way. During measurements in 10 mM HBr and 100 mM HCl, the OER activity can become almost immeasurably small (Figure 5.5C). At the same time, we observed that all measurable OER Tafel slopes are roughly similar, implying that the mechanism does not change under the effect of either Br^- and Cl^- (Figure A 9.5.14B). The retardation of the reaction is therefore probably caused by active site blocking.
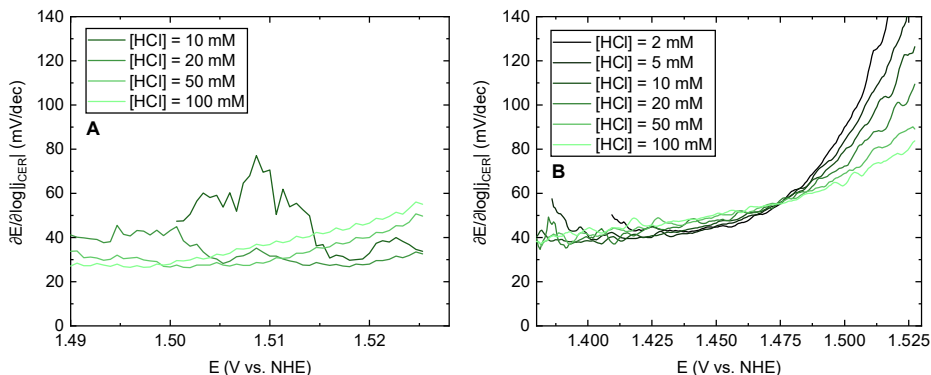
Figure 5.6: CER Tafel slopes, measured in presence (A) and absence (B) of 10 mM HBr, based on data from Figure 5.5. Data for chloride concentrations lower than 10 mM in A had insufficient signal to noise ratio and were omitted.

From the partial current densities in Figure 5.5, it is possible to determine Tafel slopes for the CER, as well as values of $\mathcal{R}_{Cl^-}$ in presence and absence of Br^-, as shown in Figure 5.6 and Figure 5.7. In Figure 5.6B, Tafel slopes for the CER competing with the OER generally start close to 40 mV/dec and then steadily increase. It is interesting to note that measurements in low [HCl] (such as 2 mM) show a sharp rise of slope beyond 120 mV/dec, like the BER did in section 5.3.3. The reason is probably the onset of diffusion limitations, as the rates measured at the high potential limit were within 40-50% of the Levich limiting current density for the 2 – 5 mM experiments. At chloride concentrations higher than 5 mM, the Levich limiting current density was approached less closely. Diffusion control thus becomes less of a factor, implying that the reaction kinetics are slowed down as a result of the increasing $[Cl^-]$.

When comparing Figure 5.6B to data in Figure 5.6A, the upward curvature in the high potential limits disappears in the presence of Br^-, as can be explained by the much lower overall reaction rates and thus the virtual absence of diffusion control (see Figure 5.5B). Linear Tafel slopes in Figure 5.6A start around 30 mV/dec, within 1.49 - 150 V vs. NHE, which is slightly lower than 40 mV/dec. These values seemingly agree with predictions by the Volmer-Tafel mechanism, but are more likely related to errors in the model describing the underlying BER limiting current density, which possibly approaches the real limiting value too quickly.

Figure 5.7 shows $\mathcal{R}_{Cl^-}$ values for the CER and the effect of Br^- (see Figure A 9.5.15). Br^- strongly lowers the activity of the CER, while at the same time, reaction orders are higher when comparing Figure 5.7A and B, where in the latter, values are usually below 1. All values decrease with increasing $[Cl^-]$. Higher reaction orders can be expected when competitive adsorption by Br^- decreases the chloride surface coverage θ_{Cl}. A lower value of θ_{Cl} at the onset of the reaction means its contribution to the measured reaction order is higher (see the SI of Chapter 4, in section 9.4.2). The range of values spanned by $\mathcal{R}_{Cl^-}$ in Figure 5.7A is mostly within 1-2, agreeing with the V-H mechanism. Only the value at the highest $[Cl^-]$ is around 0.8, which falls outside of this range. Corresponding Tafel data for $[Cl^-]$ = 50 mM and 100 mM in Figure 5.6A, which are the most accurate, are lower than in Figure 5.6B, but display roughly the same rate of change over the measured potential window. This suggests that like the BER,
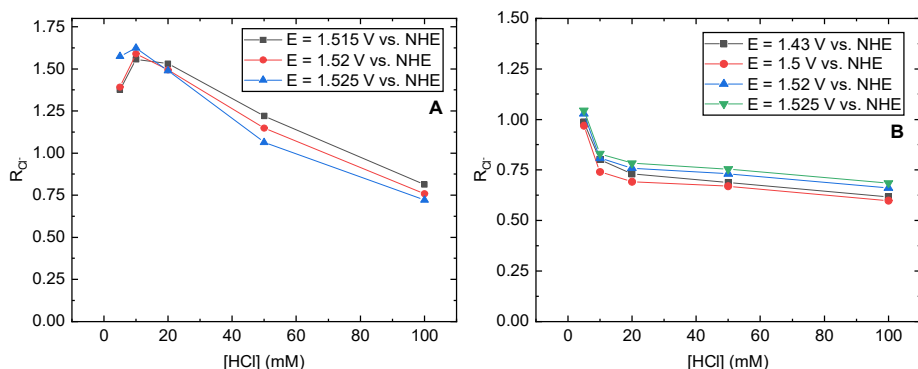
Figure 5.7: Chloride reaction orders $\mathcal{R}_{Cl^-}$ for the CER, in presence (A) and absence (B) of 10 mM HBr, based on data from Figure 5.5. Potentials were chosen to span the range where significant CER occurs, which is much narrower for the CER in presence of Br^-. Data in B are only shown for $[Cl^-]$ values where the ring collection method is reliable (see section 2.3.3).

the Tafel slopes as a whole are shifted horizontally on the potential axis. Together with the rising Tafel slopes as function of potential, this may be a coverage effect by Cl^* when considering V-H or V-K as the dominant mechanism. We further analyzed the CER using Conway-Novák and Ferro-de Battisti test plots, which clearly point towards a V-H or V-K type mechanism for the CER, including when the reaction is inhibited by Br^- (Figure A 9.5.13). It must be noted that linearity in Ferro-de Battisti test plots does not discern between the V-H and V-K mechanism, as their functional *j* vs. *E* relationship is the same. Distinction is in principle possible by investigating values of the slopes and y-intersects, but we refrained from this because these quantities are extremely sensitive to the value of the equilibrium potential, and become further convoluted when competitive adsorption is involved. It is in any case most likely that the values for $\mathcal{R}_{Cl^-}$ in Figure 5.7A and B correspond to V-H or V-K mechanisms with a first-order dependence on θ_{Cl}.

Finally, we note that the significant depressing effect of Cl^- on the OER activity is in stark contrast with results from Chapter 2, where the same IrO_x/GC electrode was studied for the CER. In a 0.5 M $KHSO_4$ electrolyte, Cl^- has only a negligible effect on the OER activity, and the reaction order for the CER approaches values slightly less than 1 (see Figure A 9.5.15). It is likely the presence of HSO_4^- that negates the suppressive effect of Cl^- on the OER and CER, because OER and CER activities in such electrolytes were significantly lower than in a solution of non-adsorbing ClO_4^-. This strengthens the idea that chloride effects on the CER and OER in the current study are related to specific adsorption of Cl^-. In presence of excess HSO_4^-, the surface is already heavily under the influence of a competitive adsorbate. Addition of Cl^- would then have a much smaller effect on the activity, because the reaction order effect from competitive adsorption is already near saturation. These results show that specific adsorption by the supporting electrolyte can have a significant effect on the apparent kinetics of the reaction and should be kept in mind when investigating concentration-dependent quantities.

5.3.6. *Molar selectivities*

Lastly, we consider the molar selectivities ε of the BER, CER and OER as function of the various halogen anion concentrations, which can be derived from data in Figure 5.7. Like Eq. 2.3, they can be calculated for a given value of E or $[Cl^-]$ via:

$$\varepsilon_{BER} = \frac{j_{BER}/2}{j_{BER}/2 + j_{CER}/2 + j_{OER}/4} \qquad \text{Eq. 5.3}$$
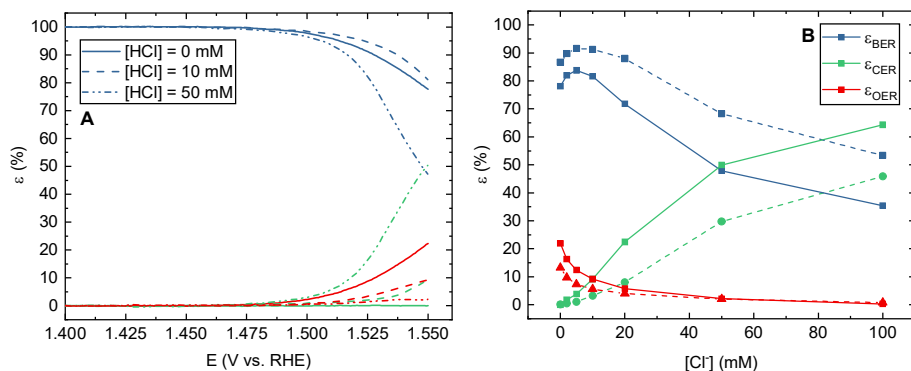
Figure 5.8: Molar selectivities of the BER, CER, and OER in 0.5 M $HClO_4$ + 10 mM HBr. A: Data as function of potential, at chloride concentrations of 0 (solid trace), 10 (dashed trace) and 50 mM (dotted trace). Blue, green and red show selectivities for the BER, CER and OER, respectively. B: Data as function of chloride concentration at potentials of 1.535 (dashed trace) and 1.55 V vs. RHE (solid trace). These are potentials where all three reactions are prevalent.

In Eq. 5.3, the BER selectivity is given as example. Figure 5.8 shows some measured selectivities of the three reactions. At lower potentials, the BER has near 100% selectivity, since it is the only possible reaction up until ~1.37 V. The CER has a significant overpotential due to the suppressive effect of Br^-, and onsets around the same potential as the OER. The BER is almost fully mass transport controlled at this point. Addition of Cl^- has a two-fold effect on ε_{BER}, which decreases due to CER activity, but also increases due to suppression of the OER by Cl^-. This is clearly visible in Figure 5.8B, where Cl^- increases the BER selectivity up until 10 mM Cl^-, after which it is decreases again with increasing CER competition. Another peculiarity of kinetic interplay arises when inspecting the OER and CER selectivities relative to each other, and the effect of bromide. In Figure A 9.5.16, when the CER and OER are the only reactions, the OER selectivity always increases with higher potential. In presence of Br^- however, the selectivity decreases. OER selectivity is always quite low (<22%), and sharply decreases when Cl^- is added. Less than 1% O_2 is formed at 100 mM Cl^-. The OER is much less sensitive to mass transport effects in an aqueous electrolyte, and should therefore still become the dominant reaction at potentials above 1.55 V vs. RHE. However, the overpotential where this happens will be dependent on Br^- and Cl^- in dual fashion. Besides the parallel BER and CER contributions, which must be outpaced, Br^- and Cl^- additionally impart significant kinetic suppression on OER itself and make the reaction even more sluggish. It was not

possible to measure reliable data at potentials higher than 1.55 V vs. RHE, because the increasing OER rates lead to persistent O_2 bubbles on the RRDE tip which compromise the measurements (see Chapter 8). We expect that generally, the OER selectivity versus halogen oxidation will depend sensitively on the electrode material, mass transport conditions and electrolyte composition. Small reactant concentrations can already significantly affect the interplay between kinetics. The possible effects of Br^- in the context of saline water electrolysis, even when present in small amounts, must thus not be underestimated.

5.4. Conclusions

In this chapter, we studied the simultaneous oxidation of Br^-, Cl^- and H_2O on GC-supported IrO_x, which served as a representative OER catalyst in practical electrolyzers. Adsorption and oxidation of Br^- and Cl^- proceeded simultaneously and had notable mutual effects on their respective evolution reactions. Bromine evolution exhibited reaction orders $\mathcal{R}_{Br^-}$ that are significantly higher than 1 at kinetically controlled potentials, but semi-linear Tafel slopes of 90-110 mV/dec. Chloride addition shifted the slopes to slightly higher values and was associated with mildly inhibiting effects ($\mathcal{R}_{Cl^-} \approx -0.1$). Together with the use of test plots, the Volmer-Heyrovský mechanism with a Langmuirian isotherm describing competitive adsorption of the halogen anions seems to describe the BER mechanism on IrO_x the most adequately. The CER displays previously reported linear Tafel slopes of ~40 mV/dec, also in presence of Br^-. Chloride reaction orders had values $0.7 < \mathcal{R}_{Cl^-} < 1$, but under the effect of Br^- they were significantly higher than 2. Together with test plots, the Volmer-Heyrovský again is the most suitable description for the experimental results. The lower limit values for chloride reaction orders which fall outside the predicted range of the V-H mechanism were ascribed to site-blocking (retardation of the CER by specific adsorption of chloride).

The OER was particularly slowed down by a compounded effect of both Br^- and Cl^-. Similar to the effects observed for the CER, the nature of this effect seemed to be a type of 'simple' competitive adsorption through site blocking, as the Tafel slopes (and therefore the underlying mechanism) did not seem to change. The selectivity for the OER was close to 0 at 1.55 V vs. RHE in conditions of 10 mM HBr and 100 mM HCl, which were the maximum concentrations tested. Contrary to findings on Pt in Chapter 4, no signs of BrCl formation were observed, even though Br^- and Cl^- interact strongly during adsorption. Kinetic analysis of the bromide oxidation region and UV-Vis experiments suggested that the only electrochemically formed products are Br_2, Cl_2 and O_2.

MnOₓ/IrOₓ AS SELECTIVE OXYGEN EVOLUTION ELECTROCATALYST IN ACIDIC CHLORIDE SOLUTION

6

An OER-selective anode is highly desired, as this would allow the electrolysis of readily available seawater without the formation of (mainly) chlorine as toxic by-product. Unfortunately, previous literature and Chapter 3 of this thesis suggest strong scaling behavior between the OER and CER, as well as an intrinsic kinetic advantage of the CER over the OER, so that optimizing the efficiency of the OER over the CER in acidic media has proven especially difficult. In this regard, we have investigated the OER vs. CER selectivity of manganese oxide (MnO_x), a known OER catalyst with unusually high OER selectivity. Thin films (~5-20 nm) of MnO_x were electrodeposited on glassy carbon-supported hydrous iridium oxide (IrO_x/GC), and tested for selectivity using rotating ring-disk electrode voltammetry and online electrochemical mass spectrometry. It was found that deposition of MnO_x onto IrO_x decreases the CER selectivity of the system in presence of 30 mM Cl^- from 86% to less than 7%, making it a highly OER-selective catalyst. Detailed studies of the CER mechanism and ex-situ structure studies using SEM, TEM and XPS suggest that the MnO_x film is in fact not a catalytically active phase, but functions as a permeable overlayer that disfavors the transport of chloride ions.

6.1. Introduction

An OER-selective anode would allow the direct splitting of saline water without the costly need of removing chloride from the system. Unfortunately, anodes that are highly OER selective in presence of Cl^- are very rare, due to the favorable kinetics of the CER and the scaling between OER vs. CER activities described previously. A notable exception is manganese oxide (MnO_x), an OER-active material that has received significant interest in recent years.[233–236] Initially reported by Bennet,[25] anodes based on MnO_x show a strong tendency to selectively evolve oxygen from acidic saline water. Hashimoto *et al.* studied a series of Mn-based mixed metal oxides (MMO) deposited on an IrO_x/Ti substrate and showed that such anodes often exhibit nearly 100% selectivity towards OER, under a variety of experimental conditions, for many hours of sustained operation.[31,237–239] Besides its high reported OER selectivity, MnO_x is also one of the few non-precious metal-based catalysts that has been reported to be moderately stable in acid under OER conditions.[240] This stability is in strong contrast with other 3d metal oxides such as CoO_x and Ni/Fe based oxyhydroxides, materials which show very high OER activity in alkaline pH, but are unstable and inactive in acid.[66,177,241–245]

In this chapter, we investigate the origin of the exceptional OER selectivity of the MnO_x-based materials studied by Hashimoto and co-workers. To our knowledge, the mechanism by which MnO_x 'breaks the scaling' between the OER and CER was never thoroughly investigated. In part, we believe this was due to the difficulty of reliably measuring OER vs. CER activity *in situ*, for which no fast, practical method existed. Fortunately, the RRDE method described in Chapter 2 can be conveniently employed for rapid and precise CER activity measurement in this particular system. We will use the RRDE method to study the effect of MnO_x deposition onto IrO_x with respect to the OER and CER selectivity during cycling voltammetry and amperometry. Product species are also studied using online electrochemical mass spectrometry (OLEMS) measurements in combination with isotopic labelling. To gain more insight in the nature of the MnO_x film, *ex situ* studies of the catalyst were performed using bulk X-ray diffraction (XRD), scanning electron microscopy (SEM), transmission electron microscopy (TEM), and X-ray photoelectron microscopy (XPS). In this way, we aim to shed more light on the mechanism by which MnO_x-based anodes selectively evolve oxygen, and how selectivity between the OER and CER may be better controlled.

6.2. Experimental

6.2.1. *Chemicals*

$KHSO_4$, $HClO_4$ (60%), KCl, NaCl, KBr and $NaClO_4$ (EMSURE) were purchased from Merck. $Na_2IrCl_6 \cdot 6H_2O$ (99.9%, trace metals basis) and NaOH (30% solution, TraceSelect) were purchased from Sigma-Aldrich. $MnSO_4$ (99.999%) and $Mn(ClO_4)_2$ (99.995%) were purchased from Alfa Aesar. High purity isotopically labeled water (97% ^{18}O, >99.99%) was purchased from Cortecnet. All chemicals were used as received. The water used for all experiments except those involving isotopic labelling was prepared by a Merck Millipore Milli-Q system (resistivity 18.2 MΩcm, TOC < 5 p.p.b.).

6.2.2. *General electrochemical procedures*

All experiments were carried out at room temperature (~20 °C). The electrochemical experiments were done using home-made two-compartment borosilicate glass cells with solution volumes of 100 mL. IrO_x deposition experiments and sample preparation for structural studies were done in borosilicate glass vials of approximately 10 mL. Before the first-time use, all glassware was thoroughly cleaned by boiling in a 3:1 mixture of concentrated H_2SO_4 and HNO_3. When not in use, all glassware was stored in a 0.5 M H_2SO_4 solution containing 1 g/L $KMnO_4$. Before each experiment, glassware was thoroughly rinsed with water, and then submerged in a dilute (~0.01 M) solution of H_2SO_4 and H_2O_2 to remove all traces of $KMnO_4$ and MnO_2. The glassware was then rinsed three times with water and boiled in water. The rinsing-boiling procedure was repeated two more times. An IviumStat potentiostat (Ivium Technologies) was used during electrochemistry experiments. All experiments except IrO_x deposition experiments and sample preparations for structural studies were 85% iR-compensated. The solution resistance was measured with electrochemical impedance spectroscopy, by observing the absolute impedance in the high frequency domain (100-10 KHz) corresponding to a zero-degree phase angle. RRDE and OLEMS experiments were performed in 0.5 M $KHSO_4$ solutions with pH values in the range of 0.88 ± 0.05, as measured with a Lab 855 meter equipped with a glass electrode (SI Analytics). Working solutions used in RRDE and OLEMS experiments were saturated with Ar (Linde, purity 6.0) before experiments. Solutions were bubbled with Ar gas during forced convection experiments, and Ar was used to blanket the solution in case of OLEMS. The reference electrode for RRDE and OLEMS experiments was a HydroFlex® reversible hydrogen electrode (Gaskatel), separated from the main solution using a Luggin capillary, to fix the reference sensing point and to prevent mixed potentials at the reference due to dissolved Cl_2 gas. A LowProfile Ag/AgCl electrode (Pine Research Instrumentation, sat. KCl, E = 0.197 V vs. NHE) was used during IrO_x deposition experiments and sample preparations for structural studies. All potentials in this chapter are reported using the RHE scale unless specified otherwise. The Ag/AgCl reference was regularly calibrated versus the RHE to check its equilibrium potential. A Pt mesh was used as counter electrode during RRDE and OLEMS experiments. During IrO_x deposition experiments and sample preparations for structural studies, the counter electrode was a Pt spiral placed axisymmetrically below the RRDE tip.

6.2.3. *Rotating ring-disk studies (RRDE) of chlorine evolution vs. MnOx deposition*

RRDE measurements were done with an MSR rotator and E6 ChangeDisk RRDE tips in a PEEK shroud (Pine Research). The Luggin tip connected to the reference electrode was aligned to the center of the RRDE electrode to minimize electrical cross-talk.[137,138] The liquid phase collection factor of the ring-disk system, N_l, was determined by studying the $Fe[CN]_6^{3-}/Fe[CN]_6^{4-}$ redox couple in a solution of 10 mM $K_3Fe[CN]_6$ and 0.1 M KNO_3, using the Pt ring with both a freshly prepared blank GC electrode and the IrO_x/GC electrode. The value was 0.244 within 5% accuracy. The collection factor for dissolved Cl_2 was also measured in the same setup, by evolving chlorine selectively on a Pt disk electrode at 1.6 V vs. RHE, well before

the kinetic onset of OER. Provided that the solution pH was lower than 1, the collection factor for dissolved chlorine was found to be 0.240, almost identical to N_l.

IrO_x/GC electrodes were prepared via electroflocculation of IrO_x nanoparticles, as described in sections 9.1.1 and 9.1.2. The GC surfaces were polished with diamond paste, followed by rinsing and sonication in water for 3 minutes. The electroflocculation amperometry step lasted 300 s.

Before RRDE experiments, the Pt ring was electropolished by scanning from -0.1 V to 1.7 V at 500 mV s^{-1} for 40 scans at 1500 RPM, after which the individual scans did not change. This step was vital to remove traces of IrO_x that deposited on the ring during IrO_x electroflocculation under rotation.[139] Hydrodynamic experiments were done at 1500 RPM by scanning the disk electrode in the range of $1.1 - 1.55$ V at 10 mV s^{-1}. The ring was kept at 0.95 V during measurement of CER rates. Presence of Mn^{2+} is not expected to interfere with the Pt ring during experiments.[177,246] In between experiments, the IrO_x/GC electrode was kept at 1.1 V. Ring currents were corrected for constant background currents and product collection delay. The latter arises from the time needed for products formed on the disk to reach the ring, and was approximately 200 ms at 1500 RPM. Before initiating quantitative measurements, the IrO_x/GC electrode was scanned 40 times in a chloride-free electrolyte between $1.3 - 1.55$ V (into the OER region) at 1500 RPM. This was done to ensure stable IrO_x film behavior during experiments. All currents were reported without normalization to catalyst surface area, since we were solely interested in selectivity trends (which are ratios of currents) and kinetic parameters such as Tafel slopes, none of which are affected by normalization.

6.2.4. *Online electrochemical mass spectroscopy (OLEMS)*

During OLEMS experiments, volatile reaction products were collected *in situ* using a 0.5 mm diameter tip with a porous PTFE membrane at a close distance ($\sim$10 μm) to the electrode surface, positioned with a micrometric screw system.[247] Mass signals were measured using an EvoLution mass spectrometer setup (ESS Ltd.) equipped with a Balzers QMS200 quadrupole (Pfeiffer). Pressure in the mass chamber was maintained lower than 10^{-6} mbar using a rotary vane pump (Edwards nXDS6i) and a TMH-071P turbo molecular pump (Pfeiffer). Before experiments, the tip was cleaned by submerging it for 1 hour in a mixture of 0.2 M $K_2Cr_2O_7$ and 2 M H_2SO_4, followed by ample rinsing with water. The IrO_x/GC disk working electrode was prepared as described in section 9.1.2, after which the disk was carefully removed from the RRDE tip and mounted to a stiff Pt wire using Cu tape. The electrode was then mounted in hanging-meniscus configuration. The Luggin tip connected to the RHE reference was placed sideways near the working electrode at a distance of approximately 1.5 cm, to accommodate the OLEMS tip. Isotopic labelling was performed in a 1.5 mL volume of 0.1 M $KHSO_4$ in $H_2^{18}O$, using a LowProfile Ag/AgCl reference and a Pt spiral as counter electrode. The reference electrode was temporarily stored in a 0.1 M $KHSO_4$ solution of regular water in-between experiments, to minimize Cl^- leakage into the isotopic solution. The IrO_x electrode surface was first rinsed with $H_2^{16}O$ water and thoroughly dried using filtered compressed air. Ir ^{18}O-exchange was done by performing OER at 1.25 V vs. Ag/AgCl for 300 s, followed by thorough

rinsing with $H_2{}^{16}O$ water. The 'Ir$^{18}O_x$'/GC electrode was submerged in the OLEMS cell strictly under potential control at 1.30 V, followed by MnO_x deposition and scanning experiments.

6.2.5. *Sample deposition for structural studies*

IrO_x/GC samples were prepared via deposition of IrO_x onto a GC disk, as described in section 9.1.2. MnO_x films were grown in solutions of 0.35 M $NaClO_4$ + 0.15 M $HClO_4$ (pH = 0.88) in presence of 0.6 mM $Mn(ClO_4)_2$. The use of a non-adsorbing ClO_4^- electrolyte allowed MnO_x deposition at lower potentials, in absence of superimposed OER (in case IrO_x was the substrate), leading to more accurate monitoring of film growth. This was necessary as it was not possible to verify the film thickness post-analysis from reductive dissolution. MnO_x/IrO_x/GC and MnO_x/GC samples were prepared by conditioning an IrO_x/GC or blank GC disk electrode at 1.45 V and 1500 RPM. In case IrO_x was the substrate, 20 mM NaCl was added to the solution and MnO_x film formation on IrO_x was monitored by keeping the ring electrode at 0.95 V and measuring the CER rate. For preparation of a MnO_x/GC sample, deposition of the film was stopped near ~1.25 * t_{max}, t_{max} being the time corresponding to the peak current during deposition.[248] In all cases, when a satisfactory MnO_x coverage was reached, the experiment was discontinued by raising the working electrode while rotating, breaking electrical contact and spin-drying the surface. This procedure was employed to minimize transient MnO_x dissolution in the acidic environment. Immediately after spin-drying, the electrode was rinsed with ample water and dried with compressed filtered air.

6.2.6. *Scanning electron microscopy (SEM)*

GC disks were carefully removed from the RRDE tip after deposition and glued to a SEM specimen mount using conductive silver epoxy. Scanning electron micrographs were made using a FEI Nova NanoSEM 200 equipped with a field emission electron source, operating at 10 kV beam accelerating voltage and 10 pA probe current. Images were recorded in immersion mode using a through-the-lens detector, at a working distance of ~4.5 mm. EDS measurements were performed in a JSM 6010LA setup (JEOL). After recording overview images at 10 kV, the beam accelerating voltage was increased to 15 kV and elemental data were recorded from a wide variety of locations on the electrode.

6.2.7. *Transmission electron microscopy (TEM)*

GC disks were carefully removed from the RRDE tip after deposition, and the IrO_x/MnO_x films were then carefully scraped off the electrode surface. The films were sonicated for 30 minutes in absolute ethanol, and the suspension was dropcasted onto a Cu TEM grid. Bright-field transmission micrographs were recorded using a JEM-1400Plus apparatus (JEOL) equipped with a LaB_6 filament and a 2kx2k Orius camera (Gatan), operating at 120 kV accelerating voltage. For measurements at higher resolution, a model JEM-2010 (JEOL) equipped with a LaB_6 filament and an Orius 831 camera (Gatan) was used, operating at 200 kV. Selected-area diffraction patterns were analyzed using the CrysTBox software suite.[249]

6.2.8. *X-ray diffraction measurements (XRD)*

GC disks were carefully removed from the RRDE tip after deposition and mounted directly in the diffractometer using a height-adjustable mount to correct for disk protrusion. X-ray diffraction spectra were recorded using a D8-Advance diffractometer (Bruker) operated in Bragg-Brentano geometry, equipped with a Co-Kα anode (λ = 1.78897 Å) and a Lynxeye position sensitive detector. Diffraction data were collected over angles ranging between 10° - 100° with a step size of 0.02° and scan speed of 0.2° s^{-1}.

6.2.9. *X-ray photoelectron spectroscopy (XPS)*

GC disks were carefully removed from the RRDE tip after deposition and mounted directly in the spectrometer. X-ray photoelectron spectroscopy measurements were performed in a K-alpha spectrometer (Thermo Fisher Scientific) using a monochromatic Al-Kα X-ray source. The measurements were carried out at a chamber pressure of about 10^{-8} mbar, a flood gun was used for charge compensation. The energy analyzer was operated with a pass energy of 200 eV and 0.25 eV energy spacing for the survey spectrum, and a pass energy of 50 eV and 0.1 eV energy spacing for the high-resolution spectrum. All binding energies were referenced to the C1s peak (284.8 ± 0.025 eV). Each spectrum reported is the statistical average of 10 measured scans. Spectral peaks were analyzed and processed using Thermo Avantage v5.903 software (Thermo Fisher Scientific). The Shirley algorithm was used to calculate background contributions. Relative atomic contributions on the surface were calculated using full width integration over the core-level signals along with tabulated atomic sensitivity factors (ASF). For the core-level Ir 4f peak deconvolution, we used a model from existing literature, excluding contributions from 4f satellite peaks.[250]

6.3. Results and discussion

6.3.1. *Effect of MnOₓ deposition on chlorine evolution*

We make use of rotating ring-disk electrode voltammetry to measure and separate individual OER and CER currents, as described in Chapter 2. During these experiments, the collection factor for Cl_2 (N_l) was reproducible within 2%, and virtually identical to that of the $Fe[CN]_6^{2-}/Fe[CN]_6^{3-}$ redox couple ($N_l = 0.244$). Figure 6.1 illustrates a experiment of parallel
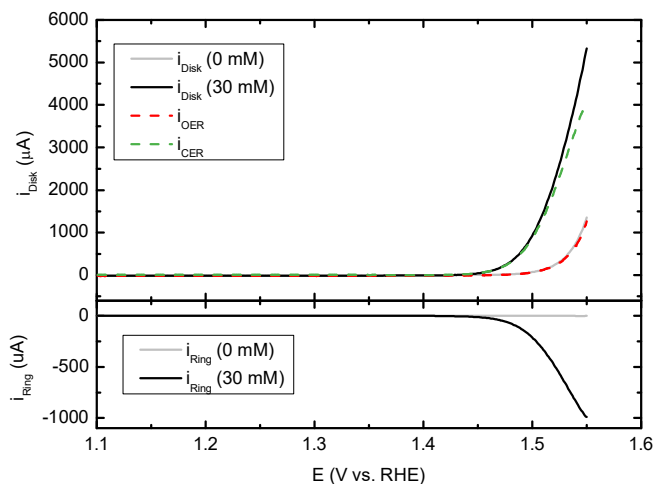
Figure 6.1: Potential scans of mixed OER and CER in 0.5 M KHSO₄ (pH = 0.88), on a 'bare' IrOₓ/GC electrode (no MnOₓ). Top panel displays currents measured on the IrOₓ/GC disk (iₚ) in a Cl⁻-free solution (grey curve), and in presence of 30 mM KCl (black curve). Rotation rate: 1500 RPM. Lower panel shows corresponding currents on the Pt ring (iᵣ) fixed at Eᵣ = 0.95 V . Calculation of i_{OER} and i_{CER} curves was performed using Eq. 2.1 and Eq. 2.2.

OER and CER on IrOₓ/GC, while scanning the disk potential in the range of 1.1 − 1.55 V in chloride concentrations of [Cl⁻] = 0 mM and [Cl⁻] = 30 mM (see also Figure 2.1). By observing the ring current in Figure 6.1, the onset of CER can be located at around 1.42 V, which means that it proceeds with negligible overpotential at pH = 0.88. Similar to results in Chapter 2, the OER is not strongly affected by either the presence of Cl⁻ or parallel CER under the used conditions. Furthermore, selectivity towards CER is approximately 86% near 1.55 V. Although a chloride concentration of 30 mM is far removed from realistic seawater concentrations, which typically exceed 0.5 M, the use of such concentrations would compromise the ability to carry out fundamental CER studies, due to increasing experimental noise levels and interference of gas bubbles in the RRDE setup. In consideration of results from section 2.3.4, a concentration of 30 mM chloride should constitute an optimal system for study.

In acidic media, deposition of MnOₓ can proceed via the following overall reaction:

$$2\ Mn^{2+} + 2\ H_2O \rightarrow MnO_2 + 4\ H^+ + 2\ e^- \qquad\qquad \text{Eq. 6.1}$$

$$E^0_{MnO_x/Mn^{2+}} = (1.23 - 0.059 * pH)\ V\ vs.\ RHE$$
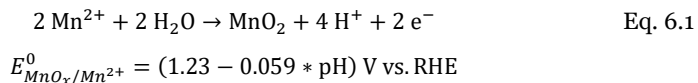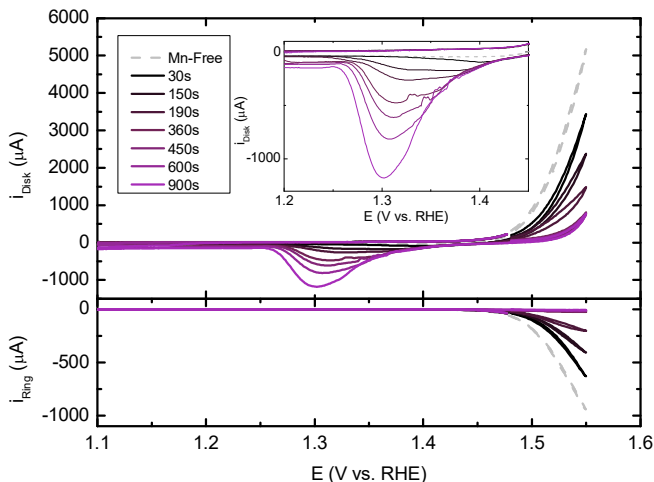
Figure 6.2: Top panel shows CVs of an IrO_x/GC rotating disk electrode (top) in 0.5 M $KHSO_4$, 30 mM KCl (pH = 0.88), and 0.6 mM $MnSO_4$ (except for the Mn^{2+}-free experiment). Rotation rate: 1500 RPM. MnO_x films were preconditioned at various times at 1.48 V before initiating the forward scan at 1.48 V. The lower panel shows the corresponding i_R ($E_R = 0.95\ V$).

To form MnO_x films on IrO_x and study their effect on CER selectivity, we resorted to growing MnO_x thin films *in situ* by 'spiking' the working solution with 0.6 mM $MnSO_4$. This small but significant concentration of Mn^{2+} ions prevents the net dissolution of the acid-unstable MnO_x films during experiments.[240,251] Despite obvious disadvantages, such as lack of precise control over film thickness during scanning, this method allows the growth and study of thin MnO_x films of variable thickness in an identical system, without the severe uncertainty of the film's integrity (and problems concerning build-up of dissolved Mn^{2+} in the solution, in case of repeated externally grown MnO_x films). It is thus possible to measure how CER kinetics depend on MnO_x film growth. Figure 6.2 shows CVs from $1.1 - 1.55$ V of an IrO_x/GC electrode, in presence of 30 mM KCl and 0.6 mM $MnSO_4$, under 1500 RPM rotation rate. Compared to a Mn^{2+}-free solution, MnO_x deposition manifests itself as a superimposed current with a slow onset near 1.37 V (see Figure A 9.6.4 for a close-up). To grow MnO_x films of variable thickness and to test their effect on CER activity, the disk electrode was first conditioned at $E_D = 1.48$ V, while rotating at 1500 RPM. The conditioning potential was chosen such that it was more positive than $E_{MnO_x/Mn^{2+}}^{eq}$ (approximately 1.13 V at pH = 0.88), but not too far into the mixed OER/CER region in order to prevent excessive gas formation during deposition. Immediately after conditioning, the electrode was scanned up to a positive potential limit of $E_D = 1.55$ V. At the same time, the ring was kept at $E_R = 0.95$ V, and still regarded as a selective probe for chlorine. Formation of Cl_2 can be seen in both the forward and reverse sweep. During the reverse scan, complete cathodic dissolution of the MnO_x films appears as a reduction wave from approximately 1.450 to 1.15 V. Dissolution of the film effectively 'resets' the working electrode, and the charge under the reduction peak (described as Q_{MnO_x}) allows to approximate the thickness of the film that was originally present in the forward scan. Repeated scanning without preconditioning led to overlapping CVs, with reproducible peak currents,

ring currents and cathodic MnO_x dissolution peaks, which shows that the original system is restored every time after traversing the negative potential limit of 1.10 V (see Figure A 9.6.5). A Mn^{2+} concentration of 0.6 mM was purposefully tested as optimum: lower concentrations led to impractically long deposition times, and higher $[Mn^{2+}]$ (> 1 mM) often resulted in films that were too thick to completely dissolve after returning to 1.10 V. This was evident from a remaining brown-red glow on the electrode surface, and significant but slowly subsiding negative current when the potential was kept at 1.10 V. Thicker films also occasionally led to mechanical instability in the form of brown MnO_x flakes peeling off the electrode during rotation. Keeping $[Mn^{2+}]$ as low as possible also reduced the extent of continuous (uncontrolled) MnO_x deposition current during scanning and allowed a more accurate comparison of i_{OER} and i_{CER}, as will be discussed below.
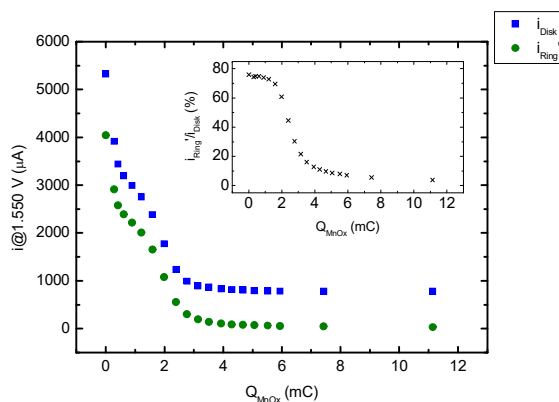
Figure 6.3: Disk (blue) and ring currents (green) measured at $E_D = 1.55$ V as function of Q_{MnO_x}, the reductive charge measured for the corresponding MnO_x film during the backward scan, which is an approximate measure of its thickness. Inset shows the ratio between i_D and i_R corrected for N_l (i_R'). Values were determined from CVs such as those in Figure 6.2.

Figure 6.3 displays the measured disk and ring currents for $E_D = 1.55$ V as a function of Q_{MnO_x}, the charge determined from the MnO_x dissolution wave in the corresponding reverse sweeps. The potential of 1.55 V was chosen for quantitative analysis, since this is the point of potential reversal and as such contains minimal current contributions from (pseudo)capacitive processes. To be able to compare directly, ring currents i_R are corrected for N_l to obtain i_R'. The distinction between i_R' and i_{CER} will be discussed shortly. The deposition of MnO_x has a profound effect on both i_D and i_R', but the most interesting aspect is the selectivity: i_R' is impacted very differently than i_D. As Q_{MnO_x} varies within 0 - 2 mC, a proportional decrease in both i_D and i_R' can be seen, leading to an approximately constant ratio i_R'/i_D (Figure 6.3, inset). For Q_{MnO_x} > 2 mC, the ratio i_R'/i_D shows a sudden drop. We also observe a change in shape of the MnO_x reduction wave as Q_{MnO_x} increases above 2 mC. Below 2 mC, a single, broad reduction peak is observed, which transforms into two peaks for Q_{MnO_x} > 2 mC, with peak potentials shifting continuously more negative as the reduction charge increases (see Figure A 9.6.6). The appearance of separate peaks may be due to proton diffusion becoming the limiting factor during film reductive dissolution.[252,253]

Unfortunately, the quantification of i_{OER} and i_{CER} in presence of Mn^{2+} is obfuscated by Mn-related redox processes, in contrast to the measurements on MnO_x-free IrO_x in Figure 6.1, where it was assumed that the OER and CER were the sole reactions. There are two reasons for this. First, i_D after subtraction of i_R' is no longer 'pure' OER current, but the sum of OER and MnO_x deposition current. Second, close inspection of the ring currents (Figure A 9.6.4) suggests reduction of a species that appears at a potential slightly more negative than the onset potential of CER. We ascribe this additional current to the reduction of solution-phase Mn^{3+} .[254] This species is a generally accepted intermediate during acidic MnO_x deposition.[252,253,255] Ring currents can thus no longer be ascribed solely to CER ($i_R' \neq i_{CER}$). To take these two sources of error into account, we use the following correction. The diffusion limited current density of MnO_x deposition ($i_{MnO_x}^L$) is estimated at 140 µA using the Levich equation (see section 9.6.1). This value serves as an 'upper limit' of the MnO_x deposition current during the OER and CER. The maximum ring current originating from Mn^{3+} reduction can be estimated at 70 µA, representing an upper limit of ring current falsely attributed to CER. For $Q_{MnO_x} < 2$ mC, where $i_R' > 1800$ µA, this error was assumed negligible, but at $Q_{MnO_x} > 4$ mC, the remaining ring current approaches 30 µA. In this regime, the ring current may not be unambiguously assigned to CER, and the real CER current could be significantly lower.

To still make an estimation of OER vs. CER selectivity, we assume that i) MnO_x deposits with diffusion limited current densities at all potentials, allowing the calculation of the *minimum* OER current after ring current subtraction, and ii) N_l-corrected ring current i_R' originates only from CER, irrespective of stray Mn^{3+} reduction reactions, leading to the *maximum possible* CER current. In other words, Eq. 2.1 applies, like the case for the 'blank' IrO_x catalyst: $i_R' = i_{CER}$. We thus use the following expression for i_{OER}:

$$i_{OER} = i_D - i_{CER} - i_{MnO_x}^L = i_D - i_R' - 140 \text{ µA} \qquad \text{Eq. 6.2}$$
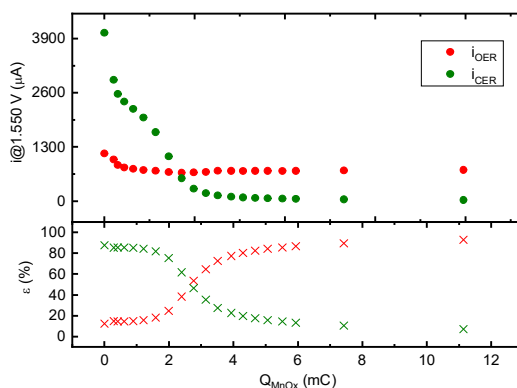
Figure 6.4: Top panel: currents for OER (red) and CER (green) at $E_D = 1.55$ V (top), calculated from Eq. 2.1 and Eq. 6.2. Lower panel: corresponding selectivities towards OER (red) and CER (green). Data is plotted as a function of Q_{MnO_x}, the charge ascribed to the corresponding MnO_x layer, which is an approximate indication of its thickness. Values were determined from CVs such as those in Figure 6.2.

Figure 6.4 displays the calculated currents and selectivities towards the OER and CER as a function of Q_{MnO_x}. As already suggested by the ratio i'_R/i_D in Figure 6.3, ε_{OER} rises sharply at the expense of ε_{CER} beyond a MnO_x reduction charge of 2 mC. We will refer to the reduction charge of the MnO_x film at which there is a strong shift of selectivity from CER towards OER as the 'critical MnO_x charge'. Figure 6.4 shows that modification of IrO_x by growth of a thick MnO_x film makes it >90% OER selective with a moderate (45%) drop in activity.
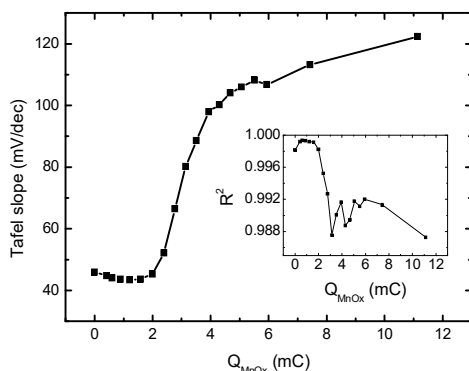
Figure 6.5: Tafel slopes for CER on the disk electrode, constructed from ring currents, as a function of Q_{MnO_x}. Values taken from CVs similar to Figure 6.2. Inset shows corresponding R^2 values (correlation coefficients), to illustrate the degree of linearity as function of Q_{MnO_x}.

The dependence of CER kinetics on MnO_x deposition can be studied by making Tafel plots based on measured ring currents (Figure 6.5), especially at high ring currents where the error from Mn^{3+} reduction is negligible. On 'bare' IrO_x, as well as during the initial stages of MnO_x film growth (Q_{MnO_x} < 2 mC), CER Tafel slopes range within 40-45 mV/dec, suggesting a rate-limiting second electron transfer step controlling the CER mechanism, in correspondence with previous literature.[56,105] The Tafel curves in this regime show good linearity, as determined from R^2-values in the inset of Figure 6.5. As Q_{MnO_x} increases beyond the critical charge, Tafel slopes increase to ca. 120 mV/dec. This value agrees remarkably well with a mechanism where the first electron transfer step becomes rate-determining, suggesting that the apparent kinetics of the reaction change. However, a pronounced departure from linearity is also apparent (Figure 6.5, inset), suggesting that the measured Tafel slopes become clouded by additional effects. Above all, we expect the error from Mn^{3+} reduction to be high here, and the measured Tafel slope may well be related to the solution phase oxidation of Mn^{2+}_{aq} to Mn^{3+}_{aq} on the disk (assuming a symmetry factor α of ~ ½).

To gain more insight in the sudden change in CER activity, ring-disk amperometry curves were recorded to study the potential-dependent deposition behavior of MnO_x on IrO_x (Figure 6.6). The ring currents in the lower panel were normalized versus their initial value ($i_{R,t=o}$), to compare the relative decrease in CER for different potentials. An increase in E_D has a twofold effect: i) i_D initially increases strongly, which is due to a rise in CER current (top panel), and ii) CER rates start declining earlier (lower panel). It was previously postulated that MnO_x deposition proceeds through a progressive electrochemical nucleation and growth mechanism,
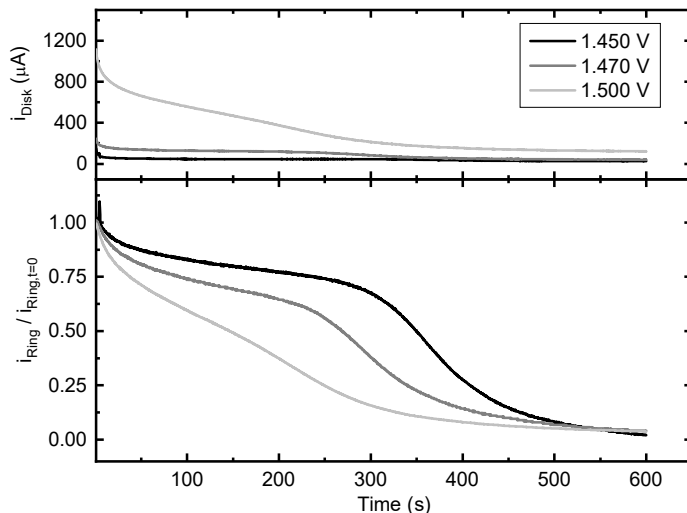
Figure 6.6: Top panel: amperometry measurements at increasing potentials of an IrO_x/GC rotating disk electrode (top) in 0.5 M KHSO$_4$, 20 mM KCl, and 0.6 mM MnSO$_4$ (pH = 0.87), rotation rate 1500 RPM. The lower panel shows the corresponding i_R normalized to their initial value $i_{R,t=0}$ (E_R = 0.95 V).

in which the current contribution from the growth of existing nuclei is larger than current from the formation of new nuclei.[248,256,257] The data presented here suggest that MnO$_x$ deposition at 1.45 V on amorphous IrO$_x$ near pH = 1 is kinetically controlled and proceeds via a similar mechanism, since the deposition current shows an induction time followed by a peak (Figure A 9.6.8). The observed drop in CER activity would then coincide with the moment where the exclusion zones of the individual MnO$_x$ nuclei intertwine and the full coverage of the IrO$_x$ surface by MnO$_x$ rapidly increases.

To corroborate the RRDE findings, we measured the competition of CER vs. OER on IrO$_x$ and the effect of MnO$_x$ deposition using OLEMS (Figure 6.7). Since the use of a stationary electrode is required in the OLEMS setup, a stirrer bar at ~600 rpm was used to enhance mass transport of chloride and Mn^{2+}, and reduce the effects of transient broadening of the diffusion layer. Despite this, mass transport to the surface was significantly lower than in the RRDE setup. To ensure a strong enough Cl$_2$ mass signal in the OLEMS and to reach MnO$_x$ film growth comparable to the RRDE experiments, a relatively high concentration of chloride (80 mM) and MnSO$_4$ (1.2 mM) was used. In Figure 6.7A, cyclic voltammetry was performed on an IrO$_x$/GC electrode with a significant amount of MnO$_x$ predeposited at 1.460 V, after which three cycles were carried out in the potential region of mixed CER, OER and MnO$_x$ deposition. The initial forward sweep starting from 1.460 V shows a relatively low maximum current, and the backward sweep shows a wave where the preformed MnO$_x$ layer is reductively removed. In scan 2 and 3, the IrO$_x$ electrode was scanned into the CER/OER region again, such that the electrode was free of pre-formed MnO$_x$. Mass signals m/z 32 and m/z 70 (corresponding to O$_2^+$ and Cl$_2^+$, ionized molecular oxygen and chlorine, respectively) were collected in the mass spectrometer during the scans. Both species have peaks in the mixed OER/CER region as expected, but there are major differences between the three cycles. The rate of Cl$_2$ formation
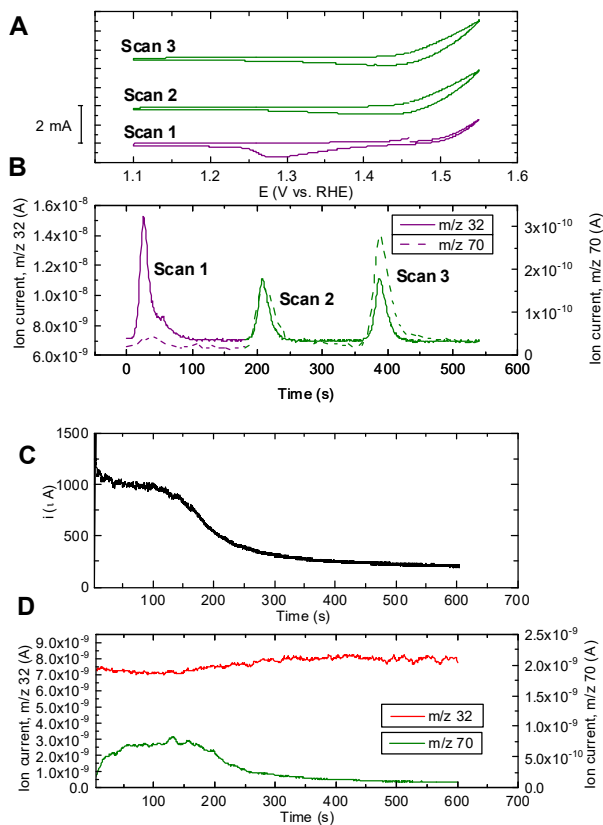
Figure 6.7: OLEMS measurements of an IrO_x/GC disk electrode in 0.5 M $KHSO_4$, 80 mM KCl, and 1.2 mM $MnSO_4$ (pH = 0.89). A: CVs of the electrode after preconditioning for 450 s at 1.46 V, followed by three scans. Scan rate: 5 mV s^{-1}. C: Amperometry at 1.500 V for 600 s. Figures B and D show corresponding OLEMS mass signals over time. Solution saturated with Ar. A stirrer bar at ~600 rpm was employed to increase mass transport.

is clearly suppressed during the first cycle, then strongly increases in cycle 2 and 3. The O_2 mass signal in the first scan shows significant trailing and is also higher than in scan 2 and 3. Comparison of results from scan 1 and scan 2 suggests that the emergence of CER activity is coupled to a decrease in OER activity. This appears to contradict the previous results from the RRDE method that the OER and CER are independent. However, we want to note that the amount of chlorine produced in cycle 2 and 3 was rather high, which was necessary to obtain a sizeable m/z 70 signal, as the majority of produced Cl_2 dissociates and recombines in the ionization chamber to form HCl^+, mass signal m/z 36.[77] It is thus highly likely that the collection efficiency of O_2 was affected by the vigorous chlorine evolution near the electrode surface. Nonetheless, we believe the most important result of the OLEMS measurements is the strong suppression of chlorine evolution in the first cycle, meaning that on an IrO_x/MnO_x electrode, O_2 is formed highly selectively.

In Figure 6.7C, current vs. time curves were recorded at 1.50 V to investigate the effect of transient MnO_x deposition, along with changes in O_2 and Cl_2 mass signals (Figure 6.7D). In

the current profile, the semi-steady current declines abruptly after ~100 s, converging to a current of around 200 μA. The abrupt decline is reminiscent of results in Figure 6.6, and correlates with a selective decrease in the Cl_2 signal.

6.3.2. *Structure of the MnO_x/IrO_x film*

The results in the previous sections show that during mixed OER and CER on an IrO_x electrode covered by a MnO_x film, there is a decrease in oxidation current coupled to strongly enhanced selectivity of OER over CER with an increase of the coverage by the MnO_x film, as well as a change in the apparent CER Tafel slope. Besides the origin of this selectivity shift, a relevant question concerns the degree to which MnO_x is catalytically active under these conditions. OLEMS measurements on a MnO_x/GC sample in an acidic solution, without IrO_x present, showed no detectable activity for OER or CER (Figure A 9.6.11), in accordance with previous literature. However, it has been reported that the crystal phase and oxide stoichiometry of MnO_x as well as the existence of metal-support interactions, can greatly affect the OER performance.[258–261] Therefore, the structure of the deposited materials was studied.
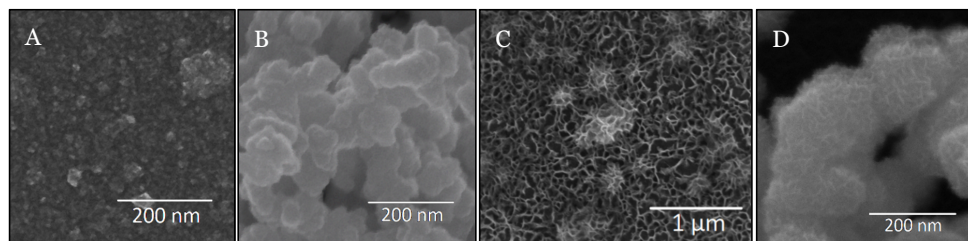
Figure 6.8: SEM micrographs of representative electrodes used in this study. A and B: an IrO_x/GC electrode, deposited according to the procedure described by Nakagawa et al. C and D: a $MnO_x/IrO_x/GC$ electrode, MnO_x was deposited onto IrO_x/GC as described in the text.

For structural studies, films were grown hydrodynamically in ClO_4^- solutions in presence of 20 mM Cl^-, allowing use of the ring electrode to monitor the rate of chlorine evolution during deposition. An amount of MnO_x was deposited such that the CER rate was approximately 50% of the initial value (Figure A 9.6.9). The nature of the MnO_x films in the following studies should therefore be close to films corresponding to the critical MnO_x charge of 2 mC discussed earlier. MnO_x films grown in ClO_4^- and HSO_4^- electrolytes showed identical morphologies in SEM and likewise behavior of ε_{CER} vs. Q_{MnO_x}, suggesting that adsorption of HSO_4^- inhibits MnO_x deposition but does not alter its mechanism (Figure A 9.6.10).

Figure 6.8A shows a SEM micrograph of a representative IrO_x/GC film, with a morphology corresponding well to previous reports.[142,143,262,263] The GC surface is covered by a thin layer of nanoparticulate IrO_x, as was revealed by drying-induced cracks of the film (see Figure A 9.6.15B). We also occasionally observed mesoporous clusters of IrO_x particles with diameters of 50-150 nm (Figure 6.8B). The clusters generally occupied less than 4% of the GC electrode surface area, as estimated from SEM images of a large section of the electrode. Figure 6.8C and D show SEM micrographs of $MnO_x/IrO_x/GC$ samples, the films grown in the presence of 20 mM Cl^- and representing '50% CER activity' compared to MnO_x-free conditions. A porous structure of thin intertwined sheets is visible on top of the IrO_x particles and layer, which is

composed of MnO_x, as verified via EDS analysis. From the SEM micrographs, the MnO_x sheet thickness is within 8-10 nm (Figure A 9.6.15A). MnO_x deposited on GC in absence of IrO_x forms a similar structure (Figure A 9.6.15C). The MnO_x morphologies resemble earlier SEM results of δ-MnO_2 (Birnessite), a poorly crystalline polymorph of MnO_6 octahedra arranged as sheets (see also Figure A 9.6.15D for a micrograph of MnO_x formed during extended deposition times).[164,264–266] However, we cannot draw conclusions about the MnO_x structure on the basis of SEM morphology alone.

We attempted to take XRD spectra of IrO_x and the combined Mn/Ir oxide, using samples as-deposited on GC (see Figure A 9.6.14). Besides the GC background, no diffraction peaks were observed, suggesting that the IrO_x and MnO_x are amorphous. Previous studies of hydrated IrO_x colloids, as well as MnO_x deposited at constant potential, also reported amorphous structures.[248,258,263,267] It must be noted that the films may be too thin to lead to sufficient signal in the diffractometer, although an attempt was made to compare the diffraction patterns to a small quantity of highly crystalline RuO_2. Alternatively, IrO_x nanoparticles were precipitated and isolated from acidified colloid solutions. Even when scanning such bulk samples, we could not observe XRD peaks.
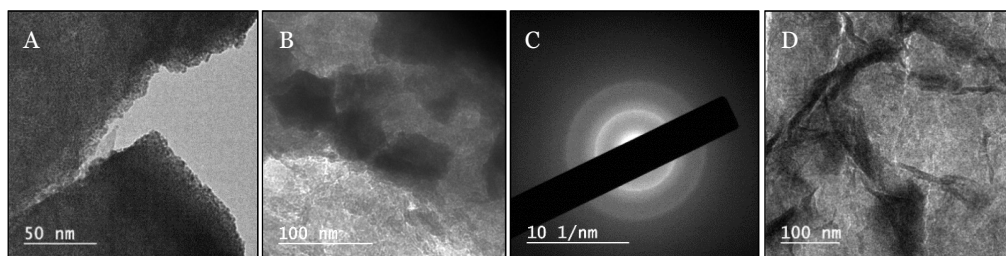
Figure 6.9: TEM micrographs of a MnO_x/IrO_x film that was grown identically to the films used for SEM in Figure 6.8, then carefully scraped off the GC support for imaging. A: Sheets of amorphous IrO_x particles, having diameters in the range of 2-4 nm. B: Larger IrO_x particles (diameter ~60 nm) within the film. C: SAED pattern of the area shown in B. Diffuse diffraction rings corresponding to rutile IrO_2 are visible. The also present MnO_x does not generate a clear contribution to the pattern. D: Intertwined MnO_x sheets perpendicular to the beam direction, as also seen in SEM micrographs.

To obtain more structural information on the MnO_x/IrO_x samples, TEM measurements were performed along with EDS and selected-area electron diffraction (SAED). Figure 6.9 shows bright-field TEM micrographs of a MnO_x/IrO_x film that was carefully scraped off the GC electrode. IrO_x nanoparticles with a diameter of 2-4 nm as well as occasionally larger particles were visible (Figure 6.9A and B), similar to results from Zhao *et al.*[262] Like the SEM results, a veiny MnO_x deposit could be seen (verified by EDS), where the ~8 nm thick sheets were visible in the microscope (Figure 6.9D). Despite the much higher diffraction cross-section in comparison with XRD, most SAED experiments led to diffuse patterns. It was possible to sporadically obtain better defined radial profiles, roughly corresponding to rutile-IrO_2 (Figure 6.9C).[268,269] In the microscope, a rare instance of a crystallite that was also properly oriented showed a d-spacing of 3.18 Å, corresponding to the rutile IrO_2 (110) plane.[270] We also generated SAED patterns at higher beam accelerating voltages of 200 keV (Figure A 9.6.18), the result of which showed sporadic rutile-related diffractions from IrO_2 and β-MnO_2.

Unfortunately, significant contributions from metallic Ir (and possibly Mn) were also present, likely due to beam radiation damage.[170]
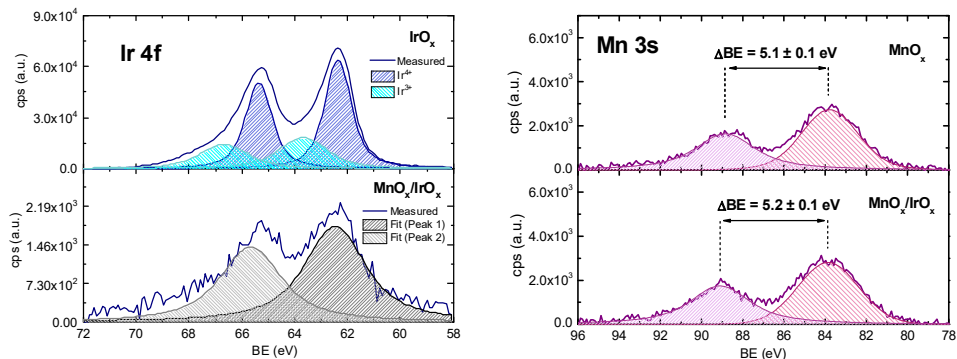
Figure 6.10: Core-level XPS scans of the Ir 4f (left) and Mn 3s (right) spectral peaks, on an absolute intensity scale. Both elements were scanned in samples of their MO_x/GC single oxides (top panels) and the mixed $MnO_x/IrO_x/GC$ sample (lower panels). Note the difference in scale in the lower left-hand panel, illustrating the relatively low intensity of the Ir 4f signal.

To probe the electronic structure and the extent of interaction between the two oxides, we performed *ex situ* XPS on a representative $MnO_x/IrO_x/GC$ film, as well as on single oxide reference samples termed MnO_x/GC and IrO_x/GC. Core-level Ir 4f scans were performed, as this peak is considered a reliable probe for determining the average Ir oxidation state.[250,270,271] The magnitude of the Mn 3s peak multiplet splitting serves a similar function in Mn.[272,273] Additional narrow spectra of the O 1s and Cl 2p peaks are shown in the supporting information (Figure A 9.6.20 and Figure A 9.6.21). In Figure 6.10, the IrO_x/GC sample has a $4f_{7/2}$ core-level binding energy of 62.4 eV, with a pronounced asymmetry indicating contributions of multiple oxidation states. The obtained binding energy is close to values reported for hydrous iridium oxides lacking long-range order.[270,274] IrO_x/GC has mainly Ir^{4+} centers but a significant contribution of Ir^{3+} is apparent, with an estimated Ir^{3+}: Ir^{4+} ratio of 0.27. The MnO_x/GC sample shows a Mn 3s peak splitting of 5.1 eV, corresponding to an average oxidation state in-between 3+ and 4+. The non-integral average oxidation states of IrO_x and MnO_x suggest non-stoichiometric oxides and disordered structures, consistent with the diffraction experiments. In the $MnO_x/IrO_x/GC$ sample, Mn peaks dominate the spectral features (Figure A 9.6.19). Most of the signal originates from the MnO_x overlayer, as was also verified from appearance of a large O 1s contribution at 529.9 eV, and by comparing Mn:Ir ratios determined from XPS and amperometry deposition data (Table A 9.6.2). It was nonetheless still possible to observe the Ir 4f peak, with a peak fitting-derived binding energy of approximately 62.5 eV (see Figure 6.10), a shift of +0.1 eV relative to IrO_x/GC. The signal intensity was too weak for a more elaborate peak deconvolution. A relevant question is whether the Ir sites contributing to the weak Ir 4f peak are covered by MnO_x, which was suggested by the SEM measurements. The reductive charge Q_{MnO_x} of grown MnO_x films corresponds to a layer roughly 10 nm thick, approaching the limit for the detection depth of XPS. The weak Ir 4f peak in the sample shows strong prevalence of inelastic scattering in the form of tailing at higher binding energies, and a rise in background scattering that is disproportionately higher than the IrO_x/GC reference

(Figure A 9.6.22). It can therefore be assumed that the weak XPS Ir 4f peaks originate from sub-surface Ir, and that this Ir must be in intimate contact with the MnO_x layer. The Mn 3s peak splitting in $MnO_x/IrO_x/GC$ is 5.2 eV, a difference of +0.1 eV with respect to the MnO_x/GC reference sample. This shift may indicate a lowering of the average oxidation state,[272] but the shift is small and negligible within the margins of experimental error (± 0.1 eV).

Summarizing our structural studies, we find that the formed MnO_x and IrO_x are amorphous and probably form non-stoichiometric oxides. The MnO_x catalyst without IrO_x showed no activity in OLEMS, and we could also see no evidence of a strong interaction between Mn and Ir from the almost identical Ir 4f binding energies and Mn 3s multiplet splitting in XPS. This makes it doubtful whether the proximity of and interaction with IrO_x could somehow activate MnO_x for the OER.

6.3.3. *Isotopically labelled OLEMS measurements and OER studies on an RDE*
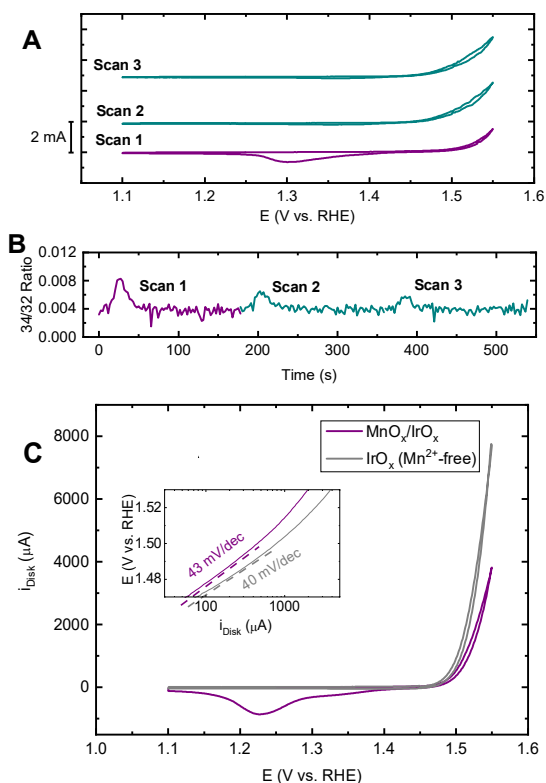
Figure 6.11: A and B: OLEMS measurements of an 'MnOx/Ir¹⁸Ox/GC' electrode in 0.5 M KHSO₄, 30 mM KCl, and 1.2 mM MnSO₄ (pH = 0.87). The isotopic labelling procedure is described in the text. The electrode was scanned three times (A), while monitoring the mass/charge ratio 34/32 (B). Scan rate: 5 mV s⁻¹. C: CVs of an IrOₓ/GC rotating disk electrode in 0.5 M Na/HClO₄ (pH = 0.85), in a Mn²⁺-free solution (grey) and in presence of 0.6 mM Mn(ClO₄)₂ with a preconditioned MnOₓ film before initiating the forward scan at 1.45 V (purple). Inset shows calculated Tafel slopes determined from forward-backward averaged disk currents. Scan rate: 10 mV s⁻¹, rotation rate 1500 RPM. All solutions saturated with Ar.

Given the lack of electronic interaction between MnO_x and IrO_x suggested by the detailed characterization described in the previous section, isotopically labelled OLEMS measurements were undertaken to further probe the origin of the OER/CER selectivity of the $MnO_x/IrO_x/GC$ electrode. We also looked more closely into the OER behavior of the selective catalyst using RDE experiments.

In Figure 6.11A and B, we performed isotopic labelling experiments on $MnO_x/IrO_x/GC$ in an attempt to determine the origin of the oxygen produced by the catalyst. This is made possible by the tendency of oxygen of the IrO_x lattice to participate in the OER mechanism.[100] First, the IrO_x lattice oxygen was partially exchanged with the ^{18}O isotope by performing OER in a 0.1 M $KHSO_4$ solution of 'marked water' ($H_2^{18}O$).[99,100] MnO_x was then grown in 'regular water' at 1.45 V (a potential just before the OER onset), and OLEMS measurements were performed on this $Mn^{16}O_x/Ir^{18}O_x/GC$ electrode. By observing changes in the ratio of mass/charge signals 34 and 32,[106] we were able to determine whether the oxygen formed originated from MnO_x (leading to $^{16}O_2$ and no enrichment in the m/z 34 signal), or $Ir^{18}O_x$ (partially producing ^{18}O-^{16}O and changing the 34/32 ratio). At this point, $^{18}O_2$ can also be formed. Unfortunately, the mass charge ratio of this species (m/z 36) coincides with that of HCl^+, a species formed in the ionization chamber, and as such this signal is ambiguous. As can be seen in Figure 6.11B, the catalyst shows an enrichment of ^{18}O during OER in the first scan. The produced oxygen thus at least partially originates from the subsurface IrO_x layer. The OLEMS experiments were conducted in presence of chloride, which allowed the monitoring and comparison of MnO_x film growth, as well as ensuring that the experimental conditions were as close as possible to previous OLEMS experiments. In scans 2 and 3, a current increase can be seen which is attributable to increased chlorine evolution after MnO_x reductive dissolution, in agreement with results from Figure 6.7. Figure 6.11C shows OER measurements in a Cl^--free solution of an IrO_x/GC catalyst with a pre-grown MnO_x film, compared to the same catalyst in a Mn^{2+}-free solution. A non-adsorbing ClO_4^- solution was chosen over HSO_4^- in this experiment since it led to higher OER rates and faster MnO_x growth. The two curves arguably have almost identical onset potentials and very similar Tafel slopes (40 vs. 43 mV/dec for IrO_x and MnO_x/IrO_x, respectively). Both experiments shown in Figure 6.11 give strong evidence for the conclusion that the MnO_x film itself is inactive for OER, and the OER activity stems from the IrO_x underneath the MnO_x film.

6.3.4. *General discussion on the origin of the OER/CER selectivity*

From the above results, we conclude that a MnO_x film facilitates the selective formation of O_2 over Cl_2, in agreement with previous literature.[25,31] However, contrary to what was previously assumed (at least implicitly), the results show that MnO_x is not actually a catalytically active phase. This conclusion is in fact in agreement with previous literature as MnO_x is generally not very active for OER in strongly acidic media (pH < 1), and certainly cannot be expected to show significant activity within the potential window employed in this work.[235,240,245,275,276] From the OLEMS results, it is clear that MnO_x/GC in absence of IrO_x is not active for either CER or OER in pH ~ 0.9, even at high potentials of 1.8 V (Figure A 9.6.11). Combined with the XPS measurements that indicate very little electronic interaction between MnO_x and IrO_x, it is

therefore highly unlikely that MnO_x 'takes over' OER and CER catalysis from IrO_x when it is deposited. Another feature that strongly disfavors MnO_x being the active catalyst is the OER ability seen in Figure 6.11C. The $MnO_x/IrO_x/GC$ electrode displayed an OER current of nearly 5 mA * cm^{-2} (electrode area 0.196 cm^2) at an overpotential of 300 mV, which is at least three orders of magnitude higher than even the most optimal performing MnO_x catalysts in alkaline media.[258] The OER current also has a Tafel slope of ~43 mV/dec, which is very close to 40 mV/dec, the OER Tafel slope of the unmodified IrO_x catalyst. We note that a Tafel slope of less than 60 mV/dec has never been reported for OER on MnO_x in any pH. Finally, OLEMS experiments with isotopically labeled IrO_x (Figure 6.11A and B, first scan) show that the IrO_x partakes in OER, despite the existence of a MnO_x layer.

Instead of MnO_x being an exceptional catalyst that breaks the apparent scaling between the CER and OER, we suggest that the catalytically inert MnO_x functions as a porous overlayer that disfavors the transport of chloride ions, as was previously proposed by Bennet.[25] Previous literature suggests that MnO_x deposited at a constant anodic potential usually forms γ-MnO_2 (Nsutite) or δ-MnO_2 (Birnessite) motifs, where formation of δ-MnO_2 seems preferred over γ-MnO_2 in case the Mn^{2+} concentration is in the mM range.[164,265,266,277–279] The δ and γ polymorphs are both nanoporous and readily intercalate water and cations. From Cl 2p XPS measurements (Figure A 9.6.21), we detected the presence of an alkali-metal chloride in the IrO_x/GC electrode, which can be ascribed to NaCl trapped within the mesoporous IrO_x clusters. By contrast, MnO_x/GC displayed no Cl 2p features (despite being grown in a Cl^--containing solution), and neither did $MnO_x/IrO_x/GC$, which we interpret as chloride being unable to penetrate the MnO_x film. Furthermore, in the OLEMS results in Figure 6.7, the O_2 signal of scan 1 shows strong tailing, persisting for nearly 100 s after starting the experiment, which translates to O_2 detected down to 1.15 V in the backward scan. This effect is ascribed to O_2 trapped in the MnO_x porous structure, which is liberated upon MnO_x dissolution.
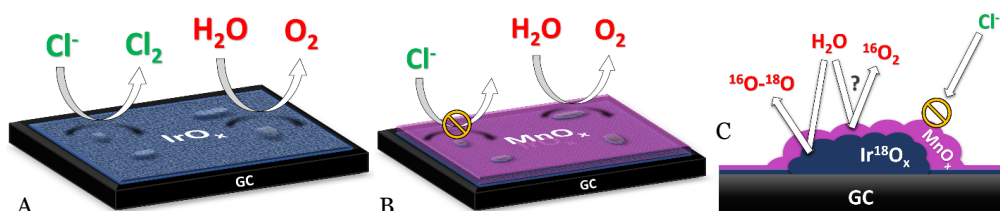
Scheme 6.1: Sketch of the IrO_x/GC catalyst (A) and the deposition structure of MnO_x deposition on $MnO_x/IrO_x/GC$ (B). The MnO_x forms a porous, amorphous network on top of the IrO_x layer, blocking CER by preventing Cl^- from reaching the IrO_x underneath. A side-view (C) shows the isotopic labelling experiment in Figure 6.11A and B. Participation of sub-surface IrO_x in OER is apparent from detection of the enriched m/z 34 signal.

Scheme 6.1 illustrates the origin of the observed selectivity behavior with MnO_x deposition. Starting from the 'bare' IrO_x film, initial MnO_x deposition ($0 < Q_{MnO_x} < 2$ mC) is accompanied by a mild and approximately proportional decrease in OER and CER activity (Figure 6.3 and Figure 6.4), implicating that at these low coverages, both reactions are hindered. The corresponding Tafel plots extracted from the rings currents (Figure 6.5 and Figure A 9.6.7) show that the CER slopes retain a value of ~40 mV/dec, but are shifted gradually upwards to higher potentials. A similar effect during the study of CER was reported before by Mozota and

Conway,[280] and would imply a decrease in the number of active sites with an unchanging reaction mechanism. From electron microscopy micrographs, the MnO_x forms a porous network of amorphous sheets. The dramatic selectivity shift at $Q_{MnO_x} > 2$ mC then presumably arises when the growing MnO_x sheets start to intertwine and fully cover the IrO_x electrode. MnO_x deposition at this stage seems to solely inhibit CER, whereas OER remains relatively unaffected, suggesting that at this point, the film growth is intrinsically different from its initial deposition stage. When 'fully grown', the amorphous MnO_x film still seems to allow transport of H_2O, H^+ and O_2 between IrO_x and the electrolyte. The decreased selectivity versus CER can thus be explained on the basis of concentration overpotentials, in line with recent reports on electrocatalysis at 'buried interfaces' by Takanabe et. al.[281] and Esposito *et al.* [282,283] The slow transport of chloride through the MnO_x phase means that near the buried IrO_x interface, both the chloride diffusion coefficient and concentration gradient are lowered. This leads to a significant increase of the diffusion layer thickness and an effective increase in the CER overpotential. We further verified the anion-deflecting behavior of MnO_x by performing OER using a $MnO_x/IrO_x/GC$ catalyst in presence of bromide ions (Figure A 9.6.12). The Pt ring was fixed at $E_R = 0.90$ V, to serve as a probe for bromine reduction. We found that the blocking of bromine evolution is strongly coupled to the presence of the MnO_x film. Lastly, the effect of MnO_x deposition on CER selectivity was verified using a Pt disk electrode as CER catalyst (Figure A 9.6.13). A MnO_x/Pt electrode evolved insignificant amounts of Cl_2, whereas the OER onset could be seen near 1.7 V, which is reminiscent of the previously reported OER onset on bare Pt.[284]

IrO_x was also present in the MnO_x-based seawater anodes by Hashimoto *et al.*, for which thick heterometal-doped MnO_x coatings were grown on Ti-supported IrO_x (IrO_x/Ti). The IrO_x was added with the intention of preventing the formation of insulating TiO_2 during electrode operation. We believe the OER selective $Mn_yM_{(1-y)}O_x/IrO_x/Ti$ anodes operate in a similar fashion as our $MnO_x/IrO_x/GC$ catalyst under study, and that the IrO_x layer may have been crucial for the relatively low polarization resistance during the galvanostatic experiments. The OER selectivity effect of different dopants may have been due to modified MnO_x film stability or morphology under the strongly oxidizing operating conditions.

Application of selective blockage of chloride in seawater electrolysis was recently demonstrated by Ravichandran *et al.*[165] An analogous case of selectivity induced by a catalytically inert film is likely at hand in the industrial chlorate process, where $Cr(OH)_3$-coated cathodes are used for selective hydrogen evolution.[34,141,285] The H_2-selectivity of the chromium film has been suggested to stem from the selective blocking of dissolved ClO^- anions and oxygen. Interestingly, MnO_x has been recently suggested as a promising alternative to the use of Cr(VI) for the selective hydrogen evolution.[286]

6.4. Conclusion

In this chapter, we have investigated the unusual OER over CER selectivity of MnO_x based anodes in the context of hydrogen production from acidic saline water electrolysis. Deposition of a thin MnO_x film onto glassy carbon-supported IrO_x moderately decreases the catalytic activity and strongly shifts the product selectivity from Cl_2 towards O_2, once a critical MnO_x

film charge Q_{MnO_x} of approximately 2 mC (10 mC cm^{-2}) is reached. The MnO$_x$ deposit is catalytically inactive, and instead seems to function as a diffusion barrier that prevents Cl$^-$ from reacting on the IrO$_x$ catalyst underneath, while still facilitating the transport of water, protons and O$_2$ between IrO$_x$ and the electrolyte, necessary for OER activity. The results of this work fit in an emerging trend of using diffusion barriers to affect selectivity. This may be a promising approach in practical brine electrolysis, in contrast to finding an OER catalyst that breaks the intrinsic scaling between selectivity and activity.

MODIFICATION OF SELECTIVITY BETWEEN CHLORINE AND OXYGEN EVOLUTION ON IRIDIUM-BASED ANODES AND Pt USING SiOₓ-BASED BURIED INTERFACES

7

In Chapter 6, it was found that a permselective effect versus chloride ions underlies the high OER selectivity of MnOx-based anodes, in effect forming a 'buried interface'. This approach would allow selective OER on an otherwise unselective catalyst, and thus seawater electrolysis without chlorine formation. Sadly, there is currently little research in this area, and more overlayer materials capable of preventing chlorine evolution are highly desired. In this chapter, we investigate the effect of thin (5-20 nm) overlayer films composed of amorphous silicon oxide (SiO_x), which is an electrochemically inert material resistant to acid. We found that the SiO_x overlayer can be an effective barrier against the CER on flat, relatively well-defined Pt surfaces. On SiO_x/IrO_x/GC electrodes, which are more closely related to Ir-based catalysts used in electrolyzers, the CER was not completely suppressed. The CER likely took place at defects in the film, caused by incompatibility of the spin-coating procedure used to produce the films. On the other hand, industrial-type Ir anodes based on Ti, to which significantly thicker films were applied, showed much better CER suppression, although this came at a cost of rather low activity. Although these initial results leave room for improvement, they can further the development of OER- selective anodes.

7.1. Introduction

In Chapter 6, we observed that an IrO_x electrocatalyst coated by electrodeposited manganese oxide (MnO_x) owes its unusually high OER selectivity in acidic chloride electrolytes to the permselective behavior of the MnO_x overlayer, which effectively shielded the catalytically active IrO_x from chloride ions. The results of this study are in-line with a recent review that suggests to steer the selectivity between competing reactions by applying a porous, electrochemically inert coating on the catalytic surface.[283] Such coatings can selectively impact the transport between the bulk and the underlying electrochemically active surface. When chosen properly, only the desired reactant can permeate the overlayer, such that a single reaction is promoted on an otherwise unselective catalyst. Besides selectivity, the coating may also improve catalyst stability by providing mechanical support and by shielding the active catalyst from harmful side-reactions, such as the specific attack by chloride on the noble-metal component of iridium-based double perovskites seen in Chapter 3. So-called membrane-coated electrocatalysts (MCEC) therefore hold great potential in solving selectivity problems, as they circumvent the apparent scaling between OER and CER activity. However, MCECs are still in a very early stage of development and have been little investigated. To realize a properly functioning overlayer, the thickness and stability have to be optimal. Ideally, the film is just thick enough to block the undesired reaction, with minimal negative impact on mass transport related to the desired reaction. At the same time, the film must be stable and durable so that its integrity is guaranteed for prolonged times of operation.

Although the MnO_x-based overlayer in Chapter 6 was effective at suppressing the CER, it is not expected to be stable for extended periods in acid.[240] Other recent work demonstrates that nanometer-thick silicon oxide (SiO_x) overlayers, which can be spin-coated onto planar Pt surfaces in a well-controlled way, can also form a buried interface.[282] The SiO_x/Pt surfaces were active for the evolution of gaseous hydrogen in presence of Cu^{2+}, which normally inhibits the reaction via under-potential deposition. In contrast to MnO_x, silicon oxides are expected to be thermodynamically stable in acid and at high potentials.[287] A SiO_x overlayer deposited onto known OER/CER catalysts could thus form a promising system for OER-selective seawater electrolysis in neutral or acidic media.

In this chapter, we explore the concept of a buried interface for enhancing selectivity towards the evolution of oxygen instead of chlorine in acidic chloride solutions, by depositing the previously described SiO_x overlayer on Pt, thin-layered amorphous iridium oxide (IrO_x), and IrO_2-based catalysts on a Ti support (termed Ti-based anodes) as model catalyst surfaces. Of these catalysts, Pt has shown significant capability for CER electrocatalysis, and as it has been studied repeatedly for SiO_x deposition, this system forms a convenient reference point.[282,283,288] IrO_x and Ti-based anodes are representative for actual anodic materials used in acidic and near-neutral water electrolysis.[152,171,289] Thin-layered IrO_x nanoparticles would be a relatively well-defined model system for Ir-based electrocatalysts and were included for this reason. Ti-based anodes were prepared by Magneto Special Anodes (an Evoqua brand) according to a procedure identical to that for large-scale, commercial anodes.[33] Results

obtained from the study of these materials could in principle be directly translated to industrial conditions.

7.2. Experimental

7.2.1. *Electrochemical procedures*

$KHSO_4$ and KCl (EMSURE) were purchased from Merck and used as received. The water used for all experiments was prepared by a Merck Millipore Milli-Q system (resistivity 18.2 MΩcm, TOC < 5 p.p.b.).

All experiments were carried out at room temperature (~20 °C). The electrochemical experiments were done using home-made two-compartment borosilicate glass cells with solution volumes of 100 mL. Before first-time use, all glassware was thoroughly cleaned by boiling in a 3:1 mixture of concentrated H_2SO_4 and HNO_3. When not in use, all glassware was stored in a 0.5 M H_2SO_4 solution containing 1 g/L $KMnO_4$. Before each experiment, glassware was thoroughly rinsed with water, and then submerged in a dilute (~0.01 M) solution of H_2SO_4 and H_2O_2 to remove all traces of $KMnO_4$ and MnO_2. The glassware was then rinsed three times with water and boiled in water. The rinsing-boiling procedure was repeated two more times.

An IviumStat potentiostat (Ivium Technologies) with the IviumSoft package was used during electrochemistry experiments. All experiments involving electrocatalytic chlorine and oxygen evolution were 95% iR-compensated. The solution resistance was measured with electrochemical impedance spectroscopy, by observing the absolute impedance in the high frequency domain (100-10 KHz) corresponding to a zero-degree phase angle. Working solutions of 0.5 M $KHSO_4$ were saturated with Ar (Linde, purity 6.0) before experiments. Solutions were bubbled with Ar gas during forced convection experiments, Ar was used to blanket the solution in case of stationary conditions. The reference electrode for all RRDE experiments was a HydroFlex® reversible hydrogen electrode (Gaskatel), separated from the main solution using a Luggin capillary, to fix the reference sensing point and to prevent mixed potentials at the reference due to dissolved Cl_2 gas. All potentials in this chapter are reported versus the RHE scale. The counter electrode was a Pt mesh, separated from the main solution by a coarse glass frit.

RRDE measurements were done with a MSR rotator and E6 ChangeDisk RRDE tips in a PEEK shroud (Pine Research). The Luggin tip connected to the reference electrode was aligned to the center of the RRDE electrode to minimize electrical cross-talk.[137,138] Before chlorine or oxygen collection experiments, the Pt ring was electropolished by scanning from -0.1 V to 1.7 V at 500 mV s^{-1} for 40 scans at 1500 RPM. The ring was kept at 0.95 V to selectively probe the CER in parallel with the OER, and at 0.40 V to probe the evolution of O_2 in chloride-free electrolytes. Ring currents were corrected for constant background currents and product collection delay. the latter arises from the time needed for products formed on the disk to reach the ring.[290]

7.2.2. *Electrode preparation*

7.2.2.1. *IrO$_x$/GC*

Commercial GC RDE disk inserts of 5 mm diameter were purchased from Pine Research. After hand-polishing the surface with diamond suspension and sonication in water, a thin IrO$_x$ layer was electroflocculated onto the GC surface from a hydrated IrO$_x$ colloid solution at acidic pH. Full details can be found in section 9.1.

7.2.2.2. *Pt/Ti/GC*

Commercial GC RDE disk inserts of 5 mm diameter were purchased from Pine Research. A 2 nm layer of Ti (99.99%) and 3 nm layer of Pt (99.99%) were sequentially deposited onto the GC surface at 0.2 A s^{-1} by electron-beam evaporation without breaking vacuum and without substrate heating in a Angstrom EvoVac evaporator system, with a base pressure of 1.0×10^{-7} Torr. A commercial Pt disk from Pine Research served as SiO$_x$-free reference material.

7.2.2.3. *Ti-based anodes*

Commercial Ti (grade 2) RDE disk inserts of 5 mm diameter were purchased from Pine Research. Two types of IrO$_2$-based catalysts, a mixture of IrO$_2$ and Ta$_2$O$_5$ and one of IrO$_2$ and Pt, were prepared on these electrodes by Magneto Special Anodes (an Evoqua brand), using a thermal decomposition method.

7.2.2.4. *SiO$_x$ deposition*

Trimethylsiloxy-terminated polydimethylsiloxane (PDMS) dissolved in toluene was spin-coated onto the fixated disk samples with an acceleration to a speed of 2400 rpm over 3 seconds, followed by a ramp to 4000 rpm over 30 seconds and maintained speed at 4000 rpm for 2 minutes following. The solvent was then evaporated by drying the electrodes in a vacuum oven at 90 °C for 60 min. To obtain SiO$_x$, the final PDMS coating was chemically oxidized in a UV-ozone cleansing chamber for 2 h (UVOCS, T10X10/OES). The eventual SiO$_x$ film thicknesses were varied by changing the concentration of PDMS in the toluene solutions, and repeating the spin-coating and drying procedure as necessary. For the SiO$_x$/Pt/Ti/GC samples with film thicknesses of 5 nm SiO$_x$, a single spin-coating step using a 5.3 mg/L solution of PDMS in toluene was chosen. Four SiO$_x$/IrO$_x$/GC samples were made with varied procedures to fabricate the SiO$_x$ overlayer. For sample 1, one drop of 10 mg/mL PDMS in toluene was used. For samples 2 and 3, two complete fabrication cycles were performed on each sample using one drop of 10 mg/mL PDMS in toluene for spin-coating, and for sample 4, two complete fabrication cycles were performed using two drops of 10 mg/mL PDMS in toluene. The targeted SiO$_x$ overlayer thicknesses for these three procedures were 5 nm, 10 nm, and 20 nm, respectively. For the Ti-based anodes, 3 complete fabrication cycles were performed using 50 mg/L PDMS in toluene for spin-coating. The targeted SiO$_x$ thickness on the Ti-based anodes was 10 nm. We note that the thickness of the overlayer may vary over the relatively rough surface of the Ir-based electrodes, especially regarding the industrial ones with Ti supports.

The thickness values for the Ir-based samples are provided as very rough estimates and not measured values.

7.2.3. *Voltammetry procedures during electrocatalysis*

All currents were reported as densities per geometrical surface area. Normalization to the 'real' catalyst surface area, which is an inherently difficult topic in electrocatalysis research (see section 3.3.2), was not pursued. In this chapter we were only interested in ratios of currents, namely selectivity values and comparisons of activity before and after applying a SiO_x overlayer. The electron beam-deposited Pt surfaces have a very low roughness (<1 nm), such that their active surface area is approximately equal to the geometrical one.[282]

7.2.3.1. Pt

All Pt electrodes were pre-treated before scanning by conditioning at 0.40 V and 0.70 V for 10 s and 3 s, respectively (see Figure A 9.7.1), while rotating. This was done to ensure that the surfaces were oxide-free and reproducible. Linear potential sweeps were performed immediately after on the Pt-based electrodes between 0.70 – 1.90 V, at 10, 20 and 50 mV s^{-1}, under varying rotation rates. In-between experiments, the electrodes were kept at 0.05 V.

7.2.3.2. *IrOx and Ti-based anodes*

Before initiating quantitative measurements, all Ir-based electrodes were scanned 20 times in a chloride-free electrolyte between 1.3 – 1.55 V (into the OER region) at 1500 RPM. This was done to ensure stable behavior during experiments by equilibrating the Ir-centers (see below). Similar to Pt, a two-step potential-holding program preceded every catalytic cycle. The IrO_x surfaces were conditioned for 10 s and 3 s at 0 V and 1.3 V, respectively; for the $IrO_2 + Ta_2O_5$ catalyst, the procedure was 10 s and 5 s at 0 V and 1.3 V, and for $IrO_2 + Pt$, it was 10 s and 6 s at 0.05 V and 1.3 V (see also Figure A 9.7.1). After the pretreatment, all Ir-based catalysts were probed for OER and CER electrocatalysis between 1.3 – 1.55 V at 10 mV s^{-1} and 1500 RPM.

7.2.4. *Scanning electron microscopy (SEM) and energy-dispersive X-ray spectroscopy (EDS)*

RDE inserts were carefully removed from the RRDE tip after electrochemical experiments and glued to a SEM specimen mount using conductive silver paint. The silver paint was dried for 3 hours in air under reduced pressure. SEM micrographs were obtained using an Apreo S SEM setup (Thermo Scientific) equipped with a field emission electron source and EDS detector. Images were recorded in immersion mode using a through-the-lens detector, at a working distance of ~4.0 mm, with 10 kV beam acceleration voltage and a beam current of 0.4 pA. EDS measurements were performed at the same beam voltage and current.

7.3. Results and discussion

In the following, RRDE voltammetry will be used to probe the kinetics and selectivity of the OER and CER on a variety of SiO_x-modified catalysts. Use of an RRDE ensures well-defined mass transport conditions, which is important concerning accurate statements of selectivity

where one reaction is fast and strongly dependent on diffusion. The use of interchangeable electrodes may cause some damage to the SiO_x overlayer films, as will be described below. Nonetheless, the method was chosen as it offers the highly attractive option to separate the OER and CER current densities as described in Chapter 2. Capacitive scanning contributions to the disk current were minimized by using relatively slow scan rates, and averaging the values from forward and backward scans for Ir-related experiments. For the Pt experiments, a constant value was subtracted from the linear sweep voltammograms based on pseudo-capacitive charging seen around the onset of platinum oxide formation.

7.3.1. _Pt_

As described in the introduction, the SiO_x/Pt electrode is a convenient reference point for looking closely at parallel OER and CER and the effect of the SiO_x overlayer. It must be noted that pure Pt is not popular for actual electrolyzers, due to its high price and rather poor OER performance.[83] At high potentials the catalytic activity is also impacted by the formation of platinum oxides (PtO_x), which will be discussed below.
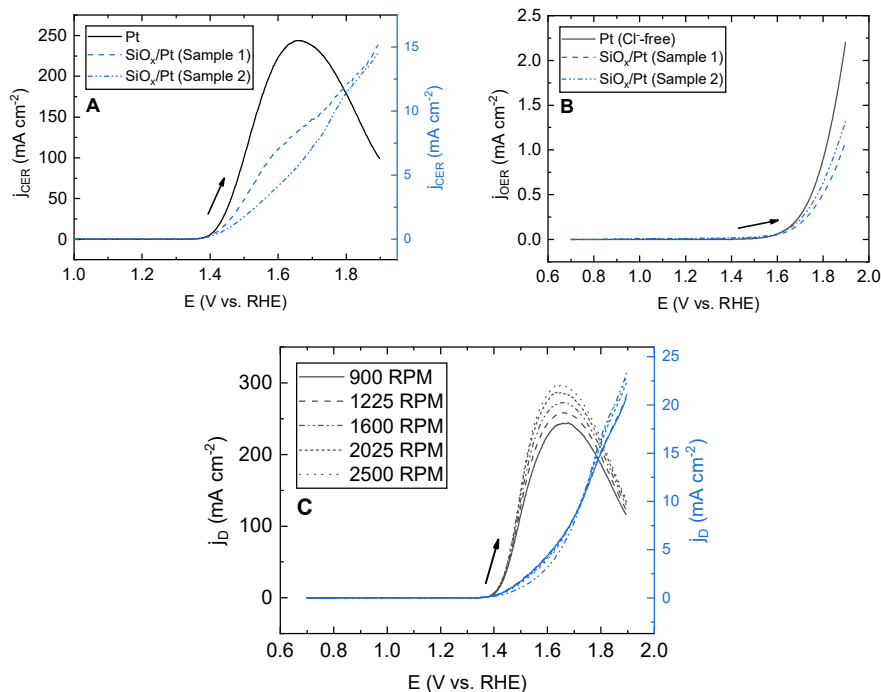
Figure 7.1: Effect of a SiO_x overlayer on the electrocatalytic behavior of Pt in acidic chloride-containing media. A: Current densities of the CER on a Pt disk electrode (black) and two SiO_x/Pt/Ti/GC electrodes with a 5 nm SiO_x overlayer (blue), in 0.5 M $KHSO_4$ + 0.6 M KCl. Note the difference in scale. j_{CER} was derived from ring currents as described in Eq. 2.3. Rotation rate 1600 RPM, LSVs recorded at 10 mV s^{-1}. B: 'Pure' OER activity on Pt (black) and on the SiO_x-coated Pt samples (blue), in in 0.5 M $KHSO_4$ (chloride-free conditions). C: Measured disk current density versus rotation rate on Pt (black) compared to a 5 nm SiO_x/Pt/GC electrode (blue), in 0.6 M chloride, recorded at 20 mV s^{-1}. Arrows indicate scan direction.

Figure 7.1 shows some typical results of parallel OER and CER on Pt surfaces both 'free' and covered by a SiO_x overlayer. The CER activity data were measured in presence of 0.6 M KCl, which corresponds to the average chloride concentration of natural seawater.[291] On an unmodified Pt electrode (black trace in Figure 7.1A), chlorine evolution has a clear onset around 1.37 V, after which the rate goes through a maximum and declines. The latter can be ascribed to inhibiting effects from PtO_x formation at high potentials.[292] It has been previously reported that PtO_x already interferes with the CER around its onset.[58,118,293] The peak CER current seen in Figure 7.1A is around 16% of the value predicted by the Levich equation, meaning that the maximum is significantly lower than would be expected from diffusion-limitations. In presence of a SiO_x overlayer (blue traces), the CER activity is strongly inhibited and decreases roughly 20-fold. The OER activity (measured in absence of chloride) in Figure 7.1B is only moderately impacted by the overlayer. It was verified that the OER still occurs on the SiO_x-encapsulated catalyst by using the RRDE with the Pt ring fixed at 0.4 V in chloride-free conditions, showing that O_2 can traverse the overlayer to be detected on the ring (Figure A 9.7.4). The rotation rate dependence of the disk current density is shown in Figure 7.1C. Contrary to bare Pt, there is very little dependence of disk current on the chloride mass transport to the SiO_x/Pt surface, suggesting that the observed potential-current response (which is largely from chlorine evolution) is dominated by chloride transport through the SiO_x overlayer.

It is noted that the CER rates on SiO_x/Pt/Ti/GC in Figure 7.1A no longer show a maximum, which suggests that the overlayer changes how PtO_x forms during the scan. The voltammetric characterizations in Figure A 9.7.2 illustrate that in presence of the SiO_x overlayer, the onset of PtO_x formation is shifted to a higher potential, but more oxide appears to be formed relative to the SiO_x-free sample, after normalizing the oxide reduction peaks to the electrochemical surface area using the hydrogen desorption region (Figure A 9.7.3). SEM micrographs (Figure A 9.7.15) suggest that the electrode surface is homogeneously covered by SiO_x. Neither Si associated with the SiO_x overlayer or Pt and Ti from the electrode and adhesion layer could be identified in EDS analysis due to the limited interaction between the electron beam and these ultrathin layers.

Even though the suppressive effect of SiO_x on the CER is large, it is not quite as large as measured during a similar study by us using stationary, ideally flat electrodes, where the residual CER activity was close to 0.[294] The samples used in that study had a much larger surface area compared to the RDE disk inserts, which means the fluid dynamics during spin-coating on the disk inserts were non-ideal near the edges. The CER activity in Figure 7.1 may originate from such imperfections since we could not find widespread defects in the overlayer

while surveying the surfaces with SEM. Additionally, the disk extremities are unavoidably exposed to force when the disk electrode is inserted into the RRDE assembly. The absence of rotation rate dependence in Figure 7.1C suggests that chloride diffusion relating to the CER activity is still somehow hindered.

The variation of the OER and CER activity as function of the chloride concentration on a SiO_x/Pt/Ti/GC sample is shown in Figure 7.2. We found that the CER rate on the bare Pt surface (Figure A 9.7.11) displays an approximately linear response to the concentration,

indicating that the chloride reaction order is close to 1, which was found in Chapter 4 as well. In Figure 7.2 however, the SiO_x-treated samples have different, more complex concentration dependencies. The top panel of Figure 7.2 shows that the OER activity at the buried interface is slightly suppressed by the addition of chloride, but otherwise not strongly dependent on the chloride concentration.

On bare Pt, the derivation of OER currents in parallel with the CER was unfortunately not possible, due to the high rates of chlorine evolution on such surfaces. These high rates led to macroscopic gas bubbles that lodged at the interspace between the disk and the ring and led to severe distortion of the ring response (see also Chapter 8). The CER currents on the $SiO_x/Pt/Ti/GC$ electrodes were much lower, so that it was still possible to use the ring-disk approach in highly concentrated chloride solutions, although the ring response was still slightly erratic; the apparent value of N_{Cl_2} varied somewhat (±10%) depending on the sample. This is possibly a result of hindered transport of Cl_2 across the SiO_x film, and leads to the
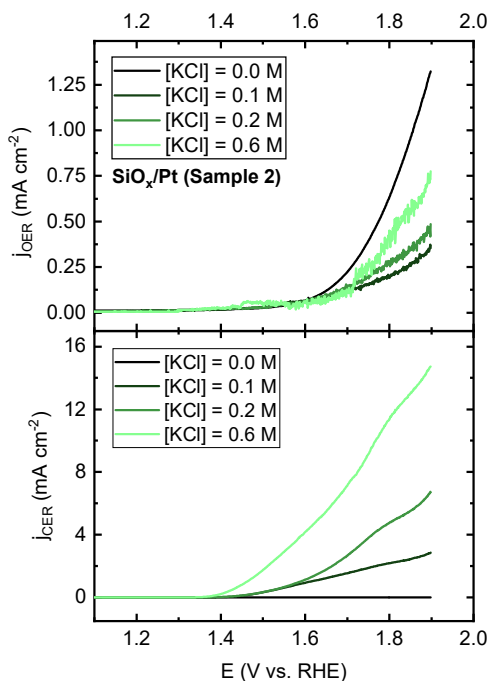
Figure 7.2: Current densities for the OER (top) and CER (bottom) as function of chloride concentration, on a $SiO_x/Pt/Ti/GC$ electrode, in 0.5 M $KHSO_4$. Rotation rate 1600 RPM, LSVs recorded at 10 mV s⁻¹.

somewhat erratic behavior of derived OER currents seen in the top panel of Figure 7.2. To minimize this source of error, N_{Cl_2} was calibrated for each experiment by comparing the disk current to the ring response while evolving chlorine in the potential region 1.50 – 1.55 V, where the CER is the sole measurable reaction.

Regarding the selectivity between the OER and CER, the precise effect of the SiO_x overlayer on Pt is not straightforward to summarize, since multiple effects are involved. On the one hand, the overlayer strongly inhibits the CER. On the other hand, it also seems to delay PtO_x formation, which can favor it. The SiO_x overlayer also leads to some inhibition of the OER activity when comparing with the free Pt surface (Figure 7.1B), which further increases ε_{CER}. Full selectivity data is shown in Figure A 9.7.5. These data, as well as the rest of the selectivity data in this chapter, were derived using Eq. 2.3. One can observe that the free Pt surface shows a significant enhancement of the OER selectivity at high potentials, due to the strong suppression of the CER by oxides. Nonetheless, the most important finding is that the SiO_x overlayer on Pt greatly impairs the CER, while still allowing the OER to occur.

7.3.2. IrO_x

SiO_x was deposited onto IrO_x and it was tested whether the CER could be selectively suppressed. The targeted SiO_x thickness was 5-20 nm, generally higher than that used for the Pt samples, as even though the IrO_x layer can be made reasonably flat, we previously found (Chapter 6 and Figure A 9.7.18) that it still has roughness features in the order of 10-100 nm. Four SiO_x/IrO_x samples were investigated, together with a SiO_x-free sample for comparison.
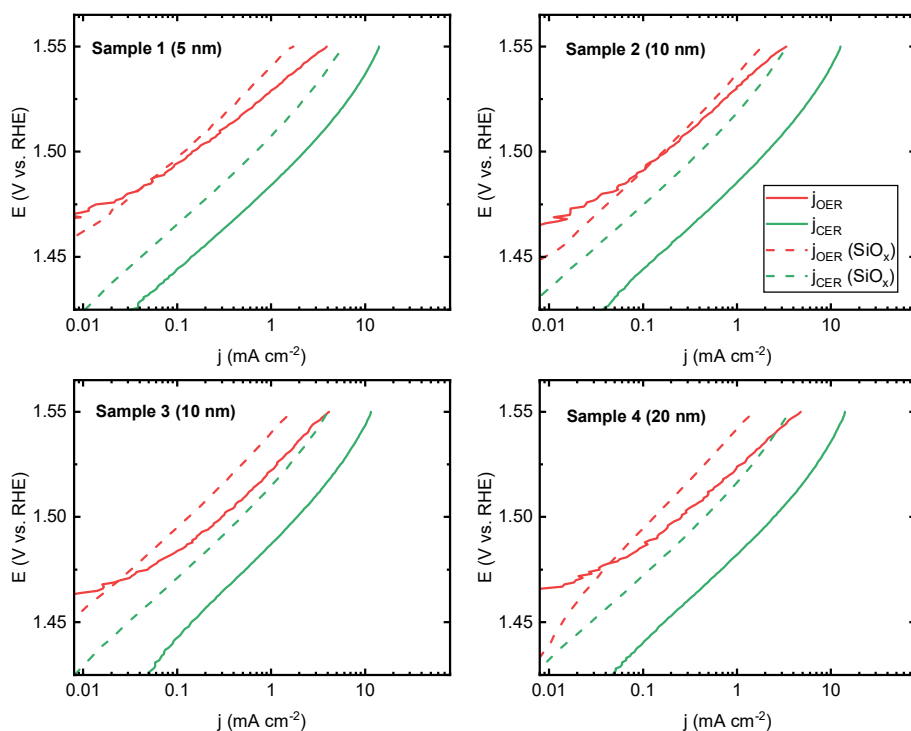
Figure 7.3: Tafel plots for parallel OER and CER on SiO_x/IrO_x samples of varying SiO_x overlayer thicknesses, before and after SiO_x deposition, in 0.5 M $KHSO_4$ + 30 mM KCl. Rotation rate 1500 RPM.

Figure 7.3 shows a comparison of Tafel curves of the OER and CER, derived using Eq. 2.3, in a chloride concentration of 30 mM as test case for comparing the sample activities before and after SiO_x deposition. The first trace of evolved oxygen appeared between 1.45-1.46 V on these samples, regardless of whether SiO_x was present (Figure A 9.7.7). In the presence of a spin-coated SiO_x layer, the electrocatalytic activity of the IrO_x samples moderately decreases. The Tafel lines of the OER and CER were both shifted to higher potentials. This lowering of activity is usually more severe for the CER, but all IrO_x samples still showed considerable CER activity after the SiO_x coating. This is contrary to the results for Pt described in section 7.3.1, where the SiO_x overlayer on Pt decreased the CER activity to less than a few % relative to the uncoated Pt reference sample. This means that either the IrO_x is incompletely covered by the films, or that the films are somehow not as effective with IrO_x as the underlayer, in the sense that they could still be permeable to chloride.
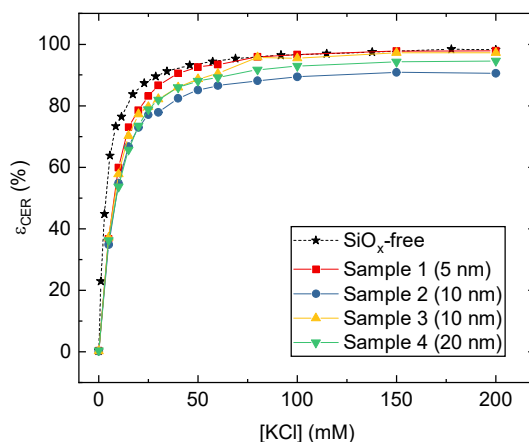
Figure 7.4: Molar selectivity towards the CER as function of chloride concentration for several $SiO_x/IrO_x/GC$ samples. Values of ε_{CER} calculated according to Eq. 2.3. Rotation rate 1500 RPM.

The CER selectivity (ε_{CER}) of the $SiO_x/IrO_x/GC$ electrodes was measured as a function of chloride concentration, where the upper limit of 200 mM KCl is reasonably close to the actual chloride concentration in seawater (Figure 7.4). Although the samples all show some reduction in CER selectivity compared to the SiO_x-free reference sample, there is no clear correlation between the selectivity and the formal SiO_x thickness.

In order to look more closely into the effect of the SiO_x overlayer, we focused on the kinetics of both reactions, particularly by looking at experimental Tafel slopes and chloride reaction orders $\mathcal{R}_{Cl^-}$ (Figure A 9.7.12 and Figure A 9.7.14). Although caution is advised when trying to directly interpret either of these quantities in relation to the 'true' underlying reaction mechanism, it is expected that they change significantly when the SiO_x overlayer exerts an influence, especially so for the CER. If mass transport is the limiting step, values of $\mathcal{R}_{Cl^-}$ for the CER should be 1 and the Tafel slope should approach infinity. These values should be attained as the potential-dependent CER rate exceeds the rate of mass transport. When comparing $\mathcal{R}_{Cl^-}$ on the bare IrO_x/GC sample and $SiO_x/IrO_x/GC$ (section 2 of the supporting

information), there is no obvious change in the values as function of potential. It needs to be noted that CER Tafel curves on all SiO_x-coated samples have slightly higher slopes around the high potential limit of 1.54 V. They are 65-70 mV/dec, compared to ~55 mV/dec in the reference. This could suggest that the chloride mass transport is decreased by the overlayer, but only to a minor extent. As the OER activity is also slightly suppressed, an additional investigation was performed on the voltammetric characterizations of the samples before and after SiO_x deposition (Figure A 9.7.6). The presence of SiO_x seems to suppress the semi-reversible peak observed around 0.94 V, which is ascribed to a redox transition between Ir^{3+} and Ir^{4+}.[168,250,295] Suppression of the peak shows that the overlayer affects the redox states in the IrO_x film, and that the overall reaction kinetics could change because the catalytic behavior

of IrO_x intimately depends on the redox state of the Ir centres.[154,296,297] However, we found

(section 2 of the supporting information) that linear Tafel slopes of the OER in all samples ranged between 40-50 mV/dec, and that likewise, the OER activity was little affected by chloride (Figure A 9.7.13), irrespective of the presence of the SiO_x overlayer. Both observations indicate that the OER mechanism remains the same after applying the SiO_x coating. Therefore, the SiO_x likely does not affect the reactivity of the IrO_x underlayer. Additionally, the significant CER electrocatalysis that occurs on the SiO_x/IrO_x samples behaves kinetically the same as on the IrO_x reference. It is thus probable that the SiO_x overlayer is incomplete, or locally delaminates during gas evolution.

The surfaces of the samples were explored using SEM, coupled to EDS analysis; Figure A 9.7.16 shows a typical EDS spectrum. Besides Si, Ir and O, large amounts of C were consistently detected due to the bulk GC electrode support. Cl was usually seen as well in low amounts, along with K and S, which correspond to traces of trapped electrolyte. Part of the Cl fraction is likely bound to Ir as a result of incomplete hydrolysis of the chloroiridate precursor (see Chapter 6).

An example micrograph of a $SiO_x/IrO_x/GC$ surface is shown in Figure 7.5, together with corresponding elemental maps of Si and Ir (see section 3 of the supporting information for additional micrographs). In Figure 7.5, the SiO_x-encapsulated IrO_x is visible as a relatively flat layer with fluffy morphology. EDS analysis shows that the SiO_x overlayer is present across the entire image. Dark grey areas and Si EDS mapping in Figure 7.5 suggest that the overlayer is not evenly distributed over the surface. Multiple SiO_x layers are visible that appear folded onto themselves. Si was found globally across the electrode surface, including areas where the IrO_x layer was interrupted or where local clusters of IrO_x nanoparticles were formed (Figure A 9.7.20 and Figure A 9.7.21). Zoomed-in micrographs in Figure A 9.7.18 illustrate the morphology of these clusters. Rugged surface structures are difficult to cover properly via spin coating, so that the SiO_x layer around these clusters could be defective on the nano-scale. It is not possible to register such imperfections with EDS, which is inherently limited to resolutions of around a micrometer. Nonetheless, no indications were found that large areas of the electrode were completely uncovered by SiO_x. The previously discussed CER activity then probably originates from a select few areas where the electrocatalytic activity is high and the Si overlayer is imperfect, or damaged by local instances of vigorous gas evolution at the buried interface (see Figure A 9.7.22 and Figure A 9.7.23). These results suggest that the adhesion of
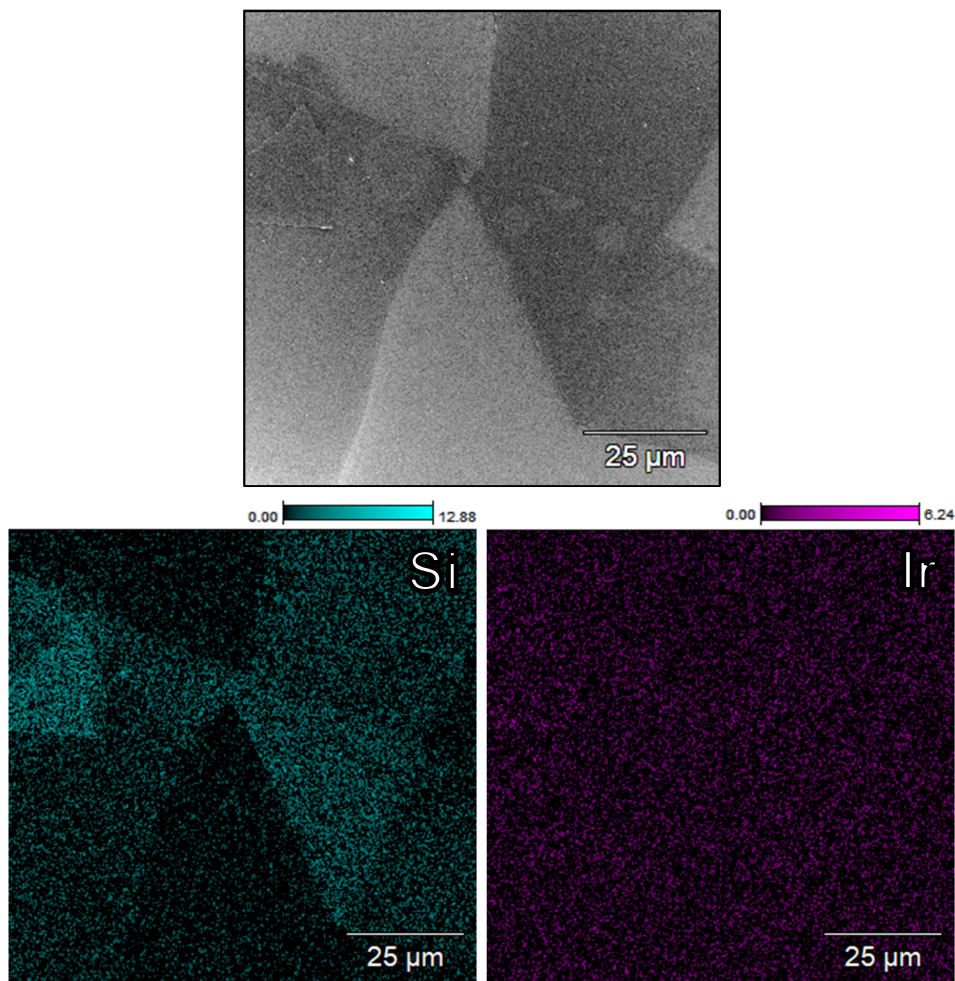
Figure 7.5: SEM micrograph and EDS analysis of a SiOₓ/IrOₓ/GC electrode surface, after extensive OER + CER electrocatalysis under forced convection conditions. In the electron image (greyscale), folded sheets of SiOₓ are visible on top of the IrOₓ layer. Color images show corresponding elemental mapping of Si and Ir. Scale bars show the amounts of the elements, as atomic percentage of total (which included O and C from the GC substrate, see Figure A 9.7.17).

a desired overlayer may differ substantially, depending on the underlayer, and that care must be taken when translating a functional overlayer design to a different catalyst.

7.3.3. *Ti-based anodes*

The Ti-based anodes are thick layers of metal oxides deposited on Ti disks, with the same method used for large surface area industrial anodes that are sold commercially by Magneto Special Anodes (an Evoqua brand). We tested a sample consisting of a Ti substrate coated by a mixture of IrO_2 and Ta_2O_5 (termed IrTa/Ti), as well as two samples of an IrO_2 anode containing Pt (termed IrPt/Ti). The samples were probed for OER and CER activity before and

after SiO_x deposition. As this type of electrode commonly has micrometer-sized roughnesses,[87,298,299] a large amount of SiO_x precursor was used during deposition to achieve an extra thick overlayer, so that the electrodes were properly encapsulated.
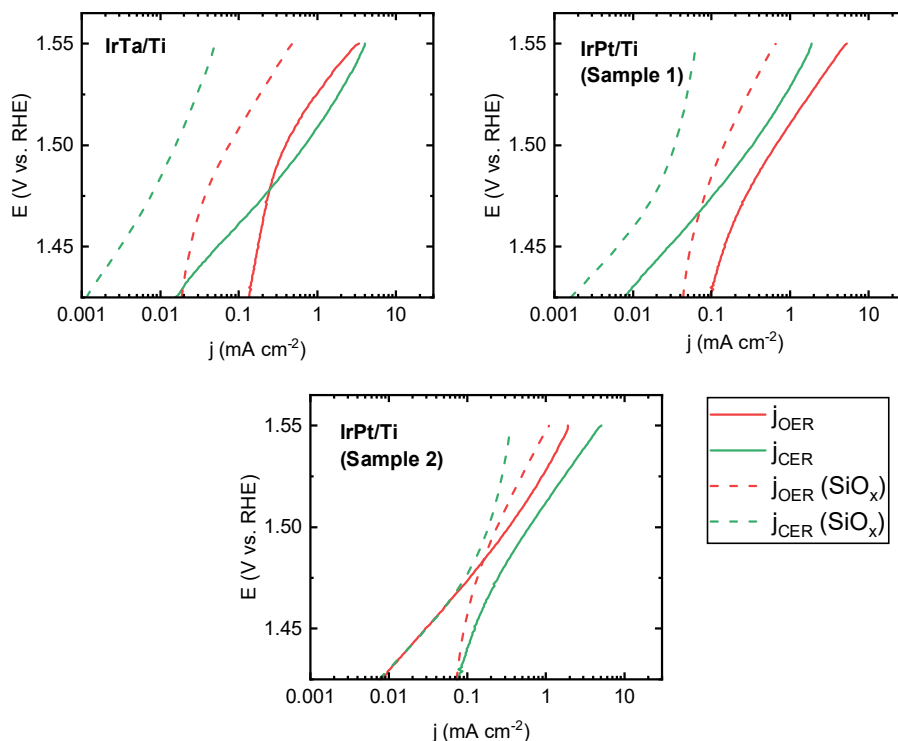
Figure 7.6: Tafel plots for parallel OER and CER on Ti-based anodes, before and after SiO_x deposition, in 0.5 M $KHSO_4$ + 30 mM KCl. Rotation rate 1600 RPM.

Like Figure 7.3, Figure 7.6 shows Tafel curves of the Ti-based anode samples in 30 mM KCl, before and after depositing SiO_x. In these results, there is a significant reduction in overall activity. This activity is roughly an order of magnitude, much more so than for IrO_x. This is most likely caused by the relatively thick overlayer, which may quickly stifle mass transport as its thickness increases.[283] Evidence for this is visible in the voltammetric characterizations of the samples, which show less features after the coating (Figure A 9.7.8). Besides lower activity, there is also significant suppression of the CER in favor of the OER, which is a favorable finding. The effect is much stronger than seen on IrO_x in section 7.3.2. In addition to the thicker SiO_x overlayer, a difference in catalyst morphology may explain the apparently more pronounced selectivity shift on these electrodes, in the sense that the adhesion of the overlayer to the catalyst could become more favorable.
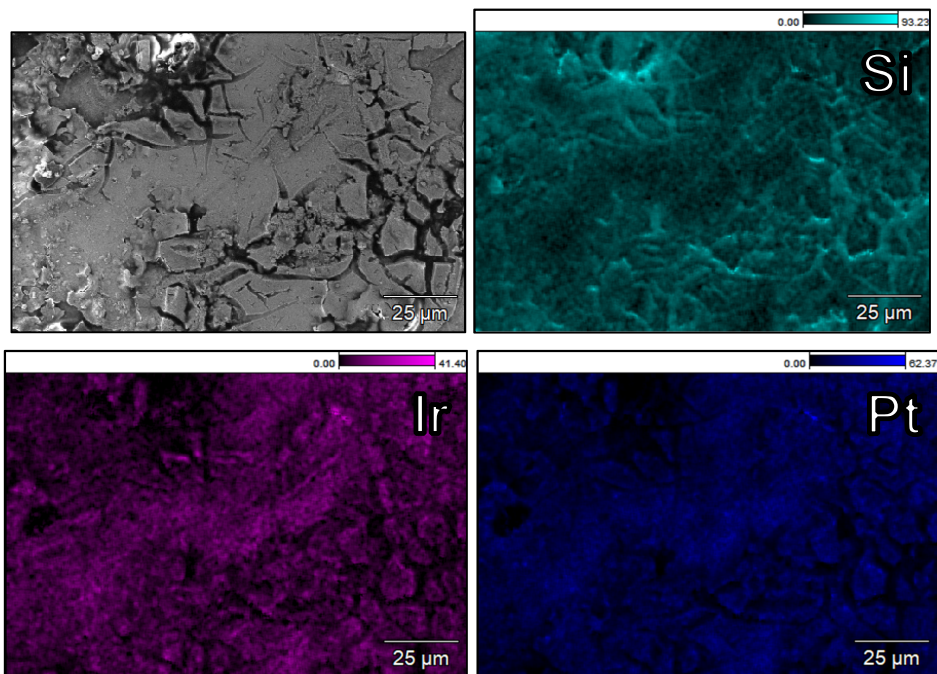
Figure 7.7: SEM micrograph and EDS mapping of an IrPt/Ti electrode surface, after extensive OER + CER experiments under rotation. The electron image is shown in grayscale, colored images show elemental mapping of Si, Ir and Pt. Scale bars show the relative amounts of the elements, as atomic percentage of total (which included Ti, data shown in Figure A 9.7.24).

SEM/EDS analysis of a IrPt sample in Figure 7.7 shows that Si has accumulated in the micrometer-sized cracks of the mixed metal oxides. This accumulation must have occurred
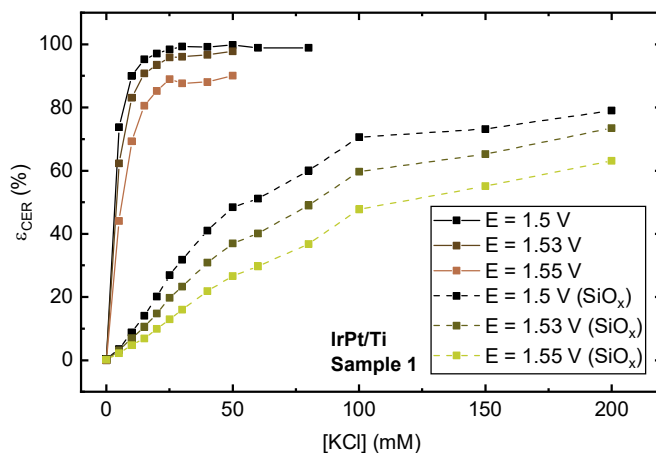
Figure 7.8: Molar selectivity towards the CER as function of chloride concentration for an IrPt/Ti sample, as in Figure 7.4. Values obtained on the original anode (solid, brown lines) are compared to those in presence of the SiO_x overlayer (beige, dotted lines). Rotation rate 1500 RPM.

during the spin-coating phase, where the PDMS solution infiltrated the catalyst cracks. As the distribution of Si around the cracks is not strongly coupled to carbon (see Figure A 9.7.24), it is probably present as the oxide and not its PDMS precursor. It suggests that despite being isolated within the cracks, the excess PDMS was still successfully oxidized during the plasma treatment, or oxidized later during polarization experiments.

We measured values of ε_{CER} as function of chloride concentration for the mixed metal oxides, as was done for the IrO$_x$ samples. The effect of the SiO$_x$ overlayer on the CER selectivity, as shown in Figure 7.8, is obvious. The OER is significantly more favored, especially at low (<30 mM) KCl concentrations. A similar trend was seen on the other Ti-based anode samples, although the effect is not perfectly reproducible among samples (see Figure A 9.7.9 and Figure A 9.7.10). This is likely due to the inhomogeneity of the surfaces.
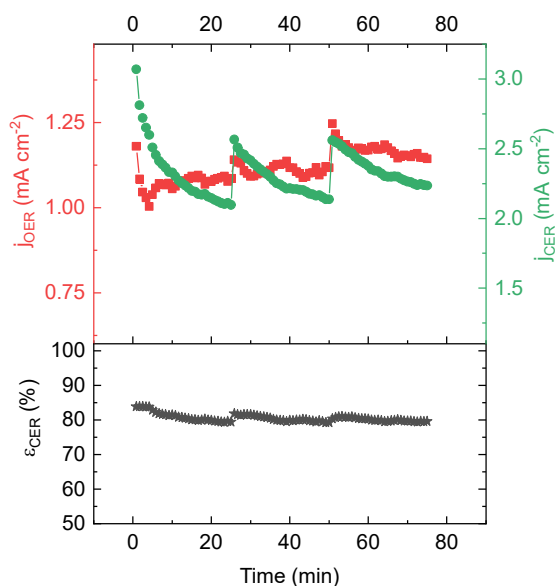
Figure 7.9: Accelerated lifetime test of IrPt/Ti sample 1 by repeatedly scanning between 1.3 – 1.55 V, in 0.5 M KHSO$_4$ + 200 mM KCl. Rotation rate 1500 RPM, OER and CER currents gathered at a potential of 1.55 V.

Finally, we also probed the SiO$_x$ overlayer for stability over extended time duration, as this property is of vital importance when the electrodes are implemented for industrial purposes. The Ti-based anodes were developed for large-scale electrolysis, and they are designed for at least several years of stable continuous operation. As an accelerated stability test, a IrPt/Ti electrode was scanned repeatedly in and out of the mixed OER + CER region under rotation in 200 mM KCl. Catalyst stability in oxygen and chlorine electrocatalysis is usually the lowest under potentiodynamic conditions.[82,300,301] A total of one hundred cycles were applied over three intervals, amounting to roughly 75 minutes. The catalytic activity and CER selectivity were monitored over time (top and lower panel of Figure 7.9). Both the OER and CER activity increased slightly as the number of scans increased, but the CER selectivity stayed very close to a constant value of ~80%, suggesting that the overlayer integrity is well preserved. Transient

increases in activity (top panel of Figure 7.9) are perhaps due to changes in the interface between the overlayer and the catalyst. As mentioned in the discussion of Figure 7.7, the Si accumulated in the catalyst cracks could still be present in the form of its PDMS precursor, since it is not expected that the UV-ozone treatment is able to fully penetrate the cracks. During electrochemical measurements the precursor may yet still be converted into the oxide, altering the catalytic activity of the catalyst which is in close contact. It is possible that the cracked morphology in the catalyst surfaces is beneficial for the mechanical stability of the overlayer by providing 'anchoring points'. All in all, the results in this section show that a SiO_x overlayer is capable of significantly increasing OER selectivity of an industrial-type catalyst. However, more research is needed to further improve this selectivity and reduce the negative impact on catalyst activity.

7.4. Concluding remarks

The work described in this chapter shows that the concept of a SiO_x-based buried interface, which has been previously successful in preventing catalyst poisoning during hydrogen evolution on Pt, may also be a promising approach to enforcing selective oxygen evolution in acidic, chloride-containing electrolytes. Results of a SiO_x overlayer on Pt showed that this type of barrier is in principle capable of preventing chloride from reacting at the buried interface, while still allowing oxygen evolution to take place. The application of the same overlayer to Ir-based catalysts, which are much more representative of actual anodic materials in electrolyzers, led to varying success. On nanoparticulate, amorphous IrO_x, the SiO_x overlayers were not effective enough to lower the CER selectivity to satisfactory values. It is most likely that the SiO_x film integrity on this type of substrate was compromised, as the residual CER activity behaved kinetically very similar to that observed on unmodified IrO_x surfaces. The overlayer failure could be due to activity hotspots on the surface leading to intense gas evolution and delamination at the buried interface, or generally insufficient interaction of the overlayer with the catalyst. Application of an extra thick SiO_x overlayer to industrial-type mixed metal oxides led to a significant increase of OER selectivity, but also a notable activity drop. Some variation in the selectivity improvement was observed among different samples. This is likely due to the inhomogeneity of the different catalyst surfaces.

It must be stressed that the results presented here are preliminary, and that the SiO_x method can and should be further adjusted to be better suited to these specific surfaces. Mainly, the procedure for synthesizing the SiO_x overlayer, which in this chapter involved spin-coating, has not been optimized for samples with higher surface roughness. It must also be stressed that other oxide materials besides SiO_x could be employed as perm-selective overlayer, such as MoO_x, VO_x, or (at high anodic polarization) CeO_x.[281,302,303] Alternatively, polymer modification or thin-membrane approaches might be used.[165] In any case, this study suggests that the morphology of the underlayer and its interaction with the overlayer are highly important in making the buried interface stable and effective. Further research into membrane-coated electrocatalysts may be a very promising pathway towards the realization of selective seawater electrolysis.

EXAMINATION AND PREVENTION OF RING COLLECTION FAILURE DURING GAS-EVOLVING REACTIONS ON A ROTATING RING-DISK ELECTRODE

8

Use of a rotating ring-disk electrode during gas-evolving reactions has been shown to be liable to errors under higher current densities, since product collection on the ring is vulnerable to the formation of gas bubbles at the disk- ring interspace. We encountered this problem on a regular basis during collection experiments where oxygen evolution was involved on the disk electrode. In this study, we explored methods of improving the reliability of the RRDE collection factor under high-intensity gas evolution. We attempted the mounting of a thin wire close to the surface, to dislodge bubbles that formed specifically on the interface between the disk and the disk-ring spacer. This approach resulted in a notable alteration of the collection efficiency. The value became lower than theoretical expectations and remained quite stable, even under higher current densities. We also coated the RRDE tip in a hydrophilic polymer, in order to reduce the tendency of bubble formation. This led to a mild increase in overall performance, allowing for higher hydrogen evolution current density without ring failure, and better oxygen collection behavior.

8.1. Introduction

The work in this thesis has made ample use of the rotating ring-disk electrode (RRDE), as it is a tool that greatly increases the amount of information that can be obtained from an electrochemical experiment when compared to a stationary electrode. Its key feature, the secondary ring electrode, can be used for collection experiments, where the extent of a reaction on the main electrode can be quantified by selectively reacting the corresponding product. This method offers a rapid and flexible means to determine selectivity in systems where parallel reaction pathways can occur and multiple products form simultaneously. An important quantity is the collection efficiency N, which is the (molar) fraction of products formed on the disk that are collected on the ring. It is defined as:

$$N = \left| \frac{n_D i_R}{n_R i_D} \right|$$
<div align="right">Eq. 8.1</div>

where i_D and i_R are the ring and disk current belonging to the reaction occurring on the disk and the reaction occurring on the ring, respectively, and n_D and n_R are the numbers of electrons in these reactions. Often, the disk and ring reaction are simply the reverse of each other, which means that n_D and n_R are the same. Importantly, N is a constant that should only depend on the ring-disk geometry.[8]

In many important processes, such as the evolution of H_2 and O_2 in water electrolysis, Cl_2 in the chlor-alkali and chlorate process, and CO_2 in direct alcohol fuel cells[304], the relevant reactions are gas-evolving reactions. Although the RRDE was not principally designed for reactions involving gas formation,[305] it has been used quite extensively and successfully for this purpose. There is however also a significant body of literature which shows that RRDE experiments involving gas formation on the disk are hindered by unreliability, or may even lead to strong ring collection failure in the sense that Equation 1 does not give a reliable and stable value for N.[66,306,315–323,307–314] Our own findings throughout this thesis confirm this tendency. The problem can be traced to gas supersaturation near the electrode surface, leading to the formation of bubbles.[144,324,325] Especially when the solubility of the product gas is low and there is heterogeneous distribution of current across the surface, as is often the case, supersaturation can easily occur. We believe this problem, in part, underlies the relative scarcity of studies attempting to use the RRDE to measure the faradaic efficiency of the OER or hydrogen evolution reaction (HER), despite the commercial availability of RRDE systems and their widespread use in the study of the closely-related oxygen reduction reaction, which does not involve gas evolution.[326–328]

During gas evolution, both nano and macro sized bubbles may form. Nanoscale bubbles nucleate directly on the electroactive surface, and can transiently isolate active surface sites or block transport through pores in case of a porous electrode, leading to irregularities in the current-potential response. This problem has been well-described in earlier publications.[101,102,104,290] Here, the focus lies exclusively on adhering macroscopic bubbles, which are large enough to be seen with the naked eye, and their disrupting effect on the

hydrodynamic flow between disk and ring on an RRDE. From previous reports and our own experience, these types of bubbles adhere strongly to the spacer between the disk and the ring, especially when the spacer is made out of highly hydrophobic materials, such as PTFE.[144] This accumulation of bubbles at the spacer strongly affects the collection factor N by forming a physical barrier that can decrease N in an erratic way. Furthermore, the gas in the bubbles, which is part of the product that originates from disk, is not properly detected by the ring, making accurate quantification impossible. In previous experiments involving the collection of H_2, N was prone to erratic behavior and strongly decreased when the HER current density exceeded a certain threshold; it also typically had a value persistently lower than the theoretical N before reaching that threshold.[306,308,310,329] Similar results were reported concerning O_2 collection during OER.[66,311,320,321,330,312−319] Many authors have resorted to an empirical correction, based on measurements of N in comparable experiments where its value should be ideal.[307,311,314,317,318,320,321,323,330]

Several solutions to lessen bubble adhesion have been suggested. Kadija *et al.* proposed the use of a rotating ring electrode (RRE),[305] optionally equipped with a secondary ring, leading to the rotating ring-ring electrode (RRRE).[144,331,332] The RRRE offers the advantage of increased liquid momentum at the electroactive areas to aid bubble detachment, which can be tuned using the ring diameter. A rotating ring cone electrode (RRCE) was suggested as well, which has a vertically angled electroactive surface, and uses gas bubble buoyancy to promote detachment.[146,333,334] In another case, a liquid jet was used to intermittently remove accumulated gas bubbles from the electrode surface.[335] Despite the obvious advantages of the RRRE and RRCE and the significant research efforts that have gone into their development, currently the RRDE is still the most widely used rotating electrode geometry, even for gas-evolving reactions. It is more easily fabricated and prepared for analytic electrochemical studies, which often require very high purity conditions and the possibility for fast throughput.

As described above, we have made extensive use of the RRDE for quantification of gaseous products, but constant vigilance was needed during the experiments to ensure reproducible ring-disk collection properties. In this chapter our attempts to improve the gas collection behavior of a typical RRDE setup are described. As test system, we studied the evolution of Cl_2, O_2 and H_2, gases that have great electrocatalytic significance, as described above. We will report results from two approaches: i) carefully placing a thin Ti wire very close to the interface of the disk and the Teflon spacer, to physically dislodge bubbles stuck at this interface, and ii) coating the RRDE tip assembly with the hydrophilic polymer poly-dopamine (p-DA), in an attempt to decrease the tendency of hydrophobic bubble formation on the surface.

8.2. Experimental

8.2.1. *Chemicals*

$HClO_4$ (70%, Suprapur/Trace analysis grade), KCl (EMSURE/Analysis grade), KOH solution (32%, EMSURE/Analysis grade), HCl (30%, Ultrapur/Trace analysis grade) and $KHSO_4$ (EMSURE/Analysis grade) were purchased from Merck. All purchased chemicals were used

as received. The water used for all experiments was prepared by a Merck Millipore Milli-Q system (resistivity 18.2 MΩcm, TOC < 5 p.p.b.).

8.2.2. *Cleaning procedures*

All experiments were carried out at room temperature (~20 °C).

Electrochemical experiments except those involving a Ti wire near the tip were done using home-made two-compartment borosilicate glass cells with solution volumes of 100 mL. Experiments with the Ti wire were done in a single compartment vial of approximately 16 mL volume. Before first-time use, all glassware was thoroughly cleaned by boiling in a 3:1 mixture of concentrated H_2SO_4 and HNO_3. When not in use, all glassware was stored in a 0.5 M H_2SO_4 solution containing 1 g/L $KMnO_4$. Before each experiment, glassware was thoroughly rinsed with water, and then submerged in a dilute (~0.01 M) solution of H_2SO_4 and H_2O_2 to remove all traces of $KMnO_4$ and MnO_2. The glassware was then rinsed three times with water and boiled in water. The rinsing-boiling procedure was repeated two more times.

8.2.3. *Cell preparation*

All experiments were done with an MSR rotator and E6 ChangeDisk RRDE tips in a PEEK shroud (Pine Research). An IviumStat potentiostat (Ivium Technologies) was used for potential control during electrochemistry experiments. All experiments were 95% iR-compensated in-situ. The solution resistance was measured with electrochemical impedance spectroscopy at 1.30 V vs. RHE (IrO_x/GC disk working electrode) or 0.05 V vs. RHE (Pt disk working electrode), by observing the absolute impedance in the high frequency domain (100-50 KHz) corresponding to a zero-degree phase angle. All used solutions were saturated with Ar (Linde, purity 6.0) before experiments. During forced convection experiments, solutions were continuously bubbled with Ar gas, in stationary conditions, Ar was used to blanket the solution. In experiments involving the placing of a Ti wire close to the RRDE tip, the reference electrode was a LowProfile Ag/AgCl electrode (Pine Research, E = 198 mV vs. NHE). In all other experiments, the reference electrode was a HydroFlex® reversible hydrogen electrode (Gaskatel), separated from the main solution using a Luggin capillary. All potentials in this chapter are reported on the RHE scale. A Pt mesh was used as counter electrode, separated from the main solution with a coarse sintered glass frit.

8.2.4. *Electrode preparation*

IrO_x/GC electrodes were prepared via electroflocculation of IrO_x nanoparticles, as described in sections 9.1.1 and 9.1.2. The GC surfaces were polished with diamond paste, followed by rinsing and sonication in water for 3 minutes. The electroflocculation amperometry step lasted 300 s. In experiments involving a Pt disk working electrode, the assembled tip was treated for 3 minutes with a solution of 0.5 M H_2SO_4 containing 0.5 g/L $KMnO_4$, followed by rinsing with water, treatment with a dilute (~0.01 M) solution of H_2SO_4 and H_2O_2 to remove any traces of $KMnO_4$ and MnO_2, and further extensive rinsing with water. During RRDE experiments, any Pt electrode (the Pt ring or, if used, the Pt disk) was electropolished by scanning from -0.1 V

to 1.7 V at 500 mV s^{-1} for 20 scans at 1500 RPM. In-between experiments, the disk electrode was kept either at 1.3 V vs. RHE (IrO$_x$/GC working electrode) or 0.05 V (Pt working electrode). Ring currents were corrected for constant background currents and product collection delay. The latter arises from the time needed for products formed on the disk to reach the ring, and was approximately 200 ms at 1500 RPM. Poly-dopamine (p-DA) deposition was done by submerging the Pt-Pt RRDE in a 20 mM sodium phosphate solution of pH ≈ 7, containing 2 g/L dopamine (DA). The tip was kept in the solution for one hour under gentle rotation (300 RPM), after which it was thoroughly rinsed with water.

8.3. Results and discussion

8.3.1. *Examples of ring failure during gas collection experiments*

We will first present some extreme examples of ring collection failure, measured during the study of parallel oxygen evolution and chlorine evolution, as well as only chlorine evolution. In this section and in section 8.3.2, the discussion will be particularly focused on the collection of Cl$_2$, which often forms in combination with O$_2$. To prevent confusion, the various collection factors will be labelled according to the species that are measured. Disk and ring currents were both normalized versus the disk geometrical surface area (the ring surface area is irrelevant since it is always used as a detector, such that all ring reactions are diffusion limited).
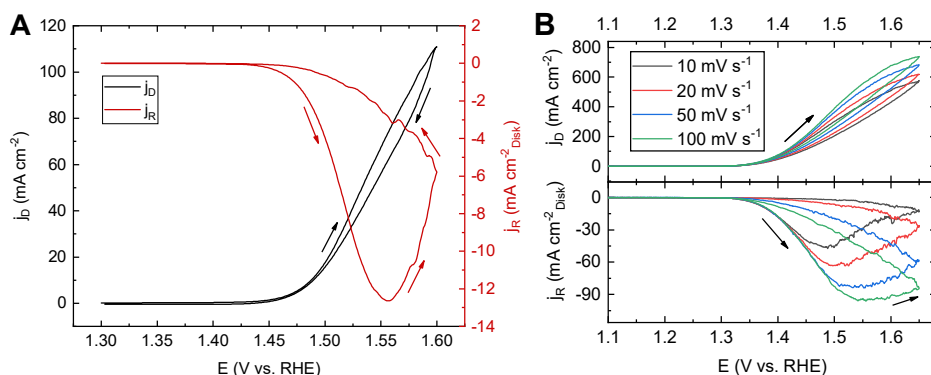
Figure 8.1: Illustration of RRDE ring failure during gas evolution. Panel A: Parallel evolution of oxygen and chlorine on a IrO$_x$/GC disk, with the Pt ring fixed at 0.95 V vs. RHE to selectively probe Cl$_2$. Solution: 0.5 M KHSO$_4$ + 100 mM KCl saturated with Ar, rotation rate 1500 RPM. B: Evolution of (mainly) Cl$_2$ on a Pt disk, while again keeping the ring fixed at 0.95 V, with varying scan rate. Solution: 1 M HCl saturated with Ar, rotation rate 1500 RPM. Arrows indicate scan directions.

In chapter 2, we showed that operating a RRDE with a Pt ring at 0.95 V allows selective probing of Cl$_2$ evolved on the disk, provided that the solution is strongly acidic (pH < 1). Compared to O$_2$, the aqueous solubility of Cl$_2$ is rather high, even at this low pH,[148] such that it was possible to use this method up until relatively large CER current densities without the formation of Cl$_2$ bubbles. However, the formation of poorly soluble O$_2$ in parallel with Cl$_2$ strongly increases the probability of bubble formation, and limits the maximum potential at which the method is still reliable. On highly OER-active GC-supported IrO$_x$, this limit was

determined by roughly 10 mA cm^{-2}, usually reached close to 1.55 V vs. RHE. Figure 8.1A illustrates the difficulties that arise when attempting measurements at higher potential.

In Figure 8.1A, parallel evolution of oxygen and chlorine on the disk leads to a continuously increasing current with more positive potential. The ring current density, which selectively probes CER, is expected to rise initially, concomitantly with the disk current, and then to level off to a limiting value as the CER on the disk becomes fully mass-transfer controlled. Instead, we observe a sharp and consistent *decrease* in the ring current density as the potential increases above 1.56 V ($\eta_{CER} \approx 170$ mV), as well as increasing noise in the signal. As mentioned, it is likely that under these conditions, the formation of O_2 bubbles disrupts the transport of Cl_2 from the disk to the ring. In our experience, once gas bubbles are formed of a poorly soluble species, such as O_2, they do so irreversibly: they stick to the electrode tip persistently, regardless of ring or disk potential, or solution flow. This is illustrated in the backward scan in Figure 8.1A, where the ring does not recover its collection efficiency, even at potentials for which the disk current has decreased to lower values than in the forward scan where the collection efficiency was still well-behaved. We also found that even under high rotation rates (>2500 RPM), the time for any formed bubbles to completely dissolve can be very long. During this period the ring collection factor is distorted and cannot be trusted. The transient nature of gas collection failure is further illustrated in Figure 8.1B. In this experiment, evolution and collection of Cl_2 was performed on a Pt-Pt RRDE in a concentrated chloride solution (1 M HCl), with varying scan rates. CER currents on the disk measure (industrially relevant[34]) densities in the range of 1 kA m^{-2}. Initially the ring current density follows, but at the slowest scan rate of 10 mV s^{-1}, N_{Cl_2} starts decreasing at approximately 1.4 V vs. RHE ($\eta_{CER} \approx 145$ mV), corresponding to 100 mA cm$^{-2}_{Disk}$. At around 1.49 V ($\eta_{CER} \approx 235$ mV), the ring fails catastrophically; this is presumably due to extensive formation of Cl_2 bubbles. The 'potential of failure' shifts to higher values for higher scan rates, suggesting that it is strongly dependent on the local build-up of gas.

In general, we find that presence of gas bubbles may not be noticeable from the ring response at first glance, as long as the bubbles are small and not too numerous. In this case, the only clear indication of transport distortion on the tip is usually an unexpectedly but reproducibly low collection factor, and perhaps a subtle periodic noise in the signal that can be rotation rate dependent. Before and in-between repeated gas evolution experiments, we recommend thorough visual inspection of the electrode tip; it is strongly advised to do this while rotation is switched off. Once it has been verified that the working electrode tip is completely free of bubbles, one can check for gas bubble interference over the course of an experiment by scanning the relevant potential window repeatedly, or by changing the scan rate. If the collection factor is reproducible during this straight-forward control experiment, no gas bubbles should have formed. A practical solution for removing persistent bubbles was to lift the electrode tip just above the working solution within the cell, rotate it momentarily to spin away liquid and bubbles, and then re-immerse it.

8.3.2. RRDE voltammetry experiments using a blocking wire

During the experiments, we saw that gas bubbles usually appear on the disk-ring interspace, which in the case of these experiments is made of Teflon. Bubbles were especially prone to adhere near the disk boundary (Figure 8.2A). Once formed, they may grow by absorbing highly concentrated gas in the nearby solution, which aggravates the problem and may explain why the ring function is usually irrecoverable after failure.

Figure 8.2: Photographs of a rotating electrode equipped with an IrO_x/GC disk (black) and Pt ring (grey). A: Tip after an experiment involving vigorous gas evolution, during which the collection factor became severely distorted. B: Tip during attempts to dislodge gas bubbles using a Ti wire. The Ti wire is mounted under the tip, with its point aimed at the disk-Teflon spacer boundary. Accumulating bubbles collided with the wire and were 'pushed off' during rotation.

Our initial, rather simple-minded attempt at preventing bubble interference was to prevent bubbles from accumulating, by specifically targeting the disk-Thesis v2019-11-18A4p127Teflon boundary. To do so, we carefully installed an acid etched and flame-annealed Ti wire very close to the surface of the tip (Figure 8.2B). The wire was made long and as thin as possible, to minimize effects that it might have on the fluid dynamics near the rotating tip.

Figure 8.3A shows results of RDDE experiments with a Ti wire, and its effect on the ring current density and N_{Cl_2} during intense evolution of O_2 and Cl_2 gas. During large currents, we observed continuous formation of bubbles over the disk electrode surface during rotation. The Ti wire quite effectively dislodged these bubbles, after which they scurried across the rotating electrode tip causing occasional current spikes (Figure 8.3A, top and middle panel). Despite this, subsequent ring scans now show rather reproducible behavior in the presence of the wire. Catastrophic collection failure, such as in Figure 8.1, is avoided, even under intense gas-evolving conditions. In the potential region $1.46 - 1.53$ V, where virtually all disk current is due to the CER, the collection factor has a value of about $N_{Cl_2} = 0.12$. This value is roughly 50% lower than the value of about 0.24 that we previously measured for chlorine collection under
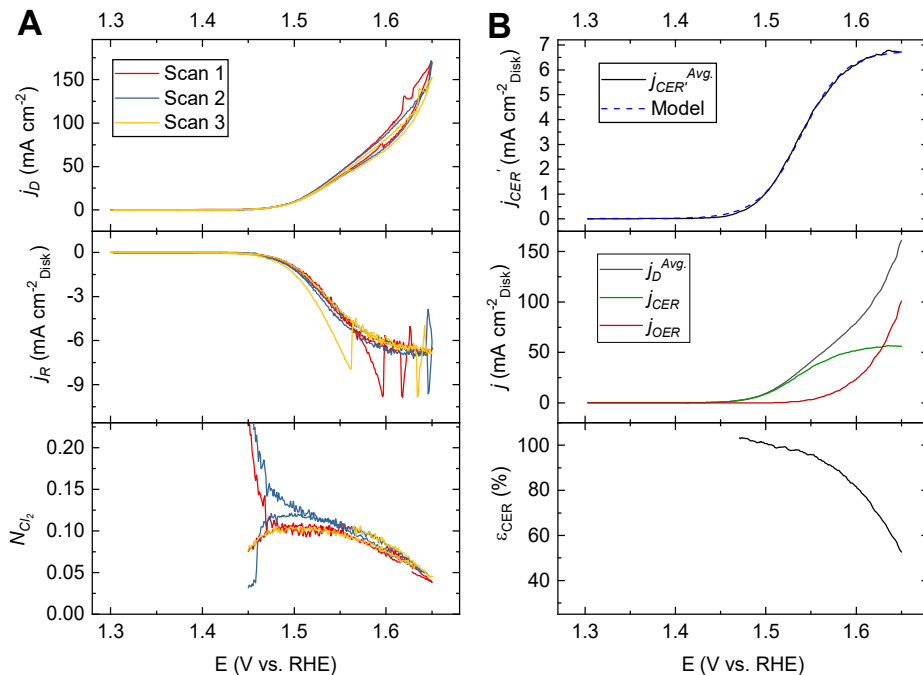
Figure 8.3: RRDE gas evolution experiments with the end of a Ti wire mounted close to the disk-spacer boundary (See Figure 8.2B). A: Repeated scans into the mixed OER + CER potential region, where vigorous gas evolution occurs. As in Figure 8.1A, the catalyst is IrO_x/GC, and a Pt ring at 0.95 V was used to selectively detect Cl_2. Shown are disk (top panel) and ring current density (middle panel), as well as the collection efficiency N_{Cl_2} (bottom panel). Scan rate: 10 mV s^{-1}. Solution: 0.5 M $KHSO_4$ + 50 mM KCl saturated with Ar, rotation rate 1500 RPM. B: 'Apparent' CER current j_{CER}', extracted from the average of the three ring scans in A. Also shown is a sigmoidal fit based on the generalized j-E curve including mass transfer effects (top panel). Middle panel shows the averaged forward and backward disk current from A, along with calculated partial CER and OER currents, assuming that $N_{Cl_2} \approx 0.12$. Bottom panel shows ε_{CER}, the molar selectivity towards CER. Current spikes were excluded from the calculation of both j_{CER}' and N_{Cl_2}.

these conditions (see chapters 2 and 6). Considering that the value of 0.12 is reached in the forward scan of the first cycle, where the tip is completely free of bubbles, it is possible to conclude that the wire causes this deviation in N_{Cl_2}. Additionally, it implies that N_{Cl_2} stays quite constant as a function of time, because approximately the same value is reached irrespective of the cycle number or scan direction. After 1.55 V, N_{Cl_2} apparently decreases due to an increasing OER contribution to the current on the disk.

The absolute values of the ring current densities from the three scans were averaged and smoothed, and termed 'apparent CER current', j_{CER}'. They are shown in the top panel of Figure 8.3B. In this calculation, potential regions containing current spikes, such as near 1.65 V in scan 2, were excluded (see Figure A 9.8.1 for details). The resulting data is reminiscent of a typical sigmoid-shaped j-E curve, where initially the current is activation controlled and rises exponentially, but then crosses over into a constant diffusion limited value. To investigate the ring behavior, j_{CER}' was fitted using the 'anodic branch':

$$j = j_0 \left(\frac{e^{\alpha f \eta}}{1 + \frac{j_0}{j_L^{an}} e^{\alpha f \eta}} \right)$$ Eq. 8.2

In Eq. 8.2, j_L^{an} is the anodic diffusion-limiting current, and $f = {}^F\!/_{(RT)}$. The model fits j_{CER}' rather well (Figure 8.3B, top), suggesting that the ring current, despite the intensive evolution of gas on the tip and presence of the wire, is quite well-behaved. The used value of α was 1.1, which slightly underestimated the exponential rise at the foot of the wave, but gave the best fit in the diffusion limited region. This allowed us to calculate a value of 6.74 mA cm$^{-2}_{Disk}$ for j_L^{an} measured on the ring. Furthermore, the CER diffusion-limitation on the disk that would be expected on the basis of the Levich equation is 61.16 mA cm$^{-2}_{Disk}$. From these values, the ring chlorine collection factor becomes $N_{Cl_2} = \frac{6.74}{61.16} \approx 0.11$ near 1.65 V. This value matches well with that measured in regimes of low current density (0.12), and implies that the Ti wire keeps N_{Cl_2} constant, irrespective of high or low gas evolution intensities. Taking $N_{Cl_2} = 0.12$, and under the reasonable assumption that no other processes besides the OER and CER are occurring on the disk, we then calculated j_{CER} and j_{OER}, the partial CER and OER current densities, by using:

$$j_{OER} = j_D - j_{CER} = j_D - \left({}^{j_{CER}'}\!/_{N_{Cl_2}} \right)$$ Eq. 8.3

where j_D are the averaged forward and backward disk current densities of the three scans. The results (Figure 8.3B, middle) suggest that whereas CER becomes diffusion limited, OER activity rises continuously, as transport phenomena play a much smaller role for this reaction. This is reflected in the molar selectivity towards CER (bottom), which decreases sharply with increasing potential. From these results, one can assume that OER always becomes the dominant reaction if the potential is high enough, regardless of the chloride concentration, which has important implications for the selectivity between the two.

In experiments with an even further extended scan window, we noticed an apparent decrease of CER rates at potentials above 1.65 V vs. RHE (see Figure A 9.8.2 and Figure A 9.8.3). At the high potential limit, it is likely that the formation hypochlorous acid starts competing with CER. Hypochlorous acid cannot be detected by the ring under these conditions (see Chapter 2). The occurrence of this reaction has been hypothesized and evidenced previously,[28,29,77,336] though indirectly and via off-line methods. We believe this is the most direct result thus-far that suggests the CER crosses over into hypochlorous acid evolution at very high overpotentials. An appreciable decrease in disk activity is also apparent during these experiments, which is most likely due to mechanical shear from intense oxygen evolution and oxidative degradation of the GC support.[337] These observations demonstrate that the possibility of extending RRDE methods into wider potential windows could lead to interesting new insights. The wire affects N quite differently depending on whether gaseous Cl_2 or dissolved $[Fe(CN)_6]^{-4}$ is collected (see Figure A 9.8.4). The value for Cl_2 collection in 1 M HCl was $N_{Cl_2} \approx 0.13$, similar to results in Figure 8.3, though it dropped to slightly lower values

during very vigorous gas evolution ($j_D > 0.5\ \mathrm{A\,cm^{-2}}$). Subsequent measurements in 0.1 M KOH + 1 M KCl + 10 mM $K_3[Fe(CN)_6]$, while ensuring that the wire stayed in the exact same position, yielded $N = 0.197$ for $[Fe(CN)_6]^{-4}$. The latter value increased to 0.212 when the wire was moved slightly further away, and became 0.252 when the wire was completely removed, which is close to the ideal theoretical value of 0.258. During the ferri/ferrocyanide experiments, the wire likely lowers N by distorting the fluid dynamics near the surface. During gas evolution, this effect is compounded by gas bubbles that are forced off the electrode surface near the point of the wire. These gas bubbles probably increase the flow distortion, and are themselves not quantified by the ring, both of which lead to a lowering of the collection efficiency. One can expect that the actual value of N when placing a wire is not universal, but depends on factors such as the wire length and thickness, and the geometry of the electrode tip.

In conclusion, it can be stated that the mounted wire aids in bubble removal, which keeps N_{Cl_2} more constant and prevents ring collection failure during vigorous gas evolution, but it also causes the value of N_{Cl_2} to deviate strongly from theoretical values, meaning that an empirical correction would be needed. There are also practical disadvantages to the wire approach: the mounting of the wire and keeping it at the required position proved to be quite precarious. An incorrectly placed wire may easily scratch and damage the tip surface.

8.3.3. *RRDE voltammetry experiments and the effect of a poly-dopamine coating*

The observation in section 8.3.2 that macroscopic gas bubbles universally appear at the disk-Teflon boundary, suggests that gas bubbles that form on the disk surface 'become stuck' on the Teflon surface as they are swept outward. However, it is likely that bubbles nucleate not so much on the hydrophilic electrode itself, but on the Teflon spacer in-between the disk and the ring,[144] caused by a sudden gas concentration increase in the solution that flows past the spacer.[338] The problem of bubble nucleation may be aggravated when using rotating electrode tips with interchangeable disk electrodes. While offering significant experimental flexibility, the surface of such tips will always have at least micrometer-sized imperfections at the boundaries between the disk, spacer and ring, irregularities which favor bubble nucleation and growth.

A promising method of disfavoring bubble nucleation would be to decrease the hydrophobicity of the electrode tip material. We attempted this by coating the pre-assembled electrode tip with poly-dopamine (p-DA), a hydrophilic polymer that preferentially deposits on hydrophobic, organic surfaces.[339,340] Successful p-DA deposition on both the Teflon spacer and PEEK outer shroud was evidenced by a large increase of tip wettability after treatment. Alternatively, we also tried coating the ejected Teflon spacers with a water insoluble but hydrophilic polymer, such as poly(4-vinylpyridine). However, an even coating could not easily be achieved, and the layer was readily damaged upon reinsertion of the spacer into the RRDE tip, which requires pressing.

After the p-DA deposition procedure, some degree of DA or p-DA adsorption on the Pt surfaces was suggested by a large drop in the open-circuit potential, which was monitored during the

coating (Figure A 9.8.5). However, after the coating treatment we were able to recover the Pt surface readily via electropolishing (Figure A 9.8.6), suggesting that this adsorption is minor and not problematic. Subsequently, the effect of the coating on the collection of O_2 and H_2 was measured. Two different gases were tested, since electrochemical bubble nucleation and growth behavior can depend heavily on the type of gas evolved;[341–343] it was therefore of interest to see whether the coating would have the same effect on each gas.
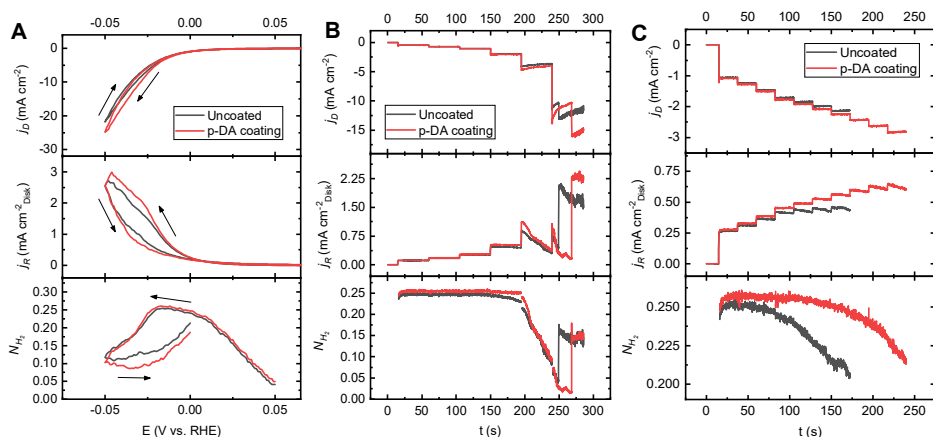
Figure 8.4: H_2 collection experiments on a Pt-Pt RRDE tip, and the effect of a p-DA coating on the collection efficiency. Displayed across the graphs are disk (top panels) and ring current densities (middle panels), bottom panels show the collection factor N_{H_2}. A: Cyclic voltammograms, scan rate 10 mV s⁻¹. Arrows indicate scan direction. B: Amperometry using 45 s steps at stepwise more negative potentials, chosen to gradually increase HER rates. C: Amperometry using 22.5 s steps and smaller potential steps, resulting currents targeted around the region where N_{H_2} starts to fail in B. The Pt ring was fixed at 0.4 V to detect H_2. Solution: 0.1 M HClO₄ saturated with Ar, rotation rate 1500 RPM. The first 0.5 s of each amperometry step is not shown for N, because of charging effects distorting its value.

Cyclic voltammograms in Figure 8.4A show hydrogen collection experiments on a Pt-Pt RRDE, at 10 mV s⁻¹. In absence of the p-DA coating, the electrode initially has a collection efficiency that approaches 0.251, which is very close to the ideal theoretical value of 0.258. At potentials lower than -18 mV, the value of N_{H_2} drops sharply and does not recover for the remainder of the scan, similar to the data of Figure 8.1. Around this potential, the HER disk current density is -2 mA cm^{-2}, a value quite similar to that found by Frazer *et al.* for ring failure for HER collection in a i_R vs. i_D plot at approximately -1.5 mA cm^{-2}, under 1200 RPM.[344] The effect of the p-DA coating is a mild but consistent increase in N_{H_2} during the negative scan. Unfortunately, the coating does not influence the potential where the ring collection starts to fail, nor is it able to help recovery of the ring as the potential is swept back to where the electrode is less active. During amperometry experiments in Figure 8.4B and Figure 8.4C, where H_2 is continuously generated and collected at gradually increasing current density steps, the main effect of the p-DA coating is again a small but visible increase in N_{H_2}, its value increasing from 0.249 to 0.256 in presence of the coating. In Figure 8.4B, the value stays quite constant up until 195 s, irrespective of the coating, but N_{H_2} drops dramatically as the disk current is increased to -4.6 mA cm^{-2}. The failure of N_{H_2} is evident here from a dramatic decrease in both the ring current density and disk current density. After the potential step at

240 s, the experiment is completely dominated by the erratic effects of bubbles accumulating on the tip. Figure 8.4C shows a series of shorter amperometry steps, with smaller current increases that are specifically targeted at the region of 140 − 195 s in Figure 8.4B, where collection failure starts to appear on the uncoated tip. One can observe that the p-DA coating helps maintain N_{H_2} for a longer time in this experiment. Comparing the disk currents where N_{H_2} starts to deviate, it can be said that the p-DA enables reliable collection measurements under currents that are roughly 50% higher than the uncoated tip.
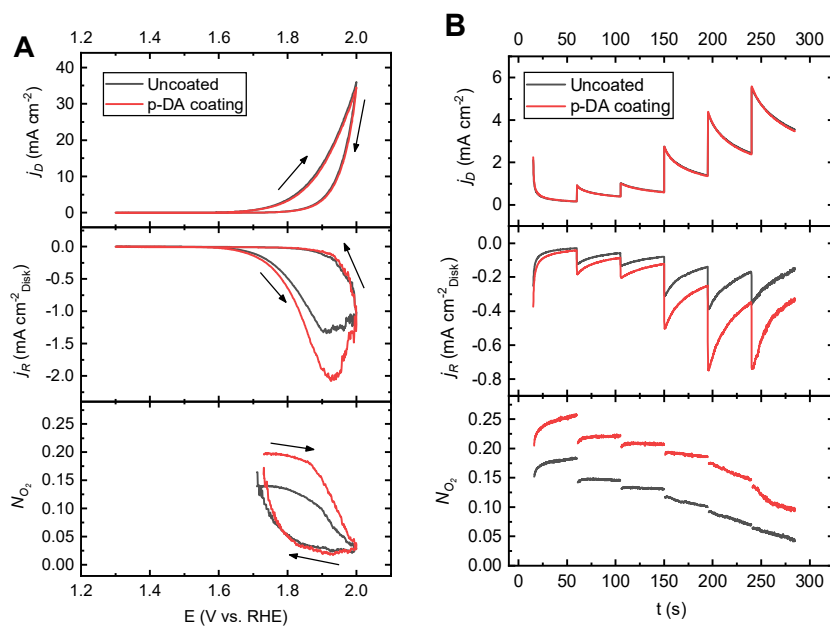
Figure 8.5: O_2 collection experiments on a Pt-Pt RRDE tip, and the effect of a p-DA coating on the collection efficiency. Displayed across the graphs are disk (top panels) and ring current densities (middle panels), bottom panels show the collection factor N_{O_2}. A: Cyclic voltammograms, scan rate 10 mV s⁻¹. B: Amperometry using 45 s steps at stepwise larger positive potentials, chosen to gradually increase OER rates. The Pt ring was fixed at 0.4 V to detect O_2. Solution: 0.1 M $HClO_4$ saturated with Ar, rotation rate 1500 RPM. The first 0.5 s of each amperometry step is not shown for N, because of charging effects distorting its value.

Figure 8.5 shows the collection factor for OER on Pt, as well as the effect of a p-DA coating, using a similar procedure as in the H_2 experiments. Pt was used for O_2 generation instead of IrO_x, since the intention was to compare the collection behavior of 'pure OER' on a non-porous catalyst, free from possible extra collection complications caused by gas bubbles in pores (see also section 8.1). It must be noted that Pt experiences a strong growth of multilayer oxides under OER potentials. As much as 20-30%[345] of disk current can be consumed in the formation of the oxide layer, meaning that the OER faradaic efficiency and the expected value for N_{O_2} are lower than 100%. We will thus discuss results from relative collection efficiencies, under the assumption that the OER faradaic efficiency has a constant value. To minimize variation in PtO_x formation, a moderately thick oxide layer was grown prior to each experiment. The OER cyclic sweep was started at 1.30 V, well before the onset of OER on Pt, and in the amperometry, a pre-step of 1.45 V vs. RHE was applied for 15 s.

In the forward sweep in Figure 8.5A, the ring current density increases significantly when a p-DA coating is applied. N_{O_2} correspondingly changes from 0.14 to 0.20 in the initial stages of the forward scan, which is a much larger collection increase (roughly 40%) compared to the H_2 collection experiments in Figure 8.4A, where N_{H_2} is initially close to the ideal value. The transport of O_2 gas from the disk to the ring is thus somehow impaired in comparison with that of H_2. This is likely caused by the same underlying principles that lead to divergent behavior in electrochemical growth of O_2 and H_2 bubbles, as previously reported.[341–343] The low O_2 collection efficiency is considerably improved by the p-DA coating. On the other hand, N_{O_2} fails irreversibly once the disk current density increases past a certain threshold, regardless of the coating, similar to the H_2 experiments. Amperometry experiments involving stepwise increases in disk current density (Figure 8.5B) show that N_{O_2} again always has higher values. However, in both cases it starts decreasing significantly after 145 s, meaning that the current density where transport to the ring starts to be negatively affected is virtually unchanged. Summing up the findings from the effect of a p-DA coating on the RRDE tip: it has a favorable effect on the collection efficiency of both H_2 and O_2, but the improvement of O_2 collection appears more significant, and the mechanism of improvement seems inherently different between the two gases. For H_2 collection, the current density threshold for irreversible collection failure is only mildly improved. On the other hand, in case of O_2, the collection behavior before the onset of ring failure is greatly improved.

Evidently, while the p-DA coating has a favorable effect on the general collection behavior of the tip, and allows a mild extension of disk current densities that can reliably be measured, irreversible ring failure still sets in rapidly once a certain threshold activity is exceeded. It is certainly possible to further improve the RRDE collection behavior using the avenue of tip coating. The p-DA coating procedure could be further optimized.[346] It should also be possible to utilize coating layers that are even more hydrophilic than p-DA, to further lower the nucleation probability of gas bubbles during measurement.

8.4. Conclusions

In this chapter, we investigated the vulnerability of disk-to-ring transport during gas-collection experiments on a rotating ring-disk electrode, as well as two methods for improving this gas collection behavior. The use of a thin wire to selectively dislodge bubbles at the disk-spacer boundary prevented ring failure due to gas bubbles, and made the collection factor more reproducible as a function of time. The wire allowed chlorine collection experiments under intense gas-evolving conditions, although it caused the measured values to become lower than theoretical predictions, and was challenging to implement in practice. It is recommended to construct a dedicated mechanical setup coupled to a micrometer system, to aid in properly mounting the wire and keeping it in position. Application of a hydrophilic poly-dopamine coating on the electrode tip led to moderate improvements in the collection of oxygen and hydrogen. Whereas for hydrogen collection, the current density threshold before ring failure was increased by roughly 50%, for oxygen instead the overall collection efficiency increased.

SUPPORTING INFORMATION

9

This chapter contains all supplementary information for the work presented in this thesis. All subsections are numbered according to chapter numbers (i.e. the supporting information for Chapter 2 is found in section 9.2).
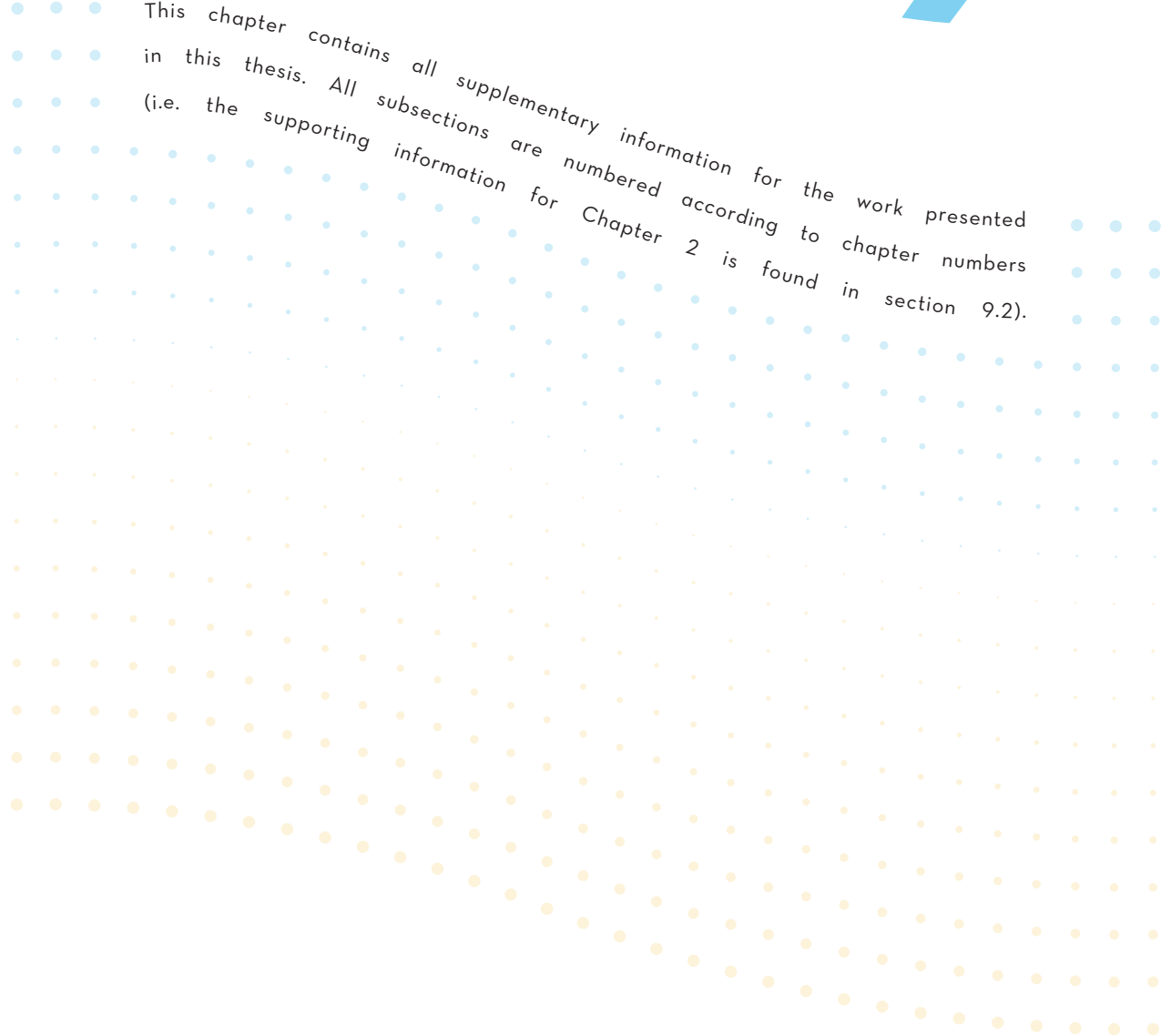
9.1. General experimental information

9.1.1. *Synthesis of hydrated IrO$_x$ nanoparticles*

Hydrated IrO$_x$ nanoparticles were prepared and used as a meta-stable IrO$_x$ colloid suspension obtained from alkaline hydrolysis of Ir[Cl]$_6^{3-}$.[142,143,262,347] Briefly, Na$_2$IrCl$_6 \cdot$ 6H$_2$O was dissolved in 0.1 M NaOH to reach a nominal Ir concentration of 2 mM. Dissolution of the complex was followed by aqueous reduction of Ir[Cl]$_6^{2-}$ to Ir[Cl]$_6^{3-}$, coupled to momentary O$_2$ gas formation on the solid.[348] The light yellow solution was then heated in a water bath to either 70 °C or 95 °C and kept there for 20 minutes, under continuous stirring. The solution turned very light blue during this period. It was subsequently transferred to an ice bath and 60% HClO$_4$ was added under stirring, until the solution pH was approximately 1. The solution colour turned dark violet after acid addition. It was stirred in the ice bath for 1 h, allowing condensation of hydrated IrO$_x$ colloids. The solution could then be used immediately for experiments. For long term storage, the solution was made alkaline (pH $\approx$ 13) by addition of 10.1 M NaOH, causing a subtle colour shift from violet to dark purple. It could be stored for up to 3 months at 4 °C.

9.1.2. *Preparation of GC-supported hydrated IrO$_x$ films (IrO$_x$/GC)*

GC disks (Pine Research Instrumentation, surface area 0.196 cm²) were prepared to a mirror finish by hand polishing with either Al$_2$O$_3$ or diamond pastes down to 0.05 μm particle size, followed by rinsing and sonication of the electrode in water for 3 minutes.

To prepare the IrO$_x$/GC electrode, the IrO$_x$ particles were electroflocculated on the GC surface under rotation. A 4 mL aliquot of the bulk alkaline solution was re-acidified with 60% HClO$_4$ down to pH $\approx$ 1.5. The removal of OH$^-$ induced the deprotection of the IrO$_x$ colloids, which manifested as a solution color change from purple to greyish violet. Care must be taken not to make the IrO$_x$ solution too acidic, since competing CER at low pH may interfere with the reproducibility of the deposition. CER originates from the Cl$^-$ which is present as byproduct from the Ir[Cl]$_6^{3-}$ hydrolysis. Deposition was then performed at a rotation rate of 600 RPM on a freshly prepared GC surface. The disk electrode was first scanned between 5-10 cycles at 250 mV s^{-1} in range of 0.16 - 1.36 V vs. Ag/AgCl, to observe the initial IrO$_x$ deposition and the onset of the mixed OER and CER. Their activities increased with each scan as progressively more IrO$_x$ deposited. The scans were followed by amperometry for 300 - 600 s (depending on the desired thickness) at a potential roughly 10-20 mV positive of the onset of the mixed OER and CER. Currents rising over time indicated further IrO$_x$ deposition. After deposition, a reflective blue film was visible on the GC surface.

9.2. Supporting information for Chapter 2

9.2.1. Supplementary figures
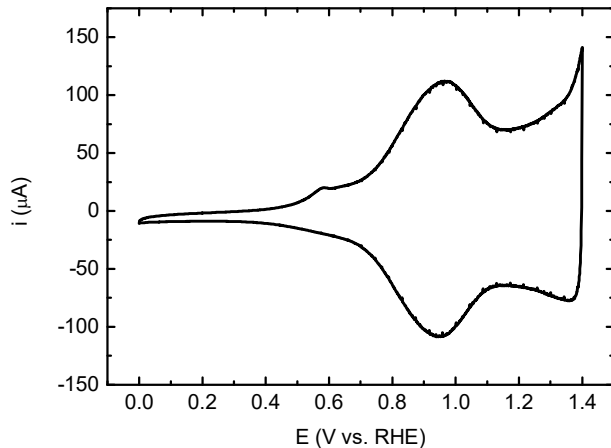
Figure A 9.2.1: Characterization CV of the electroflocculated IrO_x catalyst, in 0.5 M $KHSO_4$. Scan rate: 50 mV s^{-1}.
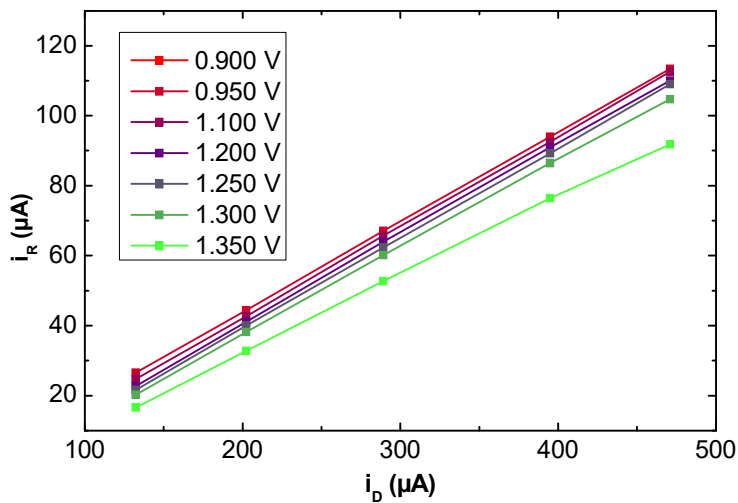
Figure A 9.2.2: Behavior of i_R vs. i_D at various ring potentials, data taken from Figure 2. Example plot for $[Cl^-] = 100$ mM used to find potential dependent slopes, which are equivalent to N_{Cl_2}.
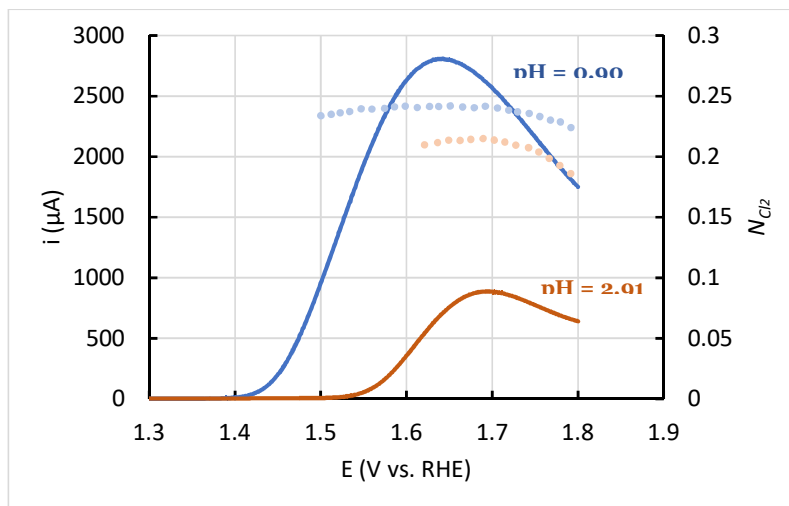
Figure A 9.2.3: Linear sweep voltammograms (10 mV/s) of the disk electrode in a Pt-Pt RRDE setup, in 0.5 M KHSO$_4$ solutions of pH = 0.90 (blue) and pH = 2.91 (orange). [Cl$^-$] = 20 mM, rotation rate = 1500 RPM. Ring currents were collected at 0.95 V vs. RHE. Dotted symbols show corresponding values of the apparent chlorine collection factor N_{Cl_2}, equivalent to $|i_R/i_D|$. Since OER onsets around 1.65 V on Pt in acidic conditions, N_{Cl_2} should approach the liquid phase collection factor close before this onset, where approximately all current can be ascribed to CER.

Formation of PtO$_x$ has a strong inhibitory effect on CER kinetics, as was previously reported by Conway and Novák (see ref. 19). The CER current rises but then decreases with increasing potentials despite hydrodynamic conditions. N_{Cl_2} reaches an approximately constant value as function of increasing E$_D$ in both experiments. It decreases above $E_D \approx 1.65$ V, which can be ascribed to the onset of parallel OER.
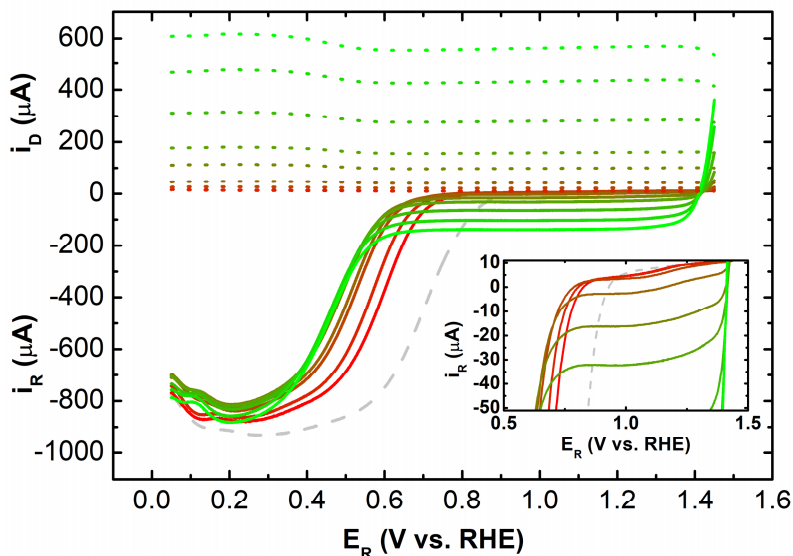
Figure A 9.2.4: LSV of the Pt ring electrode while keeping the IrO_x/GC disk electrode fixed at 1.475 V, in 0.5 M $KHSO_4$. [Cl^-] (in the form of KCl) increasing from 1 (red) to 100 mM (green). Dotted curves with positive values correspond to disk currents, remaining curves correspond to ring currents. Inset shows enlarged CRR region at low [Cl^-]. The ring LSV sweeps were taken in the anodic direction. Scan rate 5 mV s^{-1}, rotation rate 1500 RPM, pH = 0.88, solution saturated with O_2.
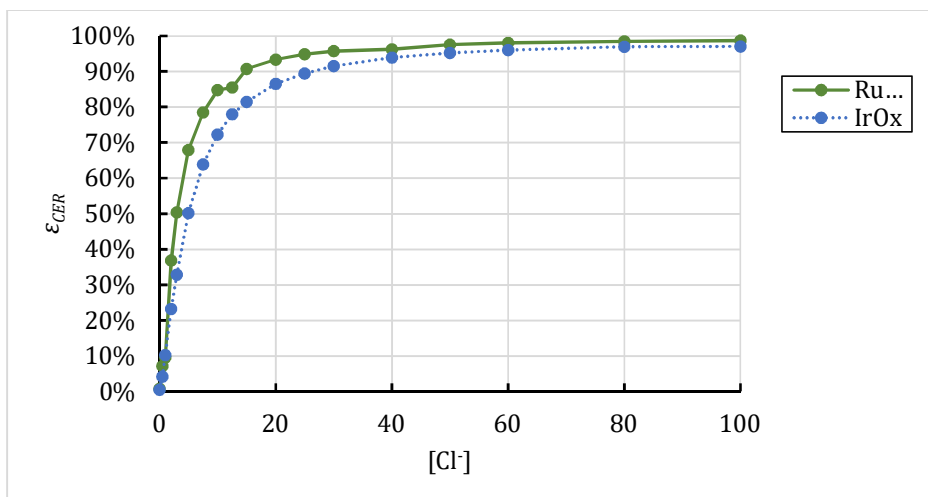
Figure A 9.2.5: ε_{CER} vs. [Cl^-] curve at E_D = 1.530 V vs. RHE for dropcasted RuO_2 (Sigma-Aldrich) versus the electroflocculated IrO_x catalyst, in 0.5 M $KHSO_4$ and increasing amounts of KCl, at 1500 RPM. The RuO_2 was dropcasted on the GC support from a 1 mg/mL suspension in EtOH, and air dried while rotating at 200 RPM. Final catalyst loading ~ 100 µg * cm^{-2}.
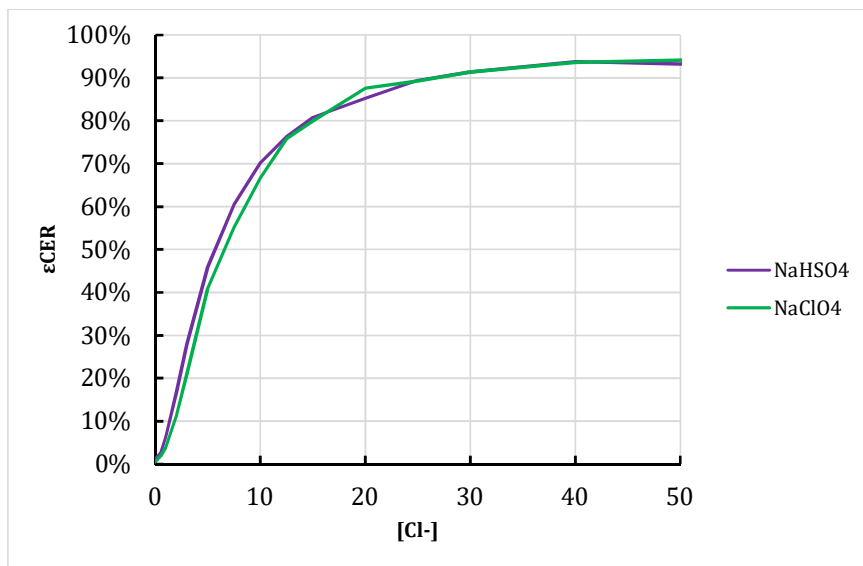
Figure A 9.2.6: ε_{CER} vs. $[Cl^-]$ on electroflocculated IrO$_x$, in a 0.5 M NaHSO$_4$ solution of pH 0.804 (purple curve) and a 0.5 M NaClO$_4$ + HClO$_4$ solution of pH 0.776 (green curve). Disk potential: ED = 1.530 V, 1500 RPM.

9.3. Supporting information for Chapter 3

9.3.1. *Estimation of error due to Ir dissolution and redeposition during RRDE experiments*

In the following, we will describe the estimation of error in the ring response caused by Ir-related dissolution during RRDE experiments. It is assumed that there are two sources of error:

- Stray ring currents due to the reduction of higher-oxidized, transiently dissolved Ir^{x+} species;
- Errors in Cl$_2$ detection due to a slowing-down of the chlorine reduction reaction (CRR) after the deposition of IrO$_x$ on the ring.

It must be noted that the latter error may in fact be vanishingly small, since prior experiments (not shown) indicated that the CRR also progresses rapidly on IrO$_x$. The reaction, like its CER counterpart, seems kinetically quite facile on metal oxides.[135,349] Nonetheless, the possible error will be considered for the sake of completeness.

From ICP-MS data, we assume that during vigorous OER and/or CER, Ir dissolves at an average rate of 1 ng cm^{-2} s^{-1} (see Figure 3.1 in the main text). For stray reduction currents on the ring, we assume that Ir in the form of the unknown Ir^{x+} species has a valency of +6, such as in the case of gaseous IrO$_3$ or soluble IrO$_4^{2-}$,[161] and that its primary reduction reaction at 0.95 V vs. RHE is 2-electron in nature. The stray reduction current density on the ring can then be estimated as:

$$j = 10^{-3} \text{ µg Ir cm}^{-2} \text{ s}^{-1} * \frac{2F}{M_{Ir}} * N \approx 0.25 \text{ µA cm}^{-2} \qquad \text{Eq. A 9.3.1}$$

where $M_{Ir} = 192.22$ µg Ir/µmol Ir is the molar mass of Ir, $N \approx 0.25$ is the collection factor, and $F = 96485$ µC/µmol Ir . This current density is orders of magnitude lower than typical experimental results and can thus be safely neglected.

Concerning IrO_x deposition on the ring, we assume that Ir^{x+} species deposit as crystalline, rutile-type IrO_2, and determine the minimum time required to form a perfect monolayer of IrO_2 on an ideal, ring-sized flat surface. This minimum time is:

$$t = \frac{1}{N} \frac{A_R}{A_D} * \frac{\rho_{IrO_2,m} * d_{IrO_2}}{10^{-3} \text{ µg Ir cm}^{-2} \text{ s}^{-1}} * \frac{10^6 \text{ µg}}{1 \text{ g}} * M_{Ir} \approx 670 \text{ s} \qquad \text{Eq. A 9.3.2}$$

This equation represents the amount of mol IrO_2 in a perfect monolayer on the ring surface divided by the molar rate of Ir deposition per surface area, which is the Ir dissolution on the disk corrected by N. $A_R = \pi \left[\left(\frac{0.75 \text{ cm}}{2} \right)^2 - \left(\frac{0.65 \text{ cm}}{2} \right)^2 \right] \approx 0.11 \text{ cm}^2$ is the ring geometric surface area, $A_D = 0.196 \text{ cm}^2$ is the disk surface area, $\rho_{IrO_2,m} = \frac{\rho_{IrO_2}}{M_{IrO_2}} = \frac{11.66 \text{ g cm}^{-3}}{224.22 \text{ g mol}^{-1}}$ is the molar density of rutile IrO_2, and $d_{IrO_2} \approx 3 * 10^{-8}$ cm is the estimated thickness of a monolayer rutile IrO_2, which was arbitrarily chosen as the c-direction (in the a-direction, $d_{IrO_2} \approx 5 * 10^{-8}$ cm, which would lead to even longer deposition times). This deposition time represents the absolute worst-case scenario for IrO_x, and is by itself at least an order of magnitude higher than the typical duration of a session of experiments. This suggests that interference with the CRR on the ring by stray IrO_x deposition is not an issue.

9.3.2. *Supplementary ICP-MS data*
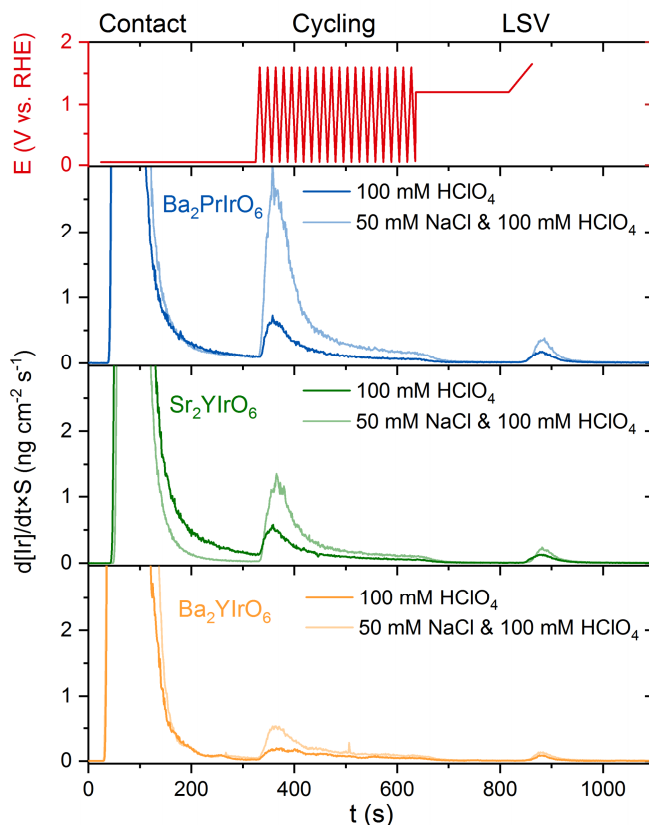
Figure A 9.3.1: ICP-MS measurements shown in Figure 3.1, including the initial contact peak.

Table A 9.3.1: Catalyst spot sizes (in cm²) and loadings during ICP measurements.

	0.1 M HClO$_4$	0.1 M HClO$_4$ + 50 mM NaCl
Ba$_2$PrIrO$_6$	0.009 (9.00 µg/cm^2)	0.011 (7.36 µg/cm^2)
Ba$_2$PrIrO$_6$ with Nafion	0.015 (5.4 µg/cm^2)	0.010 (8.1 µg/cm^2)
Sr$_2$YIrO$_6$	0.012 (6.75 µg/cm^2)	0.013 (6.23 µg/cm^2)
Ba$_2$YIrO$_6$	0.010 (8.1 µg/cm^2)	0.013 (6.23 µg/cm^2)
Ba$_2$CeIrO$_6$	0.010 (8.1 µg/cm^2)	0.014 (8.79 µg/cm^2)

Table A 9.3.2: Total dissolved amounts (TDA) of all elements after the ICP-MS experiments (in ng cm^{-2}).

Perovskite (A_2BIrO_6)	Electrolyte	Contact dissolution			Cycling dissolution			LSV dissolution			S-Number
		A	B	Ir	A	B	Ir	A	B	Ir	N_{gas}/N_{Ir}
Ba_2PrIrO_6	0.1 M HClO$_4$	1681	1134	1612	0	0	43	2	0	8	2285
	0.1 M HClO$_4$ + 50 mM NaCl	1284	965	2036	0	1	196	0	0	16	1196
Ba_2PrIrO_6 (without Nafion)	0.1 M HClO$_4$	272	361	1263	0	1	17.6	0	0	1.5	4067
	0.1 M HClO$_4$ + 50 mM NaCl	719	662	2215	0	0	23.4	0	0	3.6	2142.5
Sr_2YIrO_6	0.1 M HClO$_4$	1102	950	1577	3	0	28	0	0	6	3782
	0.1 M HClO$_4$ + 50 mM NaCl	896	673	1189	1	0	102	0	0	9	1610
Ba_2YIrO_6	0.1 M HClO$_4$	454	473	1478	0	0	24.7	0	0	2.9	3528
	0.1 M HClO$_4$ + 50 mM NaCl	641	623	2252	0	0	49.7	0	0	5	1883
Ba_2CeIrO_6	0.1 M HClO$_4$	645	385	1840	0	0	0	0	0	0	n.a.
	0.1 M HClO$_4$ + 50 mM NaCl	1580	1408	4409	0	0	21.6	0	0	4	2115

$$S = \frac{n(\text{Gas})}{n(\text{Ir})} = \frac{n(O_2 + Cl_2)}{n(\text{Ir})} = \frac{\left[\frac{\int I\,dt}{4 \times F}\right] \times Y_{O_2} + \left[\frac{\int I\,dt}{2 \times F}\right] \times Y_{Cl_2}}{\frac{m(\text{Ir})}{M(\text{Ir})}} \qquad \text{Eq. A 9.3.3}$$

Eq. A 9.3.3 was used for calculating the S-number. Here the moles of evolved gas, $n(\text{Gas})$, is comprised of $\int I\,dt$ as the charge passed during the LSV, F as Faraday's constant, Y_{O_2} and Y_{Cl_2} as the fractional yields of the OER and CER respectively, taken from RRDE experiments in presence of 50 mM NaCl. The dissolved moles of iridium, $n(\text{Ir})$, is calculated from the mass dissolved, $m(\text{Ir})$, and its molar weight $M(\text{Ir})$.

9.3.3. *Supplementary XRD and RRDE data*
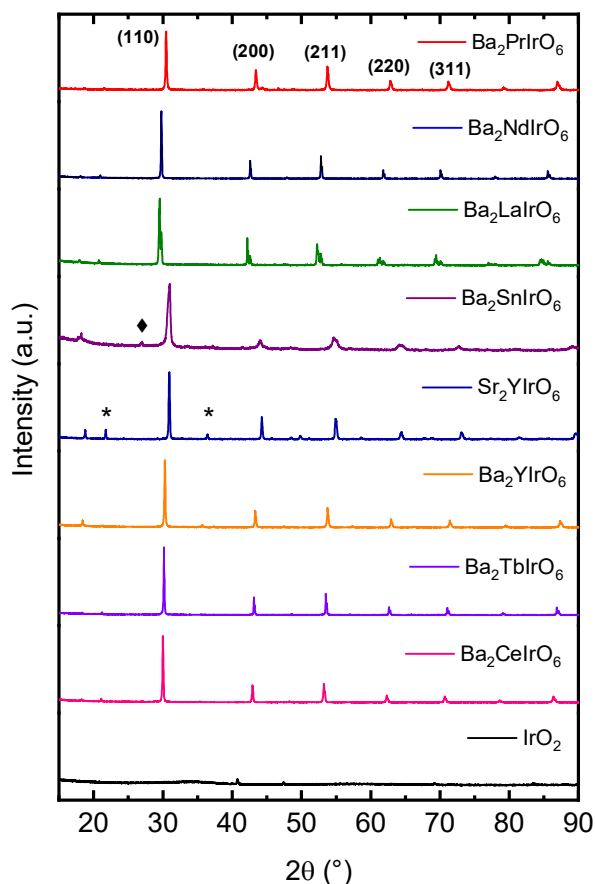
Figure A 9.3.2: X-ray powder diffraction patterns of the iridium-based double perovskites used in this study, together with the commercial IrO_2 reference. Strong lines are characteristic of the primitive perovskite and the indexing of some of these reflections is given. Some visible superlattice reflections are marked by *. Note that in Ba_2SnIrO_6, a small contamination from $BaIrO_3$ is also visible (marked by ♦).
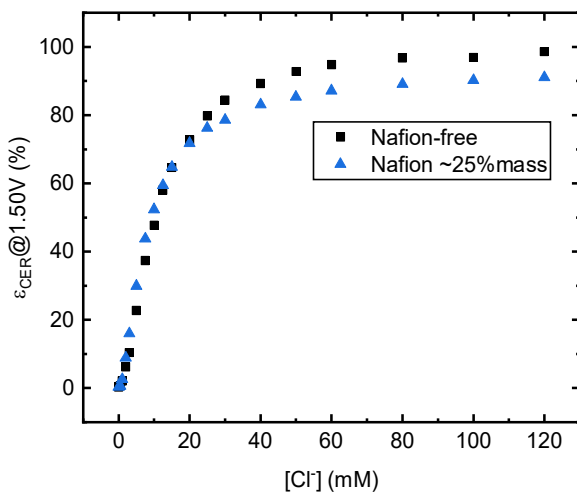
Figure A 9.3.3: The effect of Nafion binder on apparent CER selectivity. Shown is the CER selectivity ε_{CER} as a function of $[Cl^-]$ in a solution of 0.1 M $HClO_4$, for Ba_2PrIrO_6 dropcasted from an EtOH suspension (black) and Ba_2PrIrO_6 dropcasted from an EtOH suspension containing 0.23 mg Nafion copolymer per mg Ba_2PrIrO_6. Prior to mixing, the Nafion sulfonate groups were partially Na-exchanged by mixing commercial 5%wt stock solution (purchased from Sigma-Aldrich) with 0.1 M NaOH in a ratio of 2:1. Selectivity values shown at 1.50 V, obtained with the RRDE method as described in the main text.
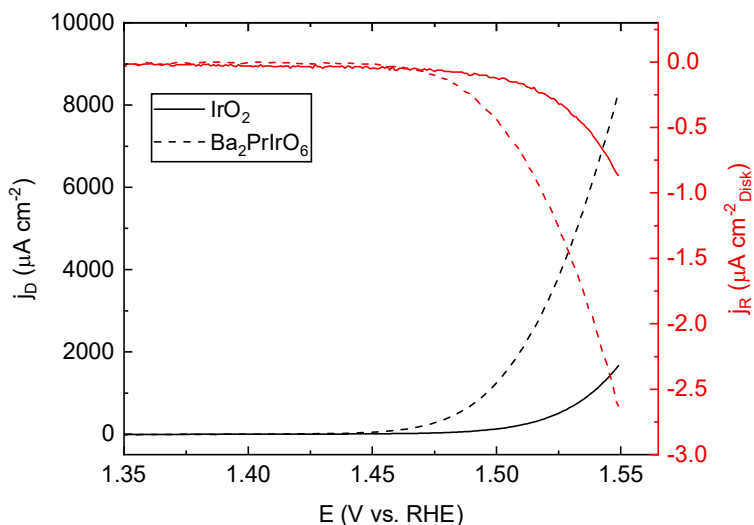
Figure A 9.3.4: The RRDE ring response at 0.95 V during OER in chloride-free conditions. Comparison of disk and ring current densities measured on IrO_2 (solid traces) and Ba_2PrIrO_6 (dotted traces) in 0.1 M $HClO_4$, with the ring fixed at 0.95 V.
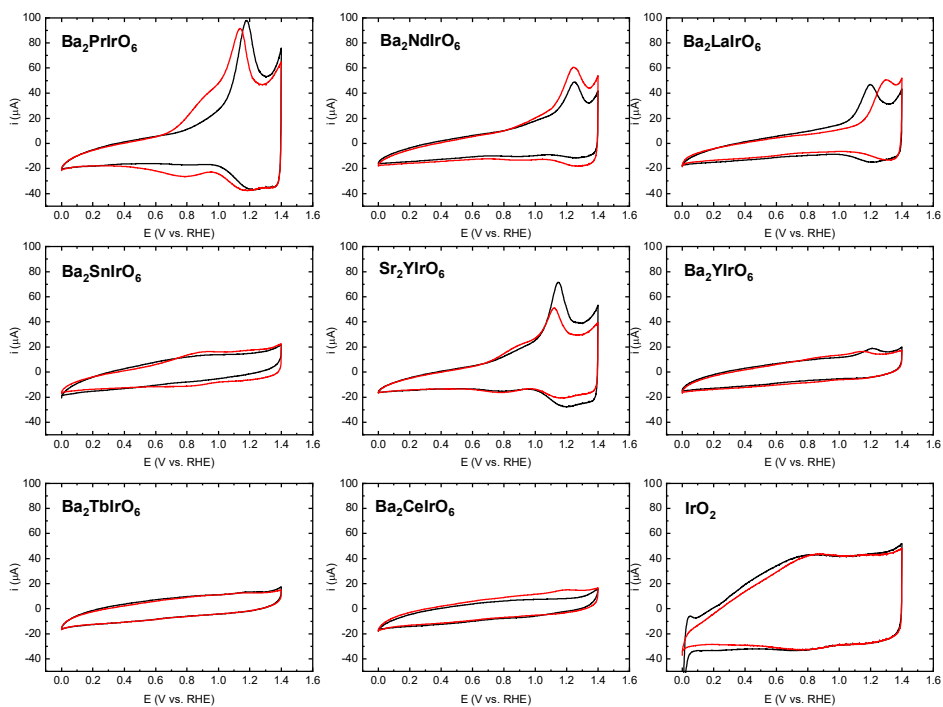
Figure A 9.3.5: The effect of repeated scanning on voltammetric characterizations. Shown are comparisons of blank voltammograms of the GC-supported materials in 0.1 M $HClO_4$. Black curves: 'pristine' state (after contact with the solution at 0.05 V for approximately 30 seconds). Red curves: surfaces after extensive scanning (at least 20 cycles) in the range of 1.30 – 1.55 V at 1500 RPM. Scan rate: 50 mV s^{-1}.
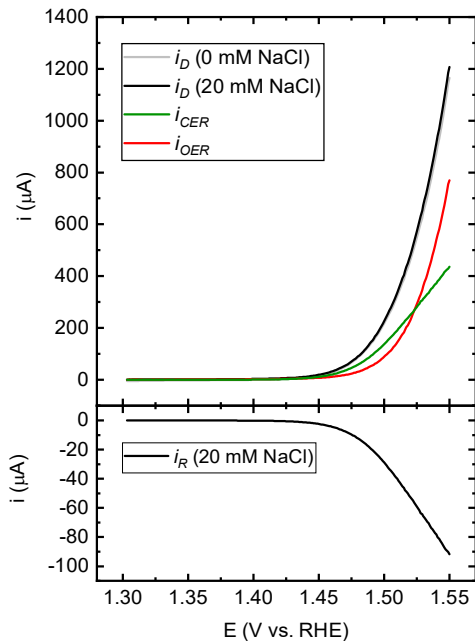
Figure A 9.3.6: Example curve of a RRDE experiment to illustrate the deconvolution of parallel evolution of oxygen and chlorine. Top panel displays disk currents (i_D) measured on a GC-supported Ba_2NdIrO_6 thin film, in a NaCl-free solution of 0.1 M $HClO_4$ (grey curve) and in a solution composed of 0.1 M $HClO_4$ and 20 mM NaCl (black curve). Rotation rate: 1500 RPM. Lower panel shows corresponding currents measured on the Pt ring (i_R) fixed at a potential of 0.95 V in presence of 20 mM NaCl. The calculation of i_{OER} and i_{CER} curves was performed using the ring currents and $N_{Cl_2} = 0.215$, see also Eq. 2.1 and Eq. 2.2.
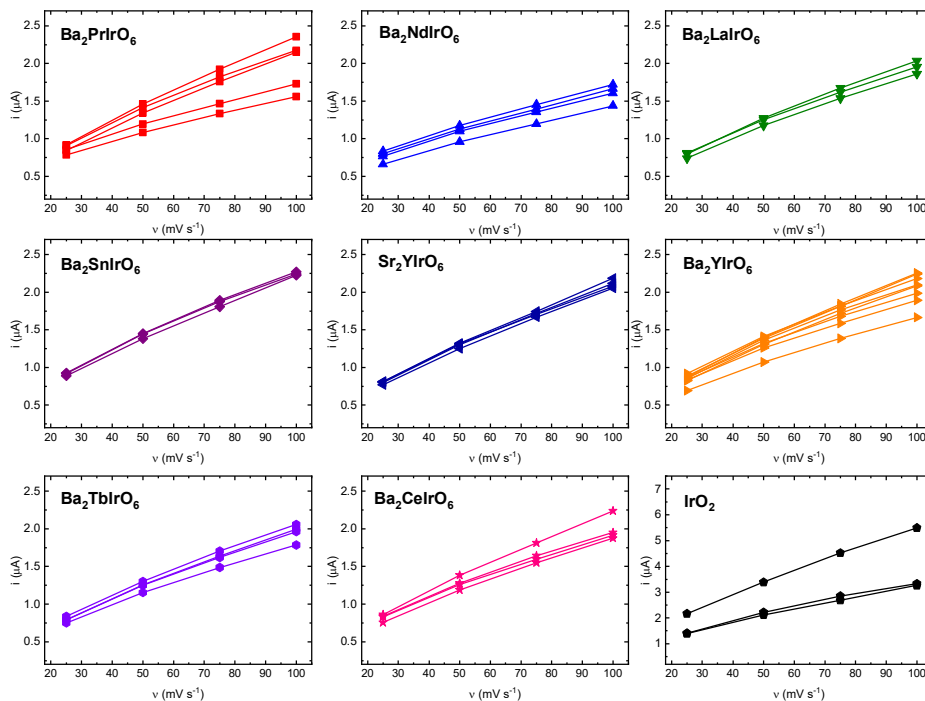
Figure A 9.3.7: Measured currents at 0.1 V as a function of scan rate in the potential region 0.05 – 0.15 V, for all performed RRDE activity experiments. Lines correspond to individual experiments for each material. Note the difference in scale for the lrO$_2$ experiments.
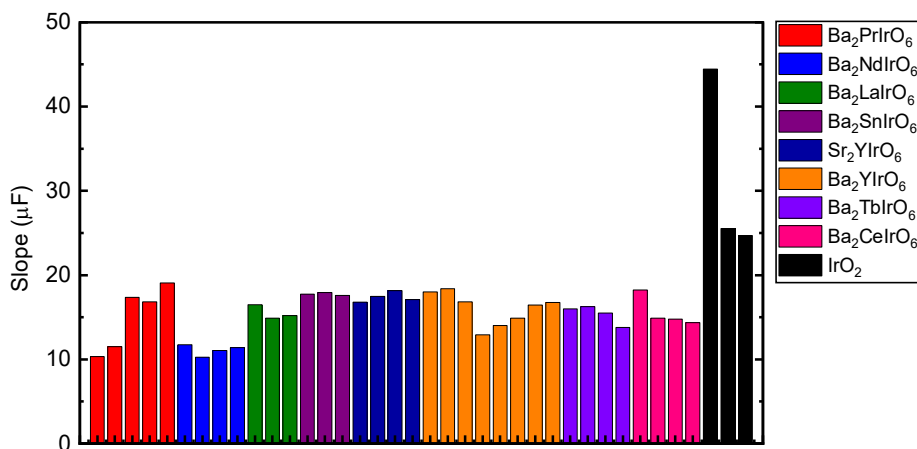
Figure A 9.3.8: Measured values of $(C_{dl})_{0.1\,V}$ for performed RRDE activity experiments on the basis of Figure A 9.3.7. Bars correspond to individual experiments.
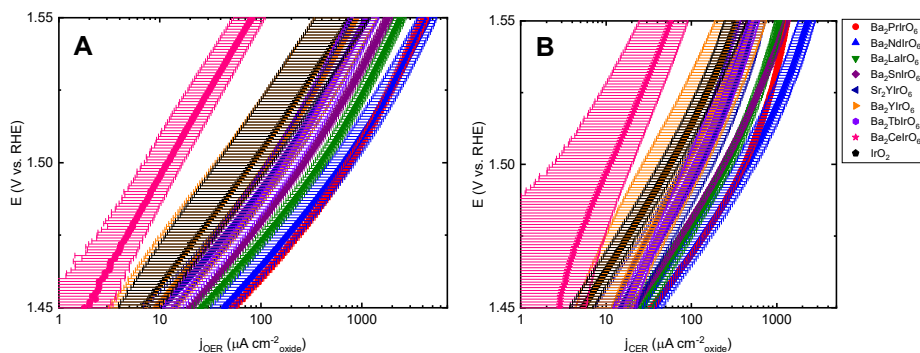
Figure A 9.3.9: Standard deviations in RRDE activity experiments. Shown are OER (A) and CER (B) Tafel curves as in Figure 3.3, including standard deviations around the average values.

Table A 9.3.3: Measured average linear Tafel slopes for OER (in Cl^--free electrolyte and in presence of 20 mM Cl^-) and CER, in potential ranges 1.45 – 1.50 V and 1.50 – 1.55 V. Standard errors of at least three independent measurements (using freshly prepared catalyst films) are indicated. Color scale (bottom) indicates the correlation coefficient, expressing the degree of linearity of each segment; green corresponds to R^2 = 1.000, red corresponds to R^2 = 0.980.

	CER (mV/dec)		OER, $[Cl^-]$ = 0 mM (mV/dec)		OER, $[Cl^-]$ = 20 mM (mV/dec)	
	1.45-1.50 V	1.50-1.55 V	1.45-1.50 V	1.50-1.55 V	1.45-1.50 V	1.50-1.55 V
Ba_2PrIrO_6	45 ± 0.8	90 ± 10	43 ± 0.7	67 ± 1.7	46 ± 2.1	55 ± 1.4
Ba_2NdIrO_6	46 ± 2.8	69 ± 2.1	42 ± 0.4	60 ± 2.1	53 ± 2.0	49 ± 1.2
Ba_2LaIrO_6	49 ± 3.0	82 ± 1.3	42 ± 0.4	64 ± 0.5	47 ± 1.4	53 ± 0.3
Sr_2YIrO_6	52 ± 2.5	80 ± 3.6	42 ± 2.4	59 ± 1.9	50 ± 17	51 ± 2.7
Ba_2SnIrO_6	47 ± 1.2	67 ± 0.4	44 ± 0.4	60 ± 0.4	65 ± 1.0	54 ± 0.3
Ba_2YdIrO_6	59 ± 9.0	66 ± 3.8	46 ± 2.0	56 ± 2.4	80 ± 25	53 ± 2.9
Ba_2TbIrO_6	60 ± 14	77 ± 1.0	45 ± 1.9	63 ± 1.0	46 ± 6.3	55 ± 1.9
Ba_2CeIrO_6	70 ± 10	67 ± 5.4	60 ± 5.7	59 ± 1.7	230 ± 22	89 ± 5.4
IrO_2	49 ± 1.0	68 ± 0.4	46 ± 0.8	52 ± 0.5	60 ± 2.0	53 ± 1.0

R^2				
0.980	0.985	0.990	0.995	1.000
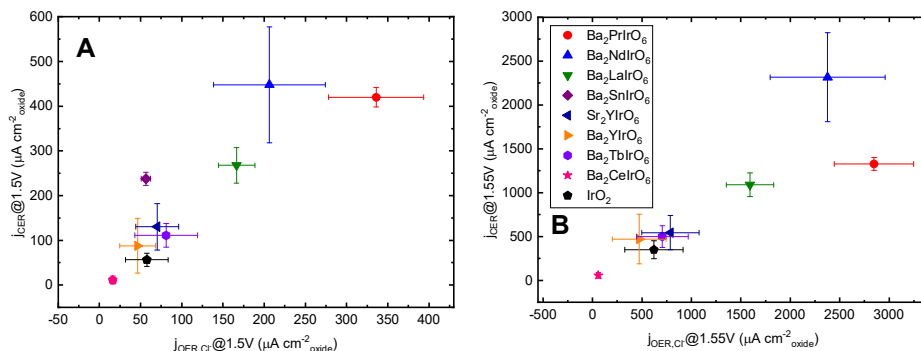
Figure A 9.3.10: Correlations between OER and CER activities, similar to Figure 3.4, but now comparing OER activity in the presence of 20 mM NaCl, at 1.50 V (A) and 1.55 V (B). Data derived from Figure 3.3B and Figure 3.6A, error bar show the standard deviation from at least three independent measurements.
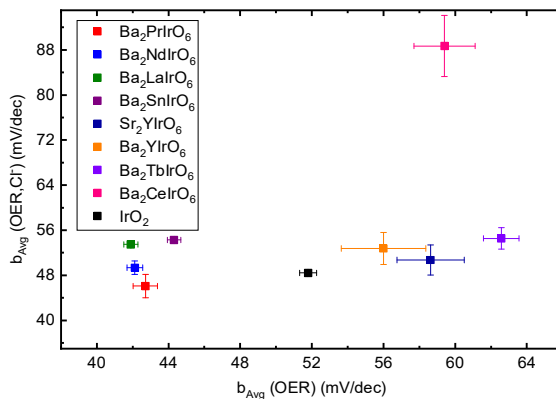
Figure A 9.3.11: Comparison of linear Tafel slope values for the OER, before and after NaCl addition (data from Table A 9.3.3).
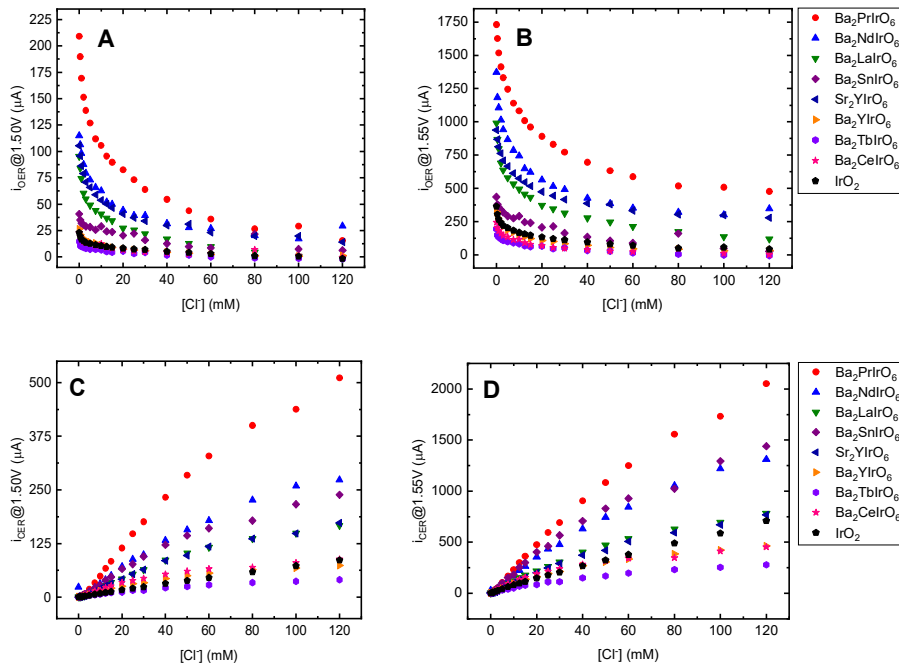
Figure A 9.3.12: Absolute OER currents (A and B) and CER currents (C and D) for all measured materials as function of increasing chloride concentration, at 1.50 V (A and C) and 1.55 V (B and D).
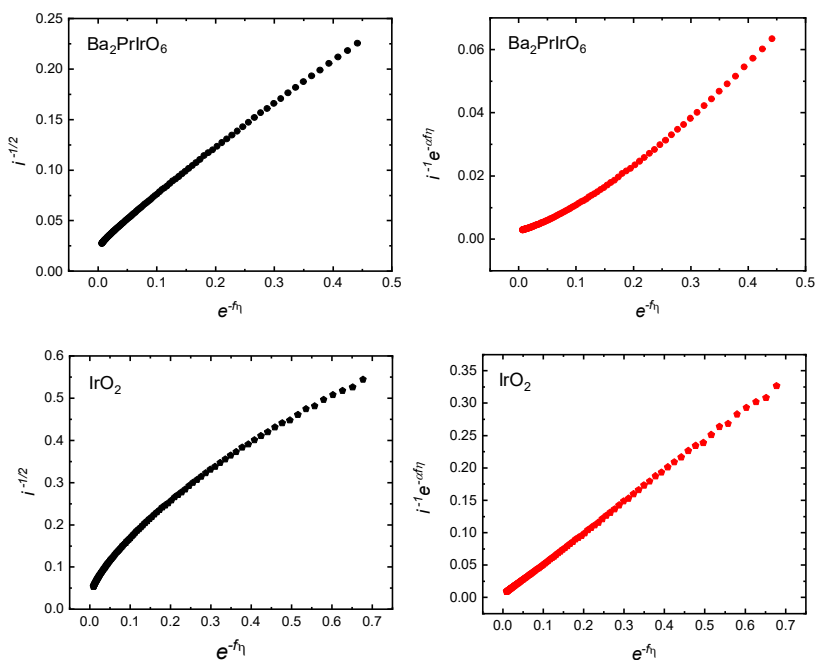
Figure A 9.3.13: Conway-Novák test plots (black) and Ferro-de Battisti test plots (red) for Ba_2PrIrO_6 and IrO_2. Conway and Novák proposed[118] that a straight line in a plot of $i^{-1/2}$ vs. $e^{-f\eta}$ is evidence of a Tafel-limited recombination mechanism with a Volmer pre-equilibrium. Extending this, Ferro *et al.*[113] proposed plotting $i^{-1}e^{\alpha f\eta}$ vs. $e^{-f\eta}$, where a straight line would instead suggest a Heyrovský (or Krishtalik) controlled mechanism. As in the main text, $\eta = E - E_0$ is the overpotential for CER, and $f = {F}/{(RT)}$. In the method by Ferro *et al.* α is not known beforehand. It can be estimated by observing the unique value of α (besides possibly $\alpha = 1$) which results in a straight line, if any. E_0 was estimated by observing the onset of linearity in E vs. $\log|i_R|$ plots. In the case of IrO_2, α was chosen such that the resulting theoretical Tafel slope was 47 mV/dec, in accordance with data from Table A 9.3.3.
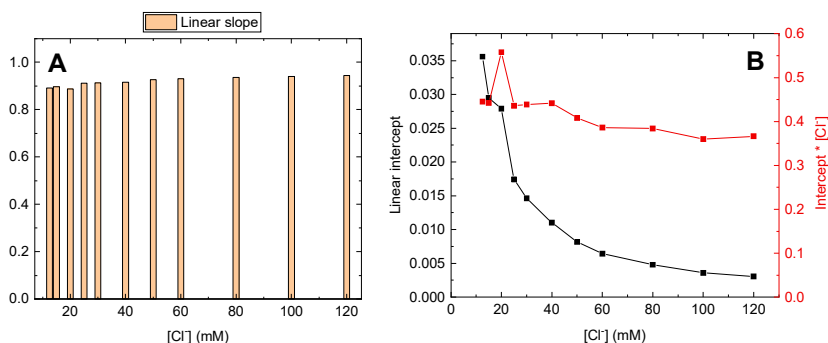
Figure A 9.3.14: Extracted values of the slope (A) and intercept (B) in the linear region as function of $[Cl^-]$, using data from Ferro-de Battisti plots as shown in Figure A 9.3.13, for IrO_2. Red trace in B shows the value of the intercept multiplied by the chloride concentration.

The appearance of a straight line in a Ferro-de Battisti plot does not discern between the V-H and the V-K mechanism. However, the method does lead to alternating predictions of the slope and intercept dependence. For the V-H pathway, these are given by $(2Fk_H^0K_V'[Cl^-]^2)^{-1}$ and $(2Fk_H^0[Cl^-])^{-1}$, respectively; In case the V-K mechanism dominates, it predicts $(2Fk_K^0K_V'[Cl^-])^{-1}$ and $(2Fk_K^0)^{-1}$. One can observe that the intercept in B shows a marked dependence on $[Cl^-]^{-1}$, which fits better with the V-H mechanism.

We further have to note that the chloride dependence of the slope remains quite constant versus $[Cl^-]$. Although this contradicts both the V-H and V-K predictions at first glance, it must be noted that the slope value is affected as well by the pseudo-equilibrium constant K_V', the value of which depends strongly on $[Cl^-]$.[118] Interpretation of the slopes is thus not straightforward.
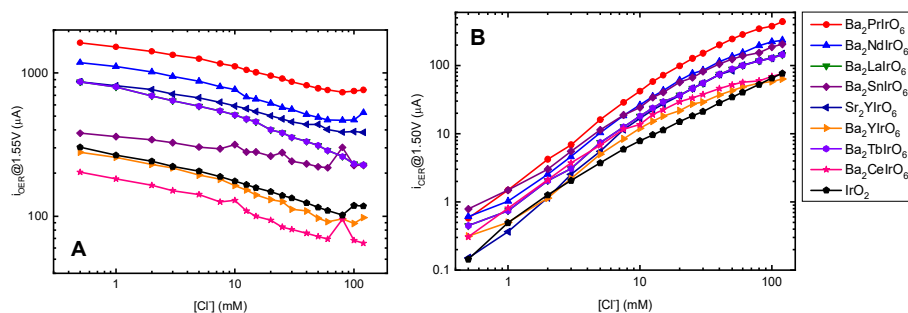
Figure A 9.3.15: Log-log plots of Figure A 9.3.12B (A) Figure A 9.3.12C (B).
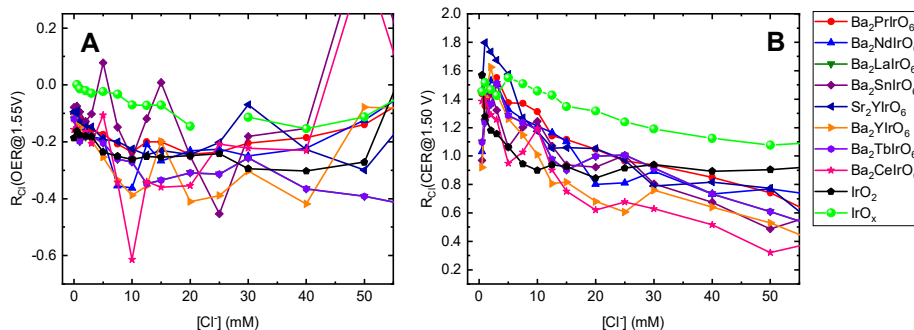
Figure A 9.3.16: Zoom of data in the 0-50 mM concentration range shown in Figure 3.7.

9.4. Supporting information for Chapter 4

9.4.1. *Thermodynamic data of (inter)halogen species*

Table A 9.4.1: Reactions of interhalogen compounds involving Cl and Br between formal oxidation states -1 and 0, in aqueous acidic conditions (pH < 1). Values as reported by Wang *et al.*[210] Additionally shown are standard redox potentials of equivalent electrochemical reactions. Participation of the species Cl_3^-, whose concentration is generally small, is ignored. Also included are standard literature values for the BER, CER, and OER. Note that the OER is pH-dependent on the NHE scale.

[a] The value of K_1 was determined from literature values and standard redox potentials.

Reaction	Equilibrium constant	Electrochemical reaction	Standard potential
$2\,BrCl \rightleftharpoons Cl_2 + Br_2$	$K_D = 5 * 10^{-3}$	$BrCl + 2\,e^- \rightleftharpoons Br^- + Cl^-$	$E^0_{BrCl} = 1.19$ V vs. NHE
$Cl_2 + Br^- \rightleftharpoons BrCl_2^-$	$K_1 = 4.6 * 10^6$ M^{-1} [a]	$BrCl_2^- + 2\,e^- \rightleftharpoons Br^- + 2\,Cl^-$	$E^0_{BrCl_2^-} = 1.16$ V vs. NHE
$BrCl + Cl^- \rightleftharpoons BrCl_2^-$	$K_2 = 6.0$ M^{-1}		
$BrCl + Br^- \rightleftharpoons Br_2Cl^-$	$K_3 = 1.8 * 10^4$ M^{-1}	$Br_2Cl^- + 2\,e^- \rightleftharpoons 2\,Br^- + Cl^-$	$E^0_{Br_2Cl^-} = 1.08$ V vs. NHE
$Br_2 + Cl^- \rightleftharpoons Br_2Cl^-$	$K_4 = 1.3$ M^{-1}		
$Br_2 + Br^- \rightleftharpoons Br_3^-$	$K_{Br} = 16.1$ M^{-1}	$Br_3^- + 2\,e^- \rightleftharpoons 3\,Br^-$	$E^0_{Br_3^-/Br^-} = 1.04$ V vs. NHE

9.4.2. *Theoretical Tafel slopes and reaction orders for elementary kinetic mechanisms involving competitive adsorption*

We will first regard the BER as the main reaction, with Cl^- as a competitive inhibitor for Br^- adsorption. As also shown in the main text, the fractional coverage of bromide θ_{Br} can be written using the mean-field Langmuir isotherm according to:

$$\theta_{Br} = \frac{K_{Br}[Br^-]e^{f\eta}}{K_{Br}[Br^-]e^{f\eta} + K_{Cl}[Cl^-]e^{f\eta} + 1} \qquad \text{Eq. A 9.4.1}$$

The theoretical BER $j–\eta$ relationships for the Volmer-Tafel and Volmer-Heyrovský mechanisms can be written as:

$$j_{VT} = 2Fk_T(\theta_{Br})^2 = 2Fk_T\left(\frac{K_{Br}[Br^-]e^{f\eta}}{K_{Br}[Br^-]e^{f\eta} + K_{Cl}[Cl^-]e^{f\eta} + 1}\right)^2 \qquad \text{Eq. A 9.4.2}$$

$$j_{VH} = Fk_H e^{\alpha_H f\eta}[\text{Br}^-]\theta_{Br} = Fk_H \frac{K_{Br}[\text{Br}^-]^2 e^{(\alpha_H+1)f\eta}}{K_{Br}[\text{Br}^-]e^{f\eta} + K_{Cl}[\text{Cl}^-]e^{f\eta} + 1} \qquad \text{Eq. A 9.4.3}$$

The Br^- reaction order $\mathcal{R}_{\text{Br}^-}$ of the overall reaction always contains a contribution from the surface-bound intermediate;[112] in case of the Langmuir isotherm, this 'surface reaction order' can be written as:

$$\mathcal{R}_{\text{Br}^-}^S = \frac{\partial \ln \theta_{Br}}{\partial \ln[\text{Br}^-]} = 1 - \theta_{Br} \qquad \text{Eq. A 9.4.4}$$

This relationship is valid regardless of whether competitive adsorption of Cl^- takes place. The effect of inhibition is implicitly included in θ_{Br} (see Eq. A 9.4.1). In case of a Volmer-Tafel mechanism, $\mathcal{R}_{\text{Br}^-}$ is then always positive and dependent on the surface coverage θ_{Br}. It can be written as:[112]

$$\mathcal{R}_{\text{Br}^-} = \frac{\partial \ln j}{\partial \ln[\theta_{Br}]} * \frac{\partial \ln \theta_{Br}}{\partial \ln[\text{Br}^-]} = 2(1 - \theta_{Br}) \qquad \text{Eq. A 9.4.5}$$

Since it is assumed that the Cl^- competitor does not react further after adsorbing, it affects the overall reaction order only through the surface reaction order. Its reaction order $\mathcal{R}_{\text{Cl}^-}$ can therefore be written as:

$$\mathcal{R}_{\text{Cl}^-} = \frac{\partial \ln \theta_{Br}}{\partial \ln[\text{Cl}^-]} = -\theta_{Cl} \qquad \text{Eq. A 9.4.6}$$

The values are always negative, as can be expected for a competitively adsorbing species. The BER dependence on Br^- and Cl^- predicted by the V-T, V-H and V-K mechanisms can then be expressed as shown below in Table A 9.4.2, along with some general limiting cases (Table A 9.4.3). In general, competitive adsorption does not change the *possible* limiting values of $\mathcal{R}_{\text{Br}^-}$, but it may change the 'width' of the Br^- isotherm. It affects the range of values of $[\text{Br}^-]$ or η within which b and $\mathcal{R}_{\text{Br}^-}$ can vary. Whereas reaction orders should always approach their lower limit at high overpotentials (0, 1 and 0 for the V-T, V-H and V-K mechanisms, respectively), competitive adsorption may lead to other limiting values for high η, depending on the values of $K_{Br}[\text{Br}^-]$ and $K_{Cl}[\text{Cl}^-]$ (see Table A 9.4.3).

Table A 9.4.2: Theoretical Tafel slopes and reaction orders for Cl^- and Br^- in case of two step Volmer-Tafel or Volmer-Heyrovský BER reaction mechanisms, where Cl^- is a competitive electrochemical adsorbate. Relations for competition-free cases are obtained by setting $[Cl^-] = 0$.

	Volmer-Heyrovský	**Volmer-Krishtalik**
Tafel slope $b = \left(\dfrac{\partial \log j}{\partial \eta}\right)^{-1}$	$\dfrac{\ln(10)}{f}\left(\dfrac{K_{Br}[Br^-]e^{f\eta} + K_{Cl}[Cl^-]e^{f\eta} + 1}{\alpha_H(K_{Br}[Br^-]e^{f\eta} + K_{Cl}[Cl^-]e^{f\eta} + 1) + 1}\right)$	Same as Volmer-Heyrovský
Br^- reaction order $\mathcal{R}_{Br^-} = \dfrac{\partial \ln j}{\partial \ln[Br^-]}$	$2 - \theta_{Br}$ $= \dfrac{K_{Br}[Br^-]e^{f\eta} + 2K_{Cl}[Cl^-]e^{f\eta} + 2}{K_{Br}[Br^-]e^{f\eta} + K_{Cl}[Cl^-]e^{f\eta} + 1}$	$1 - \theta_{Br}$ $= \dfrac{K_{Cl}[Cl^-]e^{f\eta} + 1}{K_{Br}[Br^-]e^{f\eta} + K_{Cl}[Cl^-]e^{f\eta} + 1}$
Cl^- reaction order $\mathcal{R}_{Cl^-} = \dfrac{\partial \ln j}{\partial \ln[Cl^-]}$	$-\theta_{Cl}$ $= -\left(\dfrac{K_{Cl}[Cl^-]e^{f\eta}}{K_{Br}[Br^-]e^{f\eta} + K_{Cl}[Cl^-]e^{f\eta} + 1}\right)$	Same as Volmer-Heyrovský
	Volmer-Tafel	
Tafel slope $b = \left(\dfrac{\partial \log j}{\partial \eta}\right)^{-1}$	$\dfrac{\ln(10)}{2f}\dfrac{1}{(1 - \theta_{Br} - \theta_{Cl})}$ $= \dfrac{\ln(10)}{2f}(K_{Br}[Br^-]e^{f\eta} + K_{Cl}[Cl^-]e^{f\eta} + 1)$	
Br^- reaction order $\mathcal{R}_{Br^-} = \dfrac{\partial \ln j}{\partial \ln[Br^-]}$	$2(1 - \theta_{Br})$ $= 2\left(\dfrac{K_{Cl}[Cl^-]e^{f\eta} + 1}{K_{Br}[Br^-]e^{f\eta} + K_{Cl}[Cl^-]e^{f\eta} + 1}\right)$	
Cl^- reaction order $\mathcal{R}_{Cl^-} = \dfrac{\partial \ln j}{\partial \ln[Cl^-]}$	$-2\theta_{Cl}$ $= -2\left(\dfrac{K_{Cl}[Cl^-]e^{f\eta}}{K_{Br}[Br^-]e^{f\eta} + K_{Cl}[Cl^-]e^{f\eta} + 1}\right)$	

Table A 9.4.3: Cases of limiting behavior for two-step reaction BER mechanisms involving Cl^- as competitively adsorbing (but otherwise unreactive) species. Values are shown for the overpotential η and 'adsorption strength' $K_i[i^-]$ of the various species. It was assumed that $\alpha_H = 0.5$.

Limiting case		Volmer-Heyrovský	Volmer-Krishtalik
Tafel slope b	$\eta \to 0$	$b \approx 40$ mV dec^{-1} if $K_{Br}[Br^-] = K_{Cl}[Cl^-] \approx 0$ $b \to 120$ mV dec^{-1} for either $K_{Br}[Br^-] \to \infty$ or $K_{Cl}[Cl^-] \to \infty$	Same as Volmer-Heyrovský
	$\eta \to \infty$	$b \to 120$ mV dec^{-1}	
Br^- reaction order $\mathcal{R}_{Br^-}$	$\eta \to 0$	$\mathcal{R}_{Br^-} \approx 2$ if $K_{Br}[Br^-] \approx 0$ $1 \leq \mathcal{R}_{Br^-} \leq 2$ if $K_{Cl}[Cl^-] \approx 0$	$\mathcal{R}_{Br^-} \approx 1$ if $K_{Br}[Cl^-] \approx 0$ $0 \leq \mathcal{R}_{Br^-} \leq 1$ if $K_{Cl}[Cl^-] \approx 0$
	$\eta \to \infty$	$\dfrac{K_{Br}[Br^-] + 2K_{Cl}[Cl^-]}{K_{Br}[Br^-] + K_{Cl}[Cl^-]}$	$\dfrac{K_{Cl}[Cl^-]}{K_{Br}[Br^-] + K_{Cl}[Cl^-]}$
Cl^- reaction order $\mathcal{R}_{Cl^-}$	$\eta \to 0$	$\mathcal{R}_{Cl^-} \approx 0$ if $K_{Cl}[Cl^-] \approx 0$ $-1 \leq \mathcal{R}_{Cl^-} \leq 0$ if $K_{Br}[Br^-] \approx 0$	Same as Volmer-Heyrovský
	$\eta \to \infty$	$-\left(\dfrac{K_{Cl}[Cl^-]}{K_{Br}[Br^-] + K_{Cl}[Cl^-]}\right)$	

Limiting case		Volmer-Tafel
Tafel slope b	$\eta \to 0$	$b \approx 30$ mV dec^{-1} if $K_{Br}[Br^-] = K_{Cl}[Cl^-] \approx 0$ $b \to \infty$ for either $K_{Br}[Br^-] \to \infty$ or $K_{Cl}[Cl^-] \to \infty$
	$\eta \to \infty$	$b \to \infty$
Br^- reaction order $\mathcal{R}_{Br^-}$	$\eta \to 0$	$\mathcal{R}_{Br^-} \approx 2$ if $K_{Br}[Br^-] \approx 0$ $0 \leq \mathcal{R}_{Br^-} \leq 2$ if $K_{Cl}[Cl^-] \approx 0$
	$\eta \to \infty$	$2\left(\dfrac{K_{Cl}[Cl^-]}{K_{Br}[Br^-] + K_{Cl}[Cl^-]}\right)$
Cl^- reaction order $\mathcal{R}_{Cl^-}$	$\eta \to 0$	$\mathcal{R}_{Cl^-} \approx 0$ if $K_{Cl}[Cl^-] \approx 0$ $-2 \leq \mathcal{R}_{Cl^-} \leq 0$ if $K_{Br}[Br^-] \approx 0$
	$\eta \to \infty$	$-2\left(\dfrac{K_{Cl}[Cl^-]}{K_{Br}[Br^-] + K_{Cl}[Cl^-]}\right)$

Besides exerting a simple blocking effect, chloride could also become involved in follow-up reactions when Br is co-adsorbed on the surface, such as BrCl formation. The corresponding reaction pathway would be similar to Volmer-Tafel, reminiscent of a Langmuir-Hinshelwood mechanism in heterogeneous gas-phase catalysis:

$$\text{Br}^- + * \rightleftarrows \text{Br}^* + \text{e}^- \qquad\qquad \text{Eq. A 9.4.7}$$

$$\text{Cl}^- + * \rightleftarrows \text{Cl}^* + \text{e}^- \qquad\qquad \text{Eq. A 9.4.8}$$

$$\text{Br}^* + \text{Cl}^* \rightleftarrows \text{BrCl} + 2 * \qquad\qquad \text{Eq. A 9.4.9}$$

We apply the same assumptions regarding the Cl and Br adsorption isotherms as discussed previously. Neglecting the backward reaction, the current-potential relation then becomes:

$$j_3 = 2\text{F}k_3\theta_{Br}\theta_{Cl} = 2\text{F}k_3\left(\frac{(K_{Br}K_{Cl}[\text{Br}^-][\text{Cl}^-])^{\frac{1}{2}}e^{f\eta}}{K_{Br}[\text{Br}^-]e^{f\eta} + K_{Cl}[\text{Cl}^-]e^{f\eta} + 1}\right)^2 \qquad \text{Eq. A 9.4.10}$$

where k_3 is the chemical forward rate constant for recombination in Eq. A 9.4.9. Eq. A 9.4.10 predicts Tafel slopes identical to the V-T mechanism of either the BER or CER, under the effect of competitive adsorption between Br^- and Cl^- (see Table A 9.4.2).

Although less likely on Pt, one can also consider a Volmer-Heyrovský mechanism for BrCl formation, via two analogous pathways:

$$\text{Br}^- + * \rightleftarrows \text{Br}^* + \text{e}^- \qquad\qquad \text{Eq. A 9.4.11}$$

$$\text{Br}^* + \text{Cl}^- \rightleftarrows \text{BrCl} + \text{e}^- + * \qquad\qquad \text{Eq. A 9.4.12}$$

$$\text{Cl}^- + * \rightleftarrows \text{Cl}^* + \text{e}^- \qquad\qquad \text{Eq. A 9.4.13}$$

$$\text{Cl}^* + \text{Br}^- \rightleftarrows \text{BrCl} + \text{e}^- \qquad\qquad \text{Eq. A 9.4.14}$$

On the potential scale of the second step, which concerns electrochemical desorption with two different atom types, both mechanisms have a forward reaction that (under the assumption that α_H is identical for both) is proportional to:

$$j \propto \frac{[\text{Br}^-][\text{Cl}^-]e^{(\alpha_H+1)f\eta}}{K_{Cl}[\text{Cl}^-]e^{f\eta} + K_{Br}[\text{Br}^-]e^{f\eta} + 1} \qquad \text{Eq. A 9.4.15}$$

The Tafel slopes predicted by Eq. A 9.4.15 are the same as predicted by the V-H mechanism for the BER or CER under the effect of Br^- and Cl^- competitive adsorption (Table A 9.4.2).

Finally, BrCl formation mechanisms can be written for a pathway analogous to the Volmer-Krishtalik mechanism. In the V-K pathway, the order of adsorption does matter. The reactant that adsorbs first (which is likely Br^-, due to its higher adsorption strength[218]) has a reaction order according to $\mathcal{R} = 1 - \theta$, whereas the second reactant (which is not involved in the rate-determining step or preceding steps) behaves purely competitive, such that $\mathcal{R} = -\theta$, even though it is necessary for the reaction to occur.

The theoretical Tafel slopes for the formation of BrCl from a V-T, V-H or V-K type mechanism are the same as shown in Table A 9.4.2. The reaction orders are shown in Table A 9.4.4 below. For the V-T mechanism, $\mathcal{R}_{\text{Cl}^-}$ and $\mathcal{R}_{\text{Br}^-}$ can now vary between -1 and 1.

Table A 9.4.4: Theoretical reaction orders for Cl^- and Br^- in case of BrCl reaction mechanisms.

	Volmer-Tafel	**Volmer-Heyrovský**
Br^- reaction order $\mathcal{R}_{\text{Br}^-}$	$1 - 2\theta_{Br}$ $= \dfrac{K'_{Cl}[\text{Cl}^-]e^{f\eta_1} - K_{Br}[\text{Br}^-]e^{f\eta_1} + 1}{K'_{Br}[\text{Br}^-]e^{f\eta_1} + K_{Cl}[\text{Cl}^-]e^{f\eta_1} + 1}$	$1 - \theta_{Br}$ $= \dfrac{K''_{Cl}[\text{Cl}^-]e^{f\eta_2} + 1}{K'_{Cl}[\text{Cl}^-]e^{f\eta_2} + K''_{Br}[\text{Br}^-]e^{f\eta_2} + 1}$
Cl^- reaction order $\mathcal{R}_{\text{Cl}^-}$	$1 - 2\theta_{Cl}$ $= \dfrac{K'_{Br}[\text{Br}^-]e^{f\eta_1} - K_{Cl}[\text{Cl}^-]e^{f\eta_1} + 1}{K'_{Br}[\text{Br}^-]e^{f\eta_1} + K_{Cl}[\text{Cl}^-]e^{f\eta_1} + 1}$	$1 - \theta_{Cl}$ $= \dfrac{K''_{Br}[\text{Br}^-]e^{f\eta_2} + 1}{K'_{Cl}[\text{Cl}^-]e^{f\eta_2} + K''_{Br}[\text{Br}^-]e^{f\eta_2} + 1}$
	Volmer-Krishtalik	
Br^- reaction order $\mathcal{R}_{\text{Br}^-}$	$1 - \theta_{Br}$ if $\mathcal{R}_{\text{Cl}^-} = -\theta_{Cl}$ $-\theta_{Br}$ if $\mathcal{R}_{\text{Cl}^-} = 1 - \theta_{Cl}$	
Cl^- reaction order $\mathcal{R}_{\text{Cl}^-}$	$1 - \theta_{Cl}$ if $\mathcal{R}_{\text{Br}^-} = -\theta_{Br}$ $-\theta_{Cl}$ if $\mathcal{R}_{\text{Br}^-} = 1 - \theta_{Br}$	

9.4.3. *Reaction orders measured versus constant overpotential*

Instead of referencing the applied potential to a fixed point according to $\eta = E - E^0$, it can be convenient to experimentally measure reaction orders versus constant overpotential, $\eta^* = E - E_{eq}$, where E_{eq} is the equilibrium potential of the reaction of interest under the corresponding experimental conditions.[118,350] Taking the CER as example, η and η^* are related through the Nernst equation:

$$e^{f\eta} = \frac{[\text{Cl}_2]^{\frac{1}{2}}}{[\text{Cl}^-]} e^{f\eta^*} \qquad \text{Eq. A 9.4.16}$$

When re-writing the Volmer pre-equilibrium (Eq. 1.12 in Chapter 0) according to η^*:

$$\theta_{Cl}(\eta^*) = \frac{K_1[\text{Cl}_2]^{\frac{1}{2}}e^{f\eta^*}}{1 + K_1[\text{Cl}_2]^{\frac{1}{2}}e^{f\eta^*}} \qquad \text{Eq. A 9.4.17}$$

From Eq. A 9.4.17, is it clear that $\theta_{Cl}(\eta^*)$ is no longer dependent on $[\text{Cl}^-]$. The surface reaction order of chloride is therefore always zero versus constant overpotential:

$$\mathcal{R}^{S}_{\text{Cl}^-}(\eta^*) = \frac{\partial \ln \theta_{Cl}(\eta^*)}{\partial \ln[\text{Cl}^-]} = 0 \qquad\qquad \text{Eq. A 9.4.18}$$

Eq. A 9.4.18 implies that for the V-T mechanism, the overall chloride reaction order measured versus constant overpotential $\mathcal{R}_{\text{Cl}^-}(\eta^*)$ is always zero. In case of the V-H and V-K mechanism, it can be shown that $\mathcal{R}_{\text{Cl}^-}(\eta^*)$ corresponds to $1 - \alpha_H$ and $-\alpha_K$, respectively; the expected reaction orders are non-zero (and negative in the case of V-K), but independent of $[\text{Cl}^-]$ or η^*.

9.4.4. Various supplementary RRDE data
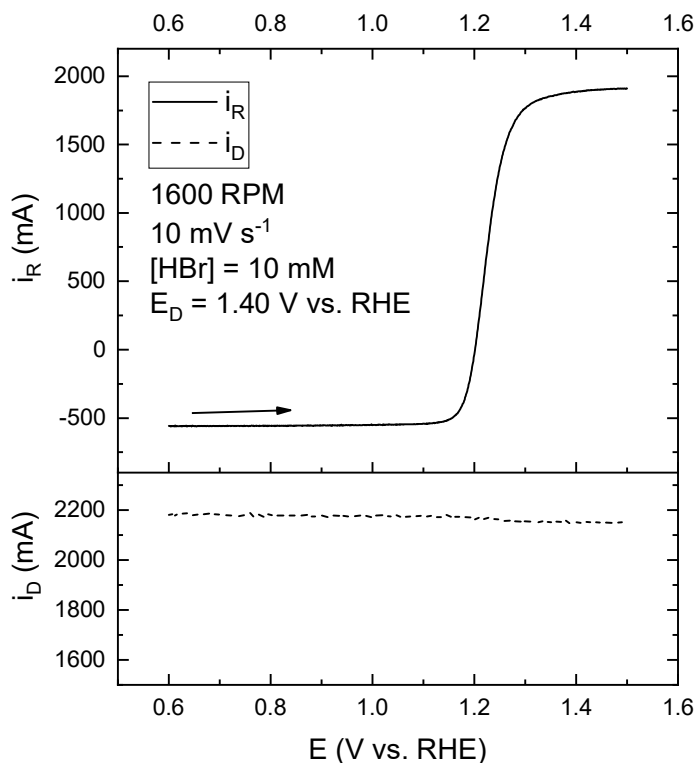
Figure A 9.4.1: Test of the bromine reduction reaction (BRR) diffusion limitation. Figure shows an LSV of a Pt-Pt RRDE electrode in a 0.1 M HClO$_4$ solution containing 10 mM HBr. The ring electrode was scanned (top) while keeping the disk at a fixed potential of 1.45 V vs. RHE (bottom), to provide a significant concentration of Br$_2$/Br$_3^-$ near the ring electrode surface. Diffusion limitation of the BRR sets in at roughly 1.05 V vs. RHE ($\eta \approx 150$ mV). Arrow indicates scan direction.
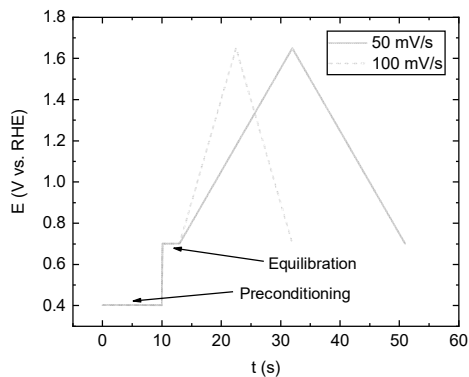
Figure A 9.4.2: Illustration of potential versus time program used during RRDE experiments, showing the preconditioning and equilibration steps during pre-treatment.
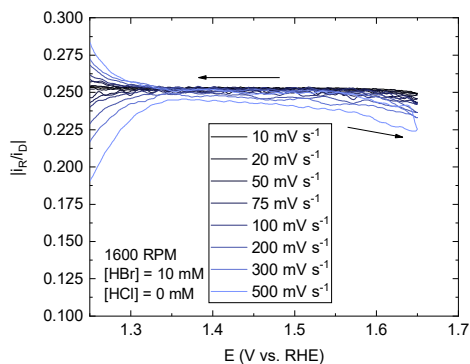
Figure A 9.4.3: Absolute values of ring/disk current ratios from Figure 4.1A. Arrows indicate scan direction.
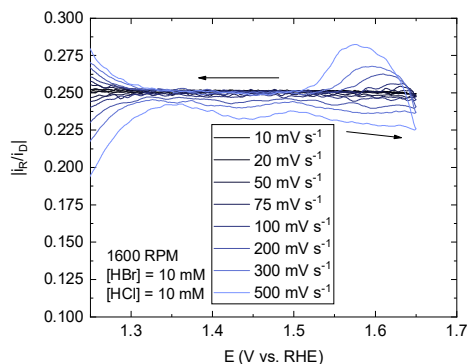
Figure A 9.4.4: Absolute values of ring/disk current ratios from Figure 4.1C. Arrows indicate scan direction.
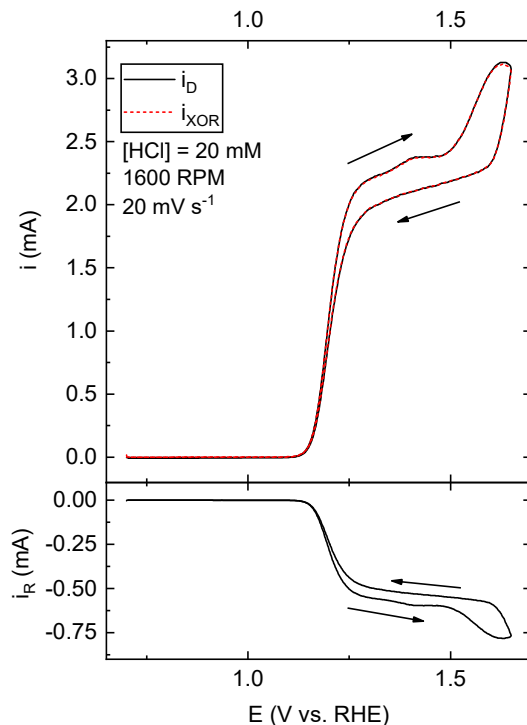
Figure A 9.4.5: Comparison of ring currents measured during an RRDE experiment. Data shown is a cyclic voltammogram of the Pt-Pt RRDE in a solution of 0.1 M $HClO_4$ + 10 mM HBr + 20 mM HCl, recorded at 20 mV s^{-1} at a fixed rotation rate of 1600 RPM. Black traces show disk (top panel) and ring (lower panel) currents. Red dashed trace shows the absolute value for the ring currents corrected for the RRDE collection factor, corresponding to currents from 'halogen oxidation reactions', i_{XOR}. Arrows indicate scan direction.
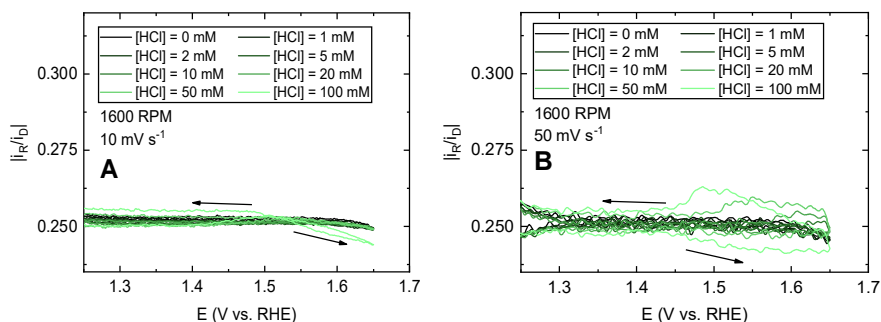
Figure A 9.4.6: Absolute values of ring/disk current ratios from Figure 4.2A (A) and Figure 4.2B (B). Arrows indicate scan direction.

9.4.5. *Supplementary bromide oxidation data*
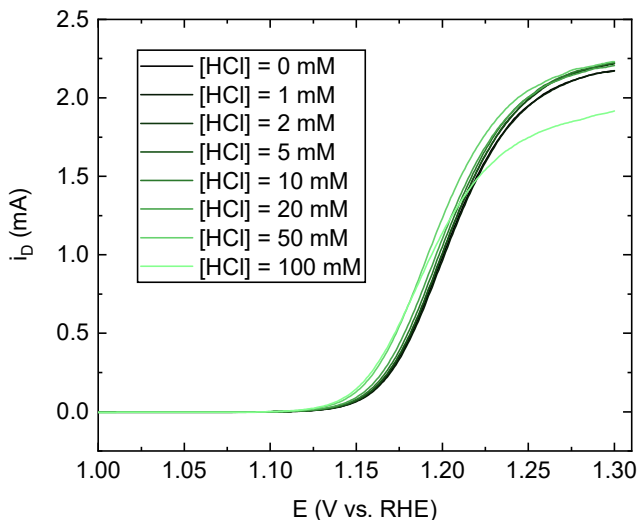
Figure A 9.4.7: Zoom of Figure 4.2A, centered around the onset of bromide oxidation as recorded on the RHE potential scale.
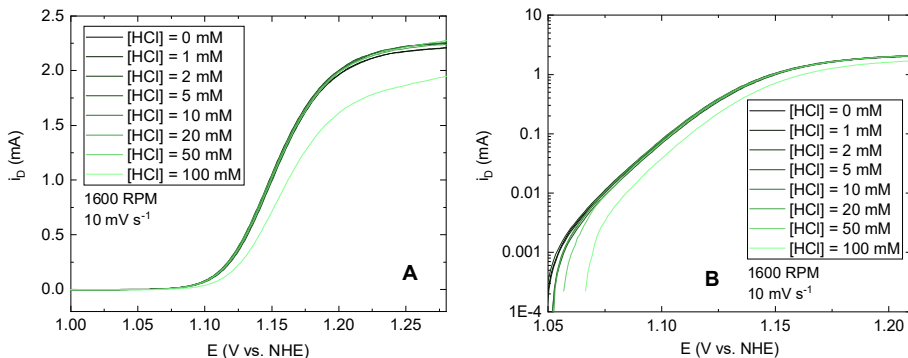
Figure A 9.4.8: Data from Figure A 9.4.7 converted to the NHE potential scale (A). B shows corresponding semilogarithmic plots of $\log(i_D)$ versus E.
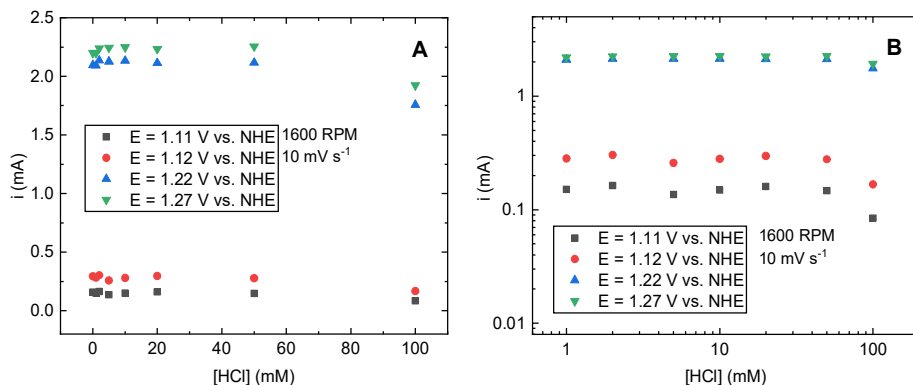
Figure A 9.4.9: Currents at constant potential values as function of HCl concentration (A), using data shown in Figure A 9.4.9. B: Corresponding log-log plots.
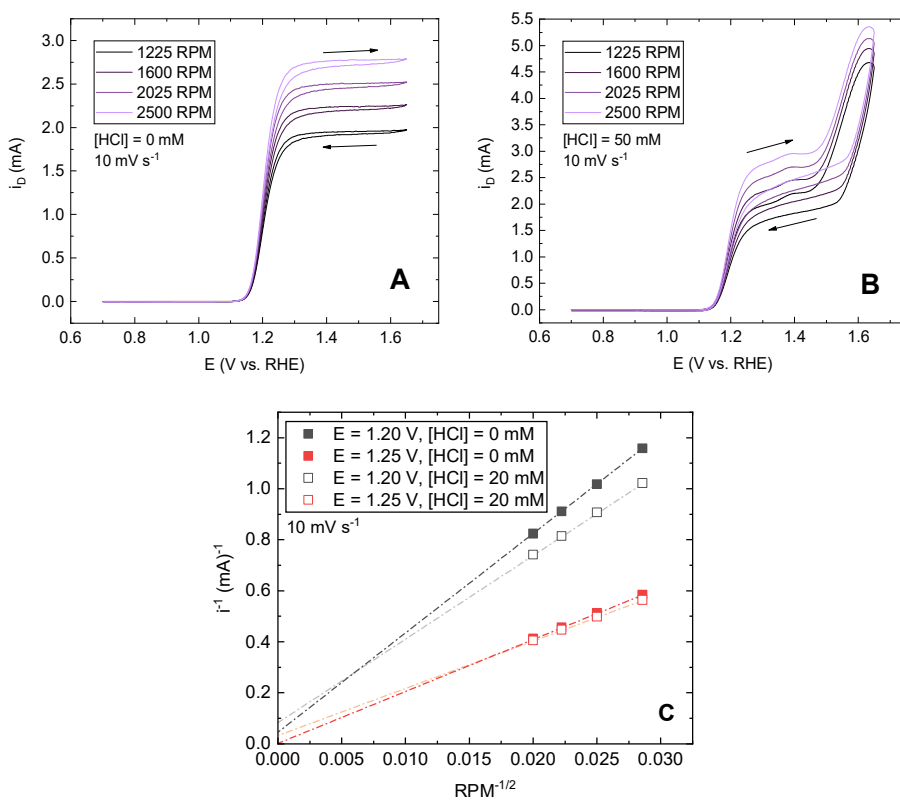
Figure A 9.4.10: Cyclic voltammograms of a Pt-Pt RRDE in a solution of 0.1 M HClO$_4$ + 10 mM HBr. A shows the effect of changing rotation rate, recorded at a scan rate of 10 mV s^{-1}. B shows the same experiment in the additional presence of 50 mM HCl. Arrows indicate scan direction. In C, typical examples of Koutecký-Levich plots are shown obtained from the forward scans of CVs such as shown in A and B.
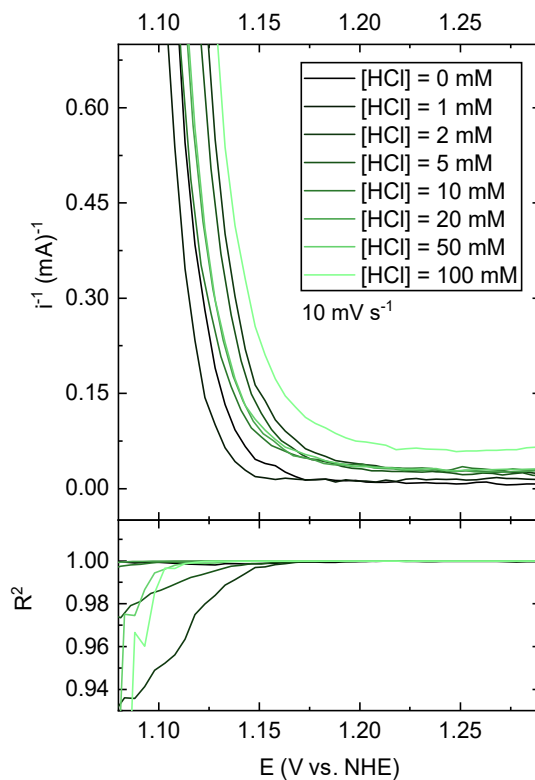
Figure A 9.4.11: Values of the y-intercept in Koutecký-Levich plots (see Figure A 9.4.10) across the bromide oxidation wave, as function of potential and chloride concentration. Lower panel shows the associated error in linearity of the underlying KL-plots.
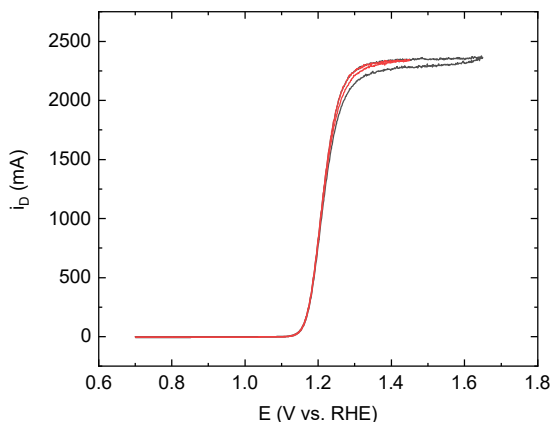
Figure A 9.4.12: Cyclic voltammogram of a Pt-Pt RRDE in a solution of 0.1 M $HClO_4$ + 10 mM HBr at a scan rate of 10 mV s^{-1} and rotation rate of 1600 RPM, showing the effect of the upper potential limit. Shown are potential cycles up to 1.65 V (black trace) and 1.45 V (red trace). Formation of PtO_x is apparent from increased hysteresis in the scan up to 1.65 V.
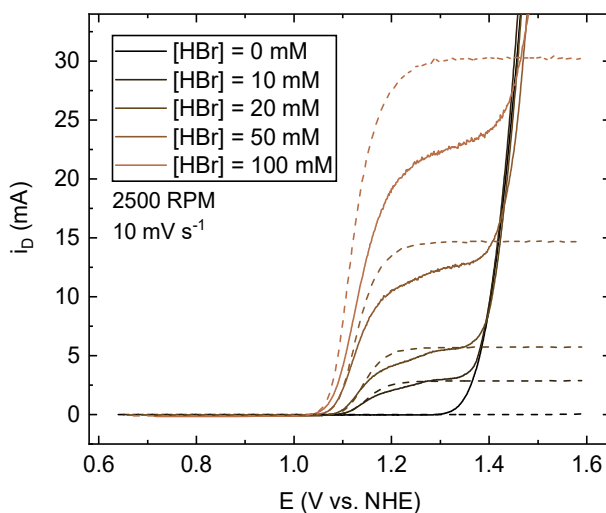
Figure A 9.4.13: Bromide oxidation currents measured under varying [HBr], in the presence of 0.1 M $HClO_4$ and 1 M HCl, measured at a fixed scan rate of 10 mV s^{-1} and rotation rate of 2500 RPM. Only forward scans are shown. Dashed lines correspond to BER data measured in absence of HCl under otherwise identical conditions.
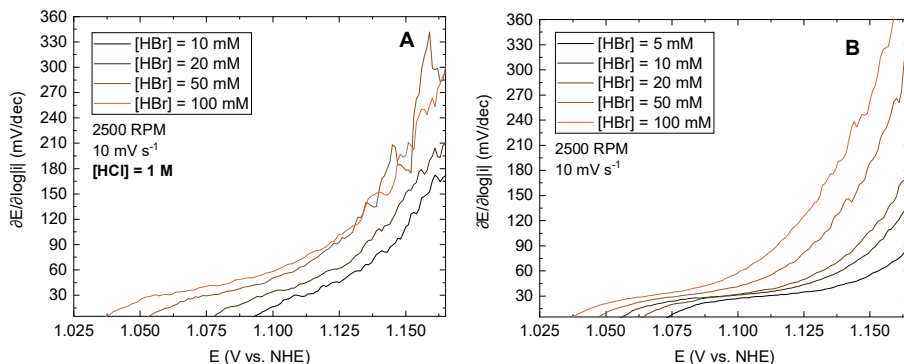
Figure A 9.4.14: Tafel slope values in activation-controlled bromide oxidation region of curves shown in Figure A 9.4.13. Only forward scans are shown. A: bromide oxidation for various [HBr] in presence of 1 M HCl (data from Figure A 9.4.13, solid lines). B: bromide oxidation for various [HBr] in absence of HCl (data from Figure A 9.4.13, dashed lines).
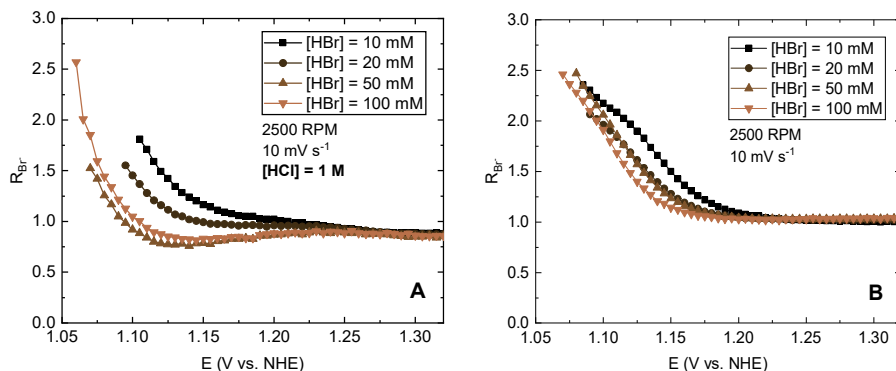
Figure A 9.4.15: Bromide reaction order $\mathcal{R}_{Br^-}$ in the bromide oxidation potential region, in presence (A) and absence (B) of 1 M HCl, based on data shown in Figure A 9.4.13. Values shown versus potential.

9.4.6. *Supplementary chloride oxidation data*
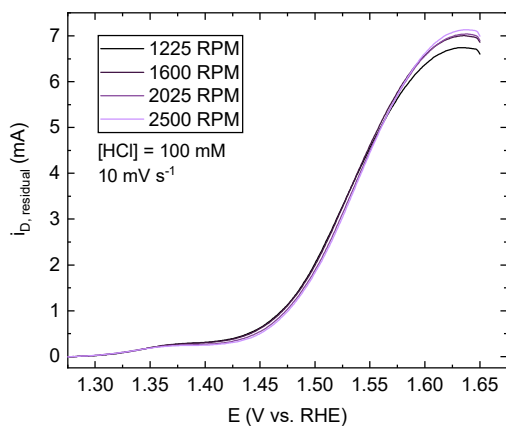
Figure A 9.4.16: Rotation rate dependence of the residual chloride oxidation currents after BER, such as in Figure 4.4, at a higher chloride concentration of 100 mM.
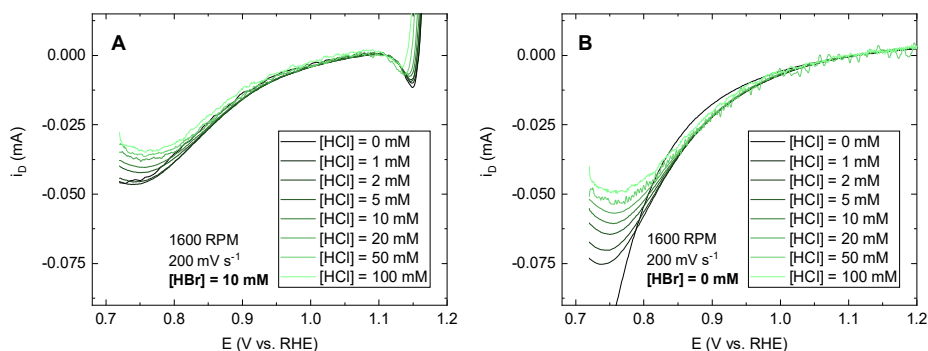
Figure A 9.4.17: PtO_x reduction peaks in the backward scans of RRDE experiments, as function of chloride concentration. Data with a relatively high scan rate (200 mV s^{-1}) were chosen where the reduction peaks are clearly visible. Shown are the reduction peaks in presence (A) and absence (B) of Br$^-$.
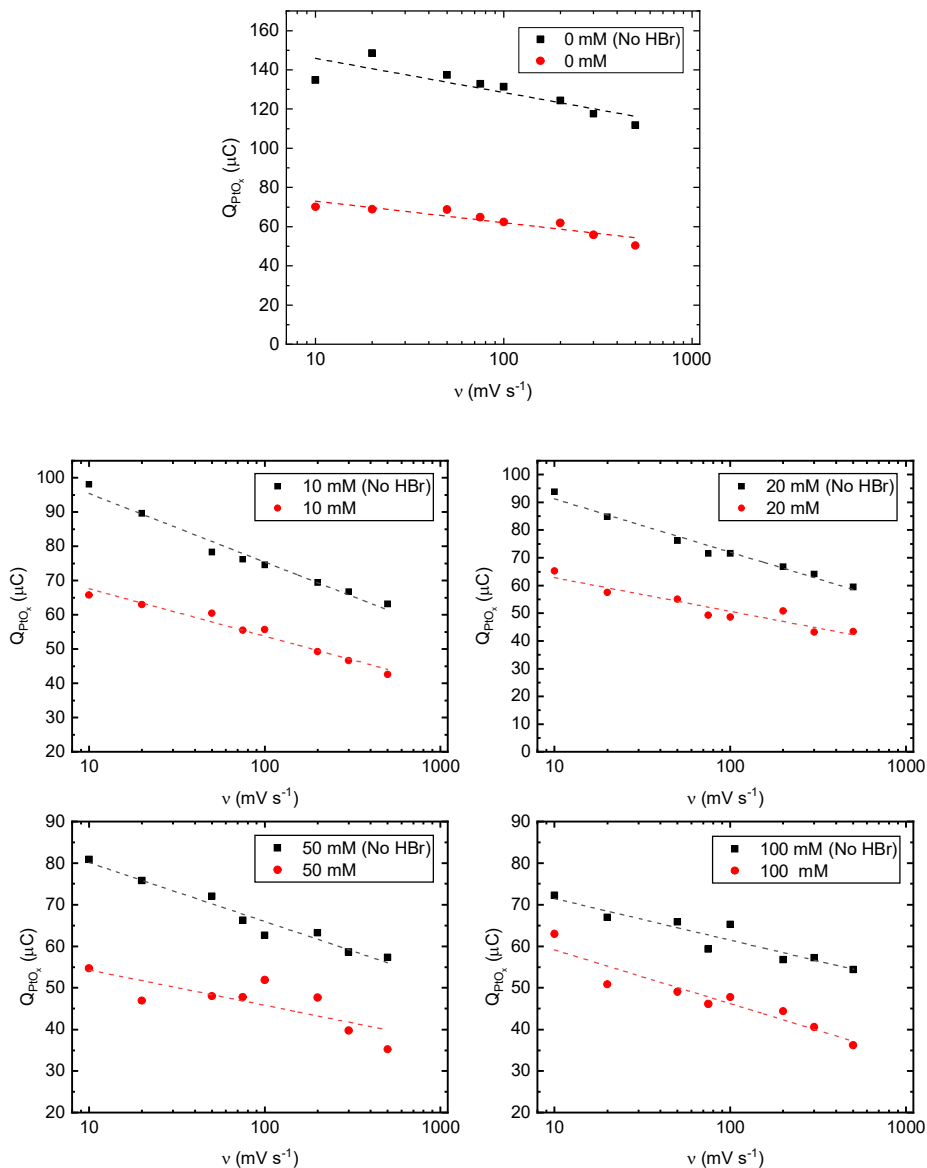
Figure A 9.4.18: Charges of the PtO$_x$ reduction peak (Q_{PtO_x}) as a function of scan rate, for varying [Cl$^-$] concentrations. Data is shown in presence (red) and absence (black) of 10 mM HBr. Top figure has data in absence of chloride ([HCl] = 0 mM). Data were determined from backward CV scans such as those in Figure A 9.4.17, by measuring the peak charge up until the potential of peak current and multiplying by two. This was made possible by the generally symmetric shape of reduction peaks.
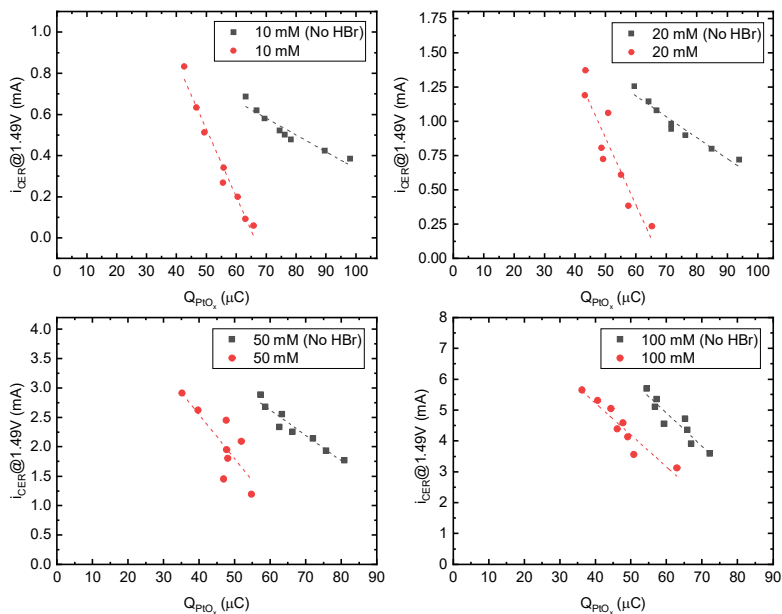
Figure A 9.4.19: CER currents obtained at 1600 RPM at 1.49 V vs. NHE, versus charges of the PtO_x reduction peak (Q_{PtO_x}), for varying $[Cl^-]/[Br^-]$ ratios (see also Figure A 9.4.18).
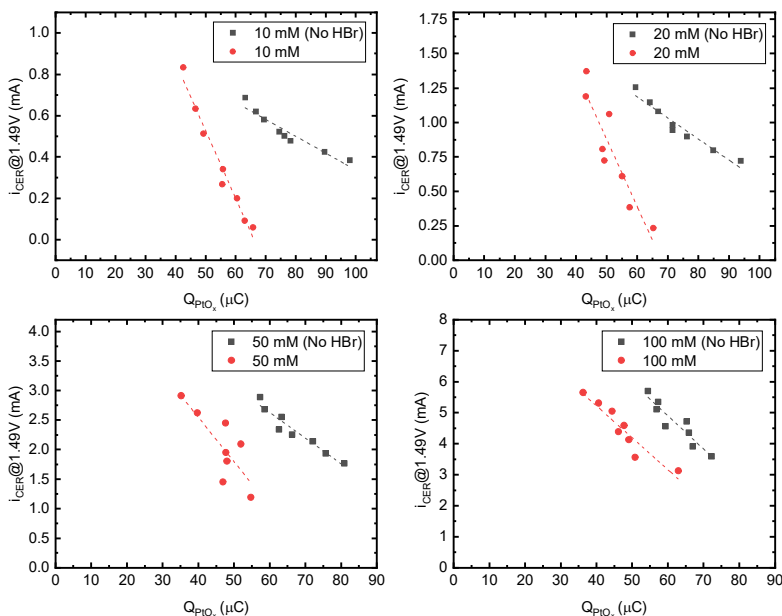
Figure A 9.4.20: Similar to Figure A 9.4.19, but showing CER currents obtained at 1.57 V vs. NHE.
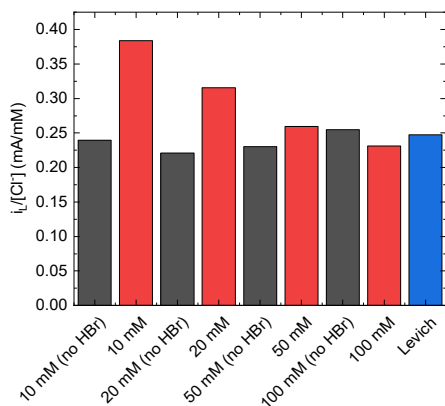
Figure A 9.4.21: Currents recorded at 1.57 V (Figure A 9.4.20) extrapolated to $Q_{PtO_x} = 0$ (a 'PtO_x-free' surface), along with diffusion-limited currents predicted by the Levich equation (blue). All values are shown normalized to the chloride concentration.

9.4.7. *Supplementary pre-peak data*
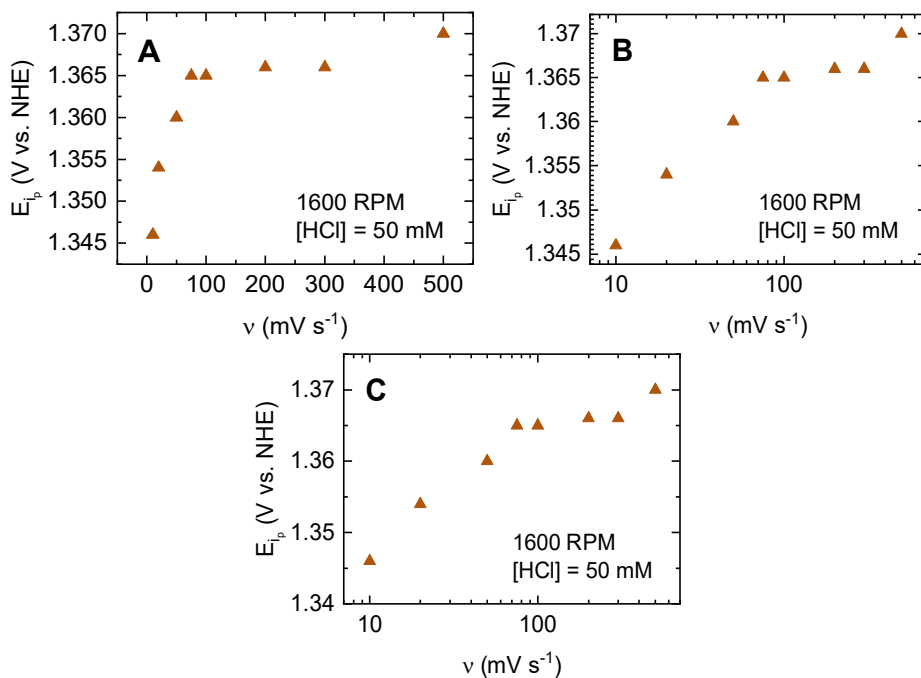
Figure A 9.4.22: Dependency of the pre-peak peak potential on the scan rate for the CER pre-peak, in linear (A), log-log (B), and semi-log plots (C). Figures B and C have nearly identical y-axes due to their y-values all being very close to 1.
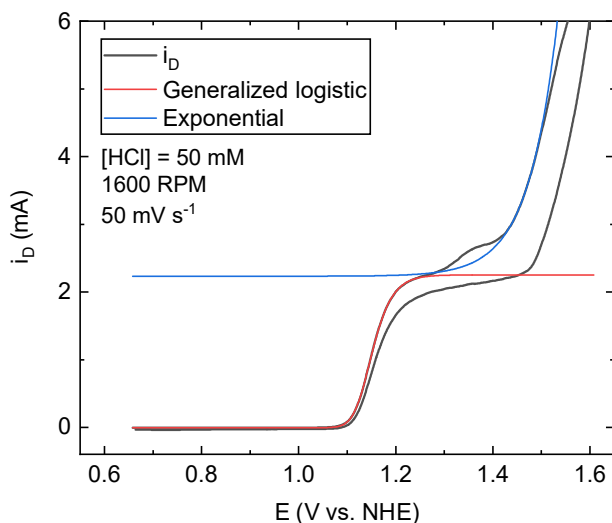
Figure A 9.4.23: Illustration of the fitting procedure to deconvolute BER currents and to isolate the chloride oxidation pre-peak.

The used generalized logistic function (blue curve) and exponential fitting functions (red curve) are given by:

$$i_D = i_{L,BOR}^{min} + \frac{i_{L,BOR}^{max} - i_{L,BOR}^{min}}{\left[1 + \left(\frac{E}{x_0}\right)^{-h}\right]^s} \qquad \text{Eq. A 9.4.19}$$

$$i_D = i_{L,BOR}^{max} + A_1 \exp\left(\frac{(E - E_0)}{t_0}\right) \qquad \text{Eq. A 9.4.20}$$

In these equations, $i_{L,BOR}^{min}$ and $i_{L,BOR}^{max}$ are the fitted limiting currents for the bromide oxidation wave in the low and high potential limit, respectively (where $i_{L,BOR}^{min} \approx 0$). E_0, x_0, h, s, A_1 and t_0 were parameters to be optimized.
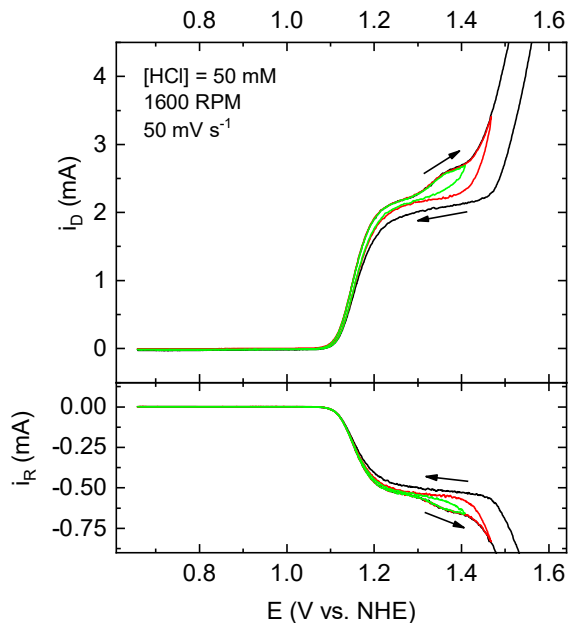
Figure A 9.4.24: CVs comparable to those measured in the main text in a solution of 0.1 M HClO$_4$ + 10 mM HBr + 50 mM HCl, but with varying upper potential windows.
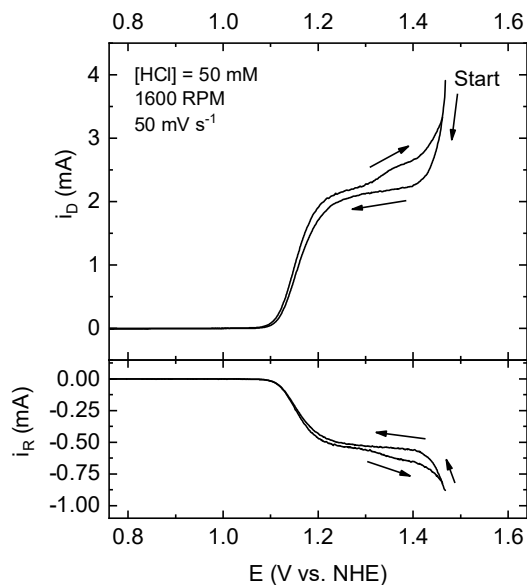
Figure A 9.4.25: CV comparable to those measured in the main text in a solution of 0.1 M HClO$_4$ + 10 mM HBr + 50 mM HCl, but with the start and end potentials reversed. The forward sweep was started at 1.51 V, and reversed at 0.7 V.

9.4.8. <u>Supplementary UV-Vis data</u>
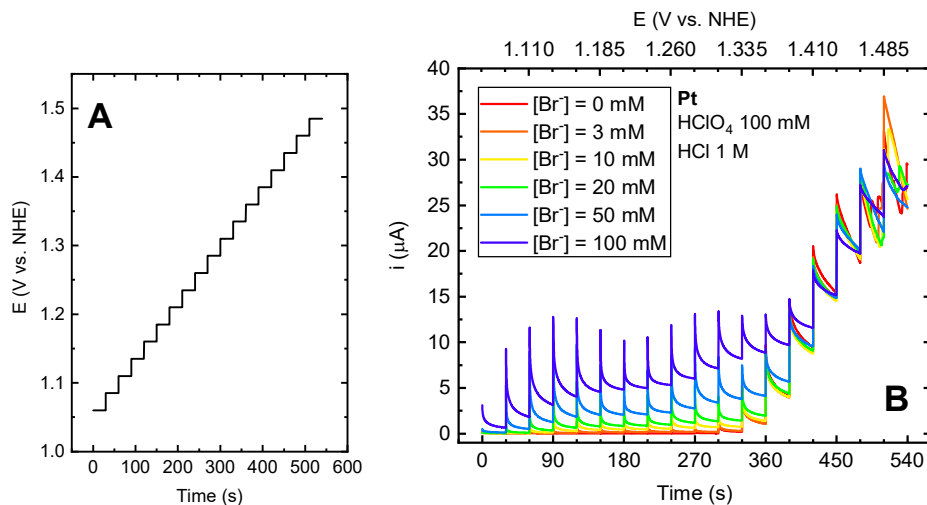
Figure A 9.4.26: E vs. t program used during the UV-Vis experiments in 1 M HCl (A). Panel B shows full data of the currents recorded during UV-Vis experiments in Figure 4.9.
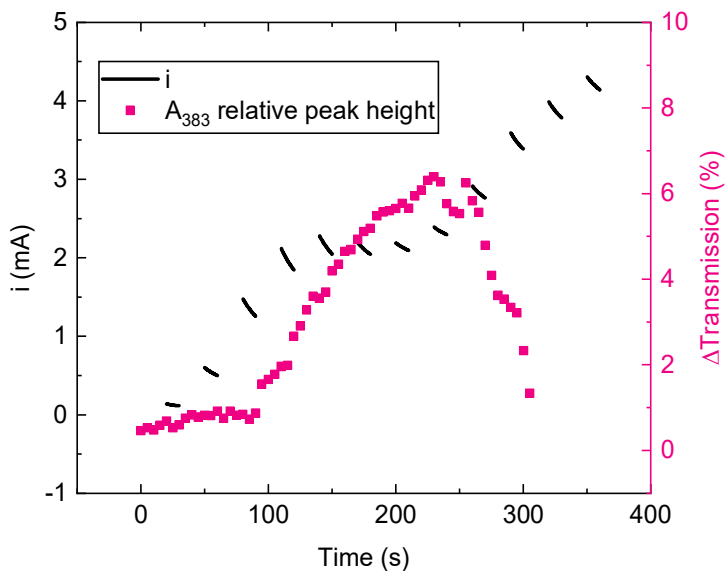
Figure A 9.4.27: Comparison of currents recorded during the BER wave belonging to data in Figure 4.10, and relative peak heights in the UV-Vis data, which can be ascribed to the extent of Br_2Cl^- formation. UV-Vis peak data were determined by calculating the difference between the local minimum and local maximum within $340 - 380$ nm in Figure 4.10.
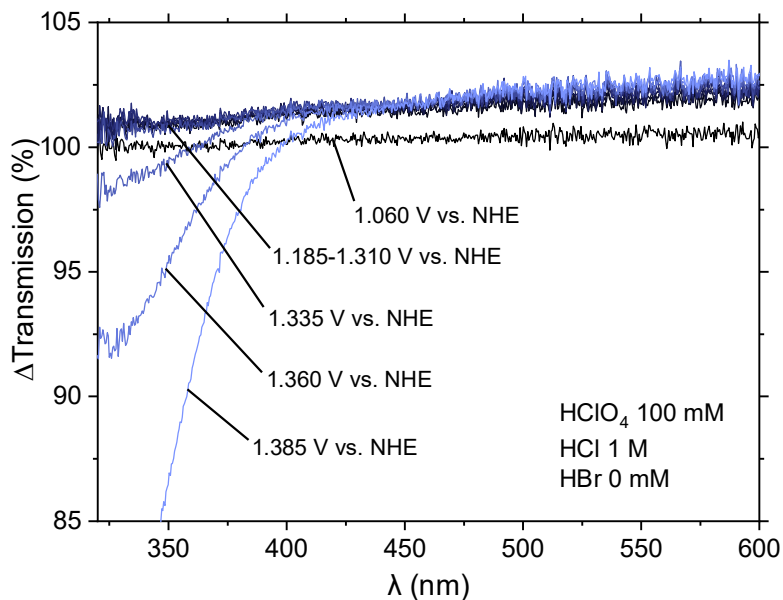
Figure A 9.4.28: UV-Vis data belonging to the experiment in Figure A 9.4.26 where [HBr] = 0 mM, such that all changes in transmission can be ascribed to the appearance of Cl_2.
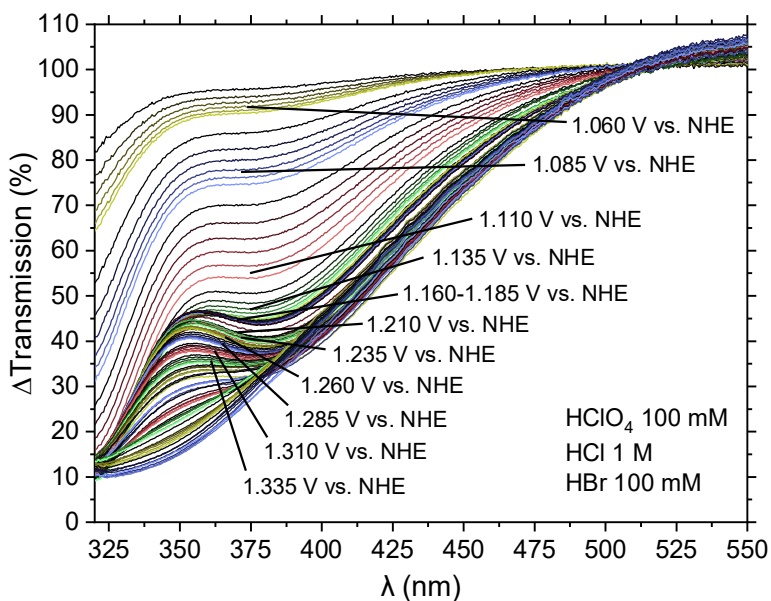
Figure A 9.4.29: Complete set of UV-Vis experiments for parallel bromide and chloride oxidation in 1 M HCl and 100 mM HBr, similar to Figure 4.10.
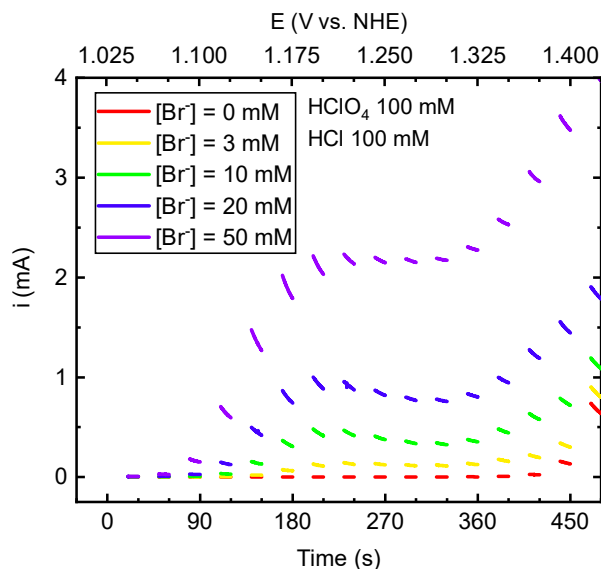
Figure A 9.4.30: Recorded currents during UV-Vis measurements such as in Figure 4.9, involving a stationary Pt/FTO electrode in a solution of 0.1 M $HClO_4$ + 0.1 M HCl, in presence of various [HBr].
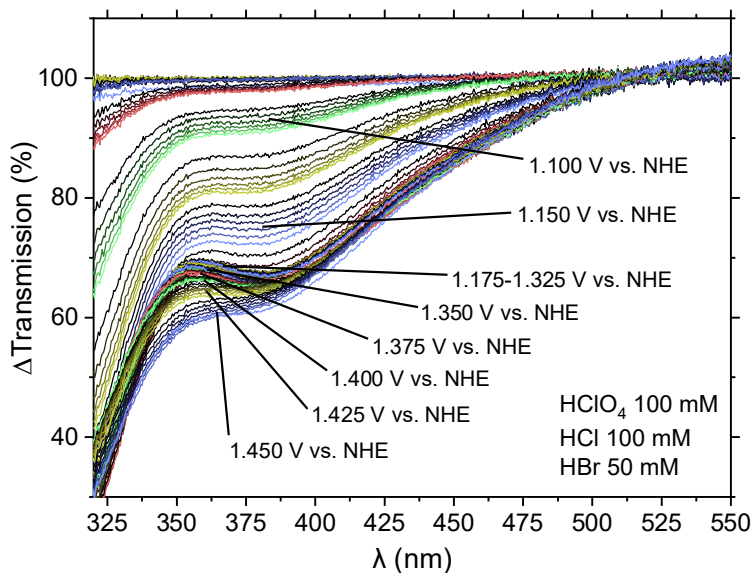
Figure A 9.4.31: Complete set of UV-Vis experiments for parallel bromide and chloride oxidation such as in Figure 4.10 and Figure A 9.4.29, corresponding to one of the experiments in Figure A 9.4.30 ([HBr] = 50 mM). The potential where the local maximum at 350 nm starts decreasing can be estimated at 1.375 V.

9.5. Supporting information for Chapter 5

9.5.1. Supplementary RRDE data
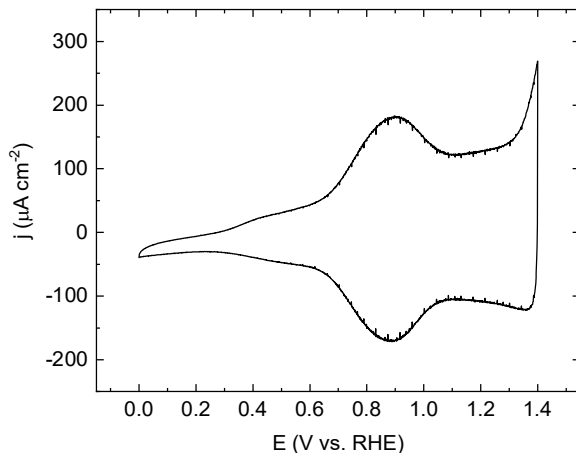
Figure A 9.5.1: Voltammetric characterization of the IrO_x/GC catalyst, in 0.1 M $HClO_4$. Scan rate: 50 mV s^{-1}.
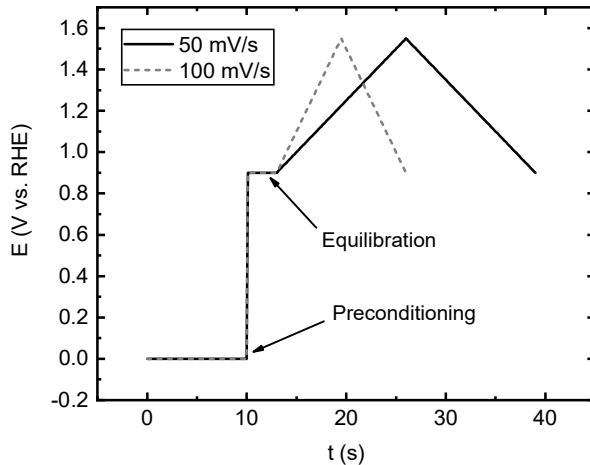
Figure A 9.5.2: Potential versus time program used during RRDE experiments, illustrating the preconditioning and equilibration steps preceding every experiment.
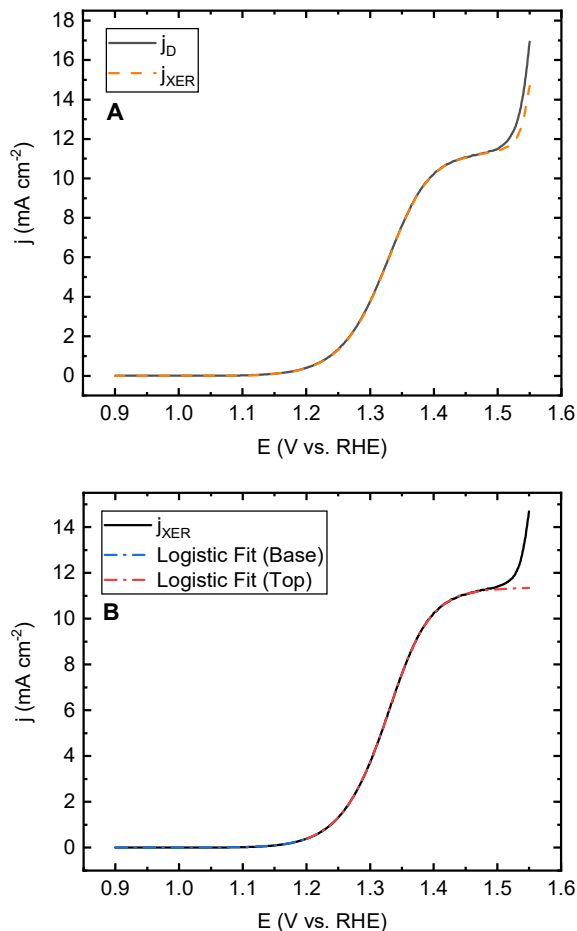
Figure A 9.5.3: Illustration of the method for separating BER, CER and OER currents. A: Comparison of experimental disk current densities (j_D, black solid trace) with halogen evolution currents (j_{XER}, orange dashed trace) which were derived as described in the main text. B: Fits of bromide oxidation in the foot and top of j_{XER} (red and blue dashed traces).

The generalized logistic function was used for both fits, as given by:

$$i_D = i_{L,BOR}^{min} + \frac{i_{L,BOR}^{max} - i_{L,BOR}^{min}}{\left[1 + \left(\frac{E}{x_0}\right)^{-h}\right]^s}$$

Eq. A 9.5.1

See Figure A 9.4.23 for more information.
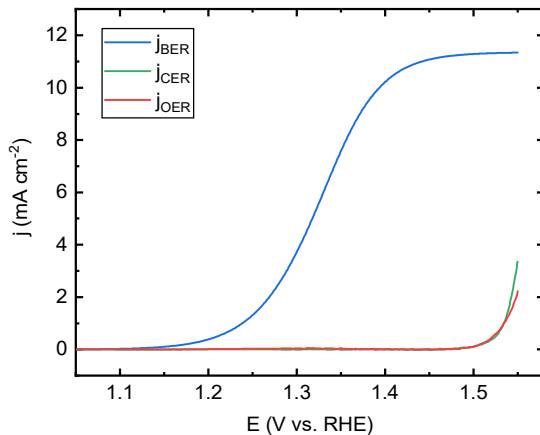
Figure A 9.5.4: Individual BER, CER and OER current densities derived from Figure A 9.5.3.
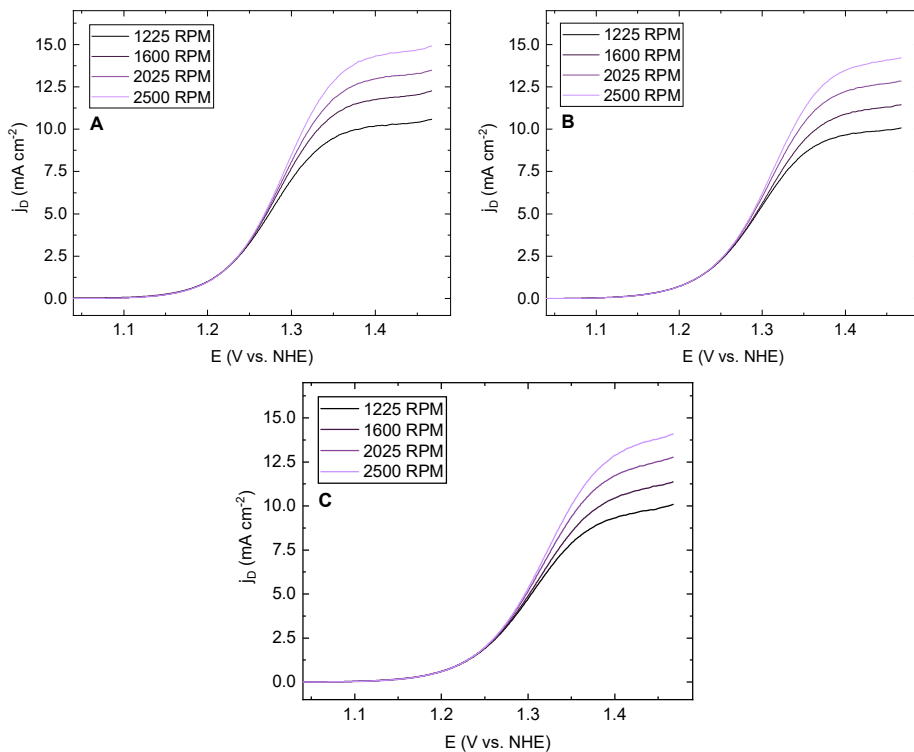
Figure A 9.5.5: Rotation rate dependence of the bromide oxidation region, in 0.5 M HClO$_4$ + 10 mM HBr + (A) 0 mM HCl, (B) 10 mM HCl, (C) 50 mM HCl.
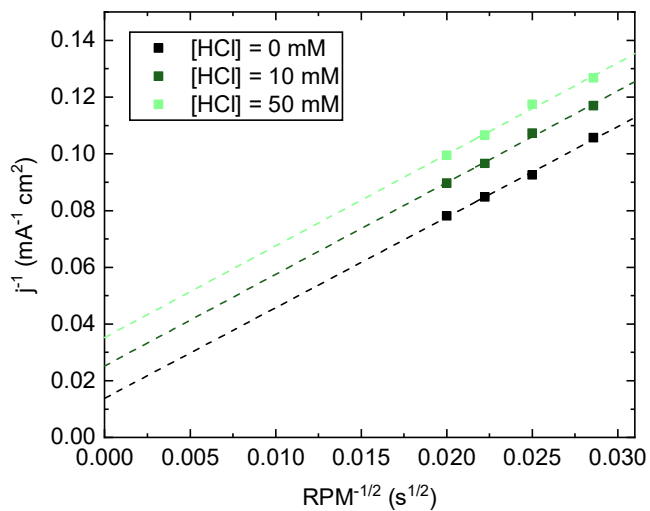
Figure A 9.5.6: Typical examples of Koutecký-Levich plots on the basis of data in Figure A 9.5.5. Shown are data from 1.35 V vs. NHE.
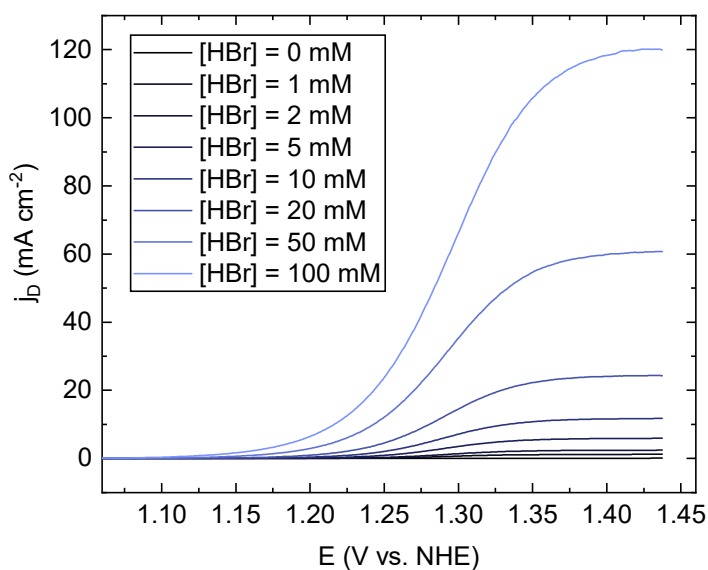
Figure A 9.5.7: Bromine evolution measured under varying [HBr], in 0.5 M HClO$_4$, at 10 mV s^{-1} and 1600 RPM. Only forward scans are shown.
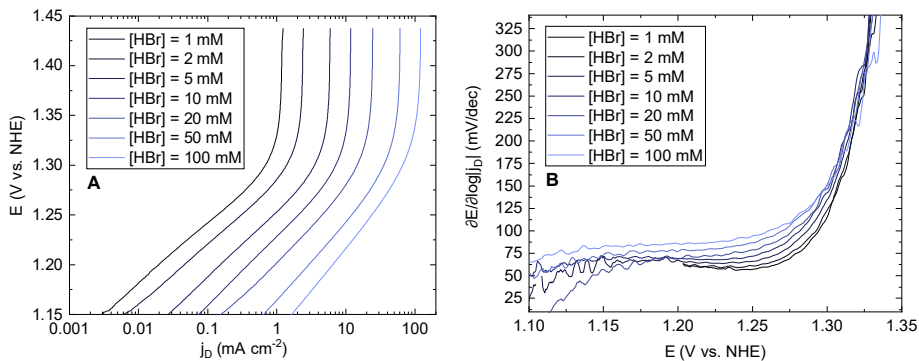
Figure A 9.5.8: Determination of Tafel slopes for bromine evolution. A: Semi-logarithmic plot of Figure A 9.5.7. B: Tafel slopes derived from A, as a function of potential.
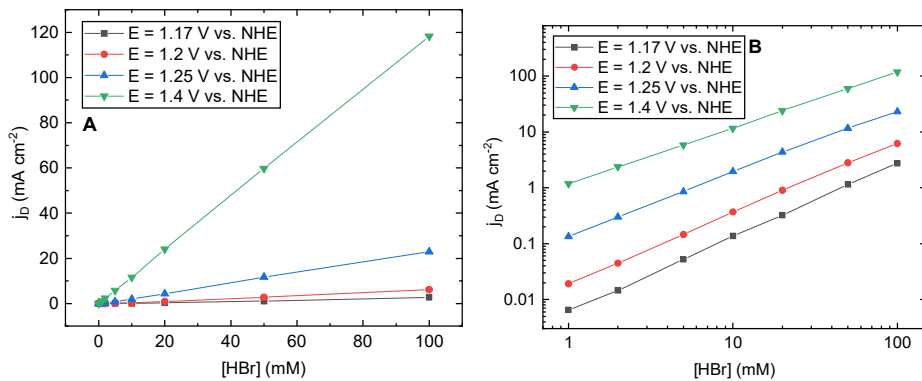
Figure A 9.5.9: Current densities at constant potential values as function of HBr concentration (A), using data shown in Figure A 9.5.7, and corresponding log-log plots (B).
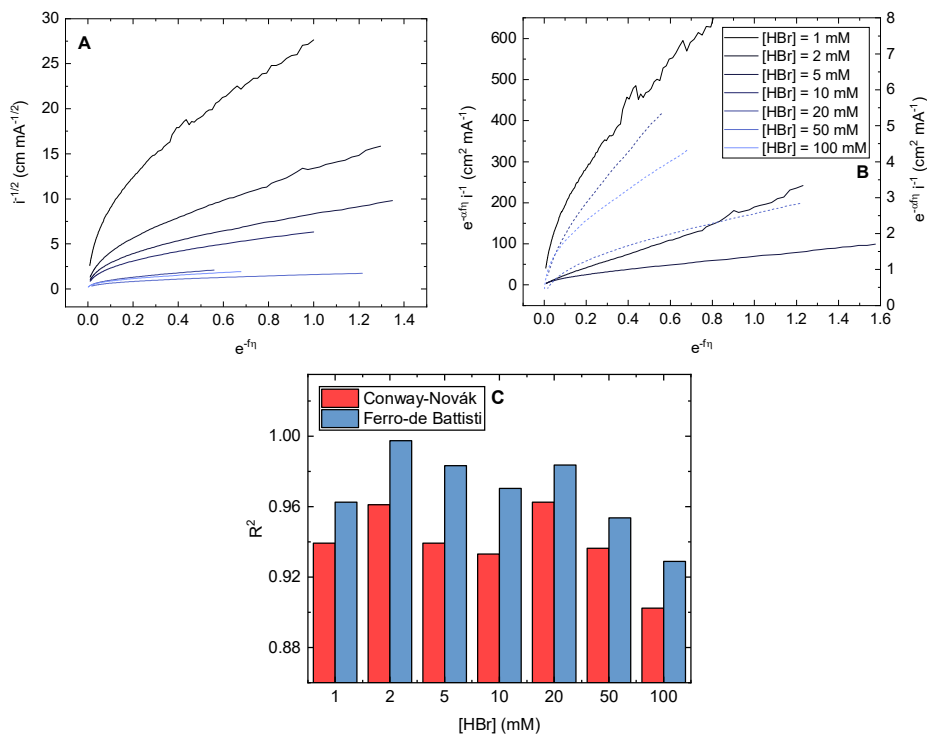
Figure A 9.5.10: Test plots using the methods proposed by Conway and Novák[118] (A) and Ferro *et al.*[113] (B), for the BER. As described in the main text, $\eta = E - E_0$ is the potential relative to a convenient reference, and $f = {}^F\!/_{(RT)}$. In the Ferro-de Battisti plots, α was estimated by observing the unique, non-unitary which results in the most straight line, if any. E_0 was estimated by observing the onset of linearity in E vs. $\log|i|$ plots. C shows the R^2 values obtained from these plots to discern the highest linearity. Values for the three highest [HBr] plots in panel B (dotted traces) are drawn on the right-side y-axis.
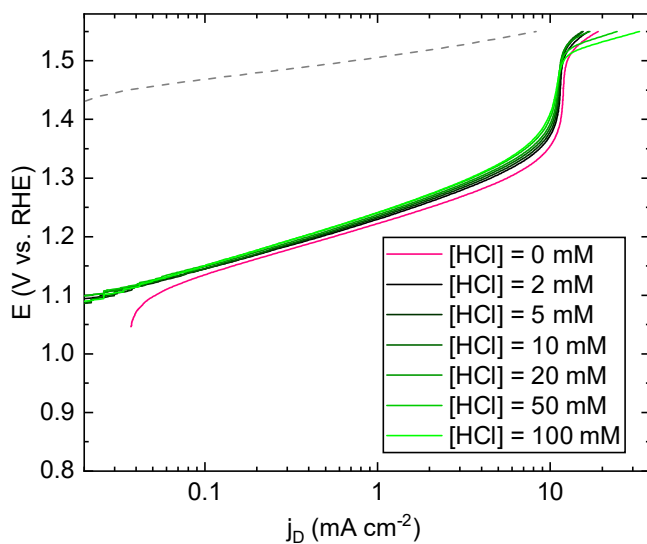
Figure A 9.5.11: Semi-logarithmic plot of Figure 5.1, top panel.
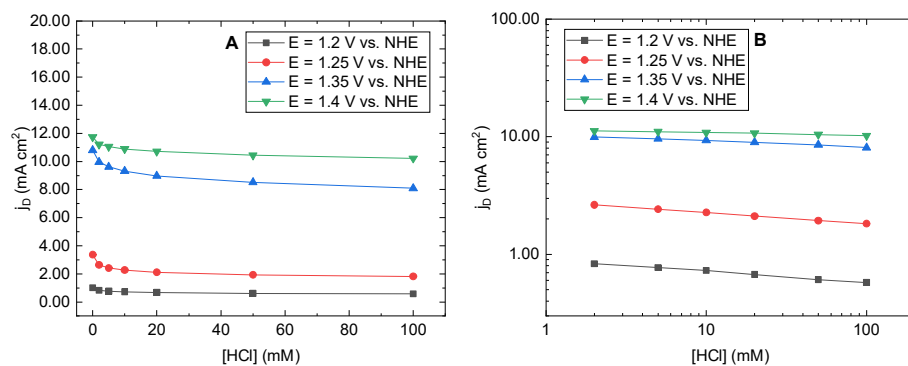
Figure A 9.5.12: Current densities of bromide oxidation at constant potential values as function of HCl concentration (A), using data shown in Figure 5.1, top panel. B: Corresponding log-log plots.
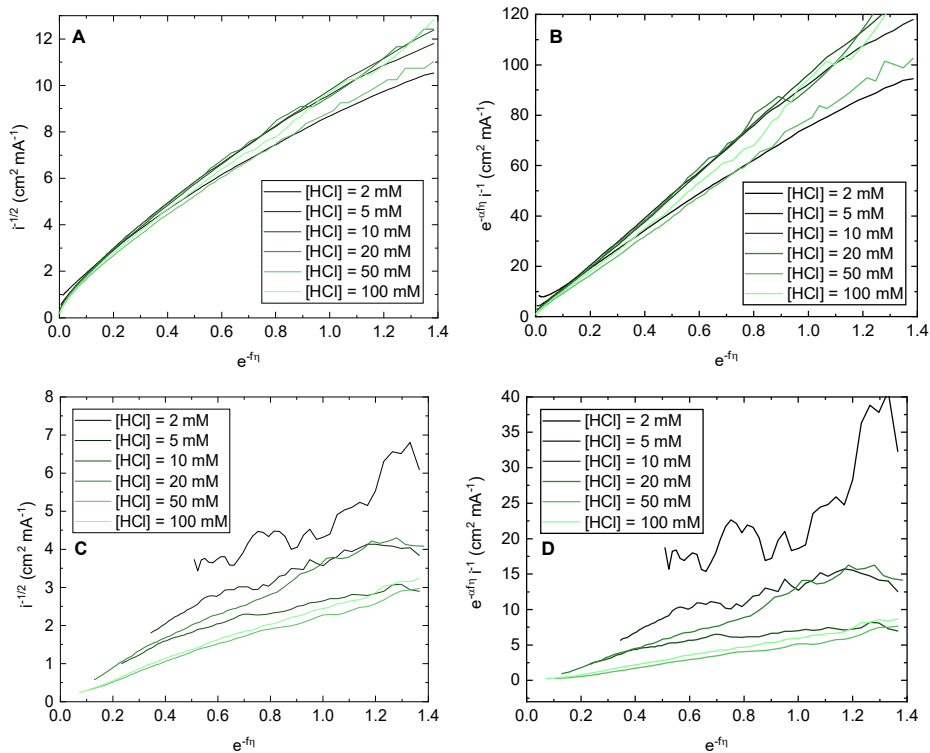
Figure A 9.5.13: Conway-Novák (A, C) and Ferro-de Battisti (B, D) test plots for the CER, as in Figure A 9.5.10. A and B show data for the CER, C and D show data of the CER in presence of 10 mM HBr.
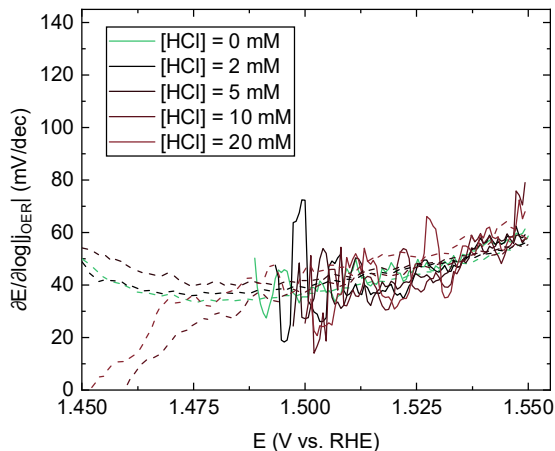
Figure A 9.5.14: OER Tafel slopes measured as function of HCl concentration, in presence of 10 mM HBr (solid traces), and in bromide-free conditions (dotted traces). Data for chloride concentrations higher than 20 mM had insufficient signal to noise ratio and were omitted Green traces show data measured in absence of Cl$^-$ (solid) and in absence of both Cl$^-$ and Br$^-$ (dashed).
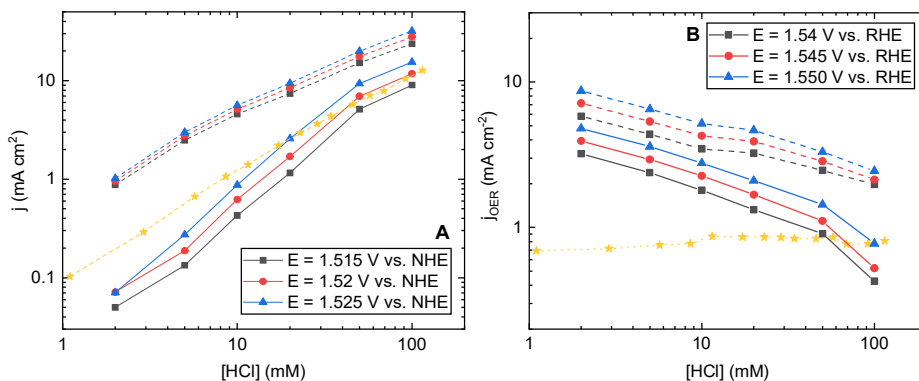
Figure A 9.5.15: Log-Log plots of CER (A) and OER (B) activities measured as function of HCl concentration in 0.5 M HClO$_4$, in presence of 10 mM HBr (solid traces), and in bromide-free conditions (dotted traces). Yellow, dashed trace shows data measured on IrO$_x$ in absence of HBr, in a 0.5 M KHSO$_4$ electrolyte, where [Cl$^-$] was increased by adding KCl.
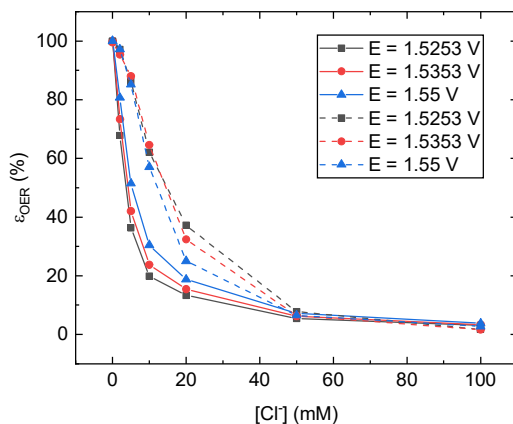
Figure A 9.5.16: Molar selectivities of the OER relative to the CER as function of chloride concentration, in presence (dashed traces) and absence (solid traces) of 10 mM HBr.

9.5.2. *Supplementary UV-Vis data*
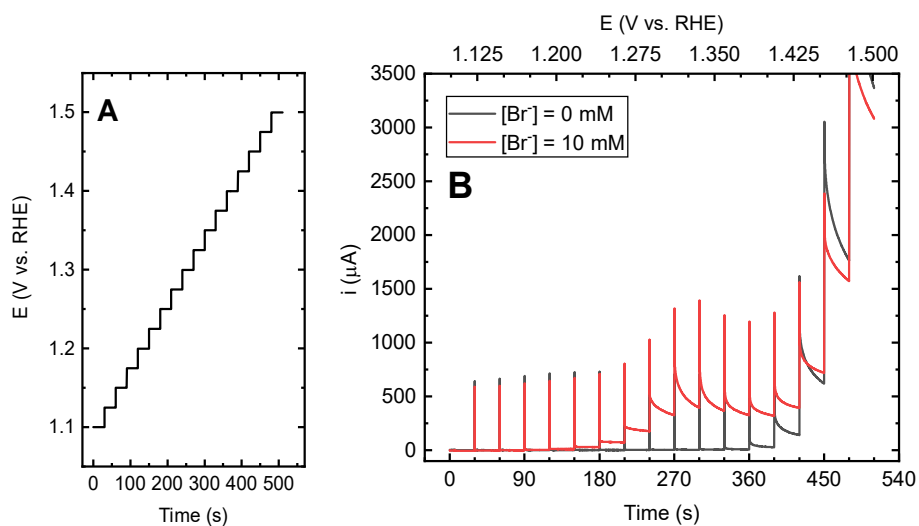
Figure A 9.5.17: E vs. t program used during the UV-Vis experiments (A). Panel B shows full data of Figure 5.4A.
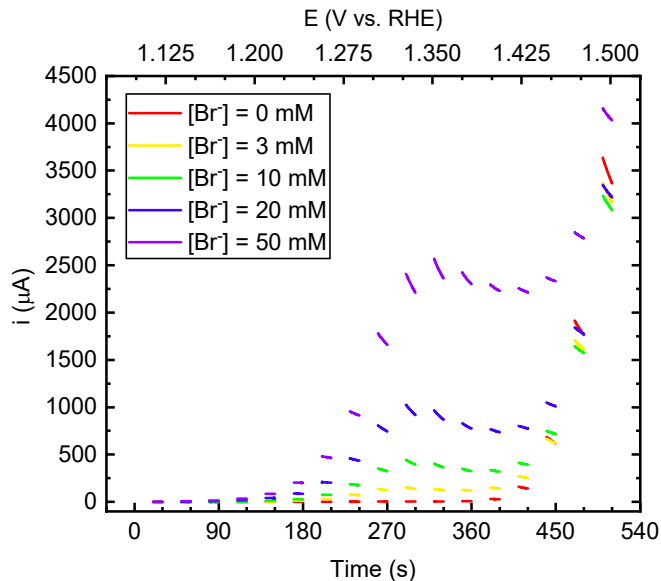
Figure A 9.5.18: Currents measured during UV-Vis experiments in a solution of 0.1 M HClO$_4$ + 0.1 M HCl with [HBr] ranging between 0 and 50 mM. The final 10 s of each potential step are shown.
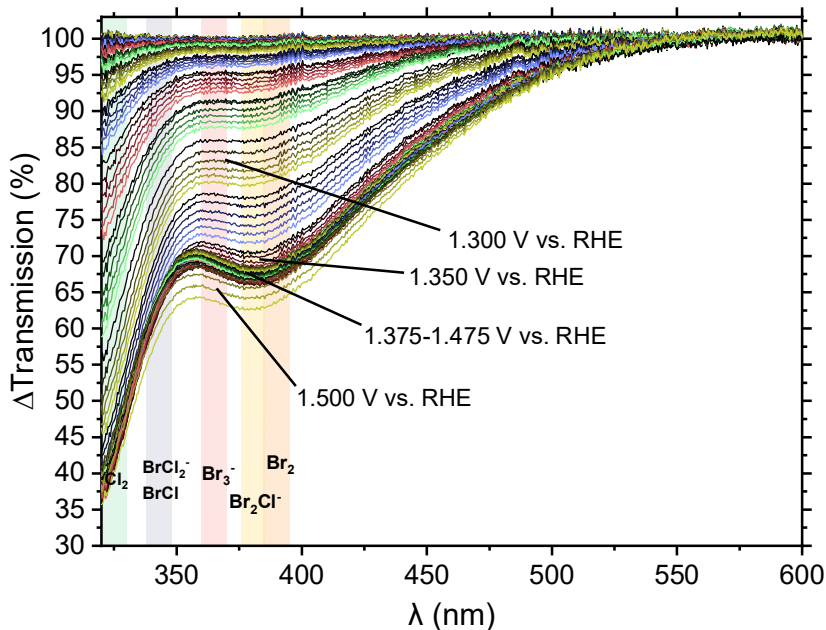
Figure A 9.5.19: Full UV-Vis transmission data similar to Figure 5.4A. Here, [HBr] = 50 mM (corresponding to the purple trace in Figure A 9.5.18).

9.6. Supporting information for Chapter 6

9.6.1. Estimation of the diffusion limiting current of MnO$_x$ deposition

The diffusion limited current of MnO$_x$ deposition at 1500 RPM was determined by means of the equation for the diffusion-limited current:

$$i_{MnO_x}^L = nFA \frac{D_{Mn^{2+}}}{\delta_{Mn^{2+}}} C_{Mn^{2+}} \qquad \text{Eq. A 9.6.1}$$

where $n = 2$ is the number of electrons transferred in the reaction, F is Faraday's constant (96485 C/mol), $D_{Mn^{2+}}$ is the diffusion constant of Mn^{2+} in water ($7.12 \cdot 10^{-10}$ m^2 s^{-1}·), $C_{Mn^{2+}}$ is the species concentration ([Mn^{2+}] = 0.6 mol m^{-3}), and $\delta_{Mn^{2+}}$ is the diffusion layer thickness, which is dependent on the rotation rate ω (157.08 rad/s). The latter can be determined via the Levich equation:

$$\delta_{Mn^{2+}} = 1.61 \, \nu^{1/6} \, D_{Mn^{2+}}^{1/3} \, \omega^{-1/2} \qquad \text{Eq. A 9.6.2}$$

The value of ν, the kinematic viscosity of the solution, can be estimated at $1.0 \cdot 10^{-6}$ m^2 s^{-1} for dilute ($C < 1$ M) aqueous salt solutions, yielding $i_{MnO_x}^L \approx 140$ µA.

9.6.2. Supplementary electrochemical data
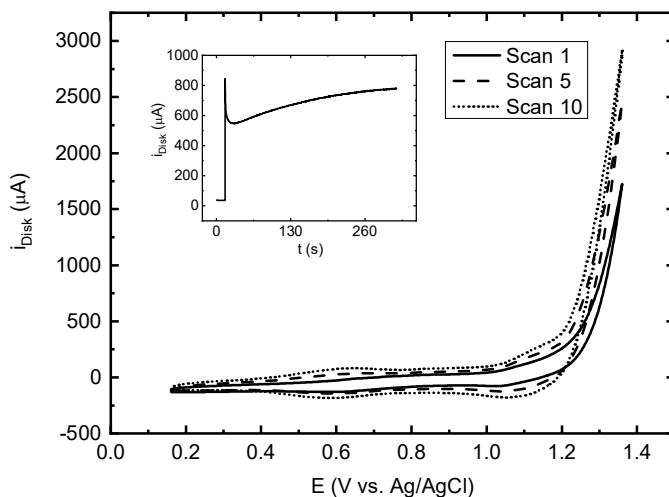
Figure A 9.6.1: Representative CVs of the trends seen during IrO$_x$ electroflocculation, using a IrO$_x$ colloid solution of pH ~ 1 with nominal [Ir] = 2 mM, containing approximately 0.4 M ClO$_4^-$, 0.3 M Na$^+$, and 0.012 M Cl$^-$. The bare GC was initially scanned ten times at 250 mV s^{-1}, during which gradual IrO$_x$ deposition can be observed in the form of increasing CER/OER activity and appearance of IrO$_x$-related pseudo-capacitance. Amperometry was then performed for 300 s (see inset) at a potential targeted 10 mV more positive than the potential of mixed OER + CER onset (1.255 V vs. Ag/AgCl).
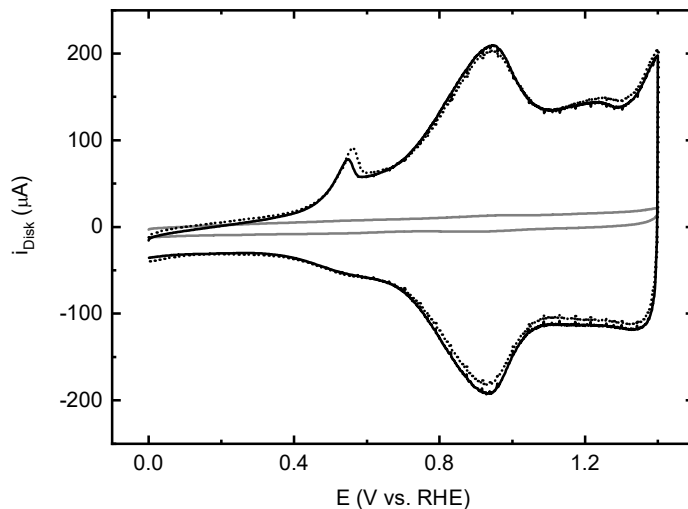
Figure A 9.6.2: Voltammetric characterization of the electroflocculated hydrous IrO_x catalyst (IrO_x/GC), in 0.5 M $KHSO_4$. Electrode is shown in the initial state (solid trace) and after experiments involving mixed OER, CER and MnO_x deposition (dotted trace). Grey trace shows the blank GC support before IrO_x electroflocculation. Scan rate: 50 mV s^{-1}, solution saturated with Ar.
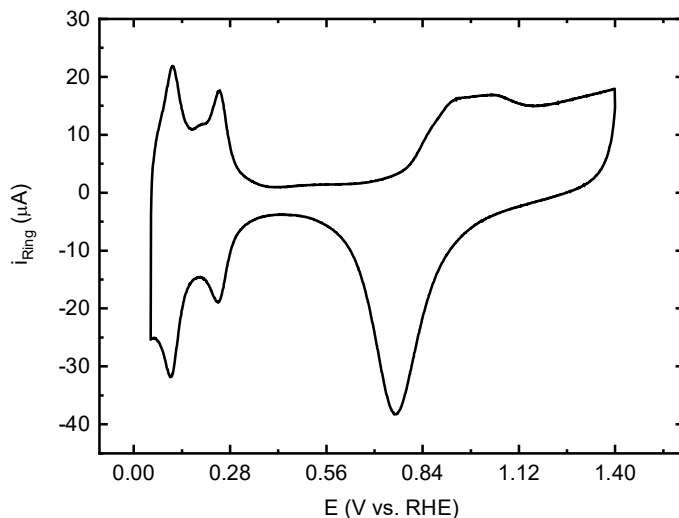

Figure A 9.6.3: Voltammetric characterization of the Pt ring used for chlorine detection, in 0.5 M $KHSO_4$. Scan rate: 50 mV s^{-1}, solution saturated with Ar.
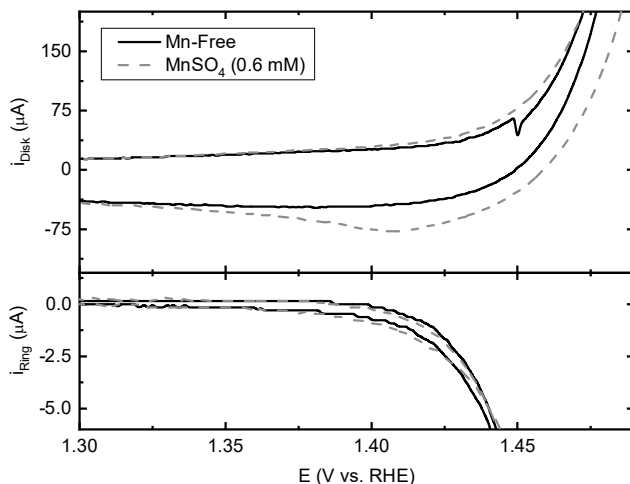
Figure A 9.6.4: Zoom of an IrO_x/GC rotating disk electrode (top) in 0.5 M $KHSO_4$, 30 mM KCl (pH = 0.88), and 0.6 mM $MnSO_4$, showing the electrode behavior (grey dashed trace) compared to a Mn^{2+}-free solution (black trace). The lower figure shows corresponding i_R ($E_R = 0.95$ V). The slow onset of MnO_x deposition is visible near 1.37 V, and is coupled to the onset of superimposed reduction current on the ring, at a potential lower than the onset of chlorine reduction. Rotation rate 1500 RPM, solution saturated with Ar, i_R was corrected for collection delay.
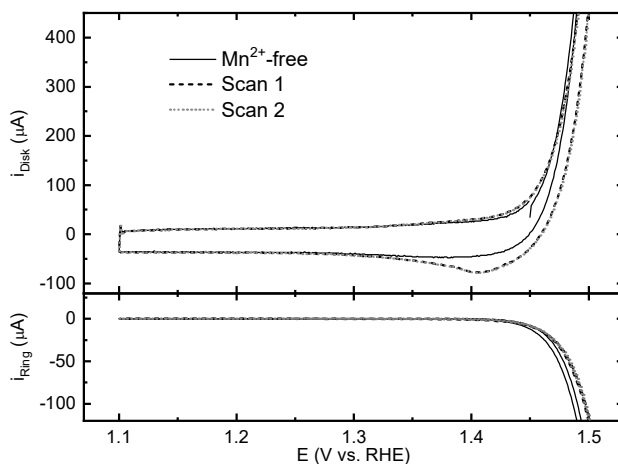
Figure A 9.6.5: CVs of an IrO_x/GC rotating disk electrode (top) in 0.5 M $KHSO_4$, 30 mM KCl (pH = 0.89), and 0.6 mM $MnSO_4$. The electrode was cycled multiple times between 1.1 V and 1.55 V, two successive scans are shown (black and grey dashed thick traces). Strong overlapping of the scans show reproducibility of MnO_x deposition-dissolution behavior during scans. Minor MnO_x reduction current can be seen as a broad peak near 1.42 V in the backward scans. The thin black trace shows the IrO_x/GC electrode in a Mn^{2+}-free solution. The lower figure shows corresponding i_R ($E_R = 0.95$ V). Rotation rate 1500 RPM, solution saturated with Ar, i_R was corrected for collection delay.
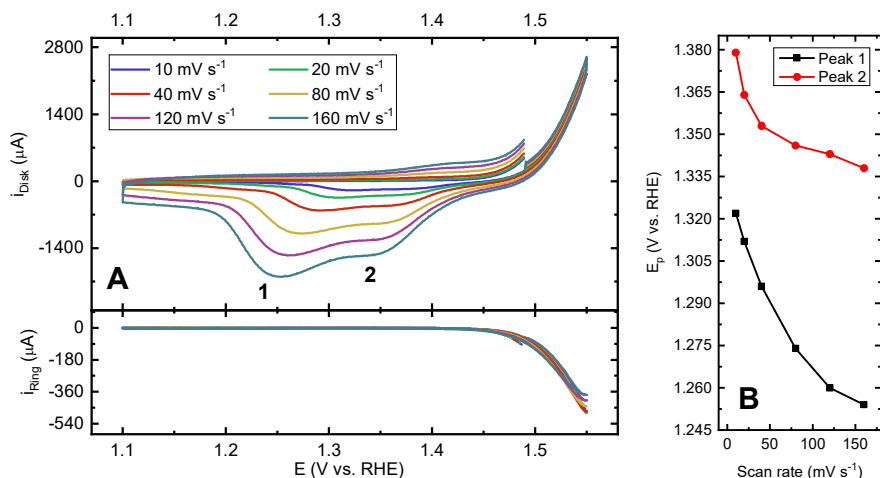
Figure A 9.6.6: (A) CVs of an IrO_x/GC rotating disk electrode (top) in 0.5 M $KHSO_4$, 30 mM KCl (pH = 0.91), and 0.6 mM $MnSO_4$. MnO_x films were preconditioned for 300 s at 1.49 V before initiating the forward scan at 1.49 V, with variable scan rate. Charges obtained during preconditioning (and hence the corresponding Q_{MnO_x}) showed a maximum variance of approximately 10%. The lower figure shows corresponding i_R (E_R = 0.95 V). Rotation rate 1500 RPM, solution saturated with Ar, i_R was corrected for collection delay. (B) Scan rate vs. peak reduction potentials of peak 1 and peak 2, in the MnO_x films of panel A.
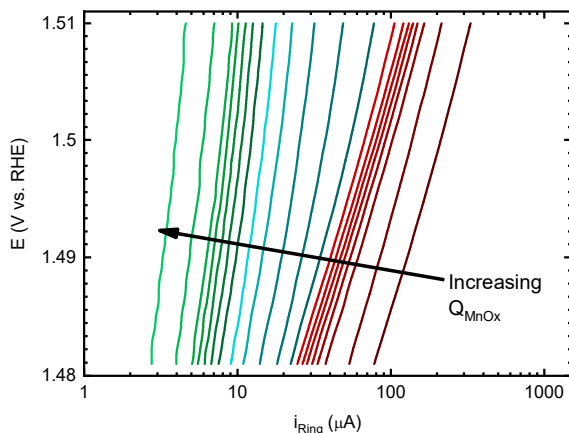
Figure A 9.6.7: Full Tafel plots for CER on the disk electrode, constructed from ring currents. No correction for N_l was applied as in Figure 6.3 in the main text. Data were measured on the Pt ring (E_R = 0.95 V) in combination with an IrO_x/GC rotating disk electrode in 0.5 M $KHSO_4$, 30 mM KCl (pH = 0.88), and 0.6 mM $MnSO_4$ (except for the Mn^{2+}-free experiment). MnO_x films were preconditioned at various times at 1.48 V before initiating the forward scan at 1.48 V. Plots are drawn in three color regimes, with increasing MnO_x reductive charge within each regime: $0\,mC < Q_{MnO_x} < 2\,mC$ (red), : $2\,mC < Q_{MnO_x} < 4\,mC$ (blue) and $Q_{MnO_x} > 4\,mC$ (green). Disk scan rate: 10 mV s⁻¹, rotation rate 1500 RPM, solution saturated with Ar, i_R was corrected for collection delay.
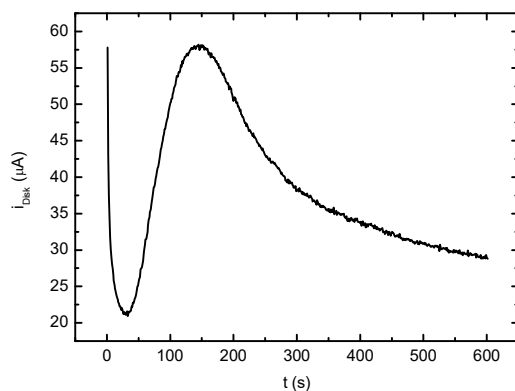
Figure A 9.6.8: Representative deposition curve of MnO_x in an acidic ClO_4^- solution. Data shown of amperometry of an IrO_x/GC electrode at 1.45 V, in a solution containing 0.5 M Na/$HClO_4$ (pH = 0.85) and 0.6 mM $Mn(ClO_4)_2$. Rotation rate 1500 RPM, solution saturated with Ar. The curve shows behavior strongly reminiscent of a progressive nucleation and growth mechanism. A non-adsorbing ClO_4^- solution was used instead of HSO_4^-, as this allowed observation of MnO_x deposition at intermediate rates at lower potentials, without the complication of superimposed OER.
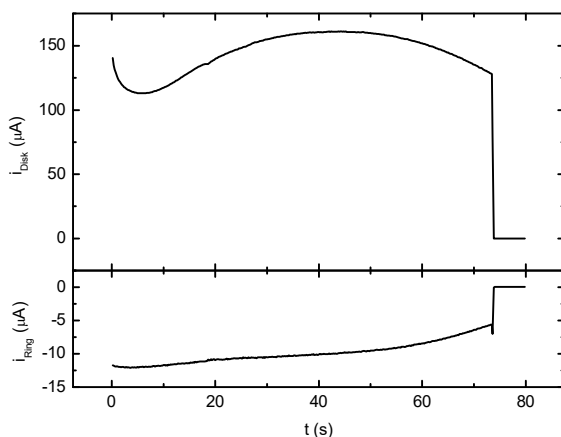
Figure A 9.6.9: Amperometry of an IrO_x/GC electrode (top) at 1.21 V vs. Ag/AgCl, in 0.1 M $HClO_4$ (pH ≈ 0.85) and 0.6 mM $Mn(ClO_4)_2$, representative of sample preparation for structural studies. The lower figure shows corresponding i_R ($E_R = 0.71$ V vs. Ag/AgCl). The deposition cut-off point can be seen at t = 73 s, where the electrode contact with the solution was interrupted. At that point, CER rates (as determined from i_R) were approximately 50% of their original value, and approaching the dramatic activity drop. Rotation rate 1500 RPM, solution saturated with Ar.
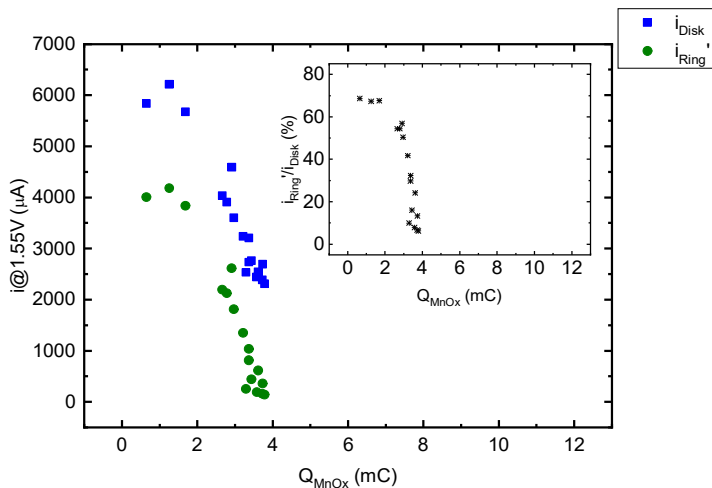
Figure A 9.6.10: Plot of disk currents (blue), ring currents (green), and ratio between i_R' and i_D (inset) measured at $E_D = 1.55$ V as function of Q_{MnO_x}, the reductive charge measured for the corresponding MnO_x film during the backward scan. Values determined in a 0.15 M $HClO_4$ + 0.35 M $NaClO_4$ solution (pH = 0.88).
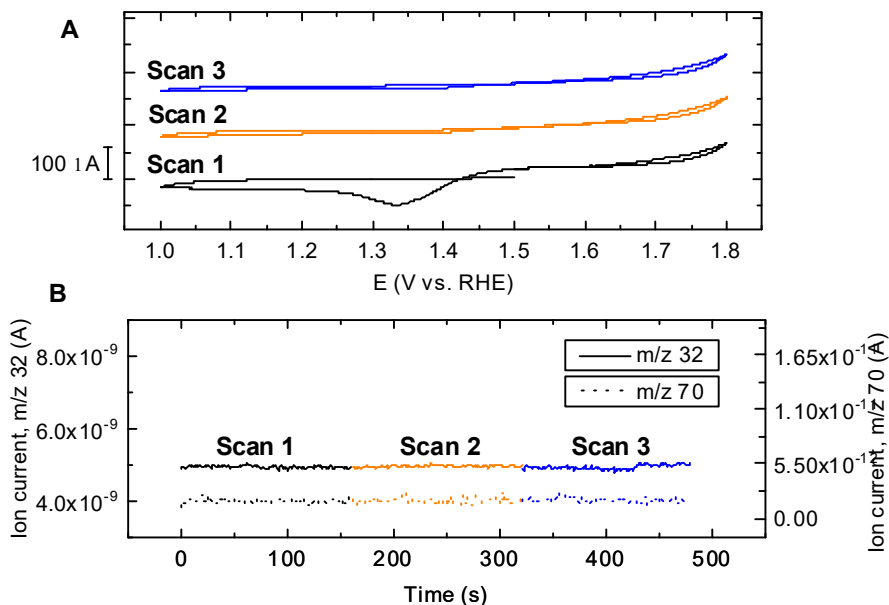

Figure A 9.6.11: OLEMS measurements of a MnO_x/GC electrode in 0.5 M $KHSO_4$, 20 mM KCl, and 1.2 mM $MnSO_4$ (pH = 0.84). A: CVs of the electrode after preconditioning for 900 s at 1.50 V, followed by three scans. Scan rate: 5 mV s^{-1}. C shows corresponding OLEMS mass signals over time. Solution saturated with Ar.
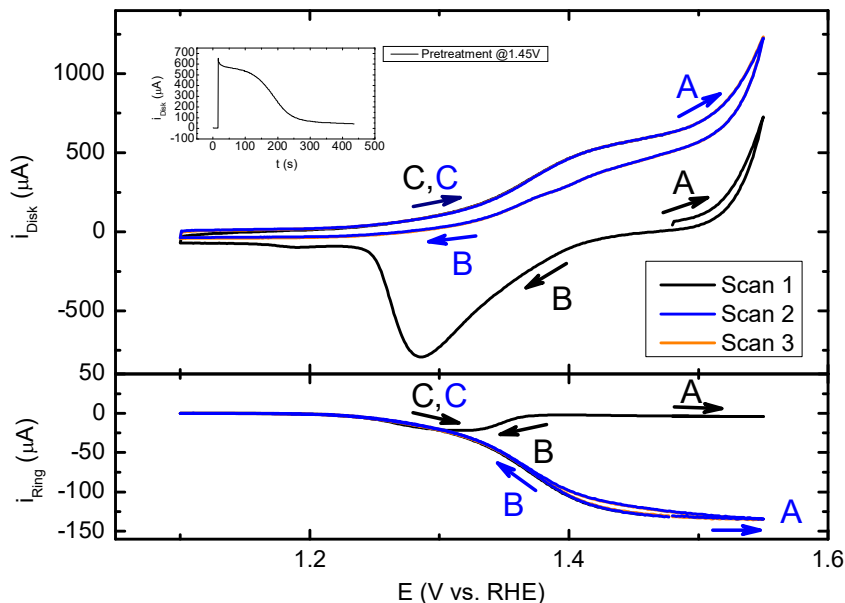
Figure A 9.6.12: CVs of an IrO_x/GC rotating disk electrode (top) in 0.5 M $KHSO_4$, 3 mM KBr (pH = 1.15), and 0.6 mM $MnSO_4$. The lower figure shows corresponding i_R ($E_R = 0.90$ V). Fixing the ring potential at 0.90 V allowed measurement of BER rates via selective reduction of Br_2 and Br_3^- back to Br^-. A MnO_x film was grown for 420 s at 1.45 V (see inset for current profile) before initiating the forward scan (black trace) at 1.45 V. Scan rate 10 mV s^{-1}, rotation rate 1500 RPM.

Several MnO_x-related shifts in behavior are visible, marked A, B and C. At the beginning of the first scan at 1.45 V (A, black) a MnO_x film is present, resulting in mainly OER-related current on the disk (onset near 1.45 V) and almost no ring current related to bromine reduction. In the backward scan, the MnO_x film starts dissolving near 1.45 V (B, black), coinciding with a rise in ring current as BER rates increase. Due to the backward scanning potential, BER rates on the ring decrease quickly after their rise. Resuming the forward direction after crossing the 1.10 V lower potential limit, the IrO_x/GC electrode is MnO_x-free, which is apparent from a rise in current near 1.20 V (C, black), corresponding to onset of BER. As the potential is scanned higher than 1.45 V, crossing into the second scan (A, blue), the disk current is composed of bromine evolution and the onset of OER. The ring shows significant bromine reduction current, approaching near diffusion limited BER rates on the disk. There is also minor hysteresis in the ring current during scan reversal, currents decrease over time due to transient MnO_x growth. In absence of an integral MnO_x film, the remainder of the second scan (B and C, blue) shows simply the decrease in OER and BER. Scan 3 (orange trace) overlapped strongly with scan 2.

A more elaborate study of the effect of MnO_x on BER selectivity was not pursued, since it is outside the scope of this thesis. The nature of bromine evolution is substantially different from CER,[196] and a more detailed study would require a different experimental approach.
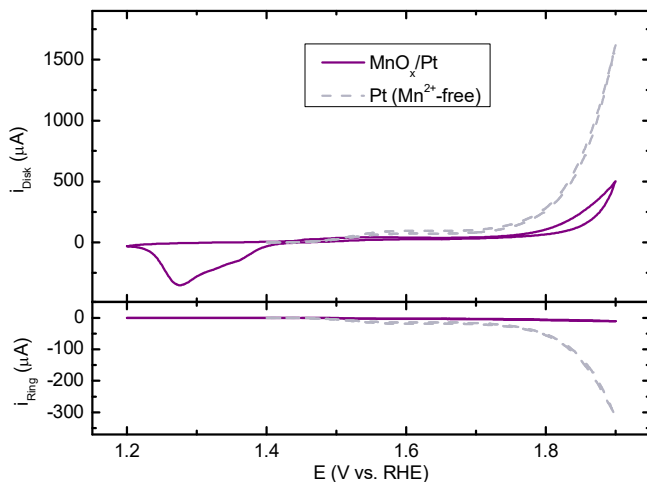
Figure A 9.6.13: CVs of a Pt rotating disk electrode (top) in 0.5 M $KHSO_4$, 100 mM KCl (pH = 1.37), and 0.6 mM $MnSO_4$. A MnO_x film was preconditioned for 300 s at 1.45 V before initiating the forward scan at 1.45 V (purple trace). Grey dashed trace shows Pt in Mn^{2+}-free conditions for comparison. The lower figure shows corresponding i_R ($E_R = 0.95$ V). Scan rate: 10 mV s^{-1}, Rotation rate 1500 RPM.
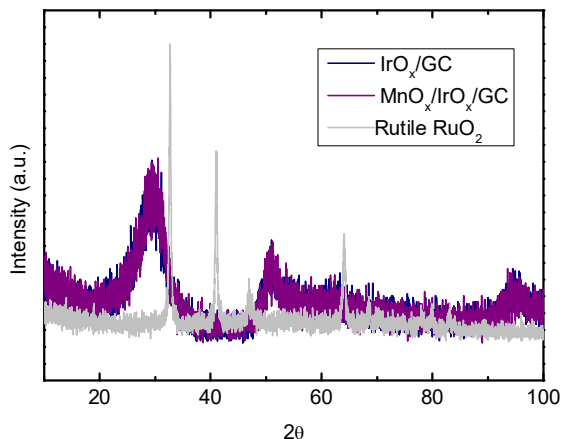
9.6.3. XRD data

Figure A 9.6.14: XRD data of IrO_x/GC and MnO_x/IrO_x/GC samples. Data of highly crystalline commercial rutile-RuO_2 was added for comparison, using a small mass loading of similar magnitude as the metal oxides on the GC disk samples (rutile-RuO_2 has lattice parameters almost identical to rutile-IrO_2). The broad amorphous peaks near $2\theta \approx 30$, 50 and 94 may originate from the GC substrate.
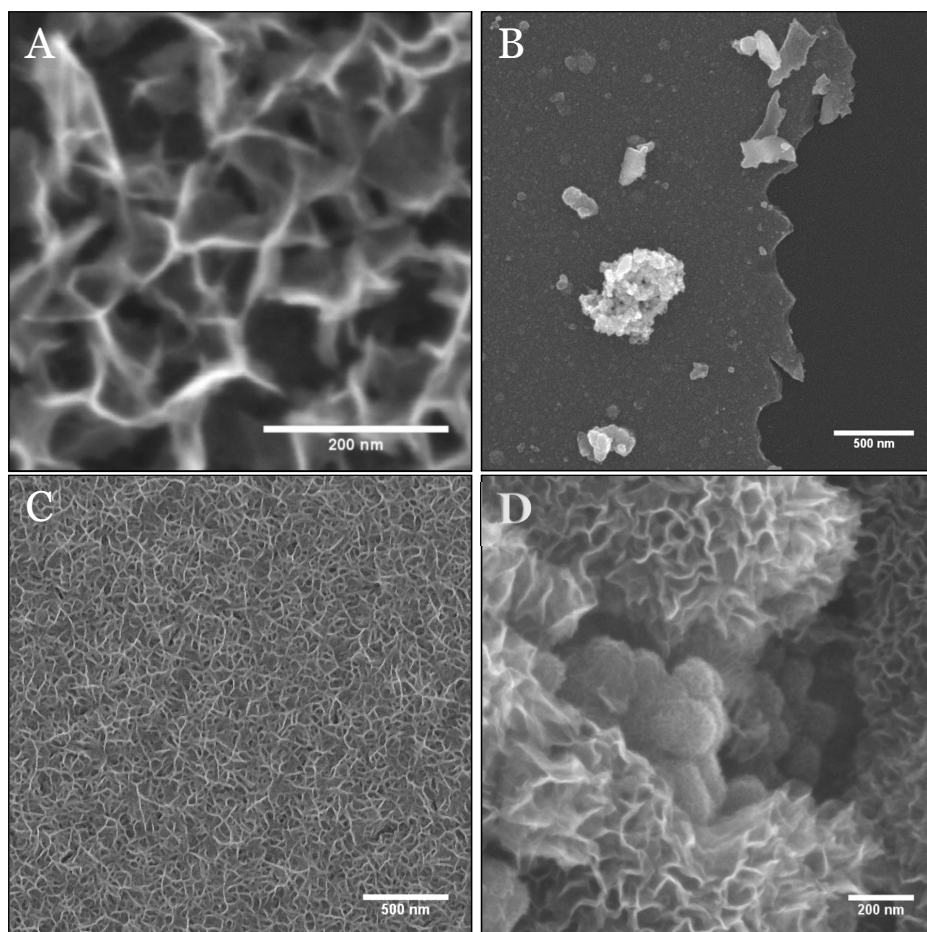
9.6.4. Supplementary microscopy data

Figure A 9.6.15: Supplementary SEM images. A: Zoom of MnO_x structure as-deposited on IrO_x/GC. B: IrO_x/GC sample showing the 'smooth' IrO_x layer with nanosized IrO_x colloid clusters on top, and bare GC (right). C: Structure of MnO_x deposited on bare GC (no IrO_x present). D: MnO_x deposited onto IrO_x for extended deposition times (a 'thick' film). An IrO_x cluster is shown. Some IrO_x nanoparticles are still visible, covered by a thin layer of MnO_x sheets as described previously. Larger MnO_x formations with thicker sheets can also be seen, often completely obscuring the IrO_x underneath.
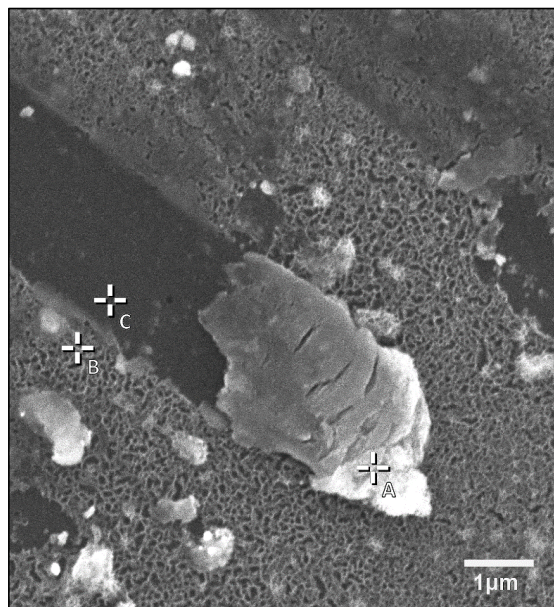
Figure A 9.6.16: MnO_x/IrO_x film used for EDS analysis.

Table A 9.6.1: EDS data from points in Figure A 9.6.16.						
	Point A		Point B		Point C	
Element	mass%	Atom%	mass%	Atom%	mass%	Atom%
C	74.46	0.03	93.89	0.04	95.85	0.04
O	21.36	0.09	5.73	0.08	4.15	0.07
Mn	3.98	0.12	0.38	0.06	-	-
Ir	0.2	0.08	-	-	-	-
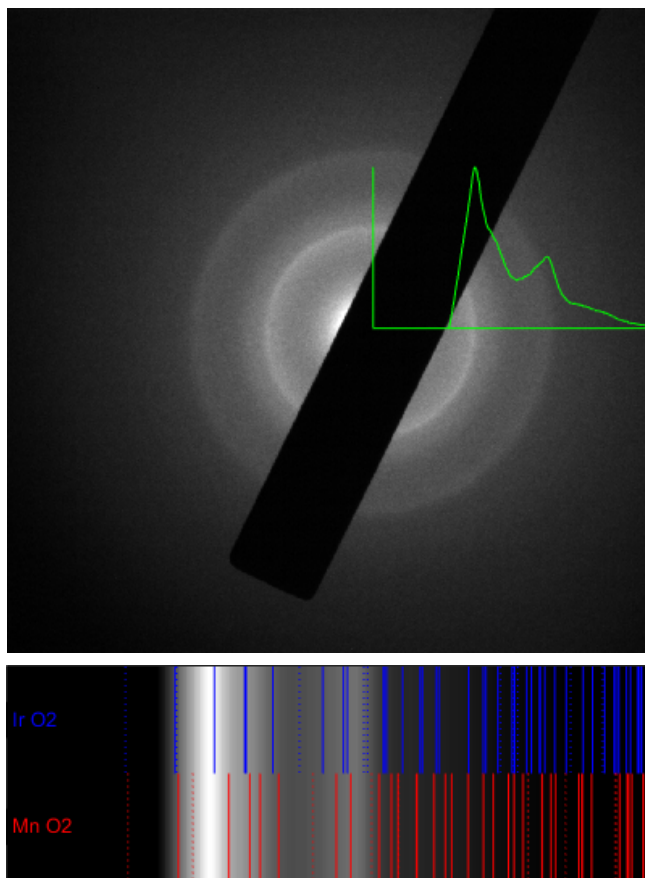
Figure A 9.6.17: SAED pattern and corresponding linear diffractogram of a $MnO_x/IrO_x/GC$ sample (accelerating voltage of 120 kV). Predicted rutile-IrO_2 and β-MnO_2 (pyrolusite) patterns shown as reference.
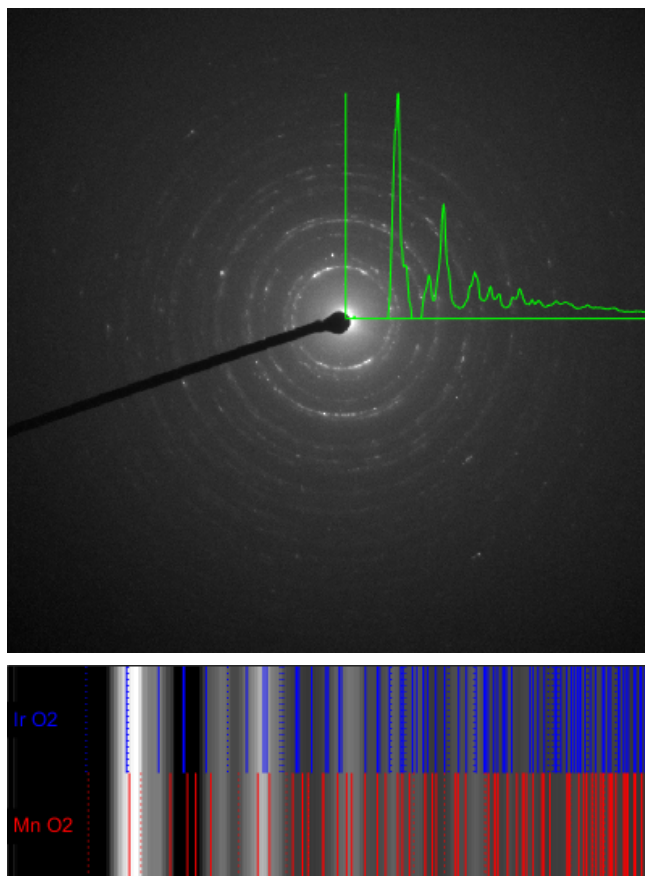
Figure A 9.6.18: SAED pattern and corresponding linear diffractogram of a $MnO_x/IrO_x/GC$ sample at higher accelerating voltage (200 kV). Predicted rutile-IrO_2 and β-MnO_2 (pyrolusite) patterns shown as reference.
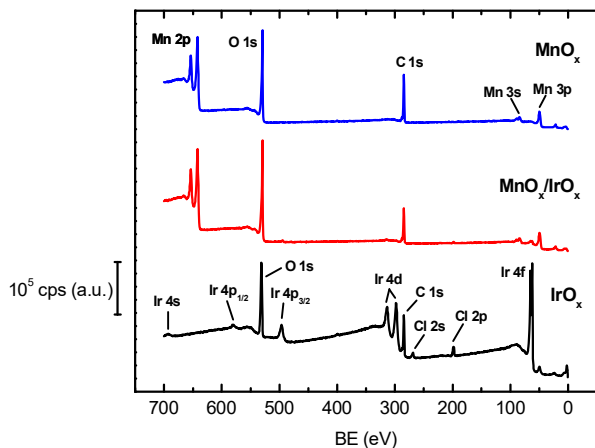
9.6.5. *Supplementary XPS data*

Figure A 9.6.19: Survey spectra of the of Mn and Ir MO_x/GC single oxides (top and bottom) and the mixed MnO_x/IrO_x/GC sample (middle).
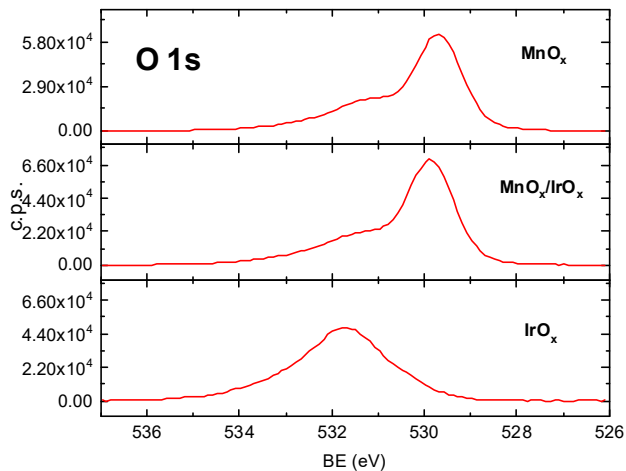

Figure A 9.6.20: Core-level XPS scans of the O 1s spectral peaks on an absolute intensity scale. Scans were made of Mn and Ir MO_x/GC single oxides (top and bottom) and the mixed MnO_x/IrO_x/GC sample (middle).
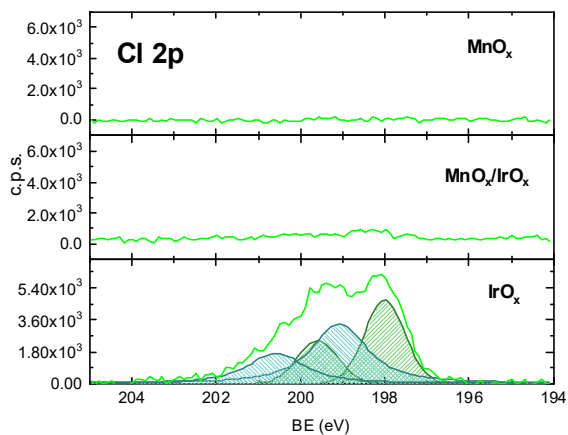
Figure A 9.6.21: Core-level XPS scans of the Cl 2p spectral peaks on an absolute intensity scale. Scans were made of Mn and Ir MO$_x$/GC single oxides (top and bottom) and the mixed MnO$_x$/IrO$_x$/GC sample (middle). The IrO$_x$/GC sample shows Cl contributions related to Ir-Cl (binding energy 199.1 eV) and alkali-metal chloride (binding energy 198.0 eV).

Table A 9.6.2: Mn:Ir atom ratios in the XPS MnO$_x$/IrO$_x$/GC sample, determined from XPS and from charge integration from the corresponding amperometry during sample preparation.
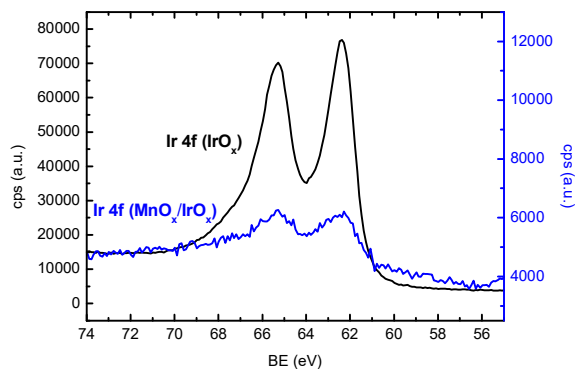
	XPS	Amperometry
Mn	**43**	**2**
Ir	**1**	**1**

Figure A 9.6.22: Ir 4f core-level spectra without background correction, comparing IrO$_x$/GC and MnO$_x$/IrO$_x$/GC samples. The ratio (peak height) : (difference of background intensity) is ~0.16 and ~0.37 for IrO$_x$/GC and MnO$_x$/IrO$_x$/GC, respectively.
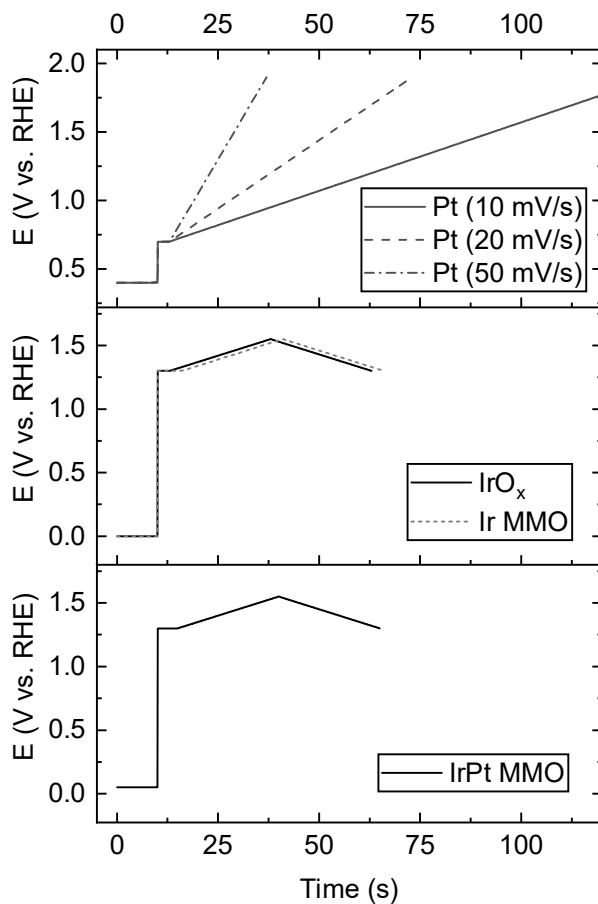
9.7. Supporting information for Chapter 7

9.7.1. Supplementary voltammetry data

Figure A 9.7.1: E vs. t programs used during the various experiments involving parallel oxygen and chlorine evolution.

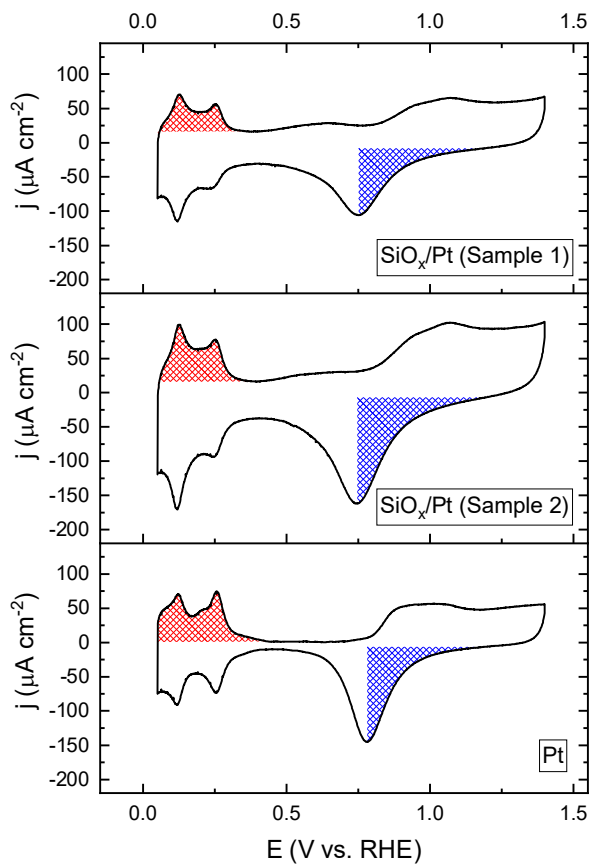Figure A 9.7.2: Voltammetric characterizations of SiO_x/Pt and Pt electrodes, in 0.5 M $KHSO_4$, recorded at 50 mV s^{-1}. Charge regions used for comparing hydrogen desorption and PtO_x reduction are illustrated in red and blue, respectively.
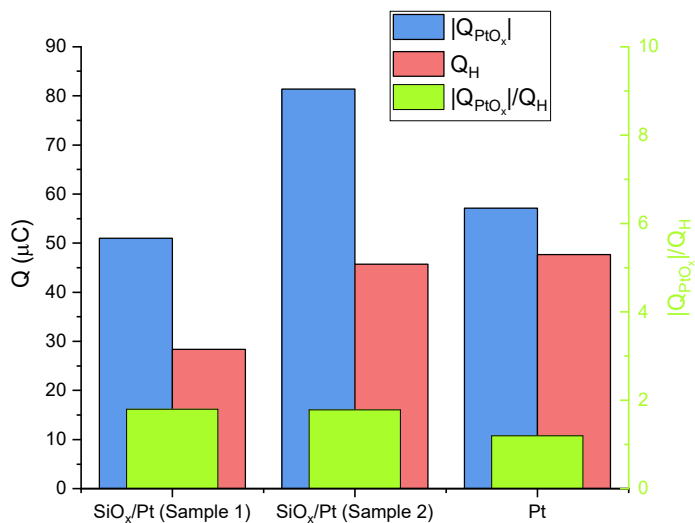
Figure A 9.7.3: Comparison of Q_H and Q_{PtO_x}, the charges corresponding to hydrogen desorption and PtO$_x$ reduction, respectively. Green bars (values on right axis) show the charge ratios. Data derived from highlighted areas in Figure A 9.7.2.
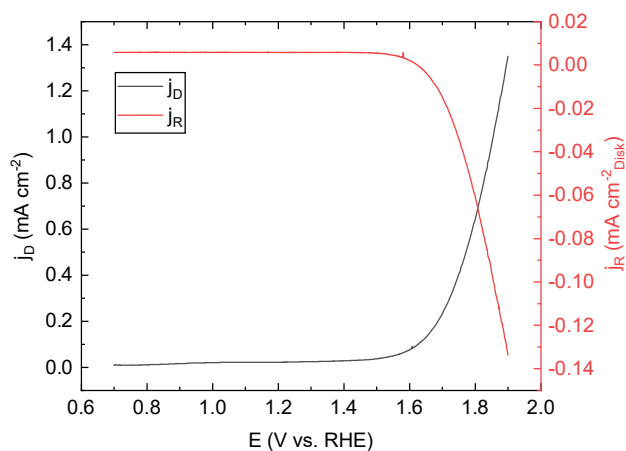
Figure A 9.7.4: Linear RRDE scan on a SiO$_x$/Pt/Ti/GC electrode (Sample 1), recorded at 10 mV s^{-1} in 0.5 M KHSO$_4$. The ring potential was fixed at 0.4 V, so that O$_2$ is detected.
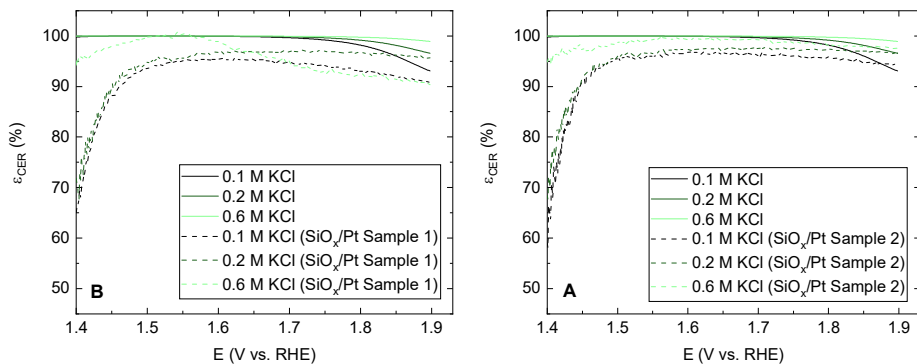
Figure A 9.7.5: Molar CER selectivities versus potential for two $SiO_x/Pt/Ti/GC$ electrodes (dotted lines in A and B). Data is shown for three different chloride concentrations, and compared with the bare Pt surface (solid lines). Data for the bare Pt surface were estimated from OER data in absence of chloride.
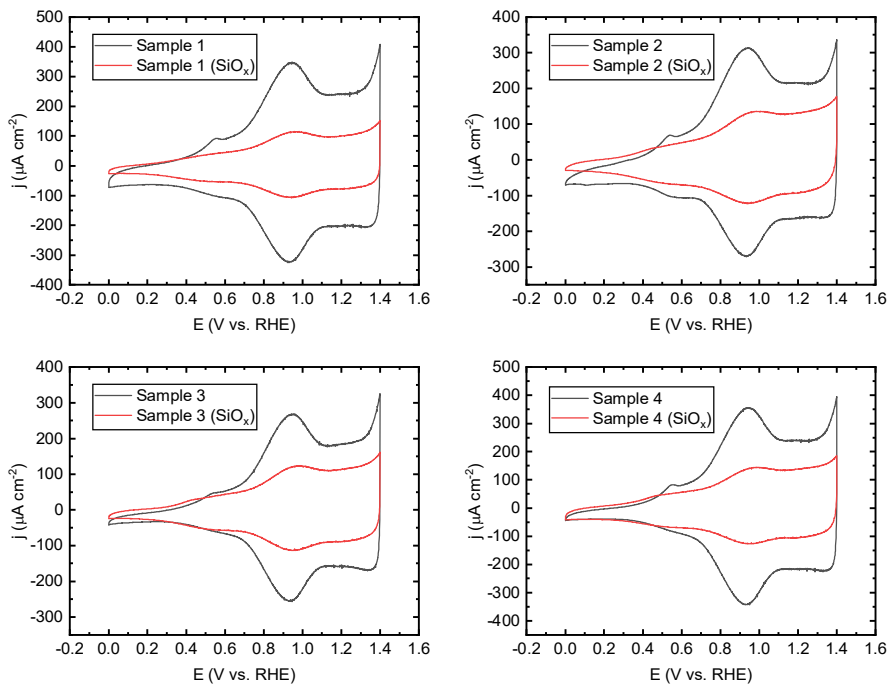
Figure A 9.7.6: Voltammetric characterization of IrO_x/GC samples, before and after the SiO_x coating.
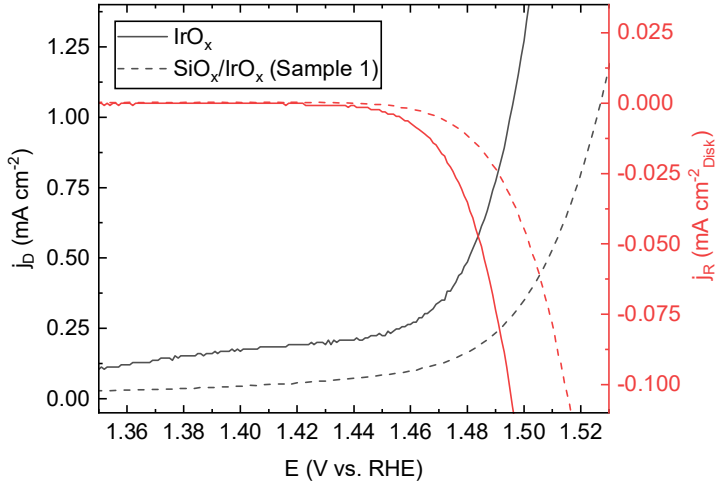
Figure A 9.7.7: Collection experiment of O_2 on an IrO_x/GC and an SiO_x/IrO_x/GC samples, as in Figure A 9.7.4.
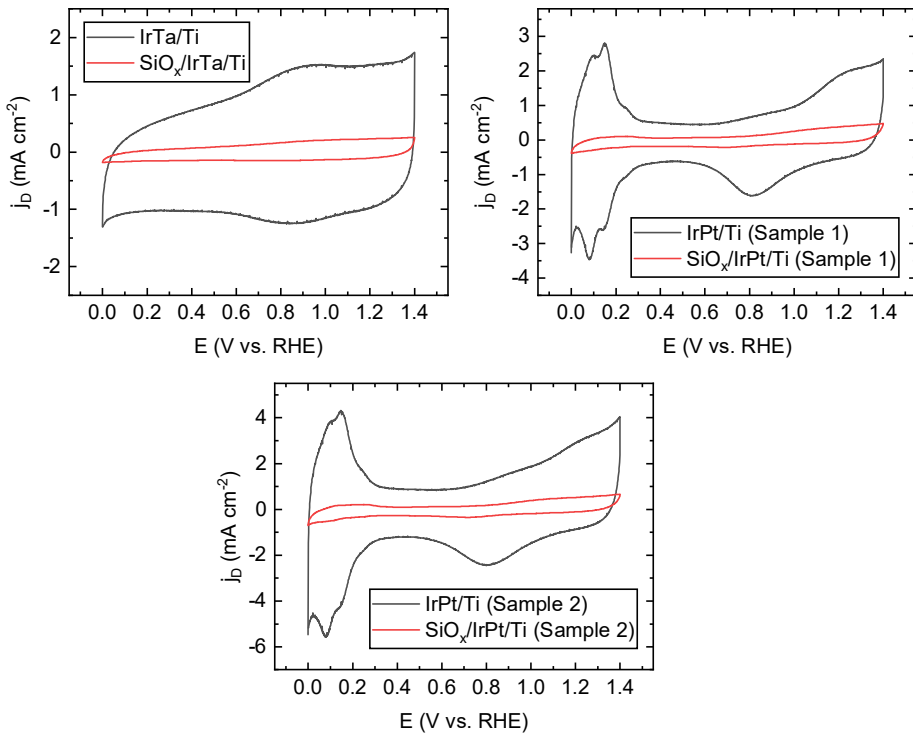
Figure A 9.7.8: Voltammetric characterization of Ti-based anodes, before and after the SiO_x coating.
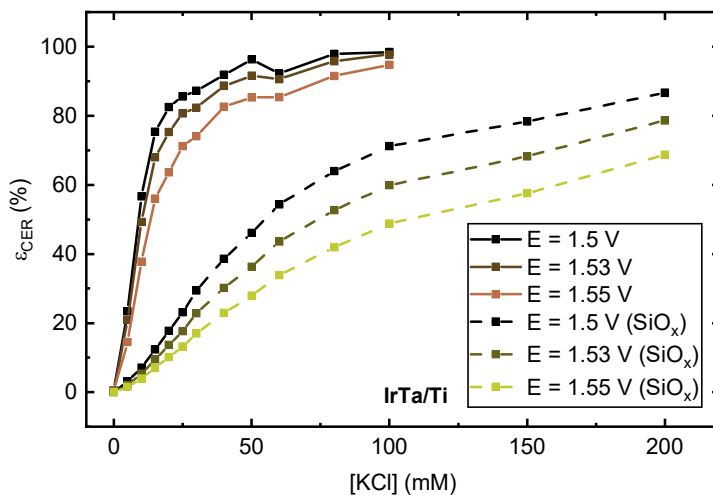
Figure A 9.7.9: Molar selectivity towards the CER as function of chloride concentration for an IrTa/Ti sample, similar to Figure 7.8 in the main text.
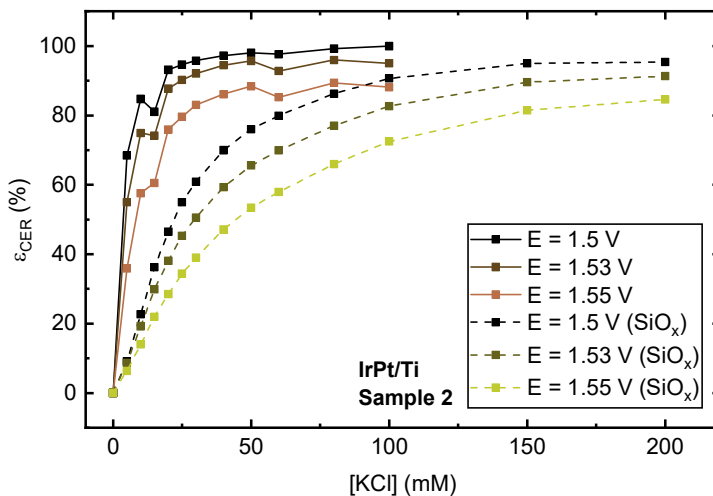
Figure A 9.7.10: Molar selectivity towards the CER as function of chloride concentration for an IrPt/Ti sample, similar to Figure 7.8 in the main text.

9.7.2. *Kinetic OER and CER data*
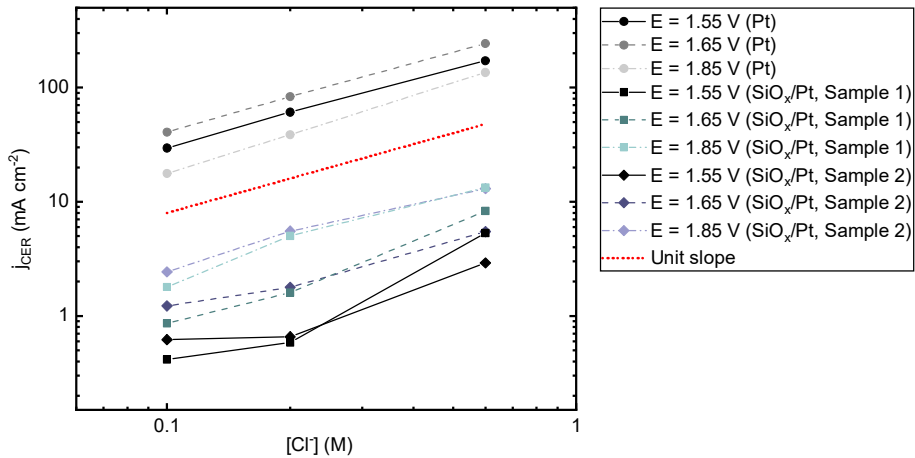
Figure A 9.7.11: Log-log plot of derived CER current densities on various Pt samples, as function of chloride concentration. Data is displayed for three different potentials. Red dotted line shows a reaction order of one (unit slope).
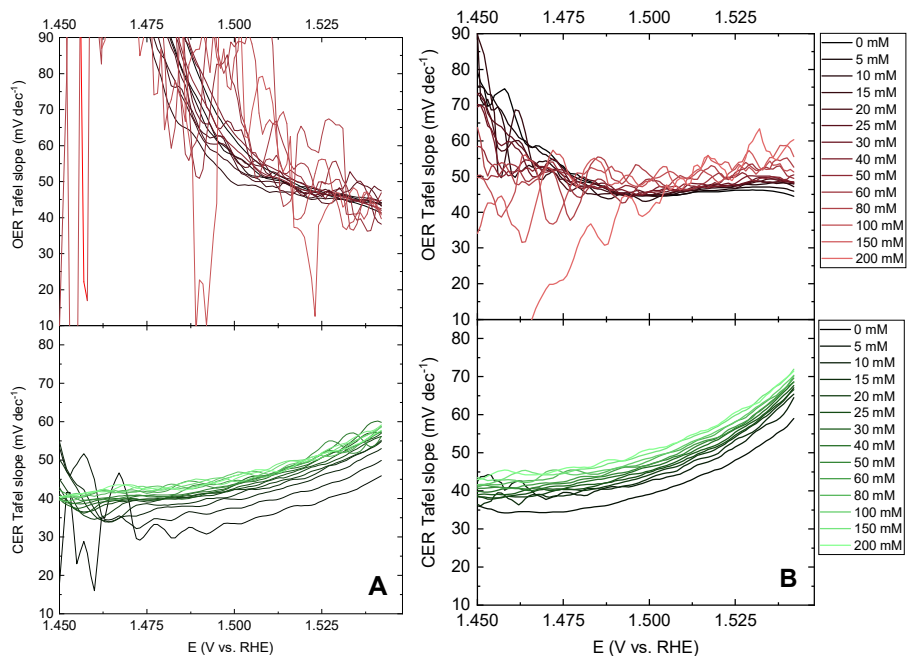
Figure A 9.7.12: Derived Tafel slopes of CER and OER current densities versus potential, on an IrO_x/GC sample and an $SiO_x/IrO_x/GC$ sample (A and B respectively). Values are shown for KCl concentrations ranging between 0 – 200 mM.
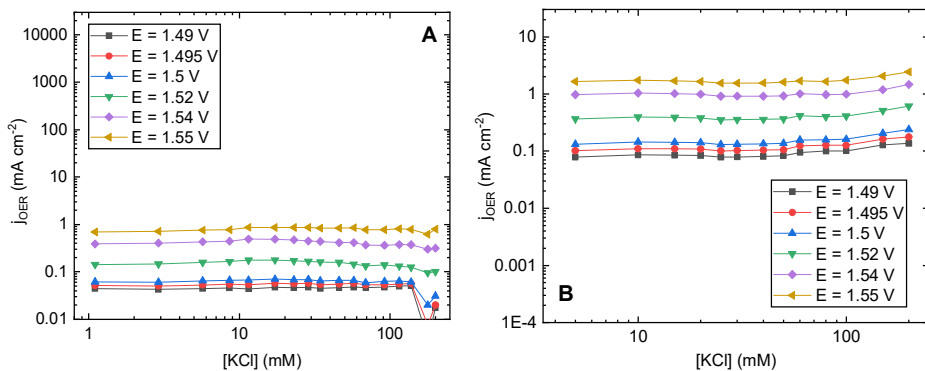
Figure A 9.7.13: Log-log plot of derived OER current densities on an IrO_x/GC sample and a $SiO_x/IrO_x/GC$ sample (A and B respectively). Data is displayed for a series of different potentials.
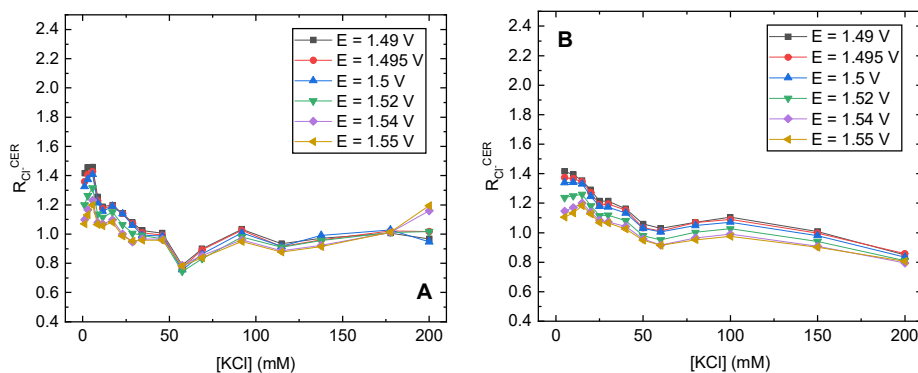
Figure A 9.7.14: CER chloride reaction orders (slopes of log-log plot) versus concentration, derived from an IrO_x/GC sample and a $SiO_x/IrO_x/GC$ sample (A and B respectively). Data is displayed for a series of different potentials.

9.7.3. *Supplementary SEM/EDS data*
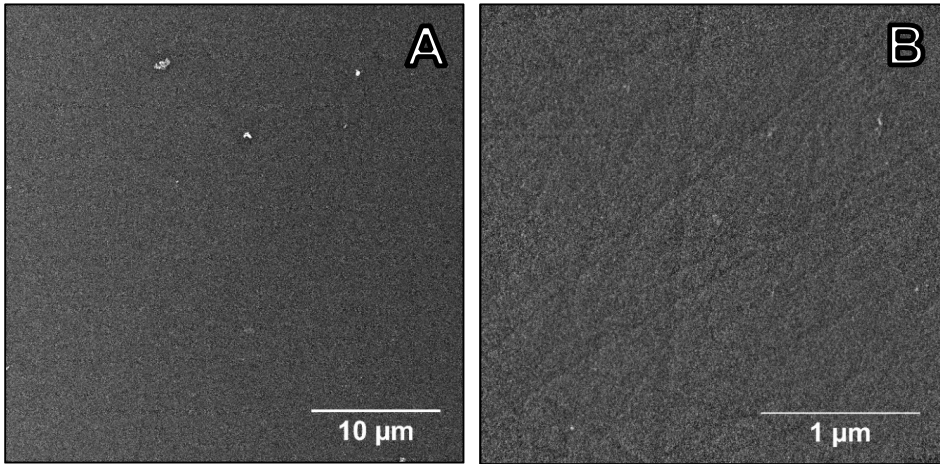
Figure A 9.7.15: SEM micrographs of a $SiO_x/Pt/Ti/GC$ electrode surface (including some minor surface impurities in A).
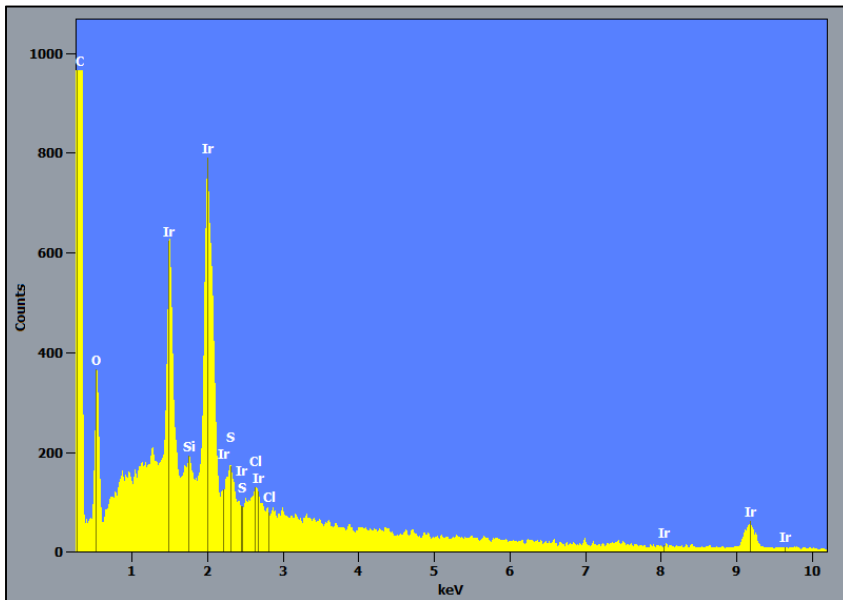
Figure A 9.7.16: EDS spectrum of a $SiO_x/IrO_x/GC$ electrode surface, showing the peaks of commonly detected elements.
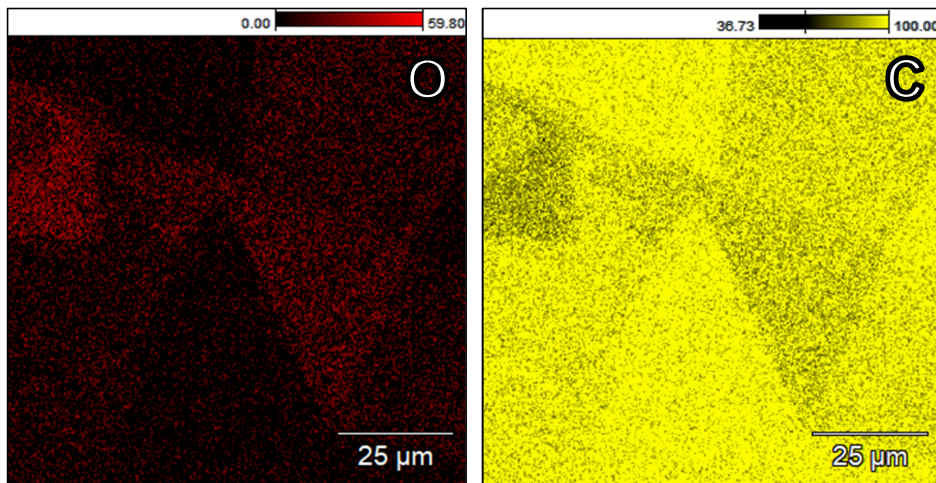
Figure A 9.7.17: Additional EDS elemental maps of O and C, corresponding to the micrograph in Figure 7.5 in the main text. The C signal is present in large amounts and originates from the bulk GC electrode.
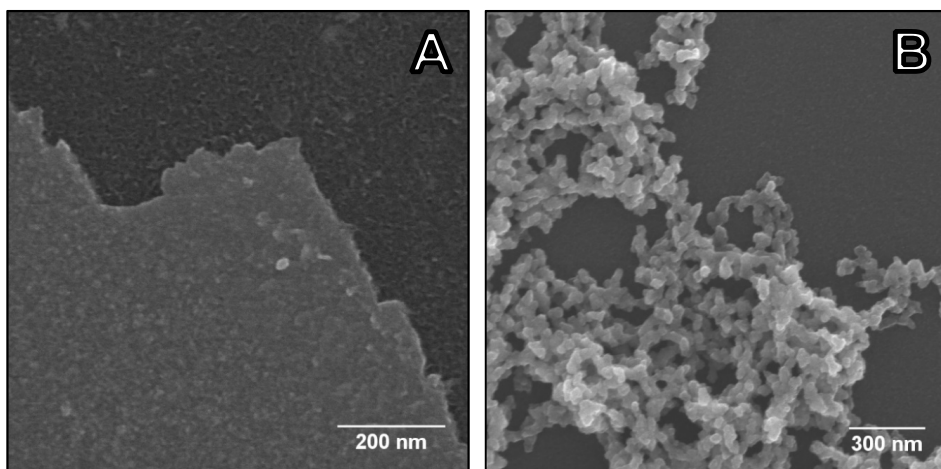
Figure A 9.7.18: Additional SEM electron images of an IrO_x /GC surface, after electrochemical experiments (no SiO_x overlayer present). A: Local edge of the 'smooth' IrO_x layer in light grey color, bottom left. The dark-colored bare GC substrate is visible in the top right. B: Close-up of an IrO_x nanoparticle cluster.
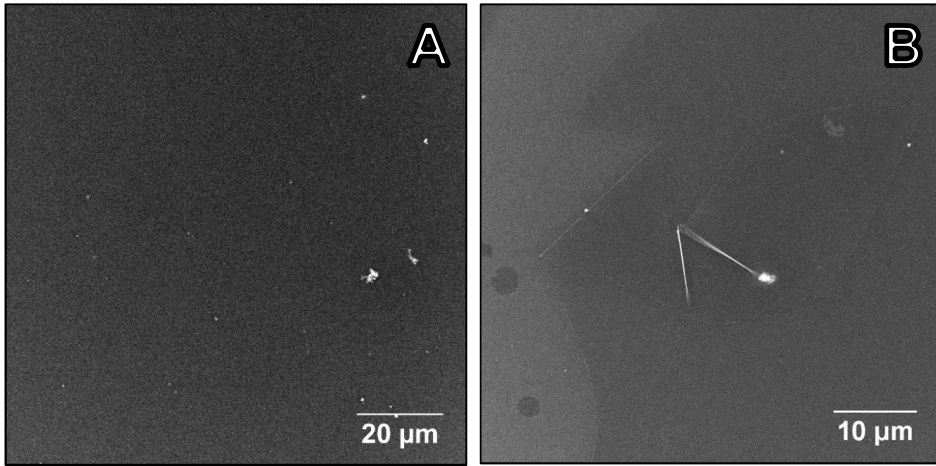
Figure A 9.7.19: Additional SEM electron images of a SiO_x / IrO_x /GC electrode, after electrochemical experiments.
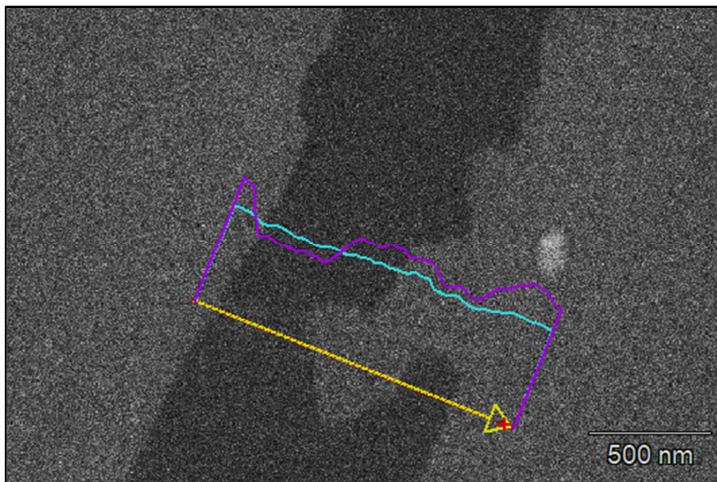
Figure A 9.7.20: SEM/EDS line scan analysis of a SiO_x / IrO_x /GC surface, after electrochemical experiments. Yellow arrows show scan trajectory with corresponding relative counts of Si (cyan) and Ir (purple). Along the scan, one can observe an inhomogeneous Ir distribution (purple) with an even distribution of Si (cyan) on top.
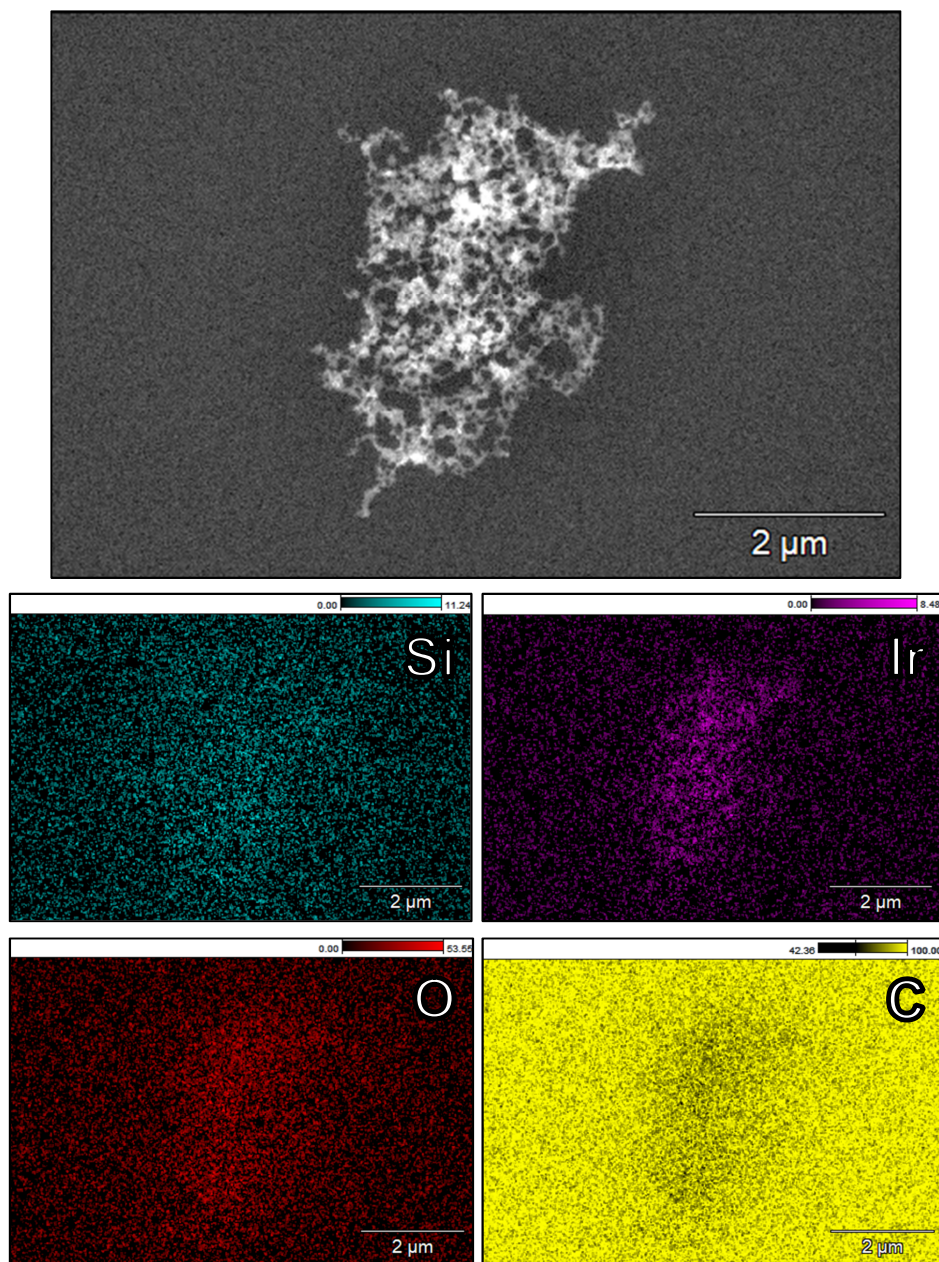
Figure A 9.7.21: Micrograph and EDS elemental mapping of an IrO_x cluster on a $SiO_x/IrO_x/GC$ electrode, after electrochemical experiments.
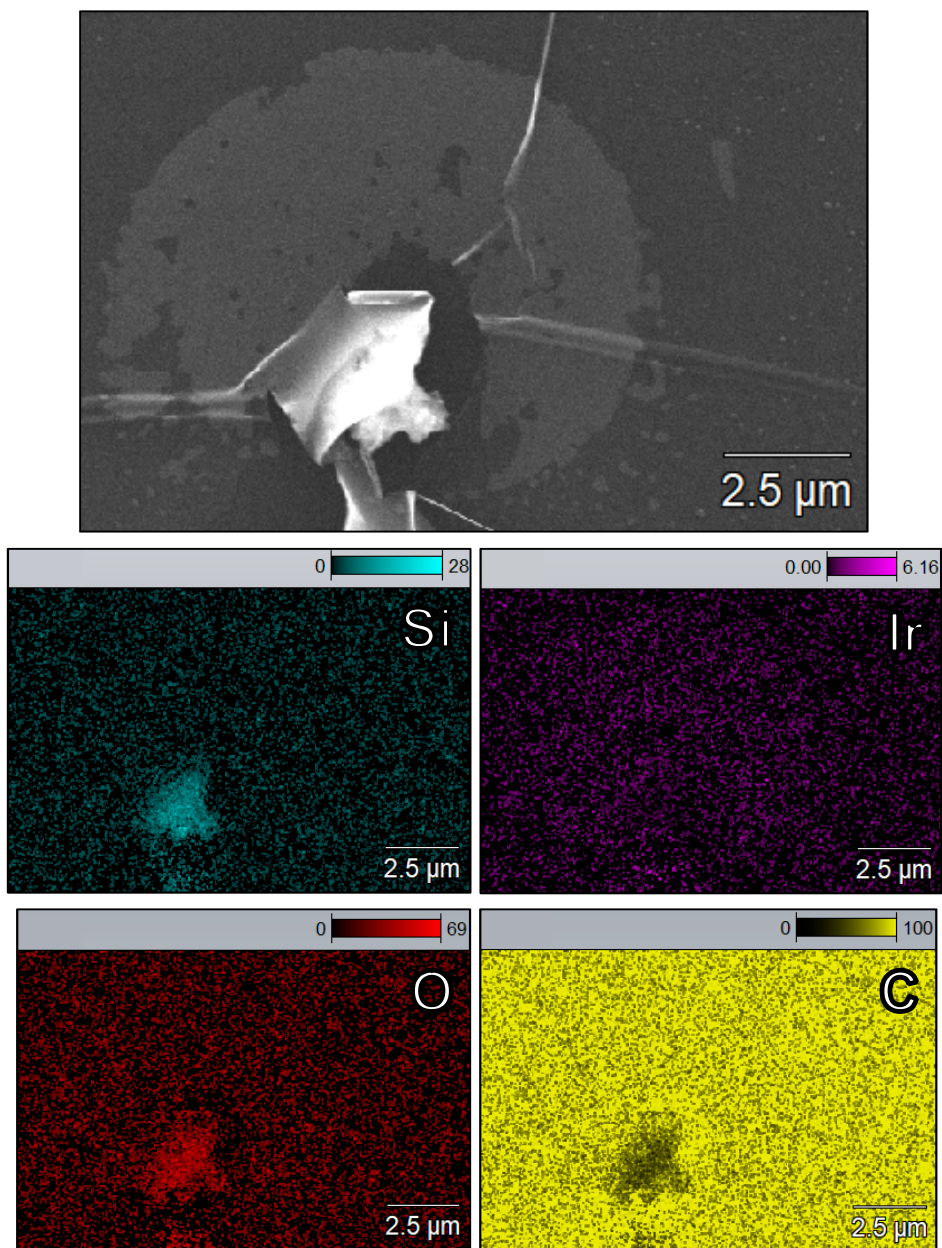
Figure A 9.7.22: Micrograph and EDS elemental mapping of a defect in the SiO_x overlayer on a SiO_x/IrO_x/GC electrode, after electrochemical experiments.
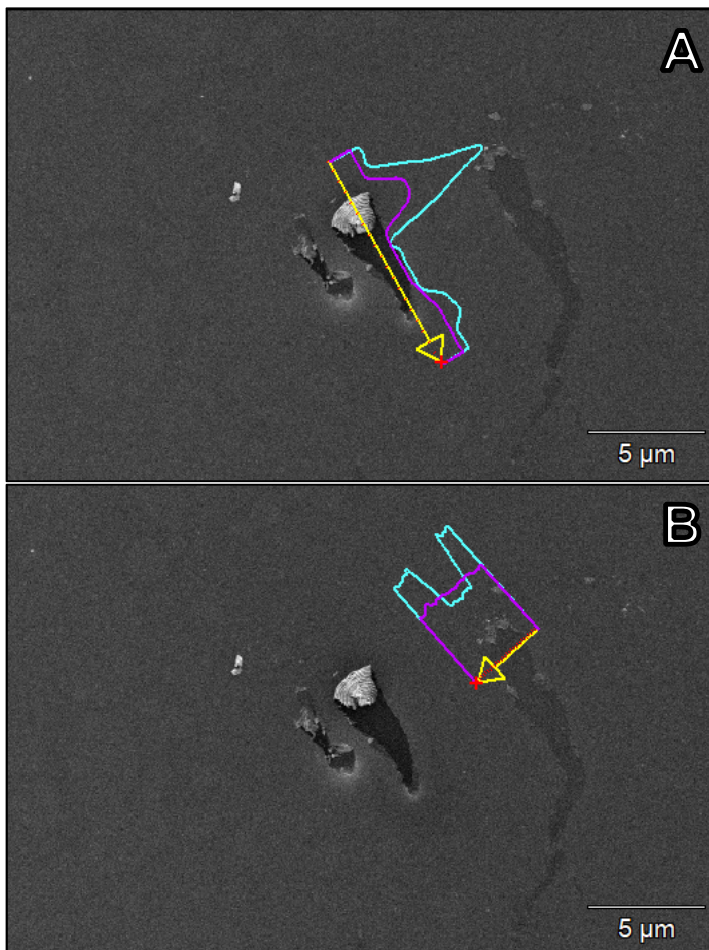
Figure A 9.7.23: SEM/EDS line scan analysis of a $SiO_x/IrO_x/GC$ surface, similar to Figure A 9.7.20. Relative amounts of Si and Ir are show in cyan and purple, respectively. In line scan A, a location is investigated where the combined SiO_x/IrO_x film was damaged. Material has accumulated around the upper area of the scan trajectory, exposing the bare GC underneath. In B, only the SiO_x overlayer was damaged, as suggested by the even Ir distribution.
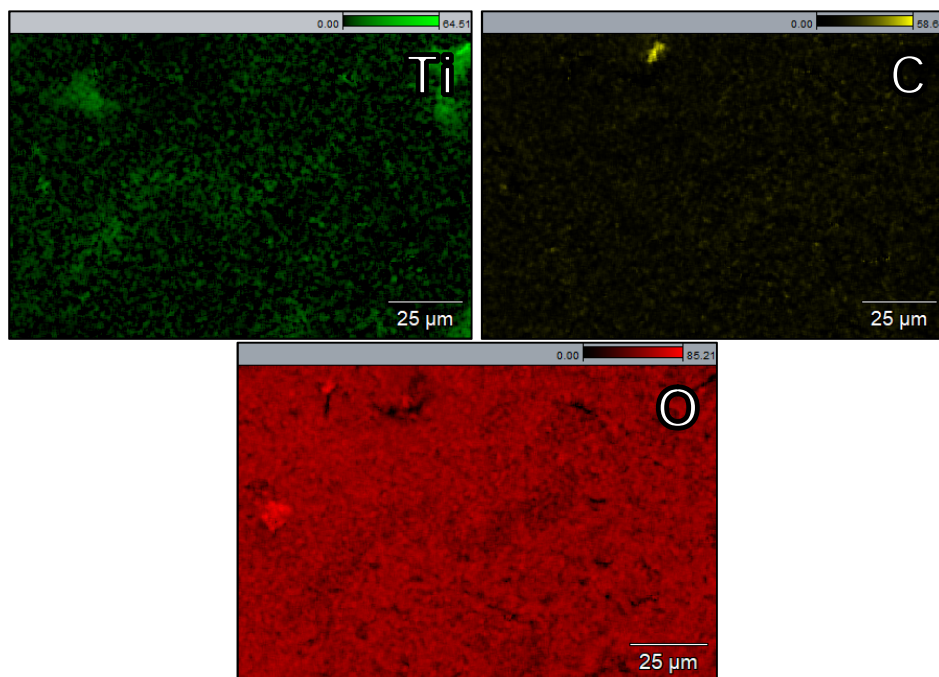
Figure A 9.7.24: Additional EDS elemental maps of Ti, C and O of the micrograph in Figure 7.7 in the main text.

9.8. Supporting information for Chapter 8

9.8.1. Supplementary data and figures
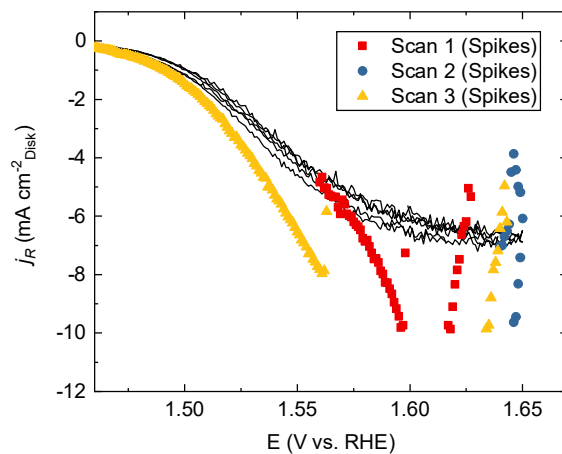
Figure A 9.8.1: Data points from three consecutive scans (red/blue/yellow) omitted from the ring current (black lines) and CER analysis in Figure 8.3.
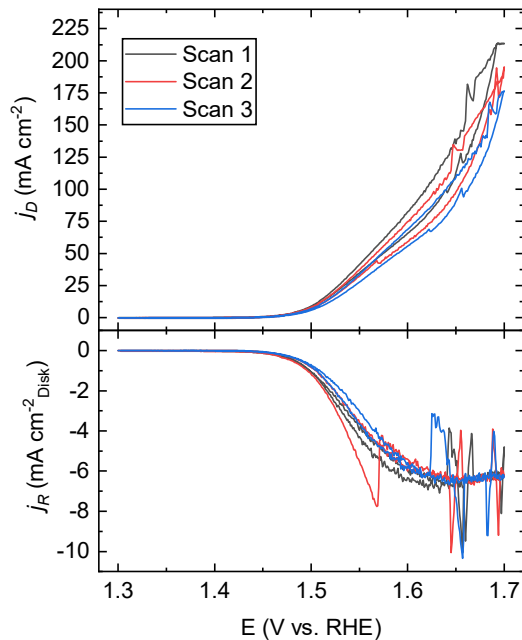
Figure A 9.8.2: RRDE gas evolution experiments under identical conditions as those in Figure 8.3A, but using a potential window extended to 1.70 V vs. RHE.
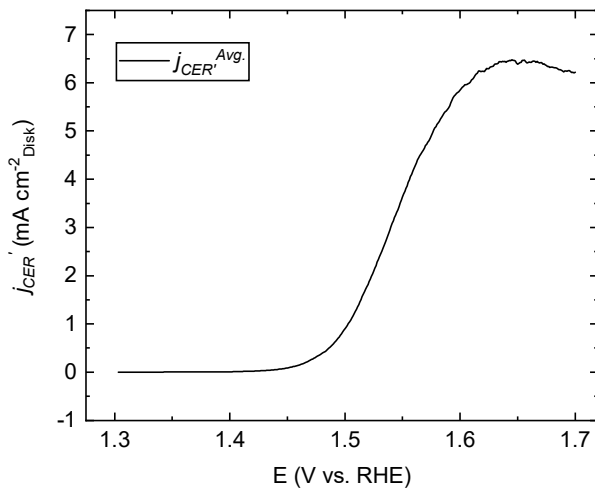
Figure A 9.8.3: Averaged, current spike-corrected forward and backward ring currents from Figure A 9.8.2, representing the CER rates during scanning, such as in the top panel of Figure 8.3.
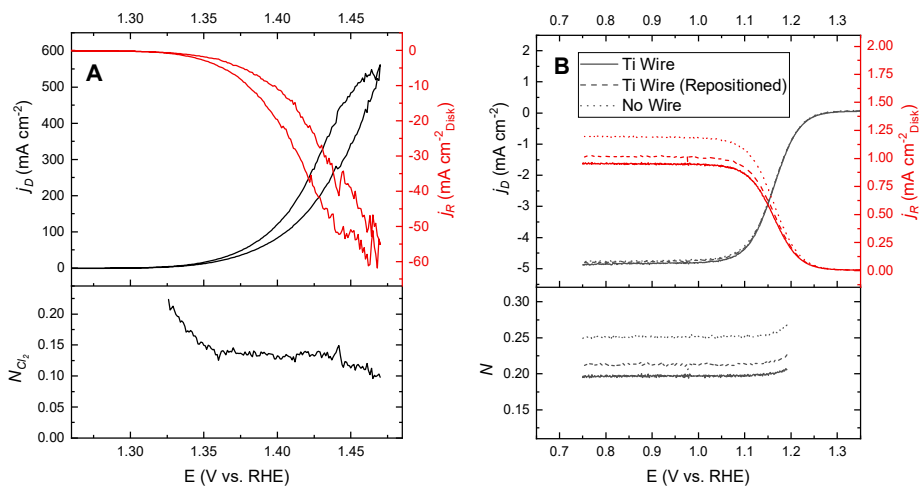
Figure A 9.8.4: Collection experiments on a Pt-Pt RRDE, comparing the collection of gaseous Cl_2 and dissolved $[Fe(CN)_6]^{-4}$ with a Ti wire mounted close to the tip surface. A: Averaged data from five repeated scans in 1 M HCl, such that vigorous Cl_2 evolution occurs on the Pt disk. The Pt ring at 0.95 V was used to detect Cl_2. Top panel shows disk (black trace) and ring current densities (red trace). Bottom panel shows the associated collection efficiency N_{Cl_2}. Scan rate: 10 mV s^{-1}, rotation rate 1500 RPM. B: Experiments involving the collection of $[Fe(CN)_6]^{-4}$. After completion of the CER experiments in A and thoroughly purging the solution to remove all traces of Cl_2, the exact same setup was made alkaline by (carefully) adding the equivalent of 1.1 M KOH. This prevented potentially dangerous situations from exposing $K_3[Fe(CN)_6]$ to strong acid, and served to suppress the HER on Pt while measuring the redox couple. Then, 10 mM $K_3[Fe(CN)_6]$ was added to the + 1 M KCl + 0.1 M KOH solution. This way, the effect of the Ti wire in a specific position could be compared for two different reactions. In the top panel of B, solid trace shows data recorded with the wire positioned in the same way as during experiments in A. Dashed trace shows results after moving the wire slightly further away (several 100 μm) from the tip surface. Dotted trace shows data with the wire removed. Red traces in the upper panel show the corresponding ring current density, black traces in the lower panel show N. Scan rate: 10 mV s^{-1}, rotation rate 1500 RPM.
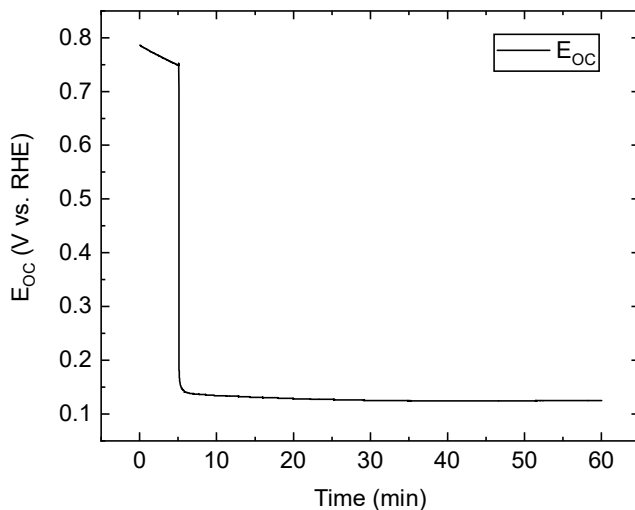
Figure A 9.8.5: Open-circuit potential (E_{OC}) of a Pt disk in a 10 mM NaH_2PO_4 + 10 mM Na_2HPO_4 solution during p-DA deposition, at a rotation rate of 300 RPM. An amount of 2 g/L DA was added to the phosphate buffer around t = 5 min. Solution exposed to air.
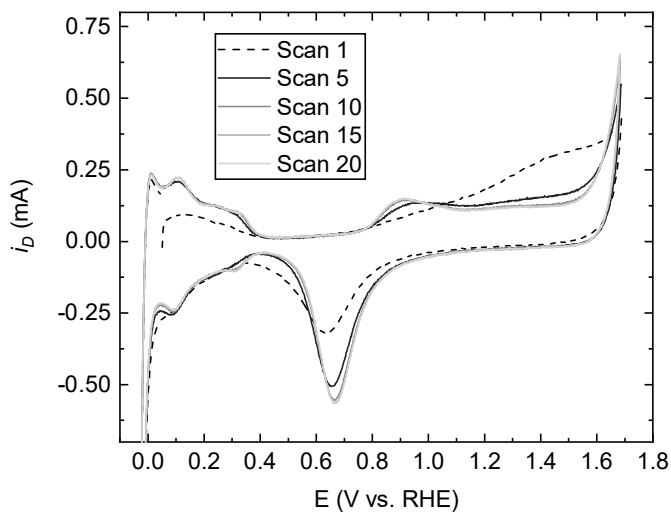
Figure A 9.8.6: Pt disk electropolishing after p-DA deposition on the RRDE tip at 1500 RPM, in a solution of 0.1 M $HClO_4$. Scan rate: 500 mV s^{-1}.

References

1) Pachauri, R. K.; Allen, M. R.; Barros, V. R.; Broome, J.; Cramer, W.; Christ, R.; Church, J. A.; Clarke, L.; Dahe, Q.; Dasgupta, P.; et al. *Climate Change 2014: Synthesis Report. Contribution of Working Groups I, II and III to the Fifth Assessment Report of the Intergovernmental Panel on Climate Change*; Ipcc, 2014.

2) Tverberg, G. E. Oil Supply Limits and the Continuing Financial Crisis. *Energy* **2012**, *37* (1), 27–34. https://doi.org/10.1016/j.energy.2011.05.049.

3) Mohr, S. H.; Wang, J.; Ellem, G.; Ward, J.; Giurco, D. Projection of World Fossil Fuels by Country. *Fuel* **2015**, *141*, 120–135. https://doi.org/10.1016/j.fuel.2014.10.030.

4) Fahrenbruch, A.; Bube, R. *Fundamentals of Solar Cells: Photovoltaic Solar Energy Conversion*; Elsevier, 2012.

5) Lewis, N. S. Toward Cost-Effective Solar Energy Use. *Science* **2007**, *315* (5813), 798–801. https://doi.org/10.1126/science.1137014.

6) Lewis, N. S.; Nocera, D. G. Powering the Planet: Chemical Challenges in Solar Energy Utilization. *Proc. Natl. Acad. Sci.* **2006**, *103* (43), 15729–15735. https://doi.org/10.1073/pnas.0603395103.

7) Dresselhaus, M. S.; Thomas, I. L. Alternative Energy Technologies. *Nature* **2001**, *414* (6861), 332–337. https://doi.org/10.1038/35104599.

8) Bard, A. J.; Faulkner, L. R.; others. Fundamentals and Applications. *Electrochem. Methods* **2001**, *2*, 482.

9) Bockris, J. A Hydrogen Economy. *Science* **1972**, *176* (4041), 1323–1323. https://doi.org/10.1126/science.176.4041.1323.

10) Veziroğlu, T.; Barbir, F. Hydrogen: The Wonder Fuel. *Int. J. Hydrogen Energy* **1992**, *17* (6), 391–404. https://doi.org/10.1016/0360-3199(92)90183-W.

11) Staffell, I.; Scamman, D.; Velazquez Abad, A.; Balcombe, P.; Dodds, P. E.; Ekins, P.; Shah, N.; Ward, K. R. The Role of Hydrogen and Fuel Cells in the Global Energy System. *Energy Environ. Sci.* **2019**, *12* (2), 463–491. https://doi.org/10.1039/C8EE01157E.

12) Kempton, W.; Tomić, J. Vehicle-to-Grid Power Implementation: From Stabilizing the Grid to Supporting Large-Scale Renewable Energy. *J. Power Sources* **2005**, *144* (1), 280–294. https://doi.org/10.1016/j.jpowsour.2004.12.022.

13) Evans, A.; Strezov, V.; Evans, T. J. Assessment of Utility Energy Storage Options for Increased Renewable Energy Penetration. *Renew. Sustain. Energy Rev.* **2012**, *16* (6), 4141–4147. https://doi.org/10.1016/j.rser.2012.03.048.

14) Yekini Suberu, M.; Wazir Mustafa, M.; Bashir, N. Energy Storage Systems for Renewable Energy Power Sector Integration and Mitigation of Intermittency. *Renew. Sustain. Energy Rev.* **2014**, *35*, 499–514. https://doi.org/10.1016/j.rser.2014.04.009.

15) Schoots, K.; Ferioli, F.; Kramer, G.; van der Zwaan, B. Learning Curves for Hydrogen Production Technology: An Assessment of Observed Cost Reductions. *Int. J. Hydrogen Energy* **2008**, *33* (11), 2630–2645. https://doi.org/10.1016/j.ijhydene.2008.03.011.

16) Schmidt, O.; Gambhir, A.; Staffell, I.; Hawkes, A.; Nelson, J.; Few, S. Future Cost and Performance of Water Electrolysis: An Expert Elicitation Study. *Int. J. Hydrogen Energy* **2017**, *42* (52), 30470–30492. https://doi.org/10.1016/j.ijhydene.2017.10.045.

17) Katsounaros, I.; Cherevko, S.; Zeradjanin, A. R.; Mayrhofer, K. J. J. Oxygen Electrochemistry as a Cornerstone for Sustainable Energy Conversion. *Angew. Chemie - Int. Ed.* **2014**, *53* (1), 102–121. https://doi.org/10.1002/anie.201306588.

18) Shao, M.; Chang, Q.; Dodelet, J.-P.; Chenitz, R. Recent Advances in Electrocatalysts for Oxygen Reduction Reaction. *Chem. Rev.* **2016**, *116* (6), 3594–3657. https://doi.org/10.1021/acs.chemrev.5b00462.

19) Tahir, M.; Pan, L.; Idrees, F.; Zhang, X.; Wang, L.; Zou, J.-J.; Wang, Z. L. Electrocatalytic Oxygen Evolution Reaction for Energy Conversion and Storage: A Comprehensive Review. *Nano Energy* **2017**, *37* (May), 136–157. https://doi.org/10.1016/j.nanoen.2017.05.022.

20) Suen, N.-T.; Hung, S.; Quan, Q.; Zhang, N.; Xu, Y.-J.; Chen, H. M. Electrocatalysis for the Oxygen Evolution Reaction: Recent Development and Future Perspectives. *Chem. Soc. Rev.* **2017**, *46* (2), 337–365. https://doi.org/10.1039/C6CS00328A.

21)   Hulme, M. 1.5 °C and Climate Research after the Paris Agreement. *Nat. Clim. Chang.* **2016**, *6* (3), 222–224. https://doi.org/10.1038/nclimate2939.

22)   You, B.; Sun, Y. Innovative Strategies for Electrocatalytic Water Splitting. *Acc. Chem. Res.* **2018**, acs.accounts.8b00002. https://doi.org/10.1021/acs.accounts.8b00002.

23)   Lu, Q.; Jiao, F. Electrochemical CO2 Reduction: Electrocatalyst, Reaction Mechanism, and Process Engineering. *Nano Energy* **2016**, *29*, 439–456. https://doi.org/10.1016/j.nanoen.2016.04.009.

24)   Kibria, M. G.; Edwards, J. P.; Gabardo, C. M.; Dinh, C.; Seifitokaldani, A.; Sinton, D.; Sargent, E. H. Electrochemical CO 2 Reduction into Chemical Feedstocks: From Mechanistic Electrocatalysis Models to System Design. *Adv. Mater.* **2019**, *31* (31), 1807166. https://doi.org/10.1002/adma.201807166.

25)   Bennett, J. Electrodes for Generation of Hydrogen and Oxygen from Seawater. *Int. J. Hydrogen Energy* **1980**, *5* (4), 401–408. https://doi.org/10.1016/0360-3199(80)90021-X.

26)   Bockris, J.; Veziroğlu, T. N. A Solar-Hydrogen Economy for U.S.A. *Int. J. Hydrogen Energy* **1983**, *8* (5), 323–340. https://doi.org/10.1016/0360-3199(83)90048-4.

27)   Dresp, S.; Dionigi, F.; Klingenhof, M.; Strasser, P. Direct Electrolytic Splitting of Seawater: Opportunities and Challenges. *ACS Energy Lett.* **2019**, *4* (4), 933–942. https://doi.org/10.1021/acsenergylett.9b00220.

28)   Juodkazytė, J.; Šebeka, B.; Savickaja, I.; Petrulevičienė, M.; Butkutė, S.; Jasulaitienė, V.; Selskis, A.; Ramanauskas, R. Electrolytic Splitting of Saline Water: Durable Nickel Oxide Anode for Selective Oxygen Evolution. *Int. J. Hydrogen Energy* **2019**, *44* (12), 5929–5939. https://doi.org/10.1016/j.ijhydene.2019.01.120.

29)   Dionigi, F.; Reier, T.; Pawolek, Z.; Gliech, M.; Strasser, P. Design Criteria, Operating Conditions, and Nickel-Iron Hydroxide Catalyst Materials for Selective Seawater Electrolysis. *ChemSusChem* **2016**, *9* (9), 962–972. https://doi.org/10.1002/cssc.201501581.

30)   Fukuzumi, S.; Lee, Y.-M.; Nam, W. Fuel Production from Seawater and Fuel Cells Using Seawater. *ChemSusChem* **2017**, *10* (22), 4264–4276. https://doi.org/10.1002/cssc.201701381.

31)   Fujimura, K.; Izumiya, K.; Kawashima, A.; Akiyama, E.; Habazaki, H.; Kumagai, N.; Hashimoto, K. Anodically Deposited Manganese-Molybdenum Oxide Anodes with High Selectivity for Evolving Oxygen in Electrolysis of Seawater. *J. Appl. Electrochem.* **1999**, *29*, 765–771. https://doi.org/10.1023/A:1003492009263.

32)   El-Moneim, A.; Kumagai, N.; Asami, K.; Hashimoto, K. Nanocrystalline Manganese-Molybdenum-Tungsten Oxide Anodes for Oxygen Evolution in Acidic Seawater Electrolysis. *Mater. Trans.* **2005**, *46* (2), 309–316. https://doi.org/10.2320/matertrans.46.309.

33)   Trasatti, S. Electrocatalysis: Understanding the Success of DSA®. *Electrochim. Acta* **2000**, *45* (15–16), 2377–2385. https://doi.org/10.1016/S0013-4686(00)00338-8.

34)   Karlsson, R. K. B.; Cornell, A. Selectivity between Oxygen and Chlorine Evolution in the Chlor-Alkali and Chlorate Processes. *Chem. Rev.* **2016**, *116* (5), 2982–3028. https://doi.org/10.1021/acs.chemrev.5b00389.

35)   Trasatti, S. Progress in the Understanding of the Mechanism of Chlorine Evolution at Oxide Electrodes. *Electrochim. Acta* **1987**, *32* (3), 369–382. https://doi.org/10.1016/0013-4686(87)85001-6.

36)   World Chlorine Council. *"Sustainable Progress", Downloaded from Https://Worldchlorine.Org/Publications/ on 28-06-2018*; 2017.

37)   Euro Chlor. *Chlorine Industry Review 2016-2017, Downloaded from Http://Fr.Zone-Secure.Net/13451/398525 on 09-04-2018*; 2017.

38)   Fauvarque, J. The Chlorine Industry. *Pure Appl. Chem.* **1996**, *68* (9), 1713–1720. https://doi.org/10.1351/pac199668091713.

39)   Euro Chlor. Chlor-alkali Industry Review 2017/2018 - Manufacturing & applications https://chlorineindustryreview.com/manufacturing-applications/ (last accessed on 28-11-2018).

40)   Moussallem, I.; Jörissen, J.; Kunz, U.; Pinnow, S.; Turek, T. Chlor-Alkali Electrolysis with Oxygen Depolarized Cathodes: History, Present Status and Future Prospects. *J. Appl. Electrochem.* **2008**, *38* (9), 1177–1194. https://doi.org/10.1007/s10800-008-9556-9.

41) Jung, J.; Postels, S.; Bardow, A. Cleaner Chlorine Production Using Oxygen Depolarized Cathodes? A Life Cycle Assessment. *J. Clean. Prod.* **2014**, *80*, 46–56. https://doi.org/10.1016/j.jclepro.2014.05.086.

42) Wang, X.; Tong, C.; Palazoglu, A.; El-Farra, N. H. Energy Management for the Chlor-Alkali Process with Hybrid Renewable Energy Generation Using Receding Horizon Optimization. In *53rd IEEE Conference on Decision and Control*; IEEE, 2014; Vol. 2015-Febru, pp 4838–4843. https://doi.org/10.1109/CDC.2014.7040144.

43) U.S. Department of Energy. Advanced Chlor-Alkali Technology (CPS #1797). *Ind. Technol. Progr.* **2006**, 1–2.

44) Lakshmanan, S.; Murugesan, T. The Chlor-Alkali Process: Work in Progress. *Clean Technol. Environ. Policy* **2014**, *16* (2), 225–234. https://doi.org/10.1007/s10098-013-0630-6.

45) Crook, J.; Mousavi, A. The Chlor-Alkali Process: A Review of History and Pollution. *Environ. Forensics* **2016**, *17* (3), 211–217. https://doi.org/10.1080/15275922.2016.1177755.

46) Panić, V. V.; Dekanski, A. B.; Milonjić, S. K.; Mišković-Stanković, V. B.; Nikolić, B. Ž. Electrocatalytic Activity of Sol-Gel-Prepared RuO2/Ti Anode in Chlorine and Oxygen Evolution Reactions. *Russ. J. Electrochem.* **2006**, *42* (10), 1055–1060. https://doi.org/10.1134/S1023193506100107.

47) Hoseinieh, S. M.; Ashrafizadeh, F.; Maddahi, M. H. A Comparative Investigation of the Corrosion Behavior of RuO[Sub 2]–IrO[Sub 2]–TiO[Sub 2] Coated Titanium Anodes in Chloride Solutions. *J. Electrochem. Soc.* **2010**, *157* (4), E50. https://doi.org/10.1149/1.3294569.

48) Shao, D.; Yan, W.; Cao, L.; Li, X.; Xu, H. High-Performance Ti/Sb–SnO2/Pb3O4 Electrodes for Chlorine Evolution: Preparation and Characteristics. *J. Hazard. Mater.* **2014**, *267*, 238–244. https://doi.org/10.1016/j.jhazmat.2013.12.064.

49) Chen, G. Electrochemical Technologies in Wastewater Treatment. *Sep. Purif. Technol.* **2004**, *38* (1), 11–41. https://doi.org/10.1016/j.seppur.2003.10.006.

50) Martínez-Huitle, C. A.; Ferro, S. Electrochemical Oxidation of Organic Pollutants for the Wastewater Treatment: Direct and Indirect Processes. *Chem. Soc. Rev.* **2006**, *35* (12), 1324–1340. https://doi.org/10.1039/B517632H.

51) Oliveira, F. H.; Osugi, M. E.; Paschoal, F. M. M.; Profeti, D.; Olivi, P.; Zanoni, M. V. B. Electrochemical Oxidation of an Acid Dye by Active Chlorine Generated Using Ti/Sn(1–x)Ir x O2 Electrodes. *J. Appl. Electrochem.* **2007**, *37* (5), 583–592. https://doi.org/10.1007/s10800-006-9289-6.

52) Naumczyk, J.; Szpyrkowicz, L.; Zilio-Grandi, F. Electrochemical Treatment of Textile Wastewater. *Water Sci. Technol.* **1996**, *34* (11), 17–24. https://doi.org/10.1016/S0273-1223(96)00816-5.

53) Lin, S. H.; Wu, C. L. Electrochemical Nitrite and Ammonia Removal from Aqueous Solution. *J. Environ. Sci. Heal. . Part A Environ. Sci. Eng. Toxicol.* **1995**, *30* (7), 1445–1456. https://doi.org/10.1080/10934529509376277.

54) Schmachtel, S.; Toiminen, M.; Kontturi, K.; Forsén, O.; Barker, M. H. New Oxygen Evolution Anodes for Metal Electrowinning: MnO2 Composite Electrodes. *J. Appl. Electrochem.* **2009**, *39*, 1835–1848. https://doi.org/10.1007/s10800-009-9887-1.

55) Trasatti, S. Electrocatalysis in the Anodic Evolution of Oxygen and Chlorine. *Electrochim. Acta* **1984**, *29* (11), 1503–1512. https://doi.org/10.1016/0013-4686(84)85004-5.

56) Consonni, V.; Trasatti, S.; Pollak, F. H.; O'Grady, W. E. Mechanism of Chlorine Evolution on Oxide Anodes: Study of PH Effects. *J. Electroanal. Chem.* **1987**, *228* (1–2), 393–406. https://doi.org/10.1016/0022-0728(87)80119-5.

57) Duby, P. The History of Progress in Dimensionally Stable Anodes. *JOM* **1993**, *45* (3), 41–43. https://doi.org/10.1007/BF03222350.

58) Conway, B. E.; Novak, D. M. Electrocatalytic Effect of the Oxide Film at Pt Anodes on Cl· Recombination Kinetics in Chlorine Evolution. *J. Electroanal. Chem. Interfacial Electrochem.* **1979**, *99* (2), 133–156. https://doi.org/10.1016/S0022-0728(79)80243-0.

59) Carmo, M.; Fritz, D. L.; Mergel, J.; Stolten, D. A Comprehensive Review on PEM Water Electrolysis. *Int. J. Hydrogen Energy* **2013**, *38* (12), 4901–4934. https://doi.org/10.1016/j.ijhydene.2013.01.151.

60) Blasco-Ahicart, M.; Soriano-López, J.; Carbó, J. J.; Poblet, J. M.; Galan-Mascaros, J. R. Polyoxometalate Electrocatalysts Based on Earth-Abundant Metals for Efficient Water Oxidation in Acidic Media. *Nat. Chem.* **2017**, No. October, 1–7. https://doi.org/10.1038/nchem.2874.

61) Moreno-Hernandez, I. A.; Brunschwig, B. S.; Lewis, N. S. Crystalline Nickel, Cobalt, and Manganese Antimonates as Electrocatalysts for the Chlorine Evolution Reaction. *Energy Environ. Sci.* **2019**, *12* (4), 1241–1248. https://doi.org/10.1039/C8EE03676D.

62) Li, A.; Ooka, H.; Bonnet, N.; Hayashi, T.; Sun, Y.; Jiang, Q.; Li, C.; Han, H.; Nakamura, R. Stable Potential Windows for Long-Term Electrocatalysis by Manganese Oxides Under Acidic Conditions. *Angew. Chemie* **2019**, *131* (15), 5108–5112. https://doi.org/10.1002/ange.201813361.

63) Zeng, K.; Zhang, D. Recent Progress in Alkaline Water Electrolysis for Hydrogen Production and Applications. *Prog. Energy Combust. Sci.* **2010**, *36* (3), 307–326. https://doi.org/10.1016/j.pecs.2009.11.002.

64) Man, I. C.; Su, H. Y.; Calle-Vallejo, F.; Hansen, H. A.; Martínez, J. I.; Inoglu, N. G.; Kitchin, J.; Jaramillo, T. F.; Nørskov, J. K.; Rossmeisl, J. Universality in Oxygen Evolution Electrocatalysis on Oxide Surfaces. *ChemCatChem* **2011**, *3* (7), 1159–1165. https://doi.org/10.1002/cctc.201000397.

65) Fabbri, E.; Schmidt, T. J. Oxygen Evolution Reaction—The Enigma in Water Electrolysis. *ACS Catal.* **2018**, *8* (10), 9765–9774. https://doi.org/10.1021/acscatal.8b02712.

66) McCrory, C. C. L.; Jung, S.; Peters, J. C.; Jaramillo, T. F. Benchmarking Heterogeneous Electrocatalysts for the Oxygen Evolution Reaction. *J. Am. Chem. Soc.* **2013**, *135* (45), 16977–16987. https://doi.org/10.1021/ja407115p.

67) Hu, J. M.; Zhang, J. Q.; Cao, C. N. Oxygen Evolution Reaction on IrO2-Based DSA?? Type Electrodes: Kinetics Analysis of Tafel Lines and EIS. *Int. J. Hydrogen Energy* **2004**, *29* (8), 791–797. https://doi.org/10.1016/j.ijhydene.2003.09.007.

68) Koper, M. T. M. Thermodynamic Theory of Multi-Electron Transfer Reactions: Implications for Electrocatalysis. *J. Electroanal. Chem.* **2011**, *660* (2), 254–260. https://doi.org/10.1016/j.jelechem.2010.10.004.

69) Burke, L. D.; O'Neill, J. F. Some Aspects of the Chlorine Evolution Reaction at Ruthenium Dioxide Anodes. *J. Electroanal. Chem. Interfacial Electrochem.* **1979**, *101* (3), 341–349. https://doi.org/10.1016/S0022-0728(79)80045-5.

70) Petrykin, V.; Macounová, K. M.; Shlyakhtin, O.; Krtil, P. Tailoring the Selectivity for Electrocatalytic Oxygen Evolution on Ruthenium Oxides by Zinc Substitution. *Angew. Chemie - Int. Ed.* **2010**, *49* (28), 4813–4815. https://doi.org/10.1002/anie.200907128.

71) Macounová, K. M.; Makarova, M.; Jirkovský, J. S.; Franc, J.; Krtil, P. Parallel Oxygen and Chlorine Evolution on Ru1−xNixO2−y Nanostructured Electrodes. *Electrochim. Acta* **2008**, *53* (21), 6126–6134. https://doi.org/10.1016/j.electacta.2007.11.014.

72) Hansen, H. A.; Man, I. C.; Studt, F.; Abild-Pedersen, F.; Bligaard, T.; Rossmeisl, J. Electrochemical Chlorine Evolution at Rutile Oxide (110) Surfaces. *Phys. Chem. Chem. Phys.* **2010**, *12* (1), 283–290. https://doi.org/10.1039/B917459A.

73) Abbott, D. F.; Petrykin, V.; Okube, M.; Bastl, Z.; Mukerjee, S.; Krtil, P. Selective Chlorine Evolution Catalysts Based on Mg-Doped Nanoparticulate Ruthenium Dioxide. *J. Electrochem. Soc.* **2014**, *162* (1), H23–H31. https://doi.org/10.1149/2.0541501jes.

74) Exner, K. S.; Anton, J.; Jacob, T.; Over, H. Chlorine Evolution Reaction on RuO2(110): Ab Initio Atomistic Thermodynamics Study - Pourbaix Diagrams. *Electrochim. Acta* **2014**, *120*, 460–466. https://doi.org/10.1016/j.electacta.2013.11.027.

75) Exner, K. S.; Anton, J.; Jacob, T.; Over, H. Full Kinetics from First Principles of the Chlorine Evolution Reaction over a RuO 2 (110) Model Electrode. *Angew. Chemie Int. Ed.* **2016**, *55* (26), 7501–7504. https://doi.org/10.1002/anie.201511804.

76) Exner, K. S.; Anton, J.; Jacob, T.; Over, H. Controlling Selectivity in the Chlorine Evolution Reaction over RuO 2 -Based Catalysts. *Angew. Chemie Int. Ed.* **2014**, *53* (41), 11032–11035. https://doi.org/10.1002/anie.201406112.

77) Sohrabnejad-Eskan, I.; Goryachev, A.; Exner, K. S.; Kibler, L. A.; Hensen, E. J. M.; Hofmann, J. P.; Over, H. Temperature-Dependent Kinetic Studies of the Chlorine Evolution Reaction over

RuO 2 (110) Model Electrodes. *ACS Catal.* **2017**, *7* (4), 2403–2411. https://doi.org/10.1021/acscatal.6b03415.

78) Lassali, T. A. F.; Boodts, J. F. C.; Trasatti, S. Electrocatalytic Activity of the Ternary Oxide Ru0.3PtxTi(0.7 − x)O2 for Chlorine Evolution. *Electrochim. Acta* **1994**, *39* (11–12), 1545–1549. https://doi.org/10.1016/0013-4686(94)85133-6.

79) Petrykin, V.; Macounová, K. M.; Okube, M.; Mukerjee, S.; Krtil, P. Local Structure of Co Doped RuO2 Nanocrystalline Electrocatalytic Materials for Chlorine and Oxygen Evolution. *Catal. Today* **2013**, *202* (1), 63–69. https://doi.org/10.1016/j.cattod.2012.03.075.

80) Martelli, G. N.; Ornelas, R.; Faita, G. Deactivation Mechanisms of Oxygen Evolving Anodes at High Current Densities. *Electrochim. Acta* **1994**, *39* (11–12), 1551–1558. https://doi.org/10.1016/0013-4686(94)85134-4.

81) Cherevko, S.; Zeradjanin, A. R.; Topalov, A. A.; Kulyk, N.; Katsounaros, I.; Mayrhofer, K. J. J. Dissolution of Noble Metals during Oxygen Evolution in Acidic Media. *ChemCatChem* **2014**, *6* (8), 2219–2223. https://doi.org/10.1002/cctc.201402194.

82) Topalov, A. A.; Katsounaros, I.; Auinger, M.; Cherevko, S.; Meier, J. C.; Klemm, S. O.; Mayrhofer, K. J. J. Dissolution of Platinum: Limits for the Deployment of Electrochemical Energy Conversion? *Angew. Chemie Int. Ed.* **2012**, *51* (50), 12613–12615. https://doi.org/10.1002/anie.201207256.

83) Danilovic, N.; Subbaraman, R.; Chang, K.-C.; Chang, S. H.; Kang, Y. J.; Snyder, J.; Paulikas, A. P.; Strmcnik, D.; Kim, Y.-T.; Myers, D.; et al. Activity–Stability Trends for the Oxygen Evolution Reaction on Monometallic Oxides in Acidic Environments. *J. Phys. Chem. Lett.* **2014**, *5* (14), 2474–2478. https://doi.org/10.1021/jz501061n.

84) Binninger, T.; Mohamed, R.; Waltar, K.; Fabbri, E.; Levecque, P.; Kötz, R.; Schmidt, T. J. Thermodynamic Explanation of the Universal Correlation between Oxygen Evolution Activity and Corrosion of Oxide Catalysts. *Sci. Rep.* **2015**, *5* (1), 12167. https://doi.org/10.1038/srep12167.

85) Reier, T.; Pawolek, Z.; Cherevko, S.; Bruns, M.; Jones, T.; Teschner, D.; Selve, S.; Bergmann, A.; Nong, H. N.; Schlögl, R.; et al. Molecular Insight in Structure and Activity of Highly Efficient, Low-Ir Ir–Ni Oxide Catalysts for Electrochemical Water Splitting (OER). *J. Am. Chem. Soc.* **2015**, *137* (40), 13031–13040. https://doi.org/10.1021/jacs.5b07788.

86) Frydendal, R.; Paoli, E. A.; Chorkendorff, I.; Rossmeisl, J.; Stephens, I. E. L. Toward an Active and Stable Catalyst for Oxygen Evolution in Acidic Media: Ti-Stabilized MnO 2. *Adv. Energy Mater.* **2015**, *5* (22), 1500991. https://doi.org/10.1002/aenm.201500991.

87) Comninellis, C.; Vercesi, G. P. Characterization of DSA-Type Oxygen Evolving Electrodes: Choice of a Coating. *J. Appl. Electrochem.* **1991**, *21* (4), 335–345. https://doi.org/10.1007/BF01020219.

88) Panić, V. V.; Dekanski, A. B.; Mišković-Stanković, V. B.; Milonjić, S. K.; Nikolić, B. Ž. On the Deactivation Mechanism of RuO2–TiO2/Ti Anodes Prepared by the Sol–Gel Procedure. *J. Electroanal. Chem.* **2005**, *579* (1), 67–76. https://doi.org/10.1016/j.jelechem.2005.01.026.

89) Chen, S.; Zheng, Y.; Wang, S.; Chen, X. Ti/RuO2–Sb2O5–SnO2 Electrodes for Chlorine Evolution from Seawater. *Chem. Eng. J.* **2011**, *172* (1), 47–51. https://doi.org/10.1016/j.cej.2011.05.059.

90) Geiger, S.; Cherevko, S.; Mayrhofer, K. J. J. Dissolution of Platinum in Presence of Chloride Traces. *Electrochim. Acta* **2015**, *179*, 24–31. https://doi.org/10.1016/j.electacta.2015.03.059.

91) Reier, T.; Nong, H. N.; Teschner, D.; Schlögl, R.; Strasser, P. Electrocatalytic Oxygen Evolution Reaction in Acidic Environments – Reaction Mechanisms and Catalysts. *Adv. Energy Mater.* **2017**, *7* (1). https://doi.org/10.1002/aenm.201601275.

92) Dau, H.; Limberg, C.; Reier, T.; Risch, M.; Roggan, S.; Strasser, P. The Mechanism of Water Oxidation: From Electrolysis via Homogeneous to Biological Catalysis. *ChemCatChem*. 2010, pp 724–761. https://doi.org/10.1002/cctc.201000126.

93) Lyons, M. E. G.; Floquet, S. Mechanism of Oxygen Reactions at Porous Oxide Electrodes. Part 2--Oxygen Evolution at RuO2, IrO2 and Ir(x)Ru(1-x)O2 Electrodes in Aqueous Acid and Alkaline Solution. *Phys. Chem. Chem. Phys.* **2011**, *13* (12), 5314–5335. https://doi.org/10.1039/c0cp02875d.

94) Macounová, K. M.; Makarova, M.; Krtil, P. Oxygen Evolution on Nanocrystalline RuO2 and

Ru0.9Ni0.1O2−δ Electrodes – DEMS Approach to Reaction Mechanism Determination. *Electrochem. Commun.* **2009**, *11* (10), 1865–1868. https://doi.org/10.1016/j.elecom.2009.08.004.

95) Haschke, S.; Mader, M.; Schlicht, S.; Roberts, A. M.; Angeles-Boza, A. M.; Barth, J. A. C.; Bachmann, J. Direct Oxygen Isotope Effect Identifies the Rate-Determining Step of Electrocatalytic OER at an Oxidic Surface. *Nat. Commun.* **2018**, *9* (1), 4565. https://doi.org/10.1038/s41467-018-07031-1.

96) Suntivich, J.; Perry, E. E.; Gasteiger, H. A.; Shao-Horn, Y. The Influence of the Cation on the Oxygen Reduction and Evolution Activities of Oxide Surfaces in Alkaline Electrolyte. *Electrocatalysis* **2013**, *4* (1), 49–55. https://doi.org/10.1007/s12678-012-0118-x.

97) Diaz-Morales, O.; Calle-Vallejo, F.; de Munck, C.; Koper, M. T. M. Electrochemical Water Splitting by Gold: Evidence for an Oxide Decomposition Mechanism. *Chem. Sci.* **2013**, *4* (6), 2334. https://doi.org/10.1039/c3sc50301a.

98) Yoo, J. S.; Rong, X.; Liu, Y.; Kolpak, A. M. Role of Lattice Oxygen Participation in Understanding Trends in the Oxygen Evolution Reaction on Perovskites. *ACS Catal.* **2018**, *8* (5), 4628–4636. https://doi.org/10.1021/acscatal.8b00612.

99) Grimaud, A.; Diaz-Morales, O.; Han, B.; Hong, W. T.; Lee, Y.; Giordano, L.; Stoerzinger, K. A.; Koper, M. T. M.; Shao-Horn, Y. Activating Lattice Oxygen Redox Reactions in Metal Oxides to Catalyse Oxygen Evolution. *Nat. Chem.* **2017**, *9* (5), 457–465. https://doi.org/10.1038/nchem.2695.

100) Fierro, S.; Nagel, T.; Baltruschat, H.; Comninellis, C. Investigation of the Oxygen Evolution Reaction on Ti/IrO2 Electrodes Using Isotope Labelling and on-Line Mass Spectrometry. *Electrochem. Commun.* **2007**, *9* (8), 1969–1974. https://doi.org/10.1016/j.elecom.2007.05.008.

101) Vogt, H.; Balzer, R. J. The Bubble Coverage of Gas-Evolving Electrodes in Stagnant Electrolytes. *Electrochim. Acta* **2005**, *50* (10), 2073–2079. https://doi.org/10.1016/j.electacta.2004.09.025.

102) Vogt, H. The Actual Current Density of Gas-Evolving Electrodes—Notes on the Bubble Coverage. *Electrochim. Acta* **2012**, *78*, 183–187. https://doi.org/10.1016/j.electacta.2012.05.124.

103) Zeradjanin, A. R.; Ventosa, E.; Bondarenko, A. S.; Schuhmann, W. Evaluation of the Catalytic Performance of Gas-Evolving Electrodes Using Local Electrochemical Noise Measurements. *ChemSusChem* **2012**, *5* (10), 1905–1911. https://doi.org/10.1002/cssc.201200262.

104) Zeradjanin, A. R. Frequent Pitfalls in the Characterization of Electrodes Designed for Electrochemical Energy Conversion and Storage. *ChemSusChem* **2018**, *11* (8), 1278–1284. https://doi.org/10.1002/cssc.201702287.

105) Guerrini, E.; Consonni, V.; Trasatti, S. Surface and Electrocatalytic Properties of Well-Defined and Vicinal RuO2 Single Crystal Faces. *J. Solid State Electrochem.* **2005**, *9* (5), 320–329. https://doi.org/10.1007/s10008-004-0602-1.

106) Stoerzinger, K. A.; Diaz-Morales, O.; Kolb, M.; Rao, R. R.; Frydendal, R.; Qiao, L.; Wang, X. R.; Halck, N. B.; Rossmeisl, J.; Hansen, H. A.; et al. Orientation-Dependent Oxygen Evolution on RuO 2 without Lattice Exchange. *ACS Energy Lett.* **2017**, *2* (4), 876–881. https://doi.org/10.1021/acsenergylett.7b00135.

107) Özer, E.; Spöri, C.; Reier, T.; Strasser, P. Iridium(1 1 1), Iridium(1 1 0), and Ruthenium(0 0 0 1) Single Crystals as Model Catalysts for the Oxygen Evolution Reaction: Insights into the Electrochemical Oxide Formation and Electrocatalytic Activity. *ChemCatChem* **2017**, *9* (4), 597–603. https://doi.org/10.1002/cctc.201600423.

108) Conway, B. E.; Gu, P. Evaluation of Cl? Adsorption in Anodic Cl2 Evolution at Pt by Means of Impedance and Potential-Relaxation Experiments. Influence of the State of Surface Oxidation of the Pt. *J. Chem. Soc. Faraday Trans.* **1991**, *87* (17), 2705. https://doi.org/10.1039/ft9918702705.

109) Gileadi, E.; Stoner, G. E. The Effect of Competition with Water on the Kinetic Parameters in Electrode Reactions. *J. Electrochem. Soc.* **1971**, *118* (8), 1316. https://doi.org/10.1149/1.2408312.

110) Krishtalik, L. I. Kinetics and Mechanism of Anodic Chlorine and Oxygen Evolution Reactions on Transition Metal Oxide Electrodes. *Electrochim. Acta* **1981**, *26* (3), 329–337. https://doi.org/10.1016/0013-4686(81)85019-0.

111) Fernández, J. L.; Gennero de Chialvo, M. R.; Chialvo, A. C. Analysis of the Volmer–Krishtalic Mechanism for the Chlorine Electrode Reaction. *Electrochem. Commun.* **2000**, *2* (9), 630–635. https://doi.org/10.1016/S1388-2481(00)00092-8.

112) Tilak, B. V.; Conway, B. E. Analytical Relations between Reaction Order and Tafel Slope Derivatives for Electrocatalytic Reactions Involving Chemisorbed Intermediates. *Electrochim. Acta* **1992**, *37* (1), 51–63. https://doi.org/10.1016/0013-4686(92)80011-A.

113) Ferro, S.; De Battisti, A. Electrocatalysis and Chlorine Evolution Reaction at Ruthenium Dioxide Deposited on Conductive Diamond. *J. Phys. Chem. B* **2002**, *106* (9), 2249–2254. https://doi.org/10.1021/jp012195i.

114) Koper, M. T. M. A Lattice-Gas Model for Halide Adsorption on Single-Crystal Electrodes. *J. Electroanal. Chem.* **1998**, *450* (2), 189–201. https://doi.org/10.1016/S0022-0728(97)00648-7.

115) Gileadi, E. The Combined Adsorption Isotherm. *Electrochim. Acta* **1987**, *32* (2), 221–229. https://doi.org/10.1016/0013-4686(87)85028-4.

116) Gileadi, E. Problems in Interfacial Electrochemistry That Have Been Swept under the Carpet. *J. Solid State Electrochem.* **2011**, *15* (7–8), 1359–1371. https://doi.org/10.1007/s10008-011-1344-5.

117) Rosestolato, D.; Fregoni, J.; Ferro, S.; De Battisti, A. Influence of the Nature of the Electrode Material and Process Variables on the Kinetics of the Chlorine Evolution Reaction. The Case of IrO2-Based Electrocatalysts. *Electrochim. Acta* **2014**, *139*, 180–189. https://doi.org/10.1016/j.electacta.2014.07.037.

118) Conway, B. E.; Novak, D. M. Chloride Ion Adsorption Effects in the Recombination-Controlled Kinetics of Anodic Chlorine Evolution at Pt Electrodes. *J. Chem. Soc. Faraday Trans. 1 Phys. Chem. Condens. Phases* **1979**, *75*, 2454–2472. https://doi.org/10.1039/F19797502454.

119) Ferro, S.; De Battisti, A.; Duo, I.; Comninellis, C.; Haenni, W.; Perret, A. Chlorine Evolution at Highly Boron-Doped Diamond Electrodes. *J. Electrochem. Soc.* **2000**, *147* (7), 2614–2619. https://doi.org/10.1149/1.1393578.

120) Evdokimov, S. V. Mechanism of Chlorine Evolution-Ionization on Dimensionally Stable Anodes. *Russ. J. Electrochem.* **2000**, *36* (3), 227–230. https://doi.org/10.1007/BF02827964.

121) Panić, V. V.; Dekanski, A. B.; Milonjić, S. K.; Atanasoski, R. T.; Nikolić, B. Ž. The Influence of the Aging Time of RuO2 and TiO2 Sols on the Electrochemical Properties and Behavior for the Chlorine Evolution Reaction of Activated Titanium Anodes Obtained by the Sol-Gel Procedure. *Electrochim. Acta* **2000**, *46* (2–3), 415–421. https://doi.org/10.1016/S0013-4686(00)00600-9.

122) Reznik, M. F.; Shub, D. M.; Kasatkin, E. V.; Kozlova, N. V. Anodic Oxide-Film of the Co—Sn—O Composition. *Russ. J. Electrochem.* **2000**, *36* (8), 889–892. https://doi.org/10.1007/BF02757064.

123) Wolter, O.; Heitbaum, J. Differential Electrochemical Mass Spectroscopy (DEMS) - a New Method for the Study of Electrode Processes. *Berichte der Bunsengesellschaft für Phys. Chemie* **1984**, *88* (1), 2–6. https://doi.org/10.1002/bbpc.19840880103.

124) Oberacher, H.; Pitterl, F.; Erb, R.; Plattner, S. Mass Spectrometric Methods for Monitoring Redox Processes in Electrochemical Cells. *Mass Spectrom. Rev.* **2015**, *34* (1), 64–92. https://doi.org/10.1002/mas.21409.

125) Takasu, Y.; Arikawa, T.; Sunohara, S.; Yahikozawa, K. Direct Detection of Competitively Evolving Chlorine and Oxygen at Anodes. *J. Electroanal. Chem.* **1993**, *361* (1–2), 279–281. https://doi.org/10.1016/0022-0728(93)87067-6.

126) Arikawa, T.; Murakami, Y.; Takasu, Y. Simultaneous Determination of Chlorine and Oxygen Evolving at RuO2/Ti and RuO2−TiO2/Ti Anodes by Differential Electrochemical Mass Spectroscopy. *J. Appl. Electrochem.* **1998**, *28* (5), 511–516. https://doi.org/10.1023/A:1003269228566.

127) Macounová, K. M.; Simic, N.; Ahlberg, E.; Krtil, P. Electrochemical Water Splitting Based on Hypochlorite Oxidation. *J. Am. Chem. Soc.* **2015**, *137* (23), 1–5. https://doi.org/10.1021/jacs.5b02087.

128) Izumiya, K.; Akiyama, E.; Habazaki, H.; Kumagai, N.; Kawashima, a.; Hashimoto, K. Anodically Deposited Manganese Oxide and Manganese–Tungsten Oxide Electrodes for Oxygen Evolution

from Seawater. *Electrochim. Acta* **1998**, *43* (98), 3303–3312. https://doi.org/10.1016/S0013-4686(98)00075-9.

129) Le Luu, T.; Kim, J.; Yoon, J. Physicochemical Properties of RuO 2 and IrO 2 Electrodes Affecting Chlorine Evolutions. *J. Ind. Eng. Chem.* **2015**, *21*, 400–404. https://doi.org/10.1016/j.jiec.2014.02.052.

130) Scholz, J.; Risch, M.; Stoerzinger, K. A.; Wartner, G.; Shao-Horn, Y.; Jooss, C. Supporting Information for: Rotating Ring–Disk Electrode Study of Oxygen Evolution at a Perovskite Surface: Correlating Activity to Manganese Concentration. *J. Phys. Chem. C* **2016**, *120* (49), 27746–27756. https://doi.org/10.1021/acs.jpcc.6b07654.

131) Spanos, I.; Auer, A. A.; Neugebauer, S.; Deng, X.; Tüysüz, H.; Schlögl, R. Standardized Benchmarking of Water Splitting Catalysts in a Combined Electrochemical Flow Cell/Inductively Coupled Plasma-Optical Emission Spectrometry (ICP-OES) Setup. *ACS Catal.* **2017**, *7* (6), 3768–3778. https://doi.org/10.1021/acscatal.7b00632.

132) Marković, N. M.; Gasteiger, H. A.; Ross, P. N. Oxygen Reduction on Platinum Low-Index Single-Crystal Surfaces in Sulfuric Acid Solution: Rotating Ring-Pt(Hkl) Disk Studies. *J. Phys. Chem.* **1995**, *99* (11), 3411–3415. https://doi.org/10.1021/j100011a001.

133) Jebaraj, A. J. J.; Georgescu, N. S.; Scherson, D. A. Oxygen and Hydrogen Peroxide Reduction on Polycrystalline Platinum in Acid Electrolytes: Effects of Bromide Adsorption. *J. Phys. Chem. C* **2016**, *120* (29), 16090–16099. https://doi.org/10.1021/acs.jpcc.5b12779.

134) Stamenkovic, V. R.; Marković, N. M.; Ross, P. N. Structure-Relationships in Electrocatalysis: Oxygen Reduction and Hydrogen Oxidation Reactions on Pt(111) and Pt(100) in Solutions Containing Chloride Ions. *J. Electroanal. Chem.* **2001**, *500* (1–2), 44–51. https://doi.org/10.1016/S0022-0728(00)00352-1.

135) Thomassen, M.; Børresen, B.; Hagen, G.; Tunold, R. Chlorine Reduction on Platinum and Ruthenium: The Effect of Oxide Coverage. *Electrochim. Acta* **2005**, *50* (5), 1157–1167. https://doi.org/10.1016/j.electacta.2004.08.013.

136) Thomassen, M.; Karlsen, C.; Børresen, B.; Tunold, R. Kinetic Investigation of the Chlorine Reduction Reaction on Electrochemically Oxidised Ruthenium. *Electrochim. Acta* **2006**, *51* (14), 2909–2918. https://doi.org/10.1016/j.electacta.2005.08.024.

137) Vesztergom, S.; Ujvári, M.; Láng, G. G. Dual Cyclic Voltammetry with Rotating Ring–Disk Electrodes. *Electrochim. Acta* **2013**, *110*, 49–55. https://doi.org/10.1016/j.electacta.2013.01.142.

138) Vesztergom, S.; Barankai, N.; Kovács, N.; Ujvári, M.; Siegenthaler, H.; Broekmann, P.; Láng, G. G. Electrical Cross-Talk in Four-Electrode Experiments. *J. Solid State Electrochem.* **2016**, *20* (11), 3165–3177. https://doi.org/10.1007/s10008-016-3294-4.

139) Michaux, K. E.; Murray, R. W. Formation of Iridium(IV) Oxide (IrOX) Films by Electroflocculation. *Langmuir* **2013**, *29* (39), 12254–12258. https://doi.org/10.1021/la4025876.

140) Wu, J. Kinetics of the Reduction of Hypochlorite Ion. *J. Electrochem. Soc.* **1987**, *134* (6), 1462. https://doi.org/10.1149/1.2100690.

141) Lindbergh, G.; Simonsson, D. The Effect of Chromate Addition on Cathodic Reduction of Hypochlorite in Hydroxide and Chlorate Solutions. *J. Electrochem. Soc.* **1990**, *137* (10), 3094. https://doi.org/10.1149/1.2086165.

142) Nakagawa, T.; Beasley, C. A.; Murray, R. W. Efficient Electro-Oxidation of Water near Its Reversible Potential by a Mesoporous IrO x Nanoparticle Film. *J. Phys. Chem. C* **2009**, *113* (30), 12958–12961. https://doi.org/10.1021/jp9060076.

143) Zhao, Y.; Vargas-Barbosa, N. M.; Hernandez-Pagan, E. A.; Mallouk, T. E. Anodic Deposition of Colloidal Iridium Oxide Thin Films from Hexahydroxyiridate(IV) Solutions. *Small* **2011**, *7* (14), 2087–2093. https://doi.org/10.1002/smll.201100485.

144) Kadija, I. V.; Nikolić, B. Ž.; Despić, A. R. Mass Transfer during Gas Evolution on the Rotating Double-Ring Electrode. *J. Electroanal. Chem. Interfacial Electrochem.* **1974**, *57* (1), 35–52. https://doi.org/10.1016/S0022-0728(74)80005-7.

145) Losev, V. V.; Buné, N. Y.; Chuvaeva, L. E. Specific Features of the Kinetics of Gas-Evolving Reactions on Highly Active Electrodes. *Electrochim. Acta* **1989**, *34* (7), 929–942. https://doi.org/10.1016/0013-4686(89)80017-9.

146) Janssen, L. J. J. Mass Transfer at Rotating Ring-Cone Electrodes. *J. Appl. Electrochem.* **1992**, *22* (11), 1091–1094. https://doi.org/10.1007/BF01029591.

147) Cornell, A.; Håkansson, B.; Lindbergh, G. Ruthenium-Based Dimensionally Stable Anode in Chlorate Electrolysis. *J. Electrochem. Soc.* **2003**, *150* (1), D6. https://doi.org/10.1149/1.1522386.

148) Alkan, M.; Oktay, M.; Kocakerim, M. M.; Çopur, M. Solubility of Chlorine in Aqueous Hydrochloric Acid Solutions. *J. Hazard. Mater.* **2005**, *119* (1–3), 13–18. https://doi.org/10.1016/j.jhazmat.2004.11.001.

149) Schmidt, T. J.; Paulus, U. A.; Gasteiger, H. A.; Behm, R. J. The Oxygen Reduction Reaction on a Pt/Carbon Fuel Cell Catalyst in the Presence of Chloride Anions. *J. Electroanal. Chem.* **2001**, *508* (1–2), 41–47. https://doi.org/10.1016/S0022-0728(01)00499-5.

150) Kuznetsova, E.; Petrykin, V.; Sunde, S.; Krtil, P. Selectivity of Nanocrystalline IrO2-Based Catalysts in Parallel Chlorine and Oxygen Evolution. *Electrocatalysis* **2015**, *6* (2), 198–210. https://doi.org/10.1007/s12678-014-0233-y.

151) Samant, M. G.; Kunimatsu, K.; Seki, H.; Philpott, M. R. In Situ FTIR Study of the Adsorption Geometry of Bisulfate Accepted Ions on a Platinum Electrode. *J. Electroanal. Chem.* **1990**, *280* (2), 391–401. https://doi.org/10.1016/0022-0728(90)87012-9.

152) Spöri, C.; Kwan, J. T. H.; Bonakdarpour, A.; Wilkinson, D. P.; Strasser, P. The Stability Challenges of Oxygen Evolving Catalysts: Towards a Common Fundamental Understanding and Mitigation of Catalyst Degradation. *Angew. Chemie Int. Ed.* **2017**, *56* (22), 5994–6021. https://doi.org/10.1002/anie.201608601.

153) Diaz-Morales, O.; Raaijman, S.; Kortlever, R.; Kooyman, P. J.; Wezendonk, T.; Gascon, J.; Fu, W. T.; Koper, M. T. M. Iridium-Based Double Perovskites for Efficient Water Oxidation in Acid Media. *Nat. Commun.* **2016**, *7* (August), 12363. https://doi.org/10.1038/ncomms12363.

154) Geiger, S.; Kasian, O.; Ledendecker, M.; Pizzutilo, E.; Mingers, A. M.; Fu, W. T.; Diaz-Morales, O.; Li, Z.; Oellers, T.; Fruchter, L.; et al. The Stability Number as a Metric for Electrocatalyst Stability Benchmarking. *Nat. Catal.* **2018**, *1* (7), 508–515. https://doi.org/10.1038/s41929-018-0085-6.

155) Fu, W. T.; IJdo, D. J. W. On the Space Group of the Double Perovskite Ba2PrIrO6. *J. Solid State Chem.* **2005**, *178* (4), 1312–1316. https://doi.org/10.1016/j.jssc.2005.02.003.

156) Fu, W. T.; IJdo, D. J. W. Re-Examination of the Structure of Ba2MIrO6 (M = La, Y): Space Group Revised. *J. Alloys Compd.* **2005**, *394* (1–2), 10–13. https://doi.org/10.1016/j.jallcom.2004.10.049.

157) Schuppert, A. K.; Topalov, A. A.; Katsounaros, I.; Klemm, S. O.; Mayrhofer, K. J. J. A Scanning Flow Cell System for Fully Automated Screening of Electrocatalyst Materials. *J. Electrochem. Soc.* **2012**, *159* (11), F670–F675. https://doi.org/10.1149/2.009211jes.

158) Klemm, S. O.; Topalov, A. A.; Laska, C. A.; Mayrhofer, K. J. J. Coupling of a High Throughput Microelectrochemical Cell with Online Multielemental Trace Analysis by ICP-MS. *Electrochem. Commun.* **2011**, *13* (12), 1533–1535. https://doi.org/10.1016/j.elecom.2011.10.017.

159) Kasian, O.; Geiger, S.; Mayrhofer, K. J. J.; Cherevko, S. Electrochemical On-Line ICP-MS in Electrocatalysis Research. *Chem. Rec.* **2018**, 1–14. https://doi.org/10.1002/tcr.201800162.

160) Seitz, L. C.; Dickens, C. F.; Nishio, K.; Hikita, Y.; Montoya, J.; Doyle, A.; Kirk, C.; Vojvodic, A.; Hwang, H. Y.; Norskov, J. K.; et al. A Highly Active and Stable IrO x /SrIrO 3 Catalyst for the Oxygen Evolution Reaction. *Science (80-.).* **2016**, *353* (6303), 1011–1014. https://doi.org/10.1126/science.aaf5050.

161) Kasian, O.; Grote, J.-P.; Geiger, S.; Cherevko, S.; Mayrhofer, K. J. J. The Common Intermediates of Oxygen Evolution and Dissolution Reactions during Water Electrolysis on Iridium. *Angew. Chemie Int. Ed.* **2018**, *57* (9), 2488–2491. https://doi.org/10.1002/anie.201709652.

162) Wakeshima, M.; Harada, D.; Hinatsu, Y. Crystal Structures and Magnetic Properties of Ordered Perovskites Ba2LnIrO6 (Ln = Lanthanide). *J. Mater. Chem.* **2000**, *10* (2), 419–422. https://doi.org/10.1039/a907586k.

163) Massué, C.; Huang, X.; Tarasov, A.; Ranjan, C.; Cap, S.; Schlögl, R. Microwave Assisted Synthesis of Stable and Highly Active Ir-Oxohydroxides for Electrochemical Oxidation of Water. *ChemSusChem* **2017**. https://doi.org/10.1002/cssc.201601864.

164) Zaharieva, I.; Chernev, P.; Risch, M.; Klingan, K.; Kohlhoff, M.; Fischer, A.; Dau, H.

Electrosynthesis, Functional, and Structural Characterization of a Water-Oxidizing Manganese Oxide. *Energy Environ. Sci.* **2012**, *5* (5), 7081–7089. https://doi.org/10.1039/C2EE21191B.

165) Balaji, R.; Kannan, B. S.; Lakshmi, J.; Senthil, N.; Vasudevan, S.; Sozhan, G.; Shukla, A. K.; Ravichandran, S. An Alternative Approach to Selective Sea Water Oxidation for Hydrogen Production. *Electrochem. Commun.* **2009**, *11* (8), 1700–1702. https://doi.org/10.1016/j.elecom.2009.06.022.

166) Mo, Y.; Stefan, I. C.; Cai, W.-B.; Dong, J.; Carey, P.; Scherson, D. A. In Situ Iridium L III -Edge X-Ray Absorption and Surface Enhanced Raman Spectroscopy of Electrodeposited Iridium Oxide Films in Aqueous Electrolytes. *J. Phys. Chem. B* **2002**, *106* (14), 3681–3686. https://doi.org/10.1021/jp014452p.

167) Sanchez Casalongue, H. G.; Ng, M. L.; Kaya, S.; Friebel, D.; Ogasawara, H.; Nilsson, A. In Situ Observation of Surface Species on Iridium Oxide Nanoparticles during the Oxygen Evolution Reaction. *Angew. Chemie Int. Ed.* **2014**, *53* (28), 7169–7172. https://doi.org/10.1002/anie.201402311.

168) Minguzzi, A.; Lugaresi, O.; Achilli, E.; Locatelli, C.; Vertova, A.; Ghigna, P.; Rondinini, S. Observing the Oxidation State Turnover in Heterogeneous Iridium-Based Water Oxidation Catalysts. *Chem. Sci.* **2014**, *5* (9), 3591. https://doi.org/10.1039/C4SC00975D.

169) Pfeifer, V.; Jones, T. E.; Velasco Vélez, J. J.; Massué, C.; Arrigo, R.; Teschner, D.; Girgsdies, F.; Scherzer, M.; Greiner, M. T.; Allan, J.; et al. The Electronic Structure of Iridium and Its Oxides. *Surf. Interface Anal.* **2016**, *48* (5), 261–273. https://doi.org/10.1002/sia.5895.

170) Massué, C.; Pfeifer, V.; van Gastel, M.; Noack, J.; Algara-Siller, G.; Cap, S.; Schlögl, R. Reactive Electrophilic O I– Species Evidenced in High-Performance Iridium Oxohydroxide Water Oxidation Electrocatalysts. *ChemSusChem* **2017**, *10* (23), 4786–4798. https://doi.org/10.1002/cssc.201701291.

171) Cherevko, S.; Geiger, S.; Kasian, O.; Kulyk, N.; Grote, J.-P.; Savan, A.; Shrestha, B. R.; Merzlikin, S.; Breitbach, B.; Ludwig, A.; et al. Oxygen and Hydrogen Evolution Reactions on Ru, RuO2, Ir, and IrO2 Thin Film Electrodes in Acidic and Alkaline Electrolytes: A Comparative Study on Activity and Stability. *Catal. Today* **2016**, *262*, 170–180. https://doi.org/10.1016/j.cattod.2015.08.014.

172) Stevens, M. B.; Enman, L. J.; Batchellor, A. S.; Cosby, M. R.; Vise, A. E.; Trang, C. D. M.; Boettcher, S. W. Measurement Techniques for the Study of Thin Film Heterogeneous Water Oxidation Electrocatalysts. *Chem. Mater.* **2017**, *29* (1), 120–140. https://doi.org/10.1021/acs.chemmater.6b02796.

173) Watzele, S.; Bandarenka, A. S. Quick Determination of Electroactive Surface Area of Some Oxide Electrode Materials. *Electroanalysis* **2016**, *28* (10), 2394–2399. https://doi.org/10.1002/elan.201600178.

174) Chow, K. F.; Carducci, T. M.; Murray, R. W. Electronic Conductivity of Films of Electroflocculated 2 Nm Iridium Oxide Nanoparticles. *J. Am. Chem. Soc.* **2014**, *136* (9), 3385–3387. https://doi.org/10.1021/ja413226j.

175) Jung, S.; McCrory, C. C. L.; Ferrer, I. M.; Peters, J. C.; Jaramillo, T. F. Benchmarking Nanoparticulate Metal Oxide Electrocatalysts for the Alkaline Water Oxidation Reaction. *J. Mater. Chem. A* **2016**, *4* (8), 3068–3076. https://doi.org/10.1039/C5TA07586F.

176) Batchellor, A. S.; Boettcher, S. W. Pulse-Electrodeposited Ni−Fe (Oxy)Hydroxide Oxygen Evolution Electrocatalysts with High Geometric and Intrinsic Activities at Large Mass Loadings. *ACS Catal.* **2015**, *5* (11), 6680–6689. https://doi.org/10.1021/acscatal.5b01551.

177) Takeno, N. Atlas of Eh-PH Diagrams Intercomparison of Thermodynamic Databases. *Natl. Inst. Adv. Ind. Sci. Technol. Tokyo* **2005**, No. 419, 1–285.

178) Zou, X.; Liu, Y.; Li, G.-D.; Wu, Y.; Liu, D.-P.; Li, W.; Li, H.-W.; Wang, D.; Zhang, Y.; Zou, X. Ultrafast Formation of Amorphous Bimetallic Hydroxide Films on 3D Conductive Sulfide Nanoarrays for Large-Current-Density Oxygen Evolution Electrocatalysis. *Adv. Mater.* **2017**, *29* (22), 1700404. https://doi.org/10.1002/adma.201700404.

179) Pi, Y.; Shao, Q.; Wang, P.; Lv, F.; Guo, S.; Guo, J.; Huang, X. Trimetallic Oxyhydroxide Coralloids for Efficient Oxygen Evolution Electrocatalysis. *Angew. Chemie Int. Ed.* **2017**, *56* (16), 4502–4506. https://doi.org/10.1002/anie.201701533.

180) Nai, J.; Lu, Y.; Yu, L.; Wang, X.; Lou, X. W. D. Formation of Ni-Fe Mixed Diselenide Nanocages

as a Superior Oxygen Evolution Electrocatalyst. *Adv. Mater.* **2017**, *29* (41), 1703870. https://doi.org/10.1002/adma.201703870.

181) Guerrini, E.; Trasatti, S. Recent Developments in Understanding Factors of Electrocatalysis. *Russ. J. Electrochem.* **2006**, *42* (10), 1017–1025. https://doi.org/10.1134/S1023193506100053.

182) Fernández, J. L.; Gennero de Chialvo, M. R.; Chialvo, A. C. Kinetic Study of the Chlorine Electrode Reaction on Ti/RuO2 through the Polarisation Resistance. *Electrochim. Acta* **2002**, *47* (7), 1137–1144. https://doi.org/10.1016/S0013-4686(01)00838-6.

183) Santana, M. H. P.; De Faria, L. A. Oxygen and Chlorine Evolution on RuO2+TiO2+CeO2+Nb2O5 Mixed Oxide Electrodes. *Electrochim. Acta* **2006**, *51*, 3578–3585. https://doi.org/10.1016/j.electacta.2005.09.050.

184) Boggio, R.; Carugati, A.; Lodi, G.; Trasatti, S. Mechanistic Study of Cl2 Evolution at Ti-Supported Co3O4 Anodes. *J. Appl. Electrochem.* **1985**, *15* (3), 335–349. https://doi.org/10.1007/BF00615986.

185) Conway, B. E.; Gu, P.; De Battisti, A.; Barbieri, A.; Battaglin, G. Behaviour of the Adsorbed Cl* Intermediate in Anodic Cl2 Evolution at Thin-Film RuO2 Surfaces. *J. Mater. Chem.* **1991**, *1* (5), 725. https://doi.org/10.1039/jm9910100725.

186) Magazinovic, R. S.; Nicholson, B. C.; Mulcahy, D. E.; Davey, D. E. Bromide Levels in Natural Waters: Its Relationship to Levels of Both Chloride and Total Dissolved Solids and the Implications for Water Treatment. *Chemosphere* **2004**, *57* (4), 329–335. https://doi.org/10.1016/j.chemosphere.2004.04.056.

187) Schulz, S.; Hahn, H. H. Generation of Halogenated Organic Compounds in Municipal Waste Water. *Water Sci. Technol.* **1998**, *37* (1), 303–309. https://doi.org/10.1016/S0273-1223(97)00782-8.

188) Sun, Y.-X.; Wu, Q.-Y.; Hu, H.-Y.; Tian, J. Effect of Bromide on the Formation of Disinfection By-Products during Wastewater Chlorination. *Water Res.* **2009**, *43* (9), 2391–2398. https://doi.org/10.1016/j.watres.2009.02.033.

189) Tian, C.; Liu, R.; Guo, T.; Liu, H.; Luo, Q.; Qu, J. Chlorination and Chloramination of High-Bromide Natural Water: DBPs Species Transformation. *Sep. Purif. Technol.* **2013**, *102*, 86–93. https://doi.org/10.1016/j.seppur.2012.09.034.

190) O'Brien, T. F.; Bommaraju, T. V.; Hine, F. *Handbook of Chlor-Alkali Technology*; Springer US: Boston, MA, 2005; Vol. 1. https://doi.org/10.1007/b113786.

191) Saadi, K.; Nanikashvili, P.; Tatus-Portnoy, Z.; Hardisty, S.; Shokhen, V.; Zysler, M.; Zitoun, D. Crossover-Tolerant Coated Platinum Catalysts in Hydrogen/Bromine Redox Flow Battery. *J. Power Sources* **2019**, *422* (6), 84–91. https://doi.org/10.1016/j.jpowsour.2019.03.043.

192) Venkatesan, N.; Archana, K. S.; Suresh, S.; Aswathy, R.; Ulaganthan, M.; Periasamy, P.; Ragupathy, P. Boron-Doped Graphene as Efficient Electrocatalyst for Zinc-Bromine Redox Flow Batteries. *ChemElectroChem* **2019**, *6* (4), 1107–1114. https://doi.org/10.1002/celc.201801465.

193) Yalçin, H.; Koç, T.; Pamuk, V. Hydrogen and Bromine Production from Concentrated Sea-Water. *Int. J. Hydrogen Energy* **1997**, *22* (10–11), 967–970. https://doi.org/10.1016/S0360-3199(96)00214-5.

194) Cohen, I.; Shapira, B.; Avraham, E.; Soffer, A.; Aurbach, D. Bromide Ions Specific Removal and Recovery by Electrochemical Desalination. *Environ. Sci. Technol.* **2018**, *52* (11), 6275–6281. https://doi.org/10.1021/acs.est.8b00282.

195) Heeb, M. B.; Criquet, J.; Zimmermann-Steffens, S. G.; von Gunten, U. Oxidative Treatment of Bromide-Containing Waters: Formation of Bromine and Its Reactions with Inorganic and Organic Compounds — A Critical Review. *Water Res.* **2014**, *48* (1), 15–42. https://doi.org/10.1016/j.watres.2013.08.030.

196) Conway, B. E.; Phillips, Y.; Qian, S. Y. Surface Electrochemistry and Kinetics of Anodic Bromine Formation at Platinum. *J. Chem. Soc. Faraday Trans.* **1995**, *91* (2), 283. https://doi.org/10.1039/ft9959100283.

197) Harrison, J. A.; Hermijanto, S. D. The Oxidation of Chloride Ions and Bromide Ions on Ruthenium Dioxide Electrodes. *J. Electroanal. Chem. Interfacial Electrochem.* **1987**, *225* (1–2), 159–175. https://doi.org/10.1016/0022-0728(87)80011-6.

198) Man, I. C. Theoretical Study of Electro-Catalysts for Oxygen Evolution, Technical University of Denmark, 2011.

199) Tymoczko, J.; Colic, V.; Ganassin, A.; Schuhmann, W.; Bandarenka, A. S. Influence of the Alkali Metal Cations on the Activity of Pt(111) towards Model Electrocatalytic Reactions in Acidic Sulfuric Media. *Catal. Today* **2015**, *244*, 96–102. https://doi.org/10.1016/j.cattod.2014.07.007.

200) Ragoisha, G. A.; Auchynnikava, T. A.; Streltsov, E. A.; Rabchynski, S. M. Electrochemical Impedance of Platinum in Concentrated Chloride Solutions under Potentiodynamic Anodic Polarization: Effect of Alkali Metal Cations. *Electrochim. Acta* **2014**, *122*, 218–223. https://doi.org/10.1016/j.electacta.2013.09.139.

201) Beckwith, R. C.; Wang, T. X.; Margerum, D. W. Equilibrium and Kinetics of Bromine Hydrolysis. *Inorg. Chem.* **1996**, *35* (4), 995–1000. https://doi.org/10.1021/ic950909w.

202) Liu, Q.; Margerum, D. W. Equilibrium and Kinetics of Bromine Chloride Hydrolysis. *Environ. Sci. Technol.* **2001**, *35* (6), 1127–1133. https://doi.org/10.1021/es001380r.

203) Conway, B. E.; Ping, G. Surface Electrochemistry of the Anodic Cl2 Evolution Reaction at Pt. Influence of Co-Deposition of Surface Oxide Species on Adsorption of the Cl? Intermediate. *J. Chem. Soc. Faraday Trans.* **1990**, *86* (6), 923. https://doi.org/10.1039/ft9908600923.

204) Conway, B. E. Method for Kinetic Analysis of a Recombination-Controlled Reaction over a Wide Range of Current-Densities from the Reversible Region up to the Limiting Current. *J. Electrochem. Soc.* **1981**, *128* (5), 1022. https://doi.org/10.1149/1.2127543.

205) Roscoe, S. G.; Conway, B. E. State of Surface Oxide Films at Pt Anodes and "Volcano" Behaviour in Electrocatalysis for Anodic Cl2 Evolution. *J. Electroanal. Chem.* **1987**, *224* (1–2), 163–188. https://doi.org/10.1016/0022-0728(87)85090-8.

206) Cooper, W. D.; Parsons, R. Kinetics of the Bromine/Bromide Electrode on Platinum in Aqueous Sulphuric Acid. *Trans. Faraday Soc.* **1970**, *66*, 1698. https://doi.org/10.1039/tf9706601698.

207) Ferro, S.; De Battisti, A. The Bromine Electrode. Part I: Adsorption Phenomena at Polycrystalline Platinum Electrodes. *J. Appl. Electrochem.* **2004**, *34* (10), 981–987. https://doi.org/10.1023/B:JACH.0000042666.25746.e6.

208) Xu, J.; Georgescu, N. S.; Scherson, D. A. The Oxidation of Bromide on Platinum Electrodes in Aqueous Acidic Solutions: Electrochemical and In Situ Spectroscopic Studies. *J. Electrochem. Soc.* **2014**, *161* (6), H392–H398. https://doi.org/10.1149/2.082406jes.

209) Horányi, G.; Rizmayer, E. M. The Problem of the Irreversibility of the Adsoprtion of Halides on Platinum. *J. Electroanal. Chem. Interfacial Electrochem.* **1977**, *83* (2), 367–373. https://doi.org/10.1016/S0022-0728(77)80181-2.

210) Wang, T. X.; Kelley, M. D.; Cooper, J. N.; Beckwith, R. C.; Margerum, D. W. Equilibrium, Kinetic, and UV-Spectral Characteristics of Aqueous Bromine Chloride, Bromine, and Chlorine Species. *Inorg. Chem.* **1994**, *33* (25), 5872–5878. https://doi.org/10.1021/ic00103a040.

211) Jung, Y.; Hong, E.; Yoon, Y.; Kwon, M.; Kang, J. Formation of Bromate and Chlorate during Ozonation and Electrolysis in Seawater for Ballast Water Treatment. *Ozone Sci. Eng.* **2014**, *36* (6), 515–525. https://doi.org/10.1080/01919512.2014.956862.

212) Marković, N. M.; Gasteiger, H. A.; Grgur, B. N.; Ross, P. N. Oxygen Reduction Reaction on Pt(111): Effects of Bromide. *J. Electroanal. Chem.* **1999**, *467* (1), 157–163. https://doi.org/10.1016/S0022-0728(99)00020-0.

213) Ferro, S.; Orsan, C.; De Battisti, A. The Bromine Electrode Part II: Reaction Kinetics at Polycrystalline Pt. *J. Appl. Electrochem.* **2005**, *35* (3), 273–278. https://doi.org/10.1007/s10800-004-6773-8.

214) Sergeev, A. V.; Zakharchenko, T. K.; Chertovich, A. V.; Itkis, D. M. Applying the Deconvolution Approach in Order to Enhance RRDE Time Resolution: Experimental Noise and Imposed Limitations. *Electrochim. Acta* **2019**, *298*, 858–865. https://doi.org/10.1016/j.electacta.2018.12.124.

215) Garcia-Araez, N.; Climent, V.; Herrero, E.; Feliu, J.; Lipkowski, J. Thermodynamic Studies of Bromide Adsorption at the Pt(111) Electrode Surface Perchloric Acid Solutions: Comparison with Other Anions. *J. Electroanal. Chem.* **2006**, *591* (2), 149–158. https://doi.org/10.1016/j.jelechem.2006.04.008.

216) Vacca, A.; Mascia, M.; Palmas, S.; Mais, L.; Rizzardini, S. On the Formation of Bromate and Chlorate Ions during Electrolysis with Boron Doped Diamond Anode for Seawater Treatment. *J. Chem. Technol. Biotechnol.* **2013**, *88* (12), 2244–2251. https://doi.org/10.1002/jctb.4095.

217) Brett, C. M. A.; Brett, A. M. O. *Electrochemistry, Principles, Methods, and Applications.* , Oxford,

1993. 427 S., Broschur 25.00 £. – ISBN; Oxford University Press, 1994.

218) Novak, D. M.; Conway, B. E. Competitive Adsorption and State of Charge of Halide Ions in Monolayer Oxide Film Growth Processes at Pt Anodes. *J. Chem. Soc. Faraday Trans. 1 Phys. Chem. Condens. Phases* **1981**, *77* (10), 2341. https://doi.org/10.1039/f19817702341.

219) Jerkiewicz, G.; Vatankhah, G.; Lessard, J.; Soriaga, M. P.; Park, Y.-S. Surface-Oxide Growth at Platinum Electrodes in Aqueous H2SO4. *Electrochim. Acta* **2004**, *49* (9–10), 1451–1459. https://doi.org/10.1016/j.electacta.2003.11.008.

220) Xu, J.; Scherson, D. Quantitative In Situ Differential Reflectance Spectroscopy Analysis of Polycrystalline Platinum Oxidation in an Aqueous Acidic Electrolyte. *ECS Electrochem. Lett.* **2015**, *4* (9), H46–H49. https://doi.org/10.1149/2.0061509eel.

221) Patil, R. S.; Juvekar, V. A.; Naik, V. M. Oxidation of Chloride Ion on Platinum Electrode: Dynamics of Electrode Passivation and Its Effect on Oxidation Kinetics. *Ind. Eng. Chem. Res.* **2011**, *50* (23), 12946–12959. https://doi.org/10.1021/ie200663a.

222) Koper, M. T. M.; Jansen, A. P. J.; Lukkien, J. J. Lattice–Gas Modeling of Electrochemical Langmuir–Hinshelwood Surface Reactions. *Electrochim. Acta* **1999**, *45* (4–5), 645–651. https://doi.org/10.1016/S0013-4686(99)00243-1.

223) Marković, N. M.; Lucas, C. A.; Gasteiger, H. A.; Ross, P. N. Bromide Adsorption on Pt(100): Rotating Ring-Pt(100) Disk Electrode and Surface X-Ray Scattering Measurements. *Surf. Sci.* **1996**, *365* (2), 229–240. https://doi.org/10.1016/0039-6028(96)00721-2.

224) Gasteiger, H. A.; Marković, N. M.; Ross, P. N. Bromide Adsorption on Pt(111): Adsorption Isotherm and Electrosorption Valency Deduced from RRD Pt(111) E Measurements. *Langmuir* **1996**, *12* (6), 1414–1418. https://doi.org/10.1021/la950826s.

225) Xu, J.; Scherson, D. Quantitative Correlations between the Normal Incidence Differential Reflectance and the Coverage of Adsorbed Bromide on a Polycrystalline Platinum Rotating Disk Electrode. *Anal. Chem.* **2013**, *85* (5), 2795–2801. https://doi.org/10.1021/ac303322c.

226) Garcia-Araez, N.; Climent, V.; Herrero, E.; Feliu, J.; Lipkowski, J. Thermodynamic Studies of Chloride Adsorption at the Pt(111) Electrode Surface from 0.1 M HClO4 Solution. *J. Electroanal. Chem.* **2005**, *576* (1), 33–41. https://doi.org/10.1016/j.jelechem.2004.10.003.

227) Campbell, D. J.; Lynch, M. L.; Corn, R. M. Second Harmonic Generation Studies of Anionic Chemisorption at Polycrystalline Platinum Electrodes. *Langmuir* **1990**, *6* (11), 1656–1664. https://doi.org/10.1021/la00101a006.

228) Marković, N. M.; Ross, P. N. The Effect of Specific Adsorption of Ions and Underpotential Deposition of Copper on the Electro-Oxidation of Methanol on Platinum Single-Crystal Surfaces. *J. Electroanal. Chem.* **1992**, *330* (1–2), 499–520. https://doi.org/10.1016/0022-0728(92)80327-Z.

229) Conway, B. E.; Tilak, B. V. Interfacial Processes Involving Electrocatalytic Evolution and Oxidation of H2, and the Role of Chemisorbed H. *Electrochim. Acta* **2002**, *47* (22–23), 3571–3594. https://doi.org/10.1016/S0013-4686(02)00329-8.

230) Garcia-Araez, N.; Lukkien, J. J.; Koper, M. T. M.; Feliu, J. M. Competitive Adsorption of Hydrogen and Bromide on Pt(100): Mean-Field Approximation vs. Monte Carlo Simulations. *J. Electroanal. Chem.* **2006**, *588* (1), 1–14. https://doi.org/10.1016/j.jelechem.2005.11.034.

231) Vesztergom, S.; Barankai, N.; Kovács, N.; Ujvári, M.; Wandlowski, T.; Láng, G. G. Rotating Ring-Disk Electrode with Dual Dynamic Potential Control: Theory and Practice. *Acta Chim. Slov.* **2014**, *61* (2), 223–232.

232) Denton, D. A.; Harrison, J. A.; Knowles, R. I. Chlorine Evolution and Reduction on RuO2/TiO2 Electrodes. *Electrochim. Acta* **1979**, *24* (5), 521–527. https://doi.org/10.1016/0013-4686(79)85027-6.

233) Najafpour, M. M.; Renger, G.; Hołyńska, M.; Moghaddam, A. N.; Aro, E.-M.; Carpentier, R.; Nishihara, H.; Eaton-Rye, J. J.; Shen, J.-R.; Allakhverdiev, S. I. Manganese Compounds as Water-Oxidizing Catalysts: From the Natural Water-Oxidizing Complex to Nanosized Manganese Oxide Structures. *Chem. Rev.* **2016**, *116* (5), 2886–2936. https://doi.org/10.1021/acs.chemrev.5b00340.

234) Hunter, B. M.; Gray, H. B.; Müller, A. M. Earth-Abundant Heterogeneous Water Oxidation Catalysts. *Chem. Rev.* **2016**, *116* (22), 14120–14136. https://doi.org/10.1021/acs.chemrev.6b00398.

235) Takashima, T.; Hashimoto, K.; Nakamura, R. Mechanisms of PH-Dependent Activity for Water Oxidation to Molecular Oxygen by MnO 2 Electrocatalysts. *J. Am. Chem. Soc.* **2012**, *134* (3), 1519–1527. https://doi.org/10.1021/ja206511w.

236) Gorlin, Y.; Jaramillo, T. F. A Bifunctional Nonprecious Metal Catalyst for Oxygen Reduction and Water Oxidation. *J. Am. Chem. Soc.* **2010**, *132* (39), 13612–13614. https://doi.org/10.1021/ja104587v.

237) Habazaki, H.; Matsui, T.; Kawashima, A.; Asami, K.; Kumagai, N.; Hashimoto, K. Nanocrystalline Manganese-Molybdenum-Tungsten Oxide Anodes for Oxygen Evolution in Seawater Electrolysis. *Scr. Mater.* **2001**, *44*, 1659–1662. https://doi.org/10.2320/matertrans.46.309.

238) Abdel Ghany, N. A.; Kumagai, N.; Meguro, S.; Asami, K.; Hashimoto, K. Oxygen Evolution Anodes Composed of Anodically Deposited Mn-Mo-Fe Oxides for Seawater Electrolysis. *Electrochim. Acta* **2002**, *48*, 21–28. https://doi.org/10.1016/S0013-4686(02)00539-X.

239) Kato, Z.; Bhattarai, J.; Kumagai, N.; Izumiya, K.; Hashimoto, K. Durability Enhancement and Degradation of Oxygen Evolution Anodes in Seawater Electrolysis for Hydrogen Production. *Appl. Surf. Sci.* **2011**, *257* (19), 8230–8236. https://doi.org/10.1016/j.apsusc.2010.12.042.

240) Huynh, M.; Bediako, D. K.; Nocera, D. G. A Functionally Stable Manganese Oxide Oxygen Evolution Catalyst in Acid. *J. Am. Chem. Soc.* **2014**, *136* (16), 6002–6010. https://doi.org/10.1021/ja413147e.

241) Fan, K.; Chen, H.; Ji, Y.; Huang, H.; Claesson, P. M.; Daniel, Q.; Philippe, B.; Rensmo, H.; Li, F.; Luo, Y.; et al. Nickel–Vanadium Monolayer Double Hydroxide for Efficient Electrochemical Water Oxidation. *Nat. Commun.* **2016**, *7* (May), 11981. https://doi.org/10.1038/ncomms11981.

242) Trześniewski, B. J.; Diaz-Morales, O.; Vermaas, D. A.; Longo, A.; Bras, W.; Koper, M. T. M.; Smith, W. A. In Situ Observation of Active Oxygen Species in Fe-Containing Ni-Based Oxygen Evolution Catalysts: The Effect of PH on Electrochemical Activity. *J. Am. Chem. Soc.* **2015**, *137* (48), 15112–15121. https://doi.org/10.1021/jacs.5b06814.

243) Yang, X.; Wang, C.-J.; Hou, C.-C.; Fu, W.-F.; Chen, Y. Self-Assembly of Ni–Fe Layered Double Hydroxide on Fe Foam as 3D Integrated Electrocatalysts for Oxygen Evolution: Dependence of the Catalytic Performance on Anions under in Situ Condition. *ACS Sustain. Chem. Eng.* **2018**, *6* (3), 2893–2897. https://doi.org/10.1021/acssuschemeng.7b04199.

244) Burke, M. S.; Kast, M. G.; Trotochaud, L.; Smith, A. M.; Boettcher, S. W. Cobalt-Iron (Oxy)Hydroxide Oxygen Evolution Electrocatalysts: The Role of Structure and Composition on Activity, Stability, and Mechanism. *J. Am. Chem. Soc.* **2015**, *137* (10), 3638–3648. https://doi.org/10.1021/jacs.5b00281.

245) Pokhrel, R.; Goetz, M. K.; Shaner, S. E.; Wu, X.; Stahl, S. S. The "Best Catalyst" for Water Oxidation Depends on the Oxidation Method Employed: A Case Study of Manganese Oxides. *J. Am. Chem. Soc.* **2015**, *137* (26), 8384–8387. https://doi.org/10.1021/jacs.5b05093.

246) Kao, W.-H.; Weibel, V. J. Electrochemical Oxidation of Manganese(II) at a Platinum Electrode. *J. Appl. Electrochem.* **1992**, *22* (1), 21–27. https://doi.org/10.1007/BF01093007.

247) Wonders, A. H.; Housmans, T. H. M.; Rosca, V.; Koper, M. T. M. On-Line Mass Spectrometry System for Measurements at Single-Crystal Electrodes in Hanging Meniscus Configuration. *J. Appl. Electrochem.* **2006**, *36* (11), 1215–1221. https://doi.org/10.1007/s10800-006-9173-4.

248) Huynh, M.; Bediako, D. K.; Liu, Y.; Nocera, D. G. Nucleation and Growth Mechanisms of an Electrodeposited Manganese Oxide Oxygen Evolution Catalyst. *J. Phys. Chem. C* **2014**, *118* (30), 17142–17152. https://doi.org/10.1021/jp501768n.

249) Klinger, M. *CrysTBox - Crystallographic Toolbox*; Institute of Physics of the Czech Academy of Sciences: Prague, 2015.

250) Pfeifer, V.; Jones, T. E.; Velasco Vélez, J. J.; Massué, C.; Greiner, M. T.; Arrigo, R.; Teschner, D.; Girgsdies, F.; Scherzer, M.; Allan, J.; et al. The Electronic Structure of Iridium Oxide Electrodes Active in Water Splitting. *Phys. Chem. Chem. Phys.* **2016**, *18* (4), 2292–2296. https://doi.org/10.1039/C5CP06997A.

251) Najafpour, M. M.; Khoshkam, M.; Jafarian Sedigh, D.; Zahraei, A.; Kompany-Zareh, M. Self-Healing for Nanolayered Manganese Oxides in the Presence of Cerium(<scp>iv</Scp>) Ammonium Nitrate: New Findings. *New J. Chem.* **2015**, *39* (4), 2547–2550. https://doi.org/10.1039/C4NJ02092H.

252) Nijjer, S.; Thonstad, J.; Haarberg, G. M. Oxidation of Manganese(II) and Reduction of Manganese Dioxide in Sulphuric Acid. *Electrochim. Acta* **2000**, *46* (2–3), 395–399. https://doi.org/10.1016/S0013-4686(00)00597-1.

253) Filipe, O.; Brett, C. M. A. Cathodic Stripping Voltammetry of Trace Mn(II) at Carbon Film Electrodes. *Talanta* **2003**, *61* (5), 643–650. https://doi.org/10.1016/S0039-9140(03)00327-8.

254) Paul, R. L.; Cartwright, A. The Mechanism of the Deposition of Manganese Dioxide. *J. Electroanal. Chem. Interfacial Electrochem.* **1986**, *201* (1), 123–131. https://doi.org/10.1016/0022-0728(86)90092-6.

255) Rogulski, Z.; Siwek, H.; Paleska, I.; Czerwiński, A. Electrochemical Behavior of Manganese Dioxide on a Gold Electrode. *J. Electroanal. Chem.* **2003**, *543* (2), 175–185. https://doi.org/10.1016/S0022-0728(03)00045-7.

256) Scharifker, B.; Hills, G. Theoretical and Experimental Studies of Multiple Nucleation. *Electrochim. Acta* **1983**, *28* (7), 879–889. https://doi.org/10.1016/0013-4686(83)85163-9.

257) Mostany, J.; Scharifker, B. *Electrochemical Nucleation and Growth*; Bard, A. J., Ed.; Wiley-VCH Verlag GmbH & Co. KGaA: Weinheim, Germany, 2007. https://doi.org/10.1002/9783527610426.

258) Huynh, M.; Shi, C.; Billinge, S. J. L.; Nocera, D. G. Nature of Activated Manganese Oxide for Oxygen Evolution. *J. Am. Chem. Soc.* **2015**, *137* (47), 14887–14904. https://doi.org/10.1021/jacs.5b06382.

259) Gorlin, Y.; Chung, C.-J.; Benck, J. D.; Nordlund, D.; Seitz, L. C.; Weng, T.-C.; Sokaras, D.; Clemens, B. M.; Jaramillo, T. F. Understanding Interactions between Manganese Oxide and Gold That Lead to Enhanced Activity for Electrocatalytic Water Oxidation. *J. Am. Chem. Soc.* **2014**, *136* (13), 4920–4926. https://doi.org/10.1021/ja407581w.

260) Seitz, L. C.; Hersbach, T. J. P.; Nordlund, D.; Jaramillo, T. F. Enhancement Effect of Noble Metals on Manganese Oxide for the Oxygen Evolution Reaction. *J. Phys. Chem. Lett.* **2015**, *6* (20), 4178–4183. https://doi.org/10.1021/acs.jpclett.5b01928.

261) Ramírez, A.; Hillebrand, P.; Stellmach, D.; May, M. M.; Bogdanoff, P.; Fiechter, S. Evaluation of MnO x , Mn 2 O 3 , and Mn 3 O 4 Electrodeposited Films for the Oxygen Evolution Reaction of Water. *J. Phys. Chem. C* **2014**, *118* (26), 14073–14081. https://doi.org/10.1021/jp500939d.

262) Zhao, Y.; Hernandez-Pagan, E. a.; Vargas-Barbosa, N. M.; Dysart, J. L.; Mallouk, T. E. A High Yield Synthesis of Ligand-Free Iridium Oxide Nanoparticles with High Electrocatalytic Activity. *J. Phys. Chem. Lett.* **2011**, *2* (5), 402–406. https://doi.org/10.1021/jz200051c.

263) Yagi, M.; Tomita, E.; Kuwabara, T. Remarkably High Activity of Electrodeposited IrO2 Film for Electrocatalytic Water Oxidation. *J. Electroanal. Chem.* **2005**, *579* (1), 83–88. https://doi.org/10.1016/j.jelechem.2005.01.030.

264) Cheney, M. A.; Bhowmik, P. K.; Moriuchi, S.; Villalobos, M.; Qian, S.; Joo, S. W. The Effect of Stirring on the Morphology of Birnessite Nanoparticles. *J. Nanomater.* **2008**, *2008* (1), 1–9. https://doi.org/10.1155/2008/168716.

265) Nakayama, M.; Kanaya, T.; Lee, J.-W.; Popov, B. N. Electrochemical Synthesis of Birnessite-Type Layered Manganese Oxides for Rechargeable Lithium Batteries. *J. Power Sources* **2008**, *179* (1), 361–366. https://doi.org/10.1016/j.jpowsour.2007.12.075.

266) Post, J. E. Manganese Oxide Minerals: Crystal Structures and Economic and Environmental Significance. *Proc. Natl. Acad. Sci.* **1999**, *96* (7), 3447–3454. https://doi.org/10.1073/pnas.96.7.3447.

267) Gorlin, Y.; Lassalle-Kaiser, B.; Benck, J. D.; Gul, S.; Webb, S. M.; Yachandra, V. K.; Yano, J.; Jaramillo, T. F. In Situ X-Ray Absorption Spectroscopy Investigation of a Bifunctional Manganese Oxide Catalyst with High Activity for Electrochemical Water Oxidation and Oxygen Reduction. *J. Am. Chem. Soc.* **2013**, *135* (23), 8525–8534. https://doi.org/10.1021/ja3104632.

268) Michell, D.; Rand, D. A. J.; Woods, R. Analysis of the Anodic Oxygen Layer on Iridium by X-Ray Emission, Electron Diffraction and Electron Microscopy. *J. Electroanal. Chem.* **1977**, *84* (1), 117–126. https://doi.org/10.1016/S0022-0728(77)80234-9.

269) Ortel, E.; Reier, T.; Strasser, P.; Kraehnert, R. Mesoporous IrO 2 Films Templated by PEO-PB-PEO Block-Copolymers: Self-Assembly, Crystallization Behavior, and Electrocatalytic Performance. *Chem. Mater.* **2011**, *23* (13), 3201–3209. https://doi.org/10.1021/cm200761f.

270) Abbott, D. F.; Lebedev, D.; Waltar, K.; Povia, M.; Nachtegaal, M.; Fabbri, E.; Copéret, C.;

Schmidt, T. J. Iridium Oxide for the Oxygen Evolution Reaction: Correlation between Particle Size, Morphology, and the Surface Hydroxo Layer from Operando XAS. *Chem. Mater.* **2016**, *28* (18), 6591–6604. https://doi.org/10.1021/acs.chemmater.6b02625.

271) Kötz, R.; Neff, H.; Stucki, S. Anodic Iridium Oxide Films: XPS-Studies of Oxidation State Changes and O2-Evolution. *J. Electrochem. Soc.* **1984**, *131* (1), 72. https://doi.org/10.1149/1.2115548.

272) Junta, J. L.; Hochella, M. F. Manganese (II) Oxidation at Mineral Surfaces: A Microscopic and Spectroscopic Study. *Geochim. Cosmochim. Acta* **1994**, *58* (22), 4985–4999. https://doi.org/10.1016/0016-7037(94)90226-7.

273) Cerrato, J. M.; Hochella, M. F.; Knocke, W. R.; Dietrich, A. M.; Cromer, T. F. Use of XPS to Identify the Oxidation State of Mn in Solid Surfaces of Filtration Media Oxide Samples from Drinking Water Treatment Plants. *Environ. Sci. Technol.* **2010**, *44* (15), 5881–5886. https://doi.org/10.1021/es100547q.

274) Smith, R. D. L.; Sporinova, B.; Fagan, R. D.; Trudel, S.; Berlinguette, C. P. Facile Photochemical Preparation of Amorphous Iridium Oxide Films for Water Oxidation Catalysis. *Chem. Mater.* **2014**, *26* (4), 1654–1659. https://doi.org/10.1021/cm4041715.

275) Morita, M.; Iwakura, C.; Tamura, H. The Anodic Characteristics of Massive Manganese Oxide Electrode. *Electrochim. Acta* **1979**, *24* (4), 357–362. https://doi.org/10.1016/0013-4686(79)87019-X.

276) Morita, M.; Iwakura, C.; Tamura, H. The Anodic Characteristics of Manganese Dioxide Electrodes Prepared by Thermal Decomposition of Manganese Nitrate. *Electrochim. Acta* **1977**, *22* (4), 325–328. https://doi.org/10.1016/0013-4686(77)85081-0.

277) Nakayama, M.; Fukuda, M.; Konishi, S.; Tonosaki, T. Effects of Reaction Parameters on the Electrochemical Formation of Multilayer Films Composed of Manganese Oxides and Tetra-Alkylammonium Ions. *J. Mater. Res.* **2006**, *21* (12), 3152–3160. https://doi.org/10.1557/jmr.2006.0385.

278) Rodrigues, S.; Shukla, a K.; Munichandraiah, N. A Cyclic Voltammetric Study of the Kinetics and Mechanism of Electrodeposition of Manganese Dioxide. *J. Appl. Electrochem.* **1998**, *28* (11), 1235–1241. https://doi.org/10.1023/A:1003472901760.

279) Biswal, A.; Chandra Tripathy, B.; Sanjay, K.; Subbaiah, T.; Minakshi, M. Electrolytic Manganese Dioxide (EMD): A Perspective on Worldwide Production, Reserves and Its Role in Electrochemistry. *RSC Adv.* **2015**, *5* (72), 58255–58283. https://doi.org/10.1039/C5RA05892A.

280) Mozota, J.; Conway, B. E. Modification of Apparent Electrocatalysis for Anodic Chlorine Evolution on Electrochemically Conditioned Oxide Films at Iridium Anodes. *J. Electrochem. Soc.* **1981**, *128* (10), 2142–2149. https://doi.org/10.1149/1.2127205.

281) Garcia-Esparza, A. T.; Shinagawa, T.; Ould-Chikh, S.; Qureshi, M.; Peng, X.; Wei, N.; Anjum, D. H.; Clo, A.; Weng, T.-C.; Nordlund, D.; et al. An Oxygen-Insensitive Hydrogen Evolution Catalyst Coated by a Molybdenum-Based Layer for Overall Water Splitting. *Angew. Chemie Int. Ed.* **2017**, *56* (21), 5780–5784. https://doi.org/10.1002/anie.201701861.

282) Labrador, N. Y.; Songcuan, E. L.; De Silva, C.; Chen, H.; Kurdziel, S. J.; Ramachandran, R. K.; Detavernier, C.; Esposito, D. V. Hydrogen Evolution at the Buried Interface between Pt Thin Films and Silicon Oxide Nanomembranes. *ACS Catal.* **2018**, *8* (3), 1767–1778. https://doi.org/10.1021/acscatal.7b02668.

283) Esposito, D. V. Membrane-Coated Electrocatalysts—An Alternative Approach To Achieving Stable and Tunable Electrocatalysis. *ACS Catal.* **2018**, *8* (1), 457–465. https://doi.org/10.1021/acscatal.7b03374.

284) Damjanovic, A.; Dey, A.; Bockris, J. Kinetics of Oxygen Evolution and Dissolution on Platinum Electrodes. *Electrochim. Acta* **1966**, *11* (7), 791–814. https://doi.org/10.1016/0013-4686(66)87056-1.

285) Endrődi, B.; Simic, N.; Wildlock, M.; Cornell, A. A Review of Chromium(VI) Use in Chlorate Electrolysis: Functions, Challenges and Suggested Alternatives. *Electrochim. Acta* **2017**, *234*, 108–122. https://doi.org/10.1016/j.electacta.2017.02.150.

286) Endrődi, B.; Sandin, S.; Smulders, V.; Simic, N.; Wildlock, M.; Mul, G.; Mei, B. T.; Cornell, A. Towards Sustainable Chlorate Production: The Effect of Permanganate Addition on Current

Efficiency. *J. Clean. Prod.* **2018**, *182*, 529–537. https://doi.org/10.1016/j.jclepro.2018.02.071.

287) Nikolaychuk, P. A. The Revised Pourbaix Diagram for Silicon. *Silicon* **2014**, *6* (2), 109–116. https://doi.org/10.1007/s12633-013-9172-0.

288) Robinson, J. E.; Labrador, N. Y.; Chen, H.; Sartor, B. E.; Esposito, D. V. Silicon Oxide-Encapsulated Platinum Thin Films as Highly Active Electrocatalysts for Carbon Monoxide and Methanol Oxidation. *ACS Catal.* **2018**, *8* (12), 11423–11434. https://doi.org/10.1021/acscatal.8b03626.

289) Reier, T.; Teschner, D.; Lunkenbein, T.; Bergmann, A.; Selve, S.; Kraehnert, R.; Schlögl, R.; Strasser, P. Electrocatalytic Oxygen Evolution on Iridium Oxide: Uncovering Catalyst-Substrate Interactions and Active Iridium Oxide Species. *J. Electrochem. Soc.* **2014**, *161* (9), F876–F882. https://doi.org/10.1149/2.0411409jes.

290) Filimonenkov, I. S.; Istomin, S. Y.; Antipov, E. V.; Tsirlina, G. A.; Savinova, E. R. Rotating Ring-Disk Electrode as a Quantitative Tool for the Investigation of the Oxygen Evolution Reaction. *Electrochim. Acta* **2018**, *286*, 304–312. https://doi.org/10.1016/j.electacta.2018.08.056.

291) Lide, D. R. *CRC Handbook of Chemistry and Physics, 90th Edition*; Taylor & Francis, 2009.

292) Conway, B. E.; Gu, P. Cl. Atom Electrosorption and Recombination at Oxide-Free and Oxide-Covered Surfaces of Pt Anodes, Evolving Cl_2 in $CF_3 \cdot COOH$. *J. Electroanal. Chem.* **1993**, *349* (1–2), 233–254. https://doi.org/10.1016/0022-0728(93)80176-I.

293) Conway, B. E.; Mozota, J. Chloride-Ion Effects on the Reversible and Irreversible Surface Oxidation Processes at Pt Electrodes, and on the Growth of Monolayer Oxide Films at Pt. *J. Chem. Soc. Faraday Trans. 1 Phys. Chem. Condens. Phases* **1982**, *78* (6), 1717. https://doi.org/10.1039/f19827801717.

294) Bhardwaj, A.; Vos, J. G.; Koper, M. T. M.; Esposito, D. V. Ultrathin Silicon Oxide Overlayers Enable Selective Oxygen Evolution from Acidic and Unbuffered PH-Neutral Seawater. Manuscript in Preparation (2019).

295) Steegstra, P.; Busch, M.; Panas, I.; Ahlberg, E. Revisiting the Redox Properties of Hydrous Iridium Oxide Films in the Context of Oxygen Evolution. *J. Phys. Chem. C* **2013**, *117* (40), 20975–20981. https://doi.org/10.1021/jp407030r.

296) Minguzzi, A.; Locatelli, C.; Lugaresi, O.; Achilli, E.; Cappelletti, G.; Scavini, M.; Coduri, M.; Masala, P.; Sacchi, B.; Vertova, A.; et al. Easy Accommodation of Different Oxidation States in Iridium Oxide Nanoparticles with Different Hydration Degree as Water Oxidation Electrocatalysts. *ACS Catal.* **2015**, *5* (9), 5104–5115. https://doi.org/10.1021/acscatal.5b01281.

297) Li, T.; Kasian, O.; Cherevko, S.; Zhang, S.; Geiger, S.; Scheu, C.; Felfer, P.; Raabe, D.; Gault, B.; Mayrhofer, K. J. J. Atomic-Scale Insights into Surface Species of Electrocatalysts in Three Dimensions. *Nat. Catal.* **2018**, *1* (4), 300–305. https://doi.org/10.1038/s41929-018-0043-3.

298) Fathollahi, F.; Javanbakht, M.; Norouzi, P.; Ganjali, M. R. Comparison of Morphology, Stability and Electrocatalytic Properties of $Ru_{0.3}Ti_{0.7}O_2$ and $Ru_{0.3}Ti_{0.4}Ir_{0.3}O_2$ Coated Titanium Anodes. *Russ. J. Electrochem.* **2011**, *47* (11), 1281–1286. https://doi.org/10.1134/S1023193511110061.

299) Mazhari Abbasi, H.; Jafarzadeh, K.; Mirali, S. M. An Investigation of the Effect of RuO_2 on the Deactivation and Corrosion Mechanism of a $Ti/IrO_2 + Ta_2O_5$ Coating in an OER Application. *J. Electroanal. Chem.* **2016**, *777*, 67–74. https://doi.org/10.1016/j.jelechem.2016.07.036.

300) Maljusch, A.; Conradi, O.; Hoch, S.; Blug, M.; Schuhmann, W. Advanced Evaluation of the Long-Term Stability of Oxygen Evolution Electrocatalysts. *Anal. Chem.* **2016**, *88* (15), 7597–7602. https://doi.org/10.1021/acs.analchem.6b01289.

301) Cherevko, S.; Geiger, S.; Kasian, O.; Mingers, A. M.; Mayrhofer, K. J. J. Oxygen Evolution Activity and Stability of Iridium in Acidic Media. Part 2. - Electrochemically Grown Hydrous Iridium Oxide. *J. Electroanal. Chem.* **2016**, *774*, 102–110. https://doi.org/10.1016/j.jelechem.2016.05.015.

302) Endrődi, B.; Smulders, V.; Simic, N.; Wildlock, M.; Mul, G.; Mei, B.; Cornell, A. In Situ Formed Vanadium-Oxide Cathode Coatings for Selective Hydrogen Production. *Appl. Catal. B Environ.* **2019**, *244* (November 2018), 233–239. https://doi.org/10.1016/j.apcatb.2018.11.038.

303) Obata, K.; Takanabe, K. A Permselective CeO x Coating To Improve the Stability of Oxygen Evolution Electrocatalysts. *Angew. Chemie* **2018**, *130* (6), 1632–1636. https://doi.org/10.1002/ange.201712121.

304) Liu, H.; Song, C.; Zhang, L.; Zhang, J.; Wang, H.; Wilkinson, D. P. A Review of Anode Catalysis in the Direct Methanol Fuel Cell. *J. Power Sources* **2006**, *155* (2), 95–110. https://doi.org/10.1016/j.jpowsour.2006.01.030.

305) Kadija, I. V.; Nakić, V. M. Ring Electrode on Rotating Disc as a Tool for Investigations of Gas-Evolving Electrochemical Reactions. *J. Electroanal. Chem. Interfacial Electrochem.* **1972**, *34* (1), 15–19. https://doi.org/10.1016/S0022-0728(72)80497-2.

306) Hessami, S.; Tobias, C. W. In-Situ Measurement of Interfacial PH Using a Rotating Ring-Disk Electrode. *AIChE J.* **1993**, *39* (1), 149–162. https://doi.org/10.1002/aic.690390115.

307) Qiu, Y.; Xin, L.; Li, W. Electrocatalytic Oxygen Evolution over Supported Small Amorphous Ni–Fe Nanoparticles in Alkaline Electrolyte. *Langmuir* **2014**, *30* (26), 7893–7901. https://doi.org/10.1021/la501246e.

308) Steegstra, P.; Ahlberg, E. In Situ PH Measurements with Hydrous Iridium Oxide in a Rotating Ring Disc Configuration. *J. Electroanal. Chem.* **2012**, *685*, 1–7. https://doi.org/10.1016/j.jelechem.2012.07.040.

309) Einerhand, R. E. F.; Visscher, W. H. M.; Barendrecht, E. Hydrogen Production during Zinc Deposition from Alkaline Zincate Solutions. *J. Appl. Electrochem.* **1988**, *18* (6), 799–806. https://doi.org/10.1007/BF01016034.

310) Horkans, J. Determination of Partial Currents for CuNi and CuCo Electrodeposition Using Rotating Ring-Disk Electrodes. *J. Electrochem. Soc.* **1991**, *138* (2), 411. https://doi.org/10.1149/1.2085600.

311) Suntivich, J.; May, K. J.; Gasteiger, H. A.; Goodenough, J. B.; Shao-Horn, Y. A Perovskite Oxide Optimized for Oxygen Evolution Catalysis from Molecular Orbital Principles. *Science (80-.).* **2011**, *334* (6061), 1383–1385. https://doi.org/10.1126/science.1212858.

312) Zhao, S.; Wang, Y.; Dong, J.; He, C.-T.; Yin, H.; An, P.; Zhao, K.; Zhang, X.; Gao, C.; Zhang, L.; et al. Ultrathin Metal–Organic Framework Nanosheets for Electrocatalytic Oxygen Evolution. *Nat. Energy* **2016**, *1* (November), 16184. https://doi.org/10.1038/nenergy.2016.184.

313) Scholz, J.; Risch, M.; Wartner, G.; Luderer, C.; Roddatis, V.; Jooss, C. Tailoring the Oxygen Evolution Activity and Stability Using Defect Chemistry. *Catalysts* **2017**, *7* (5), 139. https://doi.org/10.3390/catal7050139.

314) Hu, Y.; Tolmachev, Y. V.; Scherson, D. A. Rotating Ring-Disk Studies of Oxidized Nickel Hydrous Oxide: Oxygen Evolution and Pseudocapacitance. *J. Electroanal. Chem.* **1999**, *468* (1), 64–69. https://doi.org/10.1016/S0022-0728(99)00029-7.

315) Scholz, J.; Risch, M.; Stoerzinger, K. A.; Wartner, G.; Shao-Horn, Y.; Jooss, C. Rotating Ring–Disk Electrode Study of Oxygen Evolution at a Perovskite Surface: Correlating Activity to Manganese Concentration. *J. Phys. Chem. C* **2016**, *120* (49), 27746–27756. https://doi.org/10.1021/acs.jpcc.6b07654.

316) Gao, Q.; Ranjan, C.; Pavlovic, Z.; Blume, R.; Schlögl, R. Enhancement of Stability and Activity of MnO x /Au Electrocatalysts for Oxygen Evolution through Adequate Electrolyte Composition. *ACS Catal.* **2015**, *5* (12), 7265–7275. https://doi.org/10.1021/acscatal.5b01632.

317) Westbroek, P.; Temmerman, E. In Line Measurement of Chemical Oxygen Demand by Means of Multipulse Amperometry at a Rotating Pt Ring — Pt/PbO2 Disc Electrode. *Anal. Chim. Acta* **2001**, *437* (1), 95–105. https://doi.org/10.1016/S0003-2670(01)00927-8.

318) Popović, N. D.; Johnson, D. C. A Ring–Disk Study of the Competition between Anodic Oxygen-Transfer and Dioxygen-Evolution Reactions. *Anal. Chem.* **1998**, *70* (3), 468–472. https://doi.org/10.1021/ac9707803.

319) Kim, J.; Yin, X.; Tsao, K.-C.; Fang, S.; Yang, H. Ca 2 Mn 2 O 5 as Oxygen-Deficient Perovskite Electrocatalyst for Oxygen Evolution Reaction. *J. Am. Chem. Soc.* **2014**, *136* (42), 14646–14649. https://doi.org/10.1021/ja506254g.

320) Lee, Y.; Suntivich, J.; May, K. J.; Perry, E. E.; Shao-Horn, Y. Synthesis and Activities of Rutile IrO 2 and RuO 2 Nanoparticles for Oxygen Evolution in Acid and Alkaline Solutions. *J. Phys. Chem. Lett.* **2012**, No. pH 1, 399–404. https://doi.org/10.1021/jz2016507.

321) Yu, X.; Zhang, M.; Yuan, W.; Shi, G. A High-Performance Three-Dimensional Ni–Fe Layered Double Hydroxide/Graphene Electrode for Water Oxidation. *J. Mater. Chem. A* **2015**, *3* (13), 6921–6928. https://doi.org/10.1039/C5TA01034A.

322) Chen, D.; Dong, C.-L.; Zou, Y.; Su, D.; Huang, Y.-C.; Tao, L.; Dou, S.; Shen, S.; Wang, S. In Situ

Evolution of Highly Dispersed Amorphous CoO x Clusters for Oxygen Evolution Reaction. *Nanoscale* **2017**, *9* (33), 11969–11975. https://doi.org/10.1039/C7NR04381C.

323) Swesi, A. T.; Masud, J.; Nath, M. Nickel Selenide as a High-Efficiency Catalyst for Oxygen Evolution Reaction. *Energy Environ. Sci.* **2016**, *9* (5), 1771–1782. https://doi.org/10.1039/C5EE02463C.

324) German, S. R.; Edwards, M. A.; Chen, Q.; Liu, Y.; Luo, L.; White, H. S. Electrochemistry of Single Nanobubbles. Estimating the Critical Size of Bubble-Forming Nuclei for Gas-Evolving Electrode Reactions. *Faraday Discuss.* **2016**, *193*, 223–240. https://doi.org/10.1039/C6FD00099A.

325) Ren, H.; German, S. R.; Edwards, M. A.; Chen, Q.; White, H. S. Electrochemical Generation of Individual O2 Nanobubbles via H2O2 Oxidation. *J. Phys. Chem. Lett.* **2017**, *8* (11), 2450–2454. https://doi.org/10.1021/acs.jpclett.7b00882.

326) Marković, N. M.; Schmidt, T. J.; Stamenković, V.; Ross, P. N. Oxygen Reduction Reaction on Pt and Pt Bimetallic Surfaces: A Selective Review. *Fuel Cells* **2001**, *1* (2), 105–116. https://doi.org/10.1002/1615-6854(200107)1:2<105::AID-FUCE105>3.0.CO;2-9.

327) Ben Liew, K.; Daud, W. R. W.; Ghasemi, M.; Leong, J. X.; Su Lim, S.; Ismail, M. Non-Pt Catalyst as Oxygen Reduction Reaction in Microbial Fuel Cells: A Review. *Int. J. Hydrogen Energy* **2014**, *39* (10), 4870–4883. https://doi.org/10.1016/j.ijhydene.2014.01.062.

328) Geng, D.; Chen, Y.; Chen, Y.; Li, Y.; Li, R.; Sun, X.; Ye, S.; Knights, S. High Oxygen-Reduction Activity and Durability of Nitrogen-Doped Graphene. *Energy Environ. Sci.* **2011**, *4* (3), 760. https://doi.org/10.1039/c0ee00326c.

329) Einerhand, R. E. F.; Visscher, W. H. M.; Barendrecht, E. Hydrogen Production during Zinc Deposition from Alkaline Zincate Solutions. *J. Appl. Electrochem.* **1988**, *18* (6), 799–806. https://doi.org/10.1007/BF01016034.

330) Chen, D.; Dong, C.-L.; Zou, Y.; Su, D.; Huang, Y.-C.; Tao, L.; Dou, S.; Shen, S.; Wang, S. In Situ Evolution of Highly Dispersed Amorphous CoO x Clusters for Oxygen Evolution Reaction. *Nanoscale* **2017**, *9* (33), 11969–11975. https://doi.org/10.1039/C7NR04381C.

331) Kuiken, H. K.; Bakkers, E. P. A. M.; Ligthart, H.; Kelly, J. J. The Rotating Ring-Ring Electrode. Theory and Experiment. *J. Electrochem. Soc.* **2000**, *147* (3), 1110. https://doi.org/10.1149/1.1393321.

332) Zhu, X.; Gupta, K.; Bersani, M.; Darr, J. A.; Shearing, P. R.; Brett, D. J. L. Electrochemical Reduction of Carbon Dioxide on Copper-Based Nanocatalysts Using the Rotating Ring-Disc Electrode. *Electrochim. Acta* **2018**, *283*, 1037–1044. https://doi.org/10.1016/j.electacta.2018.07.025.

333) Bai, L.; Conway, B. E. Electrochemistry of Anodic F2 Evolution at Carbon Electrodes: Bubble Adherence Effects in the Kinetics at Rotating Cone Electrodes. *J. Appl. Electrochem.* **1988**, *18* (6), 839–848. https://doi.org/10.1007/BF01016039.

334) Kirowa-Eisner, E.; Gileadi, E. The Rotating Cone Electrode. *J. Electrochem. Soc.* **1976**, *123* (1), 22. https://doi.org/10.1149/1.2132756.

335) Miller, B. Rotating Ring-Disk Study of the Silver Electrode in Alkaline Solution. *J. Electrochem. Soc.* **1970**, *117* (4), 491. https://doi.org/10.1149/1.2407548.

336) Dresp, S.; Dionigi, F.; Loos, S.; Ferreira de Araújo, J.; Spöri, C.; Gliech, M.; Dau, H.; Strasser, P. Direct Electrolytic Splitting of Seawater: Activity, Selectivity, Degradation, and Recovery Studied from the Molecular Catalyst Structure to the Electrolyzer Cell Level. *Adv. Energy Mater.* **2018**, *8* (22), 1800338. https://doi.org/10.1002/aenm.201800338.

337) Geiger, S.; Kasian, O.; Mingers, A. M.; Nicley, S. S.; Haenen, K.; Mayrhofer, K. J. J.; Cherevko, S. Catalyst Stability Benchmarking for the Oxygen Evolution Reaction: The Importance of Backing Electrode Material and Dissolution in Accelerated Aging Studies. *ChemSusChem* **2017**, *10* (21), 4140–4143. https://doi.org/10.1002/cssc.201701523.

338) Jones, S. F.; Evans, G. M.; Galvin, K. P. Bubble Nucleation from Gas Cavities — a Review. *Adv. Colloid Interface Sci.* **1999**, *80* (1), 27–50. https://doi.org/10.1016/S0001-8686(98)00074-8.

339) Xi, Z.-Y.; Xu, Y.-Y.; Zhu, L.-P.; Wang, Y.; Zhu, B.-K. A Facile Method of Surface Modification for Hydrophobic Polymer Membranes Based on the Adhesive Behavior of Poly(DOPA) and Poly(Dopamine). *J. Memb. Sci.* **2009**, *327* (1–2), 244–253. https://doi.org/10.1016/j.memsci.2008.11.037.

340) Jiang, J.; Zhu, L.; Zhu, L.; Zhu, B.; Xu, Y. Surface Characteristics of a Self-Polymerized

Dopamine Coating Deposited on Hydrophobic Polymer Films. *Langmuir* **2011**, *27* (23), 14180–14187. https://doi.org/10.1021/la202877k.

341) Janssen, L. J. J.; Sillen, C. W. M. P.; Barendrecht, E.; van Stralen, S. J. D. Bubble Behaviour during Oxygen and Hydrogen Evolution at Transparent Electrodes in KOH Solution. *Electrochim. Acta* **1984**, *29* (5), 633–642. https://doi.org/10.1016/0013-4686(84)87122-4.

342) da Cruz, S. G.; Dutra, A. J. B.; Monte, M. B. M. The Influence of Some Parameters on Bubble Average Diameter in an Electroflotation Cell by Laser Diffraction Method. *J. Environ. Chem. Eng.* **2016**, *4* (3), 3681–3687. https://doi.org/10.1016/j.jece.2016.05.017.

343) Matsushima, H.; Nishida, T.; Konishi, Y.; Fukunaka, Y.; Ito, Y.; Kuribayashi, K. Water Electrolysis under Microgravity. *Electrochim. Acta* **2003**, *48* (28), 4119–4125. https://doi.org/10.1016/S0013-4686(03)00579-6.

344) Frazer, E. J.; Hamilton, I. C. The Estimation of the Coulombic Efficiency of Zinc Electrodeposition by Measurement of Current Efficiencies at a Rotating Ring Disc Electrode. *J. Appl. Electrochem.* **1986**, *16* (3), 387–392. https://doi.org/10.1007/BF01008849.

345) Birss, V. I. A Study of the Transition from Oxide Growth to O[Sub 2] Evolution at Pt Electrodes in Acid Solutions. *J. Electrochem. Soc.* **1983**, *130* (8), 1688. https://doi.org/10.1149/1.2120063.

346) Zangmeister, R. A.; Morris, T. A.; Tarlov, M. J. Characterization of Polydopamine Thin Films Deposited at Short Times by Autoxidation of Dopamine. *Langmuir* **2013**, *29* (27), 8619–8628. https://doi.org/10.1021/la400587j.

347) Steegstra, P.; Ahlberg, E. Involvement of Nanoparticles in the Electrodeposition of Hydrous Iridium Oxide Films. *Electrochim. Acta* **2012**, *68*, 206–213. https://doi.org/10.1016/j.electacta.2012.02.058.

348) Fine, D. A. On the Spontaneous Reduction of Hexachloroiridate(IV) in Aqueous Solution. *Inorg. Chem.* **1964**, *32* (1937), 1964–1966.

349) Hepel, T.; Pollak, F. H.; O'Grady, W. E. Chlorine Evolution and Reduction Processes at Oriented Single-Crystal RuO2 Electrodes. *J. Electrochem. Soc.* **1986**, *133* (1), 69. https://doi.org/10.1149/1.2108547.

350) Eliaz, N.; Gileadi, E. *Physical Electrochemistry: Fundamentals, Techniques, and Applications*, 2nd Editio.; Wiley-VCH Verlag GmbH & Co. KGaA, 2018.

Summary and Outlook

Summary

The work presented in this thesis concerns the electrochemical, anodic evolution of oxygen gas and chlorine gas in an aqueous environment. These two reactions can occur simultaneously in a chloride-containing electrolyte, and they play central roles in several electrochemical processes that are very energy intensive. Their kinetics, and the selectivity between them are therefore of central importance. Only one of the two reactions is usually desired, such as the Chlorine Evolution Reaction (CER) in the chlor-alkali process. On the other hand, only the Oxygen Evolution Reaction (OER) is wanted at the anode during water electrolysis for renewable energy conversion, where ideally seawater is used as a substrate. In either case, any occurrence of the other reaction strongly undermines the feasibility of the overall process. 'Separating' the two reactions is an imposing task, because their activities are highly correlated; most catalysts capable of the OER will also oxidize chloride if it is present in the electrolyte. Especially the development of highly desired OER-selective anodes is difficult, because the simpler nature of the CER reaction mechanism implies that it has a kinetic advantage over the OER. This thesis is therefore dedicated to how the OER and CER compete and interact on a very fundamental level, a subject of which surprisingly little research exists, especially regarding dilute chloride solutions.

As selectivity underlines most of this work, in Chapter 2 we first explored a new method for determining chlorine vs. oxygen selectivity using a rotating ring-disk electrode assembly, which is a widespread tool within the electrochemistry research field. A Pt ring fixed at 0.95 V vs. RHE in a solution of pH 0.88 was used to selectively reduce the Cl_2 formed on the disk. Contrary to most established methods for measuring chlorine evolved, this method has short response times and can be used within almost any potential vs. time program. It is accurate enough to deduce fundamental kinetic parameters of the CER proceeding alongside the OER, although it is limited to acidic solutions (pH $\approx$ 1) and moderate current densities. As proof of concept, we used it to show that on a glassy carbon-supported (GC) IrO_x catalyst, the selectivity towards chlorine evolution rapidly approached 100% as the chloride concentration $[Cl^-]$ increased from 0 to 100 mM. Our results furthermore suggest that on IrO_x, the OER is not suppressed or influenced by the presence of Cl^- or by the CER taking place simultaneously on the surface.

In Chapter 3, we looked deeper into the apparent fundamental link between the OER and CER, by studying the reactions on a series of closely-related iridium-based double perovskites. As has been implied by previous research, we found a strong linear correlation between OER and CER activity on these materials, providing further evidence for the scaling relationship that exists between the OER and CER. We furthermore performed online inductively coupled plasma mass spectrometry (ICP-MS) measurements on these materials, as material stability is also an important issue in the context of OER electrocatalysis. We found indications that catalyst dissolution pathways are very different between the OER and CER. In particular, chloride selectively enhanced the dissolution of the noble metal component. A chloride reaction order analysis was carried out to look at the effect of surface area changes due to

adventitious leaching, and the observed suppressing effect of chloride on the OER. The analysis suggested that the CER mechanism on the double perovskites was notably different from that on IrO_x and semi-crystalline IrO_2, which were used as reference materials.

Moving on from the study of selectivity and scaling between the OER and CER, we dedicated Chapters 4 and 5 to a deeper investigation of the reaction mechanism of the CER on Pt and IrO_x surfaces. We looked specifically into the effect of bromide, which is a small but important component of seawater, and how the oxidation mechanisms of Br^- and Cl^- may affect each other and the OER. In Chapter 4 the focus was on the parallel Bromine Evolution Reaction (BER) and the CER, using Pt as an electrochemical model system. We found that that the oxidation of bromide is hindered by competing chloride adsorption on Pt, in a way that can be quite satisfactorily modelled by a simple Langmuir isotherm describing the competing adsorption and reactivity of all species. The oxidation of chloride was however not properly captured by this same model, and may follow a substantially different mechanism. Furthermore, from voltammetry, in-situ UV-Vis experiments and considerations of solution chemistry and oxidation products that may be expected in a mixed acidic bromide/chloride electrolyte, we found that Pt seems to catalyze the formation of the interhalogen compound BrCl in-between the oxidation of bromide and chloride. Chapter 5 extends the approach introduced in Chapter 4 to GC-supported IrO_x, this time focussing on how the OER is affected by the presence of chloride and bromide, keeping in mind that Ir-based electrocatalysts are more applicable to seawater electrolyzers than Pt. Chloride and bromide also adsorb competitively on IrO_x, but contrary to Pt, we found no evidence of interhalogen BrCl formation. We also found that even a relatively small amount of bromide strongly slows down both the CER and OER, where especially the OER and its selectivity is highly affected. This knowledge can lead to a deeper understanding of the challenges to be faced when developing an OER-selective anode for seawater electrolysis.

In Chapters 6 and 7, we look more deeply into OER-selective anodes, so that electrolysis of readily available seawater may be achieved without the formation of (mainly) chlorine as toxic by-product. In Chapter 6, we first investigated the OER vs. CER selectivity of anodes based on manganese oxide (MnO_x), one of the few types of materials with unusually high OER selectivity. To model this class of catalysts, thin films (~5-20 nm) of MnO_x were electrodeposited on GC-supported IrO_x in aqueous chloride solutions of pH ~ 0.9. Using rotating ring-disk electrode voltammetry and online electrochemical mass spectrometry, it was found that deposition of MnO_x onto IrO_x decreases the CER selectivity of the system in presence of 30 mM Cl^- from 86% to less than 7%, verifying the high OER-selectivity of MnO_x-based catalysts. Interestingly, detailed studies of the CER mechanism and ex-situ structure studies using SEM, TEM and XPS suggest that the MnO_x film is in fact not a catalytically active phase, but functions as a permeable overlayer that disfavors the transport of chloride ions. This approach to enhancing the OER selectivity by selectively preventing chloride from reacting at the anode is explored further in Chapter 7, where we investigated the effect of thin (10-20 nm) overlayer films composed of amorphous silicon oxide (SiO_x), which is an electrochemically inert material resistant to acid. The SiO_x was spin-coated onto Pt and GC-supported IrO_x, as well as on two types of Ti-based anodes using Ir, the latter of which were identical to Ir-based anodes used

on an industrial scale. From the SiO_x/Pt electrode, which served as a proof of concept, it was clear that the silicon-based overlayer can be a very effective barrier against the CER on flat, relatively well-defined surfaces, while still allowing OER activity to occur on the buried platinum at higher potentials. Experiments on SiO_x/IrO_x/GC electrodes, which are more closely related to Ir-based catalysts used in electrolyzers, yielded mixed results. CER activity was again impacted, but so was the OER. More importantly, the CER was not completely suppressed regardless of the thickness of the SiO_x overlayer. SEM/EDS measurements and kinetic analysis suggested that the still significant CER-activity originated from defects in the film. It is likely that the spin-coating procedure used to produce the SiO_x films is not very compatible with rough surfaces when very thin (<20 nm) films are applied. On the other hand, the Ti-based Ir anodes, to which significantly thicker SiO_x films were applied, showed much better CER suppression, with a CER selectivity of roughly 16% in 30 mM KCl. This value is the same order of magnitude as the thickest MnO_x/IrO_x/GC electrodes measured in Chapter 6. The extra thick SiO_x overlayer was applied because the MMOs have micrometer-scale roughness. Besides good OER selectivity, this layer also resulted in rather low electrocatalytic activity. Although these initial results leave room for improvement, it is clear that the concept of buried interfaces may be a promising approach to reach OER-selective water splitting in saltwater electrolyzers. There are still abundant parameters that can be optimized regarding the SiO_x overlayer.

In Chapter 8, we explored methods of reducing ring-disk collection errors during RRDE voltammetry. These errors are caused by formation of gas bubbles during vigorous evolution of gas on the disk electrode, and were pervasive throughout the experiments performed in this thesis. We tried to improve the reliability of the RRDE collection factor by mounting a thin wire close to the surface, to dislodge bubbles that formed specifically on the interface between the disk and the disk-ring spacer. This approach was tested for the detection of chlorine during parallel chlorine and oxygen evolution, and resulted in a notable alteration of the collection efficiency. Its value became lower than theoretical expectations and also quite stable, even under higher current densities. Additionally, the RRDE tip was coated in a hydrophilic polymer, to reduce the tendency of bubble formation. This was tested for the collection of hydrogen and oxygen gas, and led to a mild increase in overall performance. The coating allowed for approximately 50% higher hydrogen evolution current density without ring failure, and for oxygen collection led to an overall improvement in behavior.

Outlook

From this thesis, several perspectives arise on the chlorine vs. oxygen selectivity problem. Primarily, the strong scaling between OER and CER activity would prohibit optimizing the selectivity purely on the basis of kinetic considerations. Apart from specific adsorption effects by chloride ions, the OER and CER seem not very strongly affected by each other, so that their selectivity can be seen as a steady ratio between their intrinsic activities. The CER then kinetically always has the upper hand, while the OER activity is small but non-zero. To improve the selectivity towards a single reaction, this work suggests that chloride mass transport is the most important factor, once effects from specific chloride adsorption are

accounted for. The CER selectivity has been optimized this way with great success in the chlor-alkali industry over the last few decades, by using highly concentrated chloride solutions. Enhancing instead the OER selectivity is certainly more challenging, and also highly desirable as it could enable chlorine-free water splitting in saltwater electrolyzers. The most effective way of achieving this would be to negatively affect chloride diffusion to the surface, compared to that of water. The concept of 'buried interfaces' relating to Chapters 6 and 7 is therefore very promising. Possibly, every highly OER-selective anode previously reported is reliant on this principle. It allows for versatility in the design of electrolyzers, since it effectively decouples the selectivity issue from the OER activity issue. When using buried interfaces to enforce selectivity, there would be no need to find wholly different catalysts for freshwater and saltwater splitting. The overlayer may also increase the mechanical stability of the catalyst, which is an attractive prospect for water electrolysis, where catalyst durability is a major issue. An extra advantage of the permselective overlayer is that it will likely also prevent the adsorption and oxidation of bromide, which may pose a serious problem (see Chapter 5).

Tailoring effective overlayers against the CER is as of yet unchartered territory, with huge potential but with many hurdles and uncertainties to be overcome as well. The material to be used, besides being permselective against chloride, should be chemically and electrochemically inert, and resistant to the harsh conditions of OER electrocatalysis. Judging from Pourbaix diagrams and previous literature, possible candidates in neutral and acidic media at high potentials could be oxides, such as those of Ti, Si, Ce, Sn, W, Mo, or Sb. Alternatively, surface modification with polymers or thin membrane-based approaches could be promising. The layer should be just thick enough to completely block chloride transport over extended times, while also as thin as possible to minimize the impact on the transport of OER-related species to the buried catalyst. Getting the material in position, homogeneously distributed across all active catalytic sites, is one of the main challenges. Ideally, electrodeposition or a deposition method indirectly dependent on current (such as electroflocculation) should be used, as this leads to the most active catalyst sites being specifically targeted. As shown in Chapter 6, another approach could be to have the overlayer precursor present in the bulk solution in dilute quantities, leading to a dynamic deposition/dissolution equilibrium and a guarantee of the overlayer integrity over extended operating times. The bulk precursor concentration, which would determine the driving force for deposition and the equilibrium thickness of the deposited overlayer, should however be chosen carefully to prevent layers of excessive thickness to form and interfere with the electrolysis process.

Although the work presented in this thesis is highly fundamental, it will hopefully offer some guidelines when searching for practical solutions to more efficient separation of the evolution of chlorine and oxygen, especially so for saltwater electrolysis. The notion that mass transport of chloride is the most important (and perhaps only) factor affecting CER selectivity could steer saltwater electrolysis in new research directions. A breakthrough there may give the general research field of hydrogen as energy carrier a welcome push of attention. It may galvanize public and corporate interest into making an energy infrastructure based on electrolysis and fuel cells a reality.

Samenvatting en Toekomstperspectieven

Samenvatting

Het werk in dit proefschrift omvat de elektrochemische vorming van zuurstofgas en chloorgas in een waterige omgeving. Deze twee kunnen gelijktijdig optreden in een chloride-bevattende elektrolyt, en spelen een centrale rol in een aantal zeer energie-intensieve elektrochemische processen. Inzicht in de kinetiek en selectiviteit van de twee processen is daarom van groot belang. Doorgaans is slechts één reactie gewenst, zoals de chloorevolutiereactie (CER) in het chlooralkali proces. Daarentegen is alleen de zuurstofevolutiereactie (OER) gewenst bij de anode tijdens waterelektrolyse voor conversie van hernieuwbare energie, waar men idealiter zeewater als substraat gebruikt. In beide situaties vormt elk optreden van de andere reactie een ernstige ondergraving van de uitvoerbaarheid van het totale proces. Het 'scheiden' van de twee reacties is een lastige opgave, omdat ze doorgaans simultaan optreden; de meeste katalysatoren die in staat zijn de OER te katalyseren zullen ook chloride oxideren als het in de elektrolyt aanwezig is. Het CER-reactiemechanisme heeft voorts een eenvoudiger karakter dan dat van de OER, wat impliceert dat de vorming van zuurstof een intrinsiek kinetisch nadeel heeft ten opzichte van chloorevolutie. Hierdoor is vooral de ontwikkeling van OER-selectieve anodes, die zeewaterelektrolyse zonder chloorvorming mogelijk zouden kunnen maken, een grote uitdaging. Dit proefschrift is derhalve gewijd aan hoe de OER en CER op een zeer fundamenteel niveau concurreren. Naar dit onderwerp is verrassend weinig onderzoek gedaan, in het bijzonder naar hoe de reacties zich gedragen in verdunde chlorideoplossingen.

Omdat selectiviteit in het grootste deel van dit werk de hoofdrol speelt, hebben we in hoofdstuk 2 eerst een nieuwe methode bestudeerd voor het bepalen van chloor versus zuurstofselectiviteit. Dit bleek mogelijk met behulp van een roterende ring-schijf elektrode, een veelgebruikt systeem binnen de elektrochemie. Een Pt ring ingesteld op 0,95 V versus RHE in een oplossing van pH 0,88 werd gebruikt om de Cl_2 gevormd op de schijf selectief te reduceren. Deze methode heeft veel kortere reactietijden dan andere gangbare methoden voor chloordetectie, en kan gebruikt worden in vrijwel elk schema van potentiaal versus tijd. De methode is nauwkeurig genoeg om fundamentele kinetische parameters af te leiden van de CER, terwijl deze tegelijkertijd met de OER optreed. De methode is wel beperkt tot zure oplossingen (pH $\approx$ 1) en gematigde stroomdichtheden. Ter demonstratie hebben we ermee aangetoond dat amorf IrO_x op glasachtig koolstof (GC) hoge selectiviteit jegens chloorevolutie vertoont, waarbij de waarde snel de 100% naderde naarmate de chlorideconcentratie [Cl⁻] toenam van 0 tot 100 mM. Onze resultaten suggereren ook dat de OER op IrO_x niet onderdrukt of beïnvloed wordt door de aanwezigheid van Cl⁻, of door de CER die gelijktijdig op het oppervlak plaatsvindt.

In hoofdstuk 3 zijn we dieper ingegaan op het fundamentele verband tussen de OER en CER, door de reacties op een reeks nauw verwante iridium-gebaseerde dubbele perovskieten te bestuderen. Overeenkomstig met eerder onderzoek vonden we een sterke lineaire correlatie tussen OER- en CER-activiteit, een duidelijk teken van het bestaan van een schalingsrelatie tussen de reacties. Aangezien materiaalstabiliteit over langere termijn een belangrijk thema is binnen OER-elektrokatalyse, hebben we in dit onderzoek ook inductief gekoppelde

plasmamassaspectrometrie (ICP-MS) uitgevoerd. Deze metingen suggereerden grote verschillen in de manier waarop katalysatoren ontbinden tijdens de OER, vergeleken met de CER. Tijdens de CER versnelde chloride selectief de dissolutie van het nobelere Ir uit de katalysatoren. We analyseerden ook de reactieorde voor chloride met betrekking tot veranderingen in de katalytische activiteit. De analyse toonde dat de dubbele perovskieten een aanzienlijk ander CER-mechanisme hadden dan IrO_x en semi-kristallijne IrO_2 , twee materialen die ter vergelijking werden gebruikt.

Na het bestuderen van selectiviteit en schaling tussen de OER en CER hebben we in hoofdstukken 4 en 5 in detail gekeken naar het reactiemechanisme van de CER op oppervlakken van Pt en IrO_x. Hierbij was speciale aandacht voor het effect van bromide, een kleine maar belangrijke component van zeewater, en hoe de oxidatiemechanismen van Br^- en Cl^- elkaar en de OER kunnen beïnvloeden. In hoofdstuk 4 hebben we ons gericht op de broomevolutiereactie (BER) in parallel met de CER, waarbij Pt diende als elektrokatalysator. Het bleek dat de oxidatie van bromide op Pt wordt gehinderd door de competitieve adsorptie van chloride, en dat het proces adequaat kan worden gemodelleerd met een eenvoudige Langmuir isotherm die de competitieve adsorptie en reactiviteit van alle halogenen beschrijft. Hetzelfde model kon de oxidatie van chloride echter niet correct beschrijven. Voorts vonden we dat Pt de vorming van de interhalogeenverbinding BrCl katalyseert. Dit bleek uit voltammetrie, experimenten met in-situ UV-Vis, en een beschouwing van oxidatieproducten die men verwacht in een gemengde zure bromide/chloride elektrolyt. In hoofdstuk 5 werd de methodologie uit hoofdstuk 4 toegepast op IrO_x op GC, waarbij de nadruk lag op hoe de OER wordt beïnvloed door de aanwezigheid van zowel chloride als bromide. De IrO_x katalysator heeft meer te maken met daadwerkelijke zeewaterelectrolyzers dan Pt. We zagen dat chloride en bromide ook competitief adsorberen op IrO_x, maar in tegenstelling tot bij Pt vonden we geen bewijs van de vorming van interhalogeen BrCl. Het bleek dat zowel de CER als de OER sterk vertraagd werden door bromide, zelfs bij een relatief kleine hoeveelheid. Vooral de selectiviteit jegens de OER sterk werd verminderd. Dit inzicht kan leiden tot een dieper begrip van de uitdagingen die moeten worden aangegaan bij het ontwikkelen van een OER-selectieve anode voor zeewaterelektrolyse.

In hoofdstukken 6 en 7 zijn we dieper ingegaan op OER-selectieve anodes, waarmee het mogelijk zou zijn om zeewater te elektrolyseren zonder de vorming van (voornamelijk) chloor als giftig bijproduct. In hoofdstuk 6 hebben we eerst de OER versus CER-selectiviteit onderzocht van anoden op basis van mangaanoxide (MnO_x), welke ongewoon hoge OER-selectiviteit hebben. Om deze soort katalysatoren te benaderen werden dunne films (~ 5-20 nm) van MnO_x depositioneerd op IrO_x, in waterige chloride-oplossingen met pH ~ 0,9. Met behulp van een roterende ring-schijf elektrode en elektrochemische massaspectrometrie vonden we dat de depositie van MnO_x op IrO_x een sterk, selectief effect heeft op chloorevolutie: in aanwezigheid van 30 mM Cl^- verschoof de CER-selectiviteit van het systeem van 86% tot minder dan 7%. Dit resultaat bekrachtigt eerdere studies van de hoge OER-selectiviteit van katalysatoren op basis van MnO_x . We deden ook gedetailleerde studies naar het CER-mechanisme, en ex-situ structuurstudies met behulp van SEM, TEM en XPS. Resultaten van deze experimenten suggereerden dat de MnO_x laag in feite niet katalytisch actief is, maar dat

deze functioneert als een permeabele afdeklaag die het transport van chloride-ionen verhindert. Deze benadering om de OER-selectiviteit te verbeteren is verder onderzocht in hoofdstuk 7, waar we deklagen onderzochten van amorf siliciumoxide (SiO_x), een elektrochemisch inert materiaal dat bestand is tegen zuur. Dunne (5-20 nm) lagen van SiO_x werden door spincoating aangebracht op Pt en IrO_x, evenals op twee soorten Ti-ondersteunde Ir anodes. Laatstgenoemde soort anodes was identiek aan op Ir gebaseerde anodes die op industriële schaal worden gebruikt. Uit experimenten op SiO_x/Pt elektroden, die dienden als modelsysteem, kwam naar voren dat de deklaag op basis van siliciumoxide een zeer effectieve barrière kan zijn tegen de CER op platte, relatief goed gedefinieerde oppervlakken, terwijl bij hogere potentialen toch nog OER-activiteit kan optreden op het bedolven platina. Experimenten met SiO_x/IrO_x/GC elektroden, die nauwer verwant zijn met op Ir gebaseerde katalysatoren die in electrolyzers worden gebruikt, leverden gemengde resultaten op. De CER-activiteit werd opnieuw verminderd, maar die van de OER ook. Bovenal werd de CER niet volledig onderdrukt, ongeacht de dikte van de SiO_x deklaag. SEM/EDS-metingen en kinetische analyse suggereerden dat de resterende CER-activiteit voortkwam uit defecten in de film. Het is waarschijnlijk dat de spincoatingprocedure die werd gebruikt om de SiO_x-films te vormen niet erg compatibel is met ruwe oppervlakken wanneer zeer dunne (<20 nm) films worden aangebracht. Anderzijds vertoonden de op Ti gebaseerde Ir-anodes, waarop aanzienlijk dikkere SiO_x films werden aangebracht, een veel betere onderdrukking van de CER, met een CER-selectiviteit van ongeveer 16% in 30 mM KCl. Deze waarde heeft dezelfde ordegrootte als de dikste MnO_x/IrO_x/GC-elektroden gemeten in Hoofdstuk 6. De extra dikke SiO_x deklaag werd toegepast omdat de Ti-gebaseerde anoden ruwheid op micrometerschaal hebben. Naast een goede OER-selectiviteit resulteerde dit ook in een lage elektrokatalytische activiteit. Hoewel deze eerste resultaten voor verbetering vatbaar zijn, is het duidelijk dat het concept van deklagen veelbelovend kan zijn om de OER-selectiviteit in zoutwaterelectrolyzers te maximaliseren. Er resteren nog vele variabelen die geoptimaliseerd kunnen worden met betrekking tot de SiO_x modificatie.

In Hoofdstuk 8 hebben we methoden onderzocht voor het verminderen van collectiefouten tijdens roterende ring-schijf voltammetrie. Deze fouten worden doorgaans veroorzaakt door de vorming van gasbellen tijdens de intense ontwikkeling van gas op de schijfelektrode, en de kans op deze fouten was alomtegenwoordig gedurende de experimenten die in dit proefschrift zijn uitgevoerd. We probeerden eerst de betrouwbaarheid van de collectie factor te verbeteren door een dunne draad dicht bij het oppervlak te monteren, om bellen te verwijderen die zich specifiek vormden op de spacer tussen de schijf en de ring. Deze benadering werd getest voor de detectie van chloor tijdens de parallelle chloor- en zuurstofevolutie en resulteerde in een opmerkelijke verandering van de collectie factor: de waarde ervan werd lager dan de theoretische verwachtingen, en bleef zelfs bij hoge stroomdichtheden redelijk stabiel. We hebben de elektrodetip ook gecoat in een hydrofiel polymeer om te proberen de neiging tot bellenvorming te verminderen. Dit werd getest tijdens de vorming van waterstof- en zuurstofgas, en leidde tot een milde verbetering van de algehele prestaties. De coating liet een ongeveer 50% hogere stroomdichtheid van waterstofevolutie toe zonder verstoring van het ringsignaal, en leidde voor het collecteren van zuurstof tot een algemene verbetering van de resultaten.

Toekomstperspectieven

Uit dit proefschrift komen diverse perspectieven naar voren op het selectiviteitsprobleem tussen chloor en zuurstof. Ten eerste zou de sterke schalingsrelatie tussen OER- en CER-activiteit het optimaliseren van de selectiviteit puur op basis van kinetische overwegingen verbieden. Afgezien van effecten veroorzaakt door specifieke adsorptie van chloride-ionen, lijken de OER en CER niet erg sterk door elkaar te worden beïnvloed, zodat hun selectiviteit kan worden gezien als een constante verhouding tussen hun intrinsieke activiteiten. De CER heeft dan kinetisch altijd een voordeel, maar gaat gekoppeld met een OER-activiteit die klein is maar niet nul. Dit werk suggereert dat massatransport van chloride de belangrijkste factor is om de selectiviteit voor één enkele reactie te verbeteren, nadat de effecten van specifieke adsorptie door chloride in aanmerking zijn genomen. Deze benadering is in de afgelopen decennia met groot succes toegepast in de chflooralkali industrie, door het gebruik van sterk geconcentreerde chloride-oplossingen. Het verbeteren van de OER-selectiviteit is daarentegen nog steeds een uitdaging, en tevens noodzakelijk om chloorvrije watersplitsing in zoutwaterelectrolyzers mogelijk te maken. De beste manier om selectieve zuurstofevolutie te bereiken zou zijn om omstandigheden af te dwingen waar chloridediffusie naar het oppervlak negatief wordt beïnvloed in vergelijking met die van water. Het concept van deklagen in hoofdstukken 6 en 7 is daarvoor een veelbelovende benadering. Mogelijk is elke eerder gerapporteerde OER-selectieve anode afhankelijk van dit principe. Het bevordert flexibiliteit in het ontwerp van electrolyzers, omdat het effectief gezien het selectiviteitsprobleem loskoppelt van het probleem aangaande de vaak lage OER-activiteit. Bij het gebruik van deklagen om selectiviteit af te dwingen is het in principe niet nodig om geheel nieuwe katalysatoren te vinden voor het splitsen van zoet en zout water. De deklaag kan ook de mechanische stabiliteit van de katalysator verhogen, een aantrekkelijk vooruitzicht voor waterelektrolyse, waar de bestendigheid van de katalysator over langere duur een groot probleem is. Een extra voordeel van de permselectieve deklaag is dat deze waarschijnlijk ook de adsorptie en oxidatie van bromide zal voorkomen, welke tevens een ernstig probleem kan vormen (zie hoofdstuk 5).

Het ontwikkelen van effectieve deklagen jegens de CER is vooralsnog onbekend terrein, met een enorm potentieel, maar ook vele horden en onzekerheden die overwonnen moeten worden. Behalve permselectief tegen chloride moet het te gebruiken materiaal chemisch en elektrochemisch inert zijn, en bestand zijn tegen de corrosieve omstandigheden van OER-elektrokatalyse. Pourbaix-diagrammen en eerdere literatuur in ogenschouw nemend kunnen diverse oxiden mogelijke kandidaten in zijn neutrale en zure media onder hoge potentialen, zoals die van Ti, Si, Ce, Sn, W, Mo of Sb. Een veelbelovend alternatief kan oppervlaktemodificatie met polymeren zijn, of methodes op basis van dunne membranen. De deklaag moet net dik genoeg zijn om het chloridetransport over langere tijd volledig te blokkeren, maar ook zo dun mogelijk om de negatieve invloed op het transport van OER-gerelateerde deeltjes naar de bedolven katalysator te minimaliseren. Eén van de belangrijkste uitdagingen zal zijn om het materiaal op zijn plaats te krijgen, homogeen verdeeld over alle actieve katalytische sites. In het ideale geval zou elektrodepositie kunnen worden gebruikt, of een depositiemethode die indirect afhankelijk is van stroom (zoals elektroflocculatie), omdat

dit ertoe leidt dat afzetting plaatsvindt op de meest actieve sites van de katalysator. Zoals beschreven in hoofdstuk 6 zou een andere benadering kunnen zijn om de chemische precursor van de deklaag in verdunde hoeveelheden in de bulkoplossing aanwezig te hebben. Dit zou leiden tot een dynamisch evenwicht van depositie/dissolutie, en een garantie van de integriteit van de deklaag gedurende werkzaamheid over lange periodes. De concentratie van de precursor in de bulk, welke de drijvende kracht bepaalt voor depositie en de evenwichtsdikte van de deklaag, moet dan wel zorgvuldig worden gekozen om te voorkomen dat zich lagen van buitensporige dikte vormen en dat het elektrolyseproces verstoord wordt.

Hoewel het in dit proefschrift gepresenteerde werk zeer fundamenteel is, biedt het hopelijk enkele richtlijnen bij het zoeken naar praktische oplossingen voor een efficiëntere scheiding van de vorming van chloor en zuurstof, in het bijzonder voor zoutwaterelektrolyse. Het idee dat massatransport van chloride de belangrijkste (en wellicht enige) factor is die de selectiviteit beïnvloedt, zou zoutwaterelektrolyse nieuwe onderzoeksrichtingen in kunnen sturen. Een doorbraak in dit onderzoeksveld kan het onderzoek naar waterstof als energiedrager de nodige aandacht geven. Het kan een sterke impuls geven aan de publieke en zakelijke interesse om een energie-infrastructuur op basis van elektrolyse en brandstofcellen te realiseren.

List of Publications

Chapter 2

Vos, J. G.; Koper, M. T. M. Measurement of Competition between Oxygen Evolution and Chlorine Evolution Using Rotating Ring-Disk Electrode Voltammetry. J. Electroanal. Chem. 2018, 819 (October), 260–268.

https://doi.org/10.1016/j.jelechem.2017.10.058

Chapter 3

Vos, J. G.; Liu, Z.; Speck, F. D.; Perini, N.; Fu, W.; Cherevko, S.; Koper, M. T. M. Selectivity Trends Between Oxygen Evolution and Chlorine Evolution on Iridium-Based Double Perovskites in Acidic Media. ACS Catal. 2019, 9 (2), 8561–8574.

https://doi.org/10.1021/acscatal.9b01159

Chapter 4

Vos, J. G.; Venugopal, A.; Smith, W.A.; Koper, M. T. M. Competition and Interhalogen Formation During Parallel Electrocatalytic Oxidation of Bromide and Chloride on Pt. Submitted to the Journal of the Electrochemical Society, under review (2019).

Chapter 5

Vos, J. G.; Venugopal, A.; Smith, W.A.; Koper, M. T. M. 5. Competition and Selectivity During Parallel Evolution of Bromine, Chlorine and Oxygen on IrO_x Electrodes. To be submitted to the Journal of Catalysis, in preparation (2019).

Chapter 6

Vos, J. G.; Wezendonk, T. A.; Jeremiasse, A. W.; Koper, M. T. M. MnOx/IrOx as Selective Oxygen Evolution Electrocatalyst in Acidic Chloride Solution. J. Am. Chem. Soc. 2018, 140 (32), 10270–10281.

https://doi.org/10.1021/jacs.8b05382

Chapter 7

Vos, J. G.; Bhardwaj, A.A.; Jeremiasse, A.W.; Esposito, D.V; Koper, M. T. M. Modification of Selectivity Between Chlorine and Oxygen Evolution on Iridium-based Anodes and Pt Using SiOx-Based Buried Interfaces. To be submitted to ACS Chemistry of Materials, in preparation (2019).

Chapter 8

Vos, J. G.; Koper, M. T. M. Examination and Prevention of Ring Collection Failure during Gas-Evolving Reactions on a Rotating Ring-Disk Electrode. J. Electroanal. Chem. 2019, 850.

https://doi.org/10.1016/j.jelechem.2019.113363

Other publications

Bhardwaj, A.; Vos, J. G.; Koper, M. T. M.; Esposito, D. V. Ultrathin Silicon Oxide Overlayers Enable Selective Oxygen Evolution from Acidic and Unbuffered PH-Neutral Seawater. To be submitted to ACS Energy Letters, in preparation (2019).

Garcia, A. C.; Kolb, M. J.; van Nierop y Sanchez, C.; Vos, J.; Birdja, Y. Y.; Kwon, Y.; Tremiliosi-Filho, G.; Koper, M. T. M. Strong Impact of Platinum Surface Structure on Primary and Secondary Alcohol Oxidation during Electro-Oxidation of Glycerol. ACS Catal. 2016, 6 (7), 4491–4500.

Versluis, F.; Voskuhl, J.; Vos, J.; Friedrich, H.; Ravoo, B. J.; Bomans, P. H. H.; Stuart, M. C. A.; Sommerdijk, N. A. J. M.; Kros, A. Coiled Coil Driven Membrane Fusion between Cyclodextrin Vesicles and Liposomes. Soft Matter 2014, 10 (48), 9746–9751.

Arulmozhi, N.; Vos, J. G.; Koper, M. T. M.; Electrocatalytic Hydrogen Evolution and Hypochlorous Acid Reduction on Graphene-Covered Pt(111). Manuscript in preparation (2019).

Curriculum Vitae

Jan Vos was born in the historic village of The Hague, in late 1987. After finishing high school at Christelijk Gymnasium Sorghvliet in The Hague in 2006, he joined the Molecular Science and Technology study program at Leiden University. During his bachelor internship, he studied how lipid liposomes interact and fuse under supervision of dr. Frank Versluis and prof. dr. Alexander Kros, and in his main master internship, he studied the electrochemistry of glycerol oxidation on platinum single crystals under supervision of dr. Youngkook Kwon and prof. dr. Marc Koper within the CASC group, both of which projects resulted in a co-authored scientific publication. During this period, he also studied the electrochemical evolution of oxygen mediated by a cobalt-based molecular complex, under supervision of dr. Konstantin Kottrup and dr. Dennis Hetterscheid.

After finishing his master studies in 2015, he pursued his PhD studies during 2015-2019 under supervision of prof. dr. Marc Koper. The results of this project, which are presented in this thesis, significantly expanded the fundamental knowledge of how the simultaneous electrochemical evolution of oxygen and chlorine interact while proceeding on metal oxide surfaces. He presented his work on several international conferences, such as during Annual Meetings of the International Society of Electrochemistry in 2016 and 2018, as well as a Topical Meeting of this organization in 2019 concerning electrochemical processes for energy conversion. He also presented during CHAINS (2018), several technical meetings of chlor-alkali and chlorate industry representatives by Nouryon (formerly AkzoNobel), and the ECCM conference in The Hague in 2019. He was awarded the Poster Prize during the 2018 Reedijk symposium within the Leiden Institute of Chemistry. His scientific publication "MnO_x/IrO_x as Selective Oxygen Evolution Electrocatalyst in Acidic Chloride Solution", which is the basis of Chapter 6 of this thesis, was featured in JACS Spotlights and in a news article in C_2W, the magazine of the Royal Netherlands Chemical Society.

Starting in 2019, after finishing his PhD studies, Jan will work with Dennis Hetterscheid within the CASC group on the electrochemical oxygen reduction reaction, focusing on the selective electrosynthesis of hydrogen peroxide using a copper-based molecular complex. In this project, he strives to deepen the understanding of how this complex reduces oxygen to peroxide instead of water, and how to optimize the selectivity of this process.